Identifying And Overcoming Catalytic Bottlenecks In CuO-Based Oxide Systems For Energy And Environmental Applications

Ph.D. Thesis

By

SURESH CHANDRA BARAL



DISCIPLINE OF PHYSICS

INDIAN INSTITUTE OF TECHNOLOGY INDORE

FEBRUARY 2026

Identifying And Overcoming Catalytic Bottlenecks In CuO-Based Oxide Systems For Energy And Environmental Applications

Ph.D. Thesis

By

SURESH CHANDRA BARAL



DISCIPLINE OF PHYSICS

INDIAN INSTITUTE OF TECHNOLOGY INDORE

FEBRUARY 2026

Identifying and Overcoming Catalytic Bottlenecks in CuO-Based Oxide Systems for Energy and Environmental Applications

A THESIS

Submitted in partial fulfillment of the

requirements for the award of the degree

of

DOCTOR OF PHILOSOPHY

by

SURESH CHANDRA BARAL



DISCIPLINE OF PHYSICS

INDIAN INSTITUTE OF TECHNOLOGY INDORE

FEBRUARY 2026

INDIAN INSTITUTE OF TECHNOLOGY INDORE

I hereby certify that the work which is being presented in the thesis entitled **"Identifying and Overcoming Catalytic Bottlenecks in CuO-Based Oxide Systems for Energy and Environmental Applications"** in the partial fulfillment of the requirements for the award of the degree of **DOCTOR OF PHILOSOPHY** and submitted in the **Department of Physics, Indian Institute of Technology Indore**, is an authentic record of my own work carried out during the time period from December 2020 to February 2026 under the supervision of Prof. Somaditya Sen, Professor, Discipline of Physics, Indian Institute of Technology Indore.

The matter presented in this thesis has not been submitted by me for the award of any other degree of this or any other institute.

Signature of the student with date: 19/06/2026

(SURESH CHANDRA BARAL)

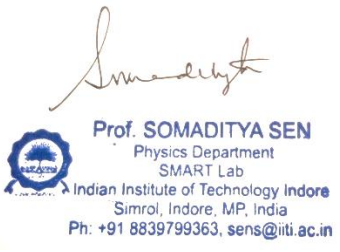
This is to certify that the above statement made by the candidate is correct to the best of my/our knowledge.

Prof. SOMADITYA SEN
Physics Department
SMART Lab
Indian Institute of Technology Indore
Simrol, Indore, MP, India
Ph: +91 8839799363, sens@iiti.ac.in

Signature of Thesis Supervisor with date: 19/06/2026

(Prof. Somaditya Sen)

SURESH CHANDRA BARAL has successfully given his/her Ph.D. Oral Examination held on **19/06/2026**.



Signature of Thesis Supervisor

Date: 19/06/2006

ACKNOWLEDGEMENTS

This thesis marks the culmination of my doctoral journey, which would not have been possible without the constant support, encouragement, and guidance of many individuals and institutions.

First and foremost, I express my sincere gratitude to God for His compassion and blessings throughout this journey. I am deeply indebted to my supervisor, Prof. Somaditya Sen, for his unwavering support, invaluable guidance, and continuous motivation. His insightful discussions, constructive criticism, and profound understanding of the subject played a pivotal role in shaping my research. Beyond academics, his principles, simplicity, and fatherly care have been a constant source of inspiration and will continue to guide me both professionally and personally. It has been a great privilege and honour to work under his supervision at IIT Indore, and I am sincerely grateful for the enriching learning experience he provided throughout my PhD.

I sincerely acknowledge Prof. Krushna Mavani and Prof. Apurba Kumar Das, members of my Post-Synopsis Progress Committee, for their valuable suggestions and critical evaluation, which significantly improved the quality of my research work. I also thank the Head of the Department of Physics, Prof. Pankaj R. Sagdeo, and Prof. Preeti Anand Bhobe for providing essential scientific and technical support during my research tenure. I am grateful to the entire Department of Physics, IIT Indore, for providing excellent facilities, infrastructure, and a stimulating research environment.

I gratefully acknowledge the support of the Central Workshop and Glass Blowing Section for their assistance in fabricating in-house experimental setups. I thank the IIT Indore administration, including the Directors and Deans, for providing a well-structured academic framework and a supportive environment that enabled the successful completion of this work. I am particularly thankful to the Dean of Academic Affairs and the academic staff for their continuous assistance in administrative and academic processes. Special thanks to Mr. Tapesh Parihar and Rahul Srivas (Academic Affairs) for their constant support. I also acknowledge SIC IIT Indore, especially Mr. Kinny Pandey, Mr. Nitin Upadhyay, Dr. Ravinder Kumar, Mr. Atul Singh, Ms. Kajal, and Mr. Ghanashyam Bhavsar, for their technical assistance and cooperation.

I would like to sincerely acknowledge Prof. Sudhagar Pitchaimuthu for hosting me as a visiting researcher at the Research Centre for Carbon Solutions (RCCS), Heriot-Watt

University, and for his valuable supervision, guidance, and support during this period. I am also grateful to Prof. Mercedes Maroto-Valer, Centre Director of RCCS, Prof. Susana García, and Dr. ir. Mijndert van der Spek for their encouragement, humility, and for creating a welcoming and intellectually stimulating research environment.

I sincerely acknowledge my research collaborators for their valuable technical contributions and support. I am grateful to Dr. Pravarthana Dhanapal, Assistant Professor, Department of Chemistry, and Dr. Krishna Kanta Haldar, Assistant Professor, Department of Chemistry, Central University of Punjab (CUPB), for their collaboration and for accommodating me in their laboratory during my short-term research visit for electrochemical measurements. I also thank the members of Dr. Haldar's research group for their assistance and cooperation during this period.

I express my sincere thanks to Dr. Arup Dasgupta, Senior Scientist, Indira Gandhi Centre for Atomic Research (IGCAR), Kalpakkam, for facilitating and supporting the transmission electron microscopy (TEM) measurements. I am also grateful to Dr. A. Mekki and Dr. K. Harribi at King Fahd University of Petroleum & Minerals (KFUPM), Saudi Arabia, for their assistance with X-ray photoelectron spectroscopy (XPS) measurements and analysis.

Their collaborative support significantly strengthened the experimental depth and quality of this research.

I would also like to sincerely acknowledge Dr. Rupesh S. Devan, Department of Metallurgical Engineering and Materials Science (MEMS), IIT Indore, for his support with UV–visible spectroscopy measurements and technical guidance. I am grateful to Prof. Mrigendra Dubey, MEMS, IIT Indore, for facilitating FTIR measurements and for his valuable insights. I also thank Dr. Sunil Kumar, MEMS, IIT Indore, for his constructive and insightful discussions that enriched the interpretation of experimental results.

I am thankful to Dr. Vishesh Manjunath for his valuable scientific discussions and suggestions that contributed to the refinement of key ideas in this work. I further acknowledge Prof. Debayan Sarkar, Department of Chemistry, IIT Indore, and his research group for their collaborative support and assistance during various stages of this research.

I express my deepest gratitude to my parents and family for their unconditional love, sacrifices, and unwavering belief in me. My mother and father have always been my greatest source of encouragement and inspiration. I'm grateful to have two wonderful brothers, Prakash and Santosh, who have been my backbone and support for the wonderful journey. Special

thanks go to my supervisor's family for helping me to become a positive person and providing a homely feeling in Indore. I want to thank my sisters Srishti and Sagnika for their constant support, encouragement, and love. I would also like to thank Soma Ma'am and Dadi for their motherly care and love.

I sincerely thank my laboratory colleagues, Dr. Ruhul, Dr. Saniya, Dr. Prashant, Mukul Kumar, Dr. Koyal, Dr. Maneesha, Rakhi, Manju, Poonam, Tabinda, and Vasim for providing a friendly and fulfilling environment in the lab. Special thanks to my colleague and brother, Dilip, for being a wonderful co-author, supportive, and constant motivation for good research. Additionally, I want to thank our MSc students, Rachit, Sayak, Kailash, Sandeep, Uttam, Prithwiraj, Prashant, and Karthik, for their support during experimental as well as lab work. Our wonderful interns, Vince, Parv, Sruti, Amit, Ankit, Payal, Ruchi, Ansh, Subhashree, Anubhav, Aditya, Mitali, Ankita, Anuradha, and Karuna were acknowledged for their fun-to-be-around environment at the lab. I thank Dr. E.G. Rini for her advice and motivation during the initial period at IITI.

I want to thank my little sister, Manusri, who has been a very positive source of energy during ups and downs at IITI, and brings rakhi every year to not get the feeling of being away from home.

I would like to express my heartfelt gratitude to my best friend, Sradhanjali, for her constant support, patience, encouragement, and care throughout this journey. Her presence played a significant role in making this period meaningful and fulfilling.

I sincerely thank my colleagues at RCCS, Michael, Michal, Neda, and Grace, for fostering a friendly and collaborative atmosphere. I am also grateful to my office mates, Dr. Amir Jahanbakhsh, Ali, Rachel, Ashween, and Arezoo, as well as the entire RCCS research group, for maintaining a positive and supportive working environment. I would like to acknowledge the support of our laboratory manager, Sean, for ensuring a pleasant, well-organized, and helpful laboratory environment. I am particularly grateful to Matthew McClean for his extensive assistance and training on various experimental facilities at RCCS, and for his continuous support whenever required.

I gratefully acknowledge the Indian Nanoelectronics Users' Programme (INUP-i2i) for providing advanced training opportunities and access to national nanofabrication and characterization facilities. I sincerely thank the centres at IIT Madras, CeNSE – Indian Institute of Science (IISc), Bangalore, IIT Kharagpur, and IIT Delhi for organizing familiarization and

hands-on training workshops on nanofabrication and advanced characterization techniques. These programs significantly enhanced my experimental expertise and broadened my understanding of cleanroom processes and device-level characterization.

I also acknowledge the workshops conducted at IIT Kharagpur on laser materials processing and surface engineering, and the Quality Improvement Program (QIP) short-term courses organized at IIT Indore, which strengthened my foundation in materials synthesis and characterization methodologies.

I would also like to express my sincere thanks to my friends Kamaljit, Ritu, Love, Susmita, and Mahnish for their constant companionship, encouragement, and support throughout this journey. I am grateful to my gym mates for their positivity and motivation, which helped me maintain both physical and mental well-being during demanding phases of my research.

I also sincerely acknowledge the support staff whose efforts often go unnoticed but are essential to a smooth academic life. I thank the GV drivers, mess and canteen staff, and security personnel for their cooperation, assistance, and dedication, which contributed to safety.

Finally, I gratefully acknowledge the Department of Science and Technology (DST), Government of India, for providing financial support through the INSPIRE Fellowship, which supported my doctoral research. I also sincerely thank the Commonwealth Scholarship Commission (CSC) for awarding me the Split-Site PhD Scholarship, which enabled me to undertake a part of my research at Heriot-Watt University, United Kingdom.

SURESH CHANDRA BARAL

Dedicated to

LORD JAGANNATH

MAA PALAPOCHHI

MY PARENTS

SUKANTI BARAL

SATYABADI BARAL

MY BROTHERS

PRAKASH CHANDRA BARAL

SANTOSH KUMAR BARAL

SYNOPSIS

Introduction and Background

The transition towards sustainable energy systems and environmentally benign chemical processes has intensified global research efforts on earth-abundant catalyst materials. Transition-metal oxides (TMOs) have attracted sustained attention due to their chemical robustness, tunable electronic structure, and applicability across a wide range of reactions relevant to energy conversion and environmental remediation. These include photocatalytic degradation of organic pollutants, advanced oxidation processes, and electrochemical water splitting for hydrogen production.

Despite their advantages, oxide catalysts frequently exhibit inferior activity when compared to expensive metal-based systems. This performance gap is often attributed to intrinsic limitations, such as charge-carrier localization, sluggish interfacial charge transfer, and strong coupling among electronic, ionic, and lattice degrees of freedom. Conventional strategies to improve oxide catalysts have focused primarily on morphology control, surface area enhancement, and compositional tuning. However, such approaches often yield incremental improvements without addressing the fundamental kinetic or interfacial steps that limit overall reaction rates.

A growing body of evidence suggests that catalytic performance in oxides is governed not by a single universal limitation, but also by reaction-specific bottlenecks that depend on how charge, mass, and redox equivalents are delivered to the active sites. Identifying these bottlenecks and designing strategies to selectively overcome them is therefore essential for rational catalyst design.

As bottlenecks have been detected in most TMOs, it is important to analyse at least one prominent TMO known to be a useful catalytic agent. One such example is Copper (II) oxide (CuO). A strong Cu 3d–O 2p hybridization is observed in CuO, which has a narrow band gap, and mixed electronic–ionic transport [1], [2] and is capable of charge-transfer. These features make CuO relevant to both photocatalytic and electrocatalytic processes, while also making it susceptible to electronic localization and kinetic constraints. As a result, CuO provides a unified platform to study how dopant valency, Cu–O covalency, and ligand-hole-associated

electronic structure collectively govern catalytic bottlenecks across diverse reaction regimes.

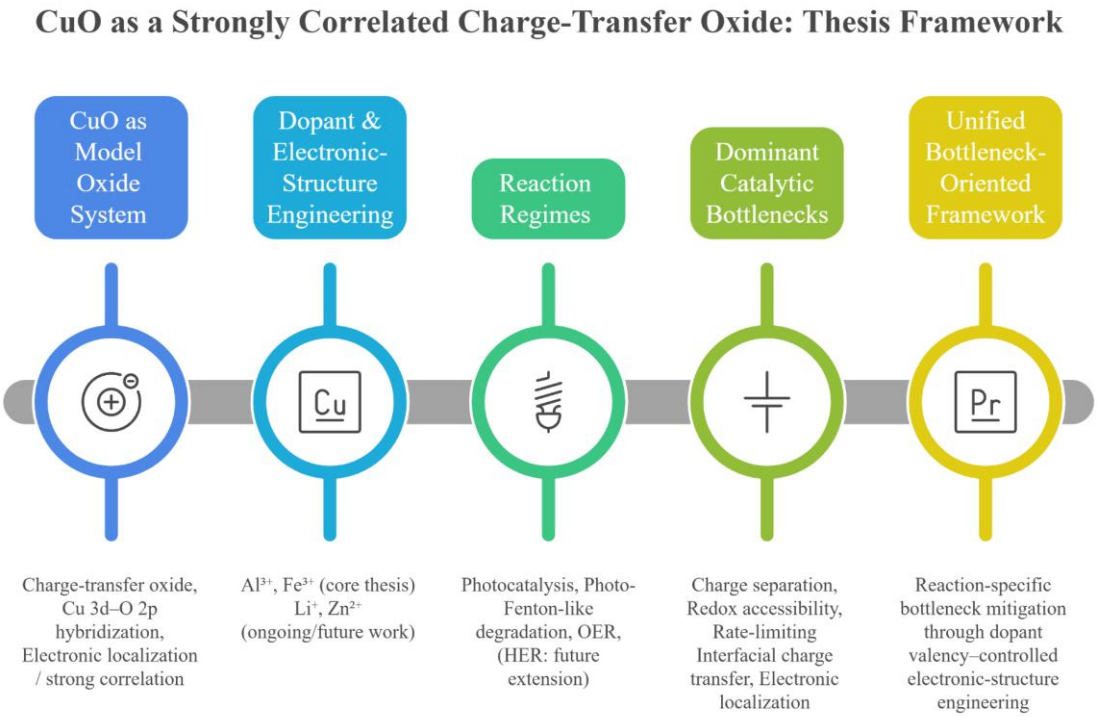


Figure S1: *Thesis roadmap and bottleneck-oriented strategy*

Gap in Existing Knowledge:

Established Understanding

Previous studies on oxide-based catalysts have established that catalytic activity can be influenced by particle size, morphology, surface area, and dopant incorporation. Numerous reports demonstrate that aliovalent and isovalent substitutions can modify optical absorption, defect concentration, and apparent reaction rates in photocatalysis and electrocatalysis. In electrochemical systems, parameters such as overpotential (determined from a linear-sweep voltammogram), reaction kinetics (determined from the Tafel slope), and electrochemically active surface area (determined from the electrical double-layer capacitance in the non-Faradaic region) are routine benchmarks for performance estimation. However, such analyses using regular tests are observed to yield several unresolved critical gaps in understanding performance and hence constitute bottlenecks in the field that need to be investigated.

Unresolved Gaps

There are several gaps in this section that are extremely important and have been somewhat overlooked so far due to the complexity of the problems. To start with, it needs to be emphasized that the nature of the elementary step becomes a dominant rate-limiting bottleneck under a given reaction condition. These elementary steps can be (i) charge separation, (ii) interfacial charge transfer, (iii) surface reaction, or (iv) mass transport. Next, the effect of dopants is not linear in nature. It is often observed that at low concentrations, dopants exhibit a promoter behavior, while at higher loadings, they become inhibitory. Such a phenomenon is rarely analyzed mechanistically. Moreover, photocatalytic, photo-Fenton-like, and electrocatalytic processes are typically treated as independent phenomena, despite sharing common electronic and interfacial constraints in oxide materials.

Most importantly, there is a lack of a unified, reaction-specific framework that explicitly links dopant valency, Cu–O covalency/charge-transfer character (ligand-hole physics), and interfacial kinetics to the identification and mitigation of catalytic bottlenecks [3]. Hence, the central motivation of the present thesis is to address this gap using CuO as a model.

Aspects discussed to meet the objective

As discussed in the previous section, the primary objective of this thesis is to identify reaction-specific catalytic bottlenecks in CuO-based oxides and selectively mitigate them through defect engineering, dopant-valency control, and morphology modulation. The work focuses on photocatalytic, photo-Fenton-like, and anodic electrocatalytic (OER) processes, while cathodic hydrogen evolution studies are treated as ongoing and future extensions.

CuO was selected as a model because its strong Cu 3d–O 2p hybridization gives it charge-transfer character, mixed transport, and pronounced electronic localization features, making catalytic bottlenecks experimentally accessible across both photo- and electro-catalytic regimes. This enables a controlled investigation of how dopant valency and Cu–O covalency (ligand-hole physics) govern bottleneck switching under different driving forces.

- To identify charge-separation and redox-accessibility limitations in photocatalytic and photo-Fenton-like degradation processes.
- To investigate aliovalent Al^{3+} substitution for defect-driven photocatalysis.
- To isolate morphology and dimensionality effects using CuO nanosheets.

- To elucidate redox-mediated photo-Fenton-like degradation in Fe-doped CuO.
- To resolve interfacial and surface-reaction bottlenecks in alkaline oxygen evolution reaction (OER) using impedance-resolved analysis.
- To develop a unified, reaction-specific bottleneck framework applicable to oxide catalysts beyond CuO.

Experimental and Analytical Methodology

CuO-based nanostructures with controlled substitution of Al^{3+} and Fe^{3+} were synthesized using wet-chemical and sol-gel routes to ensure phase purity and compositional reproducibility. Li^{+}, and Zn^{2+} substitutions were explored in parallel as part of ongoing extensions toward alkaline HER. The dopants were selected to represent distinct valency classes and catalytic roles within a single CuO host. Al^{3+} (non-redox) was chosen to perturb Cu–O covalency and ligand-hole redistribution without introducing additional redox centers; Fe^{3+} (redox-active) was selected to introduce dopant-mediated redox participation and enable promoter–inhibitor crossover analysis. Li^{+} (aliovalent, monovalent) was used to enhance electronic charge delivery in alkaline HER, while Zn^{2+} (divalent, near-isovalent with Cu^{2+}) was employed to tune adsorption/structural environment with comparatively smaller impact on bulk electronic transport.

Structural and microstructural characterization was carried out using X-ray diffraction and Raman spectroscopy, complemented by electron microscopy and Brunauer–Emmett–Teller surface area analysis.

Electronic structure and defect chemistry were investigated using X-ray photoelectron spectroscopy, with particular emphasis on Cu 2p final-state features (screened vs poorly screened components), O 1s lattice vs oxygenated surface components as proxies for surface electronic structure, and dopant-induced changes in electronic screening and Cu–O covalency (ligand-hole character) [4]. Optical properties were examined using UV–visible spectroscopy.

Photocatalytic and photo-Fenton-like degradation experiments were conducted under controlled illumination and temperature conditions. Reaction kinetics were analyzed using Arrhenius- and Eyring-based approaches to distinguish thermal activation from light-driven processes.

Electrocatalytic activity toward oxygen and hydrogen evolution was evaluated in alkaline media using linear sweep voltammetry, Tafel analysis, and electrochemical impedance spectroscopy. Impedance analysis enabled separation of charge-transfer, adsorption, and surface-reaction resistances, providing direct insight into dominant kinetic bottlenecks.

Results and Discussion

The thesis work will be discussed along the following sequence:

- Al^{3+} -substituted CuO as a ligand-hole–associated electronic modulation and redox accessibility governing photo-Fenton-like activity without redox dopants.
- CuO nanosheets as a temperature-assisted detrapping/polaronic hopping and its impact on light-driven kinetics versus dark adsorption.
- Fe^{3+}-substituted CuO (photo-Fenton-like catalysis) – dopant-mediated redox cycling and reactive oxygen species regeneration, establishing a mechanistic transition from defect-assisted to redox-assisted degradation pathways.
- Fe^{3+}-substituted CuO (oxygen evolution reaction) – impedance-resolved identification of interfacial and surface-reaction bottlenecks and demonstration of promoter–inhibitor crossover under alkaline OER conditions.

Al-Substituted CuO: Non-Redox Dopant Effects in Photo-Fenton-Like Degradation

This study investigates the role of a non-redox-active dopant (Al^{3+}) in modulating photocatalytic and photo-Fenton-like degradation over CuO [5]. Spectroscopic and kinetic analyses show that the enhancement is attributed to ligand-hole–associated charge redistribution within the Cu–O network (charge-transfer character), improving redox accessibility under illumination and H_2O_2 activation. This establishes that catalytic enhancement can be achieved through covalency- and screening-controlled electronic modulation rather than by introducing new redox-active dopants.

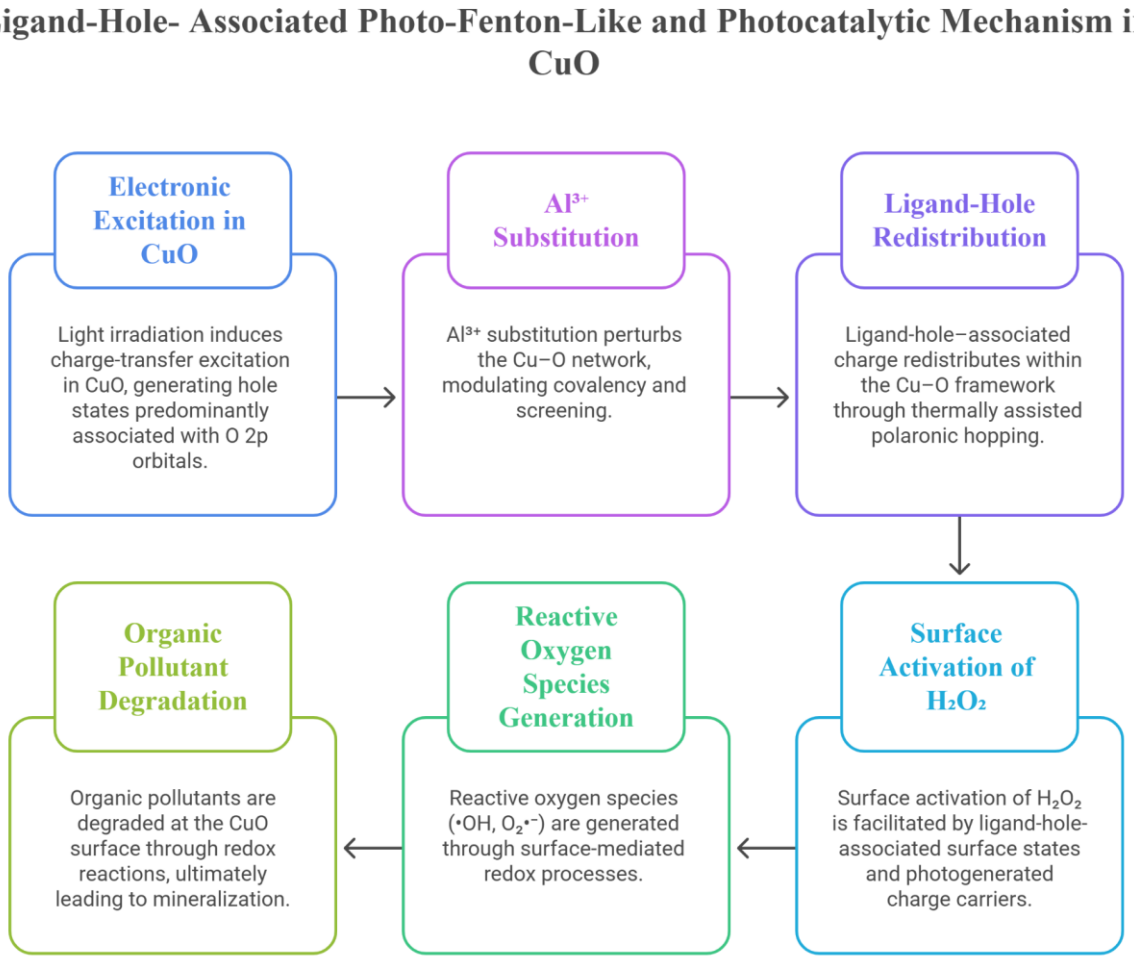


Figure S2: *Ligand-hole-associated photo-Fenton-like and photocatalytic mechanism in Al-substituted CuO.*

Temperature-Dependent Photocatalysis over CuO Nanosheets

The influence of temperature on photocatalytic degradation was examined using CuO nanosheets. While dark adsorption decreased with increasing temperature, light-driven reaction rates increased significantly. Kinetic analysis confirms that thermal activation primarily accelerates charge-carrier hopping, detrapping, and reactive oxygen species regeneration rather than adsorption [6]. This chapter demonstrates that photocatalytic performance is limited by electronic activation barriers rather than surface coverage.

Temperature-Assisted Detrapping and Ligand-Hole-Associated Polaronic Charge Transport in CuO

Characteristic	Low Temperature (T_1)	Elevated Temperature (T_2)	Light + Temperature Synergy
CuO Lattice	Cu 3d–O 2p hybridization	Cu 3d–O 2p hybridization	Cu 3d–O 2p hybridization
Charge Carriers	Localized in trap states (ligand-hole associated)	Polaronic hopping through Cu–O network	Synergistic enhancement of detrapping and hopping
Charge Mobility	Low	Thermally activated	Accelerated
Surface Redox Kinetics	Slow	Improved	Accelerated
Light Irradiation	None	None	hν inducing charge-transfer excitation ($\Delta < U$)
Key Process	Localized charges	Thermal detrapping and polaronic hopping	Synergistic detrapping and hopping

Figure S3: *Temperature-assisted detrapping and ligand-hole-associated polaronic transport in CuO (Δ: charge-transfer energy, U: on-site Coulomb repulsion).*

Fe-Substituted CuO: Redox-Active Dopant-Induced Mechanistic Transition

Fe^{3+} substitution introduces redox-active centers into the CuO lattice in addition to modifying the Cu–O electronic network, resulting in faster redox cycling and enhanced ROS regeneration (•OH-dominated). Comparative analysis with Al-substituted systems reveals a mechanistic transition from ligand-hole-assisted pathways to dopant-mediated redox processes. This chapter highlights the critical role of dopant valency in determining reaction mechanisms, not merely reaction rate.

Fe–CuO for Oxygen Evolution Reaction: Impedance-Resolved Bottleneck Identification

Electrocatalytic OER over Fe–CuO was investigated using impedance spectroscopy [7]. Two distinct resistive regimes were identified, corresponding to interfacial charge-transfer

limitations and slower surface-reaction steps. A promoter–inhibitor crossover with dopant concentration was observed, demonstrating that excessive modification can introduce new bottlenecks [8]. This chapter provides an impedance-resolved map of OER bottlenecks in CuO-based oxides.

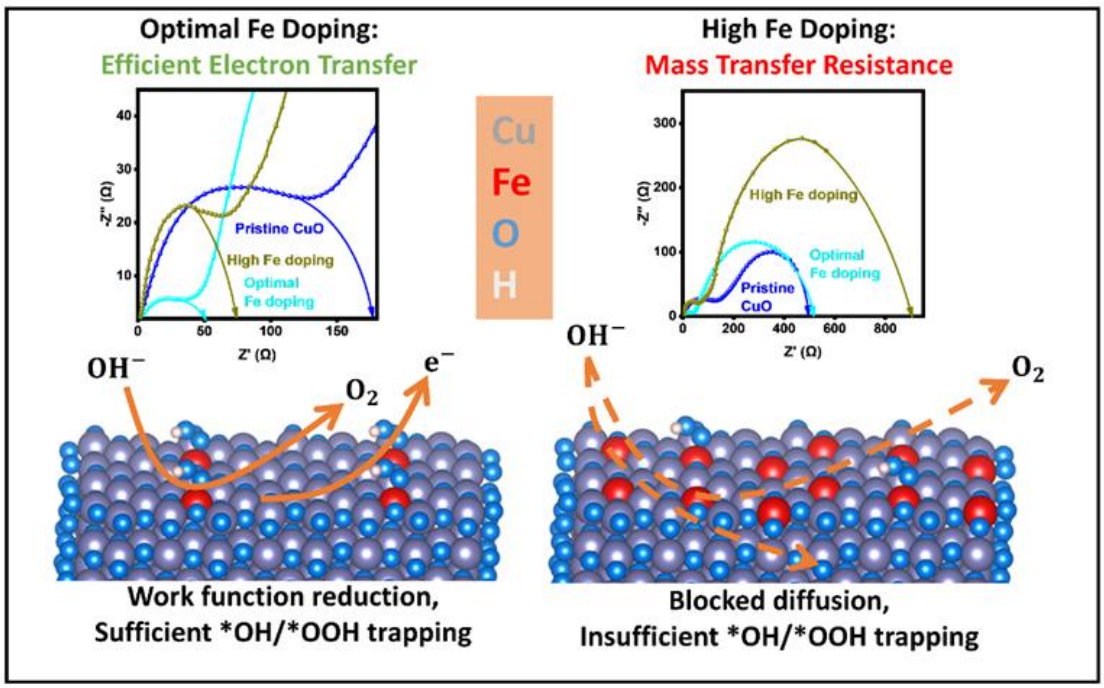


Figure S4: *Impedance-resolved promoter–inhibitor crossover in Fe-substituted CuO during alkaline OER. Schematic comparison of optimal and high Fe doping regimes correlated with the corresponding Nyquist impedance spectra. At optimal Fe content, reduced interfacial charge-transfer resistance and favorable *OH/*OOH adsorption contribute to improved electrochemical kinetics and enhanced catalytic activity. At higher Fe concentrations, excessive surface coverage and stronger intermediate binding increase interfacial and surface-reaction-related resistance, resulting in kinetically hindered OER behavior. The apparent linear-like feature observed in the zoomed impedance region arises from the magnified representation of overlapping semicircular responses and should not be interpreted as an explicit Warburg diffusion component. The figure highlights the promoter–inhibitor crossover identified through potential-dependent EIS analysis and its relation to interfacial and surface kinetic processes in Fe-substituted CuO.*

Unified Bottleneck-Oriented Framework

Across photocatalytic, photo-Fenton-like, and electrocatalytic regimes, catalytic performance in CuO-based systems is governed by how efficiently the Cu–O charge-transfer network delivers redox equivalents to the surface, i.e., by ligand-hole density, Cu–O covalency, electronic screening, and interfacial kinetics. The catalytic bottleneck is dominated by dopant valency, which tunes the situation by shifting the balance between localized and delocalized compensation and the accessibility of surface redox steps. This establishes a generalizable bottleneck-oriented design paradigm for oxide catalysts [9].

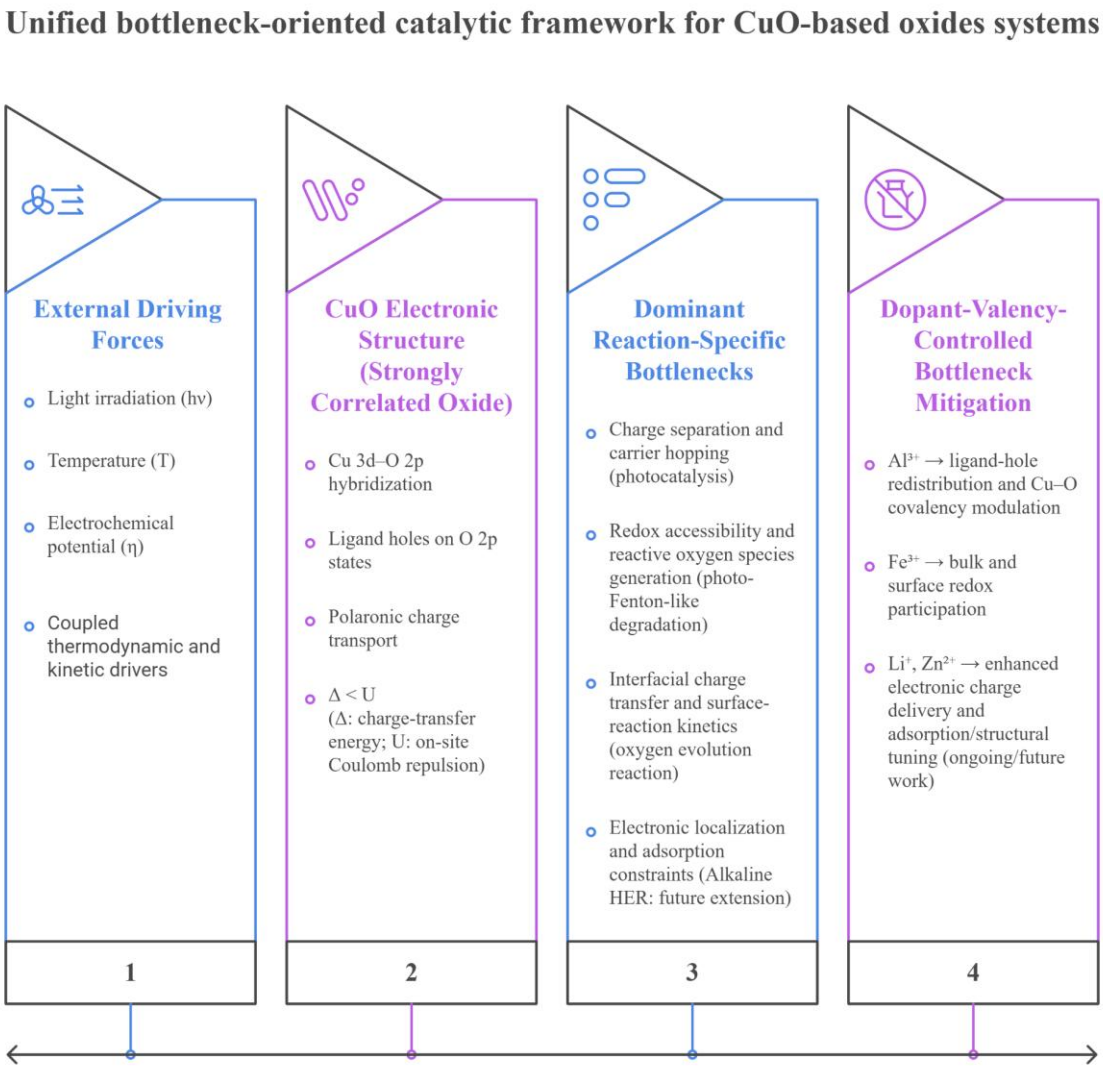


Figure S5: *Unified bottleneck-oriented framework for CuO-based photocatalytic and electrocatalytic processes. Schematic framework illustrating how external driving forces (light, temperature, and electrochemical potential) interact with the strongly correlated Cu–O*

electronic structure to determine reaction-specific catalytic bottlenecks. Dopant valency selectively modulates ligand-hole density, Cu–O covalency, and charge transport, enabling targeted mitigation of bottlenecks across photocatalysis, photo-Fenton-like degradation, oxygen evolution (with hydrogen evolution as an ongoing/future extension).

Ongoing and Future Work

Investigations on Li^{+}- and Zn^{2+}-substituted CuO for alkaline hydrogen evolution reaction (HER) are ongoing. These studies extend the bottleneck-oriented framework developed in this thesis to cathodic reactions but are not included as core chapters of the thesis.

Major Contributions of the Thesis

- Introduced a reaction-specific, bottleneck-oriented strategy for oxide catalyst design.
- Demonstrated ligand-hole–associated electronic modulation inferred from XPS and kinetic analysis of photo-Fenton-like degradation without introducing redox-active dopants.
- Established thermally assisted polaronic hopping/detrapping as a key factor in light-driven kinetics in CuO-based photocatalysis.
- Identified promoter–inhibitor crossover in CuO-based OER using impedance-resolved analysis.
- Unified photocatalytic and electrocatalytic behavior under a single conceptual framework.

Summary and Concluding Remarks

This thesis demonstrates that the apparent limitations of oxide catalysts arise from reaction-specific bottlenecks rather than intrinsic material inadequacy. By explicitly identifying and addressing these bottlenecks, oxide-based catalysts can be rationally optimized for both environmental remediation and energy conversion. The framework developed in this work is transferable to other correlated oxide systems and provides a foundation for future operando studies and device-level implementation.

References

[1] J. Zaanen, G. A. Sawatzky, and J. W. Allen, “Band gaps and electronic structure of transition-metal compounds,” *Phys. Rev. Lett.*, vol. 55, no. 4, pp. 418–421, Jul. 1985, doi: 10.1103/PhysRevLett.55.418.

[2] J. Ghijsen *et al.*, “Electronic structure of ${\mathrm{Cu}}_{2}$O and CuO,” *Phys. Rev. B*, vol. 38, no. 16, pp. 11322–11330, Dec. 1988, doi: 10.1103/PhysRevB.38.11322.

[3] J. Suntivich, H. A. Gasteiger, N. Yabuuchi, H. Nakanishi, J. B. Goodenough, and Y. Shao-Horn, “Design principles for oxygen-reduction activity on perovskite oxide catalysts for fuel cells and metal-air batteries,” *Nat. Chem.*, vol. 3, no. 7, pp. 546–550, Jun. 2011, doi: 10.1038/nchem.1069.

[4] M. A. van Veenendaal and G. A. Sawatzky, “Nonlocal screening effects in 2p x-ray photoemission spectroscopy core-level line shapes of transition metal compounds,” *Phys. Rev. Lett.*, vol. 70, no. 16, pp. 2459–2462, Apr. 1993, doi: 10.1103/PhysRevLett.70.2459.

[5] J. J. Pignatello, E. Oliveros, and A. MacKay, “Advanced Oxidation Processes for Organic Contaminant Destruction Based on the Fenton Reaction and Related Chemistry,” *Crit. Rev. Environ. Sci. Technol.*, vol. 36, no. 1, pp. 1–84, Jan. 2006, doi: 10.1080/10643380500326564.

[6] I. G. Austin and N. F. Mott, “Polarons in crystalline and non-crystalline materials,” *Adv. Phys.*, vol. 18, no. 71, pp. 41–102, Jan. 1969, doi: 10.1080/00018736900101267.

[7] A. Lasia, *Electrochemical Impedance Spectroscopy and its Applications*. New York, NY: Springer, 2014. doi: 10.1007/978-1-4614-8933-7.

[8] N. Danilovic *et al.*, “Activity-Stability Trends for the Oxygen Evolution Reaction on Monometallic Oxides in Acidic Environments,” *J. Phys. Chem. Lett.*, vol. 5, no. 14, pp. 2474–2478, Jul. 2014, doi: 10.1021/jz501061n.

[9] J. O. Bockris, A. K. N. Reddy, and M. Gamboa-Aldeco, Eds., “The Electrified Interface,” in *Modern Electrochemistry 2A: Fundamentals of Electrodics*, Boston, MA: Springer US, 2000, pp. 771–1033. doi: 10.1007/0-306-47605-3_1.

LIST OF PUBLICATIONS

Publications Arising from the Thesis

1. **Suresh Chandra Baral**, P. Maneesha, Prashant Kumar Mishra, Pravarthana Dhanapal, and Somaditya Sen (2024). "Rapid Photocatalytic Degradation of Organic Pollutants by Al^{3+} doped CuO Powders under Low Power Visible Light and Natural Sunlight." Optical Materials, Volume 147, 114653. DOI: https://doi.org/10.1016/j.optmat.2023.114653

2. **Suresh Chandra Baral**, P. Maneesha, Sayak Datta, Kailash Dukiya, Dilip Sasmal, Koyal Suman Samantaray, Vaishnavi Krupa B R, Arup Dasgupta, and Somaditya Sen (2024). "Enhanced Photocatalytic Degradation of organic pollutants in Water using Copper Oxide (CuO) Nanosheets for Environmental Application." JCIS Open, 100102. DOI: https://doi.org/10.1016/j.jciso.2024.100102

3. **Suresh Chandra Baral**, Dilip Sasmal, Manju Kumari, Rakhi Saha, Sayak Datta, Mange Ram, Krishna Kanta Haldar, A. Mekki, K. Harrabi, Sudhagar Pitchaimuthu, and Somaditya Sen, "Interfacial and Kinetic Limitations in Alkaline OER: A case study of Electronic Modifications using Fe in CuO lattice." [**Accepted for Publications, Small Methods, Wiley]**

4. **Suresh Chandra Baral**, Dilip Sasmal, Sayak Datta, A Mekki, K. Harrabi, Sudhagar Pitchaimuthu, and Somaditya Sen " Defect-Engineered Fe-Doped CuO Ceramics: Local Coordination, Electronic-Structure and Surface Modulation for Enhanced Photo-Fenton Activity under Low-Power Visible Illumination" [**Under Review]**

5. **Suresh Chandra Baral**, Dilip Sasmal, Manusri Ajmeera, Sradhanjali Lenka, Krishna Kanta Haldar, A Mekki, K. Harrabi, Sudhagar Pitchaimuthu, and Somaditya Sen "Dopant-Charge-Driven Modulation of Alkaline Hydrogen Evolution on CuO: A Comparative Study of Li^{+} and Zn^{2+} Substitution." [**In Preparation**]

List of Publications During PhD

1. **Suresh Chandra Baral**, Uttama Kumar Saint, Dilip Sasmal, Sradhanjali Lenka, Ashish Kalkal, A. Mekki, and Sudhagar Pitchaimuthu (2024). "Interfacial Synergy in Ag-Doped CuO-AgCl-g-C_3N_4 Composites for Efficient Charge Separation and Low-power Methylene Blue Degradation." DOI: https://doi.org/10.48550/arXiv.2512.04825 [Under Review]
2. **Suresh Chandra Baral**, Dilip Sasmal, Mitali Hupele, Sradhanjali Lenka, Somaditya Sen (2024). "Recent advances in hydrogen production using sulfide-based photocatalysts." [Under Review] DOI: https://doi.org/10.48550/arXiv.2412.05658
3. **Suresh Chandra Baral**, P. Maneesha, E.G. Rini, Somaditya Sen (2023). "Recent advances in La_2NiMnO_6 double perovskites for various applications: challenges and opportunities." Progress in Solid State Chemistry, Volume 72. DOI: https://doi.org/10.1016/j.progsolidstchem.2023.100429
4. P. Maneesha, **Suresh Chandra Baral**, E.G. Rini, Somaditya Sen (2023). "An overview of the recent developments in the structural correlation of magnetic and electrical properties of Pr_2NiMnO_6 double perovskite." Progress in Solid State Chemistry, Volume 70. DOI: https://doi.org/10.1016/j.progsolidstchem.2023.100402
5. Uttama Kumar Saint, **Suresh Chandra Baral**, Dilip Sasmal, P Maneesha, Sayak Datta, Farzana Naushin, Somaditya Sen (2024). "Effect of pH on photocatalytic degradation of Methylene Blue in water by facile hydrothermally grown TiO_2 Nanoparticles under Natural Sunlight." DOI: https://doi.org/10.1016/j.jciso.2025.100150
6. P. Maneesha, Koyal Suman Samantaray, **Suresh Chandra Baral**, Grace Brzykcy, Indranil Bhaumik, Abdelkrim Mekki, Arjun K. Pathak, Somaditya Sen (2024). "Effect of oxygen vacancies and cationic valence state on multiferroicity and magnetodielectric coupling in (1-x)$BaTiO_3$·x$LaFeO_3$ solid solution." Journal of Alloys and Compounds, Volume 971. DOI: https://doi.org/10.1016/j.jallcom.2023.172587
7. P. Maneesha, Koyal Suman Samantaray, **Suresh Chandra Baral**, R. Mittal, Mayanak K. Gupta, Somaditya Sen (2024). "Defect/disorder correlated modification of transport properties from hopping to tunneling processes in $BaTiO_3$-$LaFeO_3$ solid solution." J. Appl. Phys., 135(19), 194102. DOI: https://doi.org/10.1063/5.0195109
8. Rakhi Saha, Koyal Suman Samantaray, P Maneesha, **Suresh Chandra Baral**, Sachin Sarangi, Rajashri Urkude, Biplab Ghosh, Abdelkrim Mekki, Khalil Harrabi, Somaditya Sen (2025). "Room temperature ferromagnetism induced by high valence cation (V^{4+}/V^{5+})

substitution in $SrFeO_{3-x}$." Ceramics International. DOI: https://doi.org/10.1016/j.ceramint.2025.06.220

9. Koyal Suman Samantaray, Sourabh Kumar, P Maneesha, Dilip Sasmal, **Suresh Chandra Baral**, B.R. Vaishnavi Krupa, Arup Dasgupta, K Harrabi, A Mekki, Somaditya Sen (2024). "Contribution of piezoelectric effect on piezo-phototronic coupling in ferroelectrics: A theory assisted experimental approach on NBT." The Journal of Chemical Physics, J. Chem. Phys. 161, 184711. DOI: https://doi.org/10.1063/5.0227731
10. Manju Kumari, Dilip Sasmal, **Suresh Chandra Baral**, Maneesha P, Poonam Singh, Abdelkerim Mekki, Khalil Harrabi, Somaditya Sen, "Increased Covalence and V-center mediated Dark Fenton-Like Reactions in V-doped TiO2: Mechanisms of Enhanced Charge-Transfer." [Under Review]
11. Michael Robert Furness, Ashish Kalkal, Tia Wardlaw, Jessica Valli, **Suresh Chandra Baral**, Pablo Lozano Sanchez, Marco Caffio, Sudhagar Pitchaimuthu, Jason Webber, Anitha Devadoss (2025). "Electroactive 3D Porous Graphene Foam based Ultrasensitive Impedimetric Biosensor for Detection of MCF-7 cells derived Extracellular Vesicles in Human Serum." [Under Review]
12. Dilip Sasmal, **Suresh Chandra Baral**, Ashis Maharathi, and Somaditya Sen (2025). "H_2 production from water using metal oxide-based photocatalysts." [In Preparation]

List of Book Chapters Published During PhD

1. **Suresh Chandra Baral**, P. Maneesha, Srishti Sen, Sagnika Sen and Somaditya Sen (2023). "An introduction to the metal oxides." In: Optical Properties of Metal Oxide Nanostructures, Progress in Optical Science and Photonics, vol 26. Springer, Singapore. DOI: https://doi.org/10.1007/978-981-99-5640-1_1
2. **Suresh Chandra Baral**, P. Maneesha, Ananya T. J, Srishti Sen, Sagnika Sen, Somaditya Sen and E. G. Rini (2022). "Rare earth manganites and related multiferroicity." CRC Press, Emerging Applications of Low Dimensional Magnets, 163-180. DOI: https://doi.org/10.1201/9781003196952
3. P. Maneesha, **Suresh Chandra Baral**, E. G. Rini and Somaditya Sen (2022). "Crystal structures and properties of nanomagnetic materials." CRC Press, Fundamentals of Low Dimensional Magnets V1, 207-223. DOI: https://doi.org/10.1201/9781003197492

List of Conferences & workshop

presentation/attended during PhD

1. Poster Presentation at the RSC 5th International Solar Fuels Conference, 1 - 5 September 2025, Newcastle, United Kingdom.

2. Poster Presentation at the 2nd International Conference on "Advanced Nanomaterials for Energy, Environment and Healthcare Applications", Tamil Nadu, India

    - Symposia-I Green Energy Technologies UK-India Workshop on Hydrogen Generation and Storage (Funded by British Council, UKIERI, SPARC India)

    - Symposia II: Nanomaterials Synthesis, Characterization, and Healthcare/Environmental Applications

3. Hands-on training, 9-19 October 2023, Semiconductor device fabrication and characterization, IISc, Bangalore.

4. Hands-on training, 16-25 August 2023, Optoelectronic device fabrication and characterization, IIT, Kharagpur.

5. Hands-on training, 10-19 July 2023, Silicon and Perovskite solar cell fabrication and characterization, IIT, Madras.

TABLE OF CONTENTS

LIST OF FIGURES xxxviii
LIST OF TABLES xlviii
NOMENCLATURE l
ACRONYMS liii
Chapter 1 Introduction 1
1.1. Motivation and Background 2
1.1.1. Global Energy Demand and the Role of Fossil Fuels 2
1.1.2. Climate Change and the Urgency of Carbon Neutrality 2
1.1.3. Hydrogen as a Clean Energy Carrier 5
1.1.4. Environmental Pollution and Water Contamination 6
1.2. Fundamentals of Photocatalysis and Electrocatalysis 12
1.2.1. Photocatalysis 12
1.2.1.1 Photon Absorption and Charge Generation 13
1.2.1.2 Charge Separation and Migration 13
1.2.1.3 Interfacial Surface Reactions 14
1.2.1.4 Generation of Reactive Oxygen Species (ROS) 14
1.2.1.5 Role of ROS in Photocatalytic Degradation 14
1.2.2 Electrocatalysis 15
1.2.2.1 Concepts in Electrocatalysis 16
1.2.2.2 Hydrogen Evolution Reaction (HER) Mechanism 16
1.2.2.3 Oxygen Evolution Reaction (OER) Mechanism 17
1.2.2.4 Electrocatalytic Performance Descriptors 18

1.2.2.4.1 Overpotential (η) 18
1.2.2.4.2 Tafel Slope 19
1.2.2.4.3 Exchange Current Density (j_0) 19
1.2.2.4.4 Electrochemical Active Surface Area (ECSA) 19
1.2.2.4.5 Charge-Transfer Resistance (R_{ct}) 19
1.2.2.4.6 Turnover Frequency (TOF) 19
1.2.2.4.7 Stability Metrices 19
1.2.2.5 Relevance to Transition Metal Oxides 20
1.2.3 Transition Metal Oxides as Catalysts 20
1.2.3.1 Electronic Structure and Redox Flexibility 20
1.2.3.2 Defect Chemistry and Catalytic Function 21
1.2.3.3 Band Structure and Photocatalytic Properties 22
1.2.3.4 Electrocatalytic Activity of TMOs 22
1.3. CuO as Catalyst 23
1.3.1. Crystal Structure, Electronic Configuration, and Crystal Field Effects 23
1.3.2 Structure and Electronic Properties 24
1.3.3 Defects and Conduction Mechanisms 25
1.3.4 Catalytic Applications of CuO 26
1.3.5 Limitations of Pristine CuO 27
1.3.6 Strategies for Performance Enhancement 27
1.4. Scope and Objectives of the Thesis 29
1.4.1. Scope 29

1.4.2. Objectives 30
1.5. Structure of the Thesis 31
Chapter 2 Experimental Methods and Characterization Techniques .34
2.1. Experimental Methods 35
2.1.1. Materials and Reagents 35
2.1.2. Synthesis of CuO-Based Materials 35
2.1.2.1. Sol-Gel synthesis of CuO 35
2.1.2.2. Sol-Gel synthesis of Al^{3+} doped CuO 36
2.1.2.3. Sol-Gel synthesis of Fe^{3+} doped CuO 37
2.1.2.4. Sol-Gel synthesis of Li- and Zn-doped CuO 38
2.1.3. Hydrothermal synthesis of CuO 39
2.1.4. Photocatalytic and Photo-Fenton-like Experiments 40
2.1.5. Electrode Preparation 43
2.2. Physicochemical Characterization Techniques 43
2.2.1. X-Ray Diffraction (XRD) 44
2.2.2. Raman Spectroscopy 49
2.2.2.1. Laser Source 51
2.2.2.2. Sample illumination system 51
2.2.2.3. Spectrometer 51
2.2.3. Fourier Transform Infrared (FT-IR) Spectroscopy 53
2.2.4. Field Emission Scanning Electron Microscope (FE-SEM) 55
2.2.5. TEM, High Resolution TEM (HRTEM), and SAED 57

2.2.5.1. Instrumentation 58
2.2.6. UV-Vis Diffuse Reflectance Spectroscopy (UV-Vis DRS) 62
2.2.7. X-ray Photoelectron Spectroscopy (XPS) 67
2.2.8. Brunauer-Emmett-Teller (BET) 69
2.2.9. Brunauer-Emmett-Teller (BET) ..... **Error! Bookmark not defined.**
2.2.10. Electrochemical Characterization Techniques 72
2.2.10.1. Cyclic Voltammetry (CV) 72
2.2.10.2. Linear Sweep Voltammetry (LSV) 73
2.2.10.3. Electrochemical Impedance Spectroscopy (EIS) 73
2.2.10.4. Chronopotentiometry (CP) 74
2.2.10.5. Chronoamperometry (CA) 74
2.3. Chapter Summary 74
Chapter 3 Aliovalent Al^{3+} Substitution in CuO: Defect-Driven and Ligand-Hole-Associated Photo-Fenton-Like Photocatalysis 76
3.1. Chapter Introduction and Scope 77
3.2. Chapter Introduction and Scope ..... **Error! Bookmark not defined.**
3.3. Structural, Optical, and Surface Properties 79
3.3.1. XRD Analysis 79
3.3.2. Raman spectroscopy 83
3.3.3. FTIR Analysis 84
3.3.4. UV-Vis DRS Analysis 85
3.3.5. Surface Morphology 87

3.3.6. Surface area analysis 89

3.3.7. Dynamic light scattering (DLS) analysis 91

3.4. Photocatalytic Performance and Kinetics 94

3.4.1. Photocatalysis under household LED 94

3.4.1.1. Effect of Temperature on dye degradation of Al^{3+} doped CuO 94

3.4.1.2. Comparison of Photocatalytic activity of C0 and CA1 at 59 ^{0}C: 96

3.4.1.3. Effect of catalyst concentration 97

3.4.1.4. Effect of H_2O_2 concentration 97

3.4.1.5. Photocatalytic degradation of Methyl orange (MO) and Rhodamine B (RhB) 100

3.4.2. Photocatalysis under Sunlight 101

3.5. Photo-Fenton-Like Degradation Mechanism 104

3.5.1. Scavenger test 109

3.5.2. Hydroxyl radicals' detection by Steady-State Fluorescence spectroscopy: .. 110

3.6. Stability, Reusability, and Practical Implications 110

3.6 Chapter Summary 116

Chapter 4 CuO Nanosheets: Morphology-Controlled and Temperature-Assisted Charge Transport in Photocatalysis 118

4.1. Chapter Introduction and Objectives 119

4.2. Synthesis and Experimental Methods 120

4.3. Structural, Optical, and Surface Properties 120

4.4. Photocatalytic Performance and Kinetics 125

4.4.1. Photocatalysis with commercially available 11 W UV light 126

4.4.2. Photocatalysis under Direct Sunlight 133
4.5. Photo-Fenton-Like Degradation Mechanism 134
4.6. Stability, Reusability, and Practical Implications 139
4.7. Chapter Summary 142
Chapter 5 Redox-Active Fe-Substituted CuO: Photo-Fenton-Like Oxidation and Reaction-Pathway Switching 145
5.1. Chapter Introduction and Objectives 146
5.2. Synthesis and Experimental Methods 148
5.3. Structural, Optical, and Surface Properties 149
5.3.1. Structural studies 149
5.3.2. Surface Morphological 152
5.3.3. Phonon studies 154
5.3.4. Optical Studies 157
5.3.5. Surface Area Analysis 159
5.3.6. Chemical Composition Analysis 161
5.3.7. Surface Charge and Hydrodynamic Analysis 165
5.4. Photo-Fenton activity of Fe-doped and Kinetics 166
5.5. Photo-Fenton-Like Degradation Mechanism 171
5.6. Chapter Summary 178
Chapter 6 Resolving Oxidation-Side Catalytic Bottlenecks in Alkaline Oxygen Evolution Using Fe-Substituted CuO 180
6.1. Chapter Introduction and Objectives 180
6.2. Synthesis and Electrochemical Experimental Methods 183
6.3. Results and Discussion 184

6.3.1. Structural and Electronic Baseline: Context for Oxidation Kinetics 184

6.3.2. Apparent OER Performance 185

6.3.3. Impedance-Resolved Kinetic Analysis of Oxidation-Side Bottlenecks 188

6.3.3.1. Impedance-Resolved Kinetic Analysis of Oxidation-Side Bottlenecks 188

6.3.3.2. Equivalent Circuit Fitting and Resistance Deconvolution 190

6.3.3.3. Distribution of Relaxation Time (DRT) Analysis 192

6.3.4. Promoter–Inhibitor Crossover and Dopant-Valency Effects 194

6.3.5. Mechanistic Framework: Electronic Structure–Kinetics Coupling in Fe-Substituted CuO 195

6.3.5.1. Surface Electronic Descriptors and Interfacial Kinetics 195

6.3.5.2. DFT-Derived Energetics and Surface-Reaction Limitations 199

6.3.5.3. Unified Oxidation-Side Kinetic Model 203

6.4. Chapter Summary and Forward Link 204

Chapter 7 Conclusions and Scope for Future Work 207

7.1. Chapter-wise Conclusion 207

7.1.1. Chapter 3 - Al^{3+} Substituted CuO: Non-Redox Electronic Modulation 207

7.1.2. Chapter 4 - CuO Nanosheets: Temperature-Dependent Kinetics 208

7.1.3. Chapter 5 - Fe^{3+} Substitution: Dopant-Mediated Redox Activation 208

7.1.4. Chapter 6 - Fe-CuO for Alkaline OER: Impedance-Resolved Bottleneck Separation 209

7.2. Integrated Overall Conclusion 209

7.3. Thematic Synthesis 211

7.4. Scientific Contributions 212

7.5. Limitations 212
7.6. Ongoing Work 213
7.7. Scope for Future Work 213
7.8. Broader Impact and Technological Relevance 214
7.9. Final Closing Statement 214
Appendix-A: DFT used 215
Appendix-B: XPS peak fittings 221
1. XPS Peak Fitting Methodology and Descriptor Definition 221
1.1. 1s Deconvolution and O_D/O_L Descriptor 221
1.2. Cu $2p_{3/2}$ Deconvolution and Electronic Flexibility Descriptors 222
Appendix-C: Preliminary Investigation of Li^+ and Zn^{2+} Substitution in CuO for Alkaline HER 226
References 231

LIST OF FIGURES

Figure 1.1.2.1: Global temperature change relative to 1850–1900 showing observed human-induced warming to ~1 °C by 2017, projected crossing of 1.5 °C in the early 2030s, and uncertainty ranges for 1.5 °C-limited pathways. Reprinted from Ref. [9], with permission from IPCC. 3

Figure 1.1.2.2: Annual average solar irradiance distribution over the surface of the Earth. Reprinted from Ref. [10], under the terms of the CC BY license. 4

Figure 1.1.4.1: Various categories of dyes and their possible industrial applications. Reprinted from Ref. [18], under the terms of the CC BY license. 7

Figure 1.1.4.2: Ecotoxicological impacts of dye-containing textile wastewater on the environment and living microorganisms. Reprinted from Ref. [18], under the terms of the CC BY license. 9

Figure 1.1.4.3: Negative impacts of textile dyes on human health, from dermatitis to the central nervous system. Reprinted from Ref. [18], under the terms of the CC BY license. 10

Figure 1.1.4.4: Classification of AOPs for water and wastewater treatment into chemical-based, energy-based, and hybrid systems, with examples including ozonation and photo-lysis. Reprinted from Ref. [24], with permission from Springer. 11

Figure 1.2.1.5.1: The mechanism of heterogeneous photocatalysis for the breakdown of micropollutants. Reprinted from Ref. [28], with permission from Springer. 15

Figure 2.1.2.1: Schematic of sol-gel synthesis of Pristine CuO. 36

Figure 2.1.2.2: Schematic of sol-gel synthesis of Al^{3+} doped CuO 37

Figure 2.1.2.3: Schematic of sol-gel synthesis of Fe^{3+} doped CuO. 38

Figure 2.1.3.1: Schematic of the Synthesis Procedure of Copper Oxide Nanosheets. Reprinted from Ref. [73] 40

Figure 2.1.4.1: Spectrum of the commercially available household LED light used. 41

Figure 2.1.4.2: Spectrum of the 11 W Phillips light used. 42

Figure 2.2.1.1: Flow chart of the different information obtained from the powder diffraction. 44

Figure 2.2.1.2: Schematic representation of X-ray diffraction in a crystal. 45

Figure 2.2.1.3: Schematic diagram of the Bragg Brantano geometry. 46

Figure 2.2.1.4: Flow chart of steps in the process of structural analysis from Powder

Diffraction Data. 47
Figure 2.2.1.5: Picture of D2 PHASER XRD. 49
Figure 2.2.2.1: (a) Schematic of the different lines in Raman scattering, (b) Energy excitation diagram of different Raman lines. 50
Figure 2.2.2.2: Block diagram of the instrumentation of the Raman spectrometer. 50
Figure 2.2.2.3: Raman spectrometer. 53
Figure 2.2.4.1: Schematic of the different kinds of radiation emitted when high-energy electrons impinge on the sample. 55
Figure 2.2.4.2: Block diagram of the FE-SEM. 56
Figure 2.2.4.3: FE-SEM Instrument used. 57
Figure 2.2.5.1: Block diagram of the TEM instrument. 59
Figure 2.2.5.2: Schematic diagram of TEM. 62
Figure 2.2.6.1: Schematic of the specular reflection and Diffuse reflectance. 62
Figure 2.2.6.2: Schematic of the instrumentation of the UV-DRS. 65
Figure 2.2.6.3: Shimadzu UV-Vis DRS spectrophotometer. 66
Figure 2.2.7.1: Schematic diagram representing the (a) Photoemission of X-rays from the K-shell, (b) working principle of XPS. 68
Figure 2.2.7.2: Schematic representation of the working of the XPS instrument. 69
Figure 2.2.8.1: Schematic of (a) adsorption of gas molecules on the surface of the sample, considering the monolayer adsorption (left, Langmuir theory) and multilayer adsorption (right, BET theory), (b) BET instrument. 71
Figure 2.2.10.1: Autolab electrochemical workstation. 72
Figure 3.3.1.1: Represents (a) XRD pattern for all the samples, where the inset shows the peak shift of the highest intensity peak, (b), (c) lattice parameters and lattice volume, and (d) Crystallite size and lattice strain variation with partial doping percentage. 80
Figure 3.3.2.1: Represents (a) Raman spectra for all the samples, where the insets show the peak shift of A_g mode, (b) the Raman shifts and FWHM that were observed for A_g mode. 83
Figure 3.3.4.1: Represents (a) bandgap analysis where the insets show the corresponding F(R) as a function of wavelength, (b) the FTIR spectra, and the insets show the lower wavenumber spectra for all the samples. 87
Figure 3.3.5.1: Represents FESEM image of (a) C0, (b) CA1, (c) CA2, (d) CA3. 88

Figure 3.3.5.2: Represents (a), (b), (c), (d) calculated particle sizes using ImageJ software. 89
Figure 3.3.6.1: Represents (a), (b), (c), (d) N_2 adsorption/desorption isotherm, and the insets show the BJH pore size distribution. 90
Figure 3.4.1.1: Represents (a) the degradation percentage of all the samples at different temperatures for a fixed irradiation time of 10 min, (b), (c) relative concentration and calculated rate constants, and (d) Degradation percentage of the CA1 sample as a function of catalyst concentration after a fixed visible-light irradiation time of 10 min at 59 °C. The figure was used to determine the optimum catalyst loading for subsequent photocatalytic experiments. 96
Figure 3.4.1.2: (a, b, c, d) absorbance of MB dye (d) relative concentration changes with irradiation time, (e) calculated rate constants at different H_2O_2 concentrations, i.e, 90 mM, 120 mM, 150 mM, and 180 mM, respectively, for the CA1 sample at 59 ^{0}C. 99
Figure 3.4.1.3: Represents (a, b) relative concentration change, and calculated rate constants of MO and RhB dye under household LED light, Initial dye conc. = 10 ppm (10 mg/L), catalyst loading = 0.6 mg/mL, 180 mM H_2O_2 at 59 ^{0}C. 101
Figure 3.4.2.1a: (a), (b), (c) represent the absorbance of MB, RhB, and MO solutions, (d) relative concentration, (e) fitted rate constants, and (f) degradation percentage at different irradiation times under sunlight. 102
Figure 3.4.2.1b: Schematic degradation mechanism of Al^{3+}-modified copper oxide. The conduction-band and valence-band positions shown here were estimated using the Mulliken electronegativity method described above, together with the experimentally determined optical bandgap values. 105
Figure 3.4.2.2: shows Arrhenius plots and Eyring plots for all the chemical reactions. 107
Figure 3.5.2.1a: : (a) The Fluorescence spectra of the solution after irradiating the light for a given period, (b) Conversion of Terephthalic acid to Fluorescent 2-hydroxyterephthalic acid with reacting hydroxyl radical generated from the reaction. 110
Figure 3.5.2.1b: (a), (b), (c) The scavenger test results reveal the importance of hydroxyl radical in the photodegradation process for all three dyes, (d) Assurance of re-usability of the materials for all three dyes. 111
Figure 3.5.2.2:represents the XRD pattern of the CA1 sample before and after five times of

repeated use for photocatalytic degradation. 112
Figure 3.5.2.3: (a, b, c) are the TEM image, HRTEM Image, and SAED pattern of the Fresh CA1 sample. Similarly, (d, e, f) are the TEM image, HRTEM Image, and SAED pattern of the recycled CA1 sample, showing there is no chemical change in the material, which confirms the stability of the given material even after five times repeated use. 113
Figure 4.3.1: The monoclinic structure and phonon modes of the CuO nanosheets were investigated from (a) the XRD pattern and (b) the Raman spectra. The pore size of the nanosheets was estimated at ~3.42 nm from the (c) BET adsorption-desorption isotherms, with the inset representing the corresponding BJH pore size distribution. The band gap was estimated at ~ 1.575 eV using the (d) tauc plot of the DRS spectra (inset). 122
Figure 4.3.2: The nanosheet morphology with a width of ~580 nm and a length of ~1240 nm was estimated using (a) FESEM. The (b, c) TEM bright field micrograph confirms a similar morphology. In contrast (c), the corresponding HRTEM image confirms the crystalline nature of the samples, with a lattice spacing of 0.273 nm corresponding to a CuO 110 plane. (d) The SAED pattern further confirms the presence of the CuO phase. 123
Figure 4.3.3: The EDX Analysis of the CuO nanosheets obtained from TEM. 124
Figure 4.4.1: (Left Panel) Photocatalytic properties of the CuO nanosheets (with catalyst concentration = 1 mg/mL and H_2O_2 concentration = 50 mM) revealed from the reduction of absorbance from the MB dye with time at different temperatures at (a) 25°C, (c) 35°C, and (e) 45°C (Right Panel) Relative concentration change with UV-irradiation time at (b) 25°C, (d) 35°C, and (f) 45°C for four different situations: MB + H_2O_2 + Light (black), MB + Catalyst + Light (red), MB + Catalyst + H_2O_2 + No Light (blue), and MB + Catalyst + H_2O_2 + Light (green), revealing the fastest degradation for the MB + Catalyst + H_2O_2 + Light combination. 128
Figure 4.4.2: (a) Rate of change of concentration of MB dye with time for different temperatures, revealing faster kapp with increasing temperature. (b) CuO nanosheet concentration dependence of the degradation process at 45°C and H_2O_2 concentration = 50 mM, revealing the highest degradation at 1 mg/mL. 129

Figure 4.4.3: (a) Photocatalytic properties of the CuO nanosheets (with catalyst concentration = 1 mg/mL and H_2O_2 concentration = 50 mM) revealed from the reduction of absorbance from the RhB dye with time at 45°C. (b) Relative concentration change with UV-irradiation time at 45°C for four different situations: RhB + H_2O_2 + Light (black), RhB + Catalyst + Light (red), RhB + Catalyst + H_2O_2 + No Light (blue), and RhB + Catalyst + H_2O_2 + Light (green), revealing the fastest degradation for the RhB + Catalyst + H_2O_2 + Light combination. (c, d) Effect of pollutant (organic dye) concentration on photocatalytic degradation, where the insets show the degradation percentage with varying concentrations of dye for 10 min of light illumination for MB and RhB, respectively. 130

Figure 4.4.4: (Top Panel) Photocatalytic properties of the CuO nanosheets (with catalyst concentration = 1 mg/mL and H_2O_2 concentration = 50 mM) were revealed from the reduction of absorbance from the (a) MB and (b) RhB dye with time at ambient conditions. (Bottom Panel) Relative concentration changes with natural sunlight-irradiation at ambient conditions for Dye catalyst, H_2O_2, and light, revealing (c) faster degradation for MB (green) than RhB (red) and (d) faster rate constant for MB (green) than RhB (red) 133

Figure 4.5.1: Mechanism of dye degradation involving photon-irradiated e-h pair generation and subsequent radical formation during oxidation and reduction processes. 135

Figure 4.5.2: (a, b) shows Arrhenius plots and Eyring plots for the chemical reactions. 137

Figure 4.5.3: (a, b) Scavenger test of the nanosheets for MB and RhB dye, confirming the role of different reactive oxygen species that contribute to the photocatalytic process, respectively. 139

Figure 4.6.1: (a, b) Assurance of reusability of the nanosheets for MB and RhB dye, respectively. 140

Figure 4.6.2: XRD of the CuO Nanosheets before and after Photocatalytic Degradation. 140

Figure 5.3.1.1: (a) XRD patterns of pure and Fe-doped CuO ($Cu_{1-x}Fe_xO$; x = 0, 0.0156, 0.0312) showing a single-phase monoclinic CuO structure (JCPDS No. 48-1548) without secondary impurities. The inset highlights a shift of the (110) peak toward higher 2θ with increasing Fe content, indicating lattice contraction due to the substitution of smaller Fe^{3+} ions for Cu^{2+}. (b) Rietveld

refinement of $Cu_{0.9687}Fe_{0.03125}O$ showing excellent agreement between observed and calculated data (χ^2 = 3.690, wRp = 0.0236, Rp = 0.0175), confirming phase purity and successful Fe incorporation into the CuO lattice 151

Figure 5.3.2.1: FE-SEM images and corresponding EDS elemental mapping of (a–d) pure CuO, (e–i) low Fe-doped CuO, and (j–n) high Fe-doped CuO samples. All samples exhibit agglomerated sub-micrometre grains; Fe incorporation results in increased surface roughness and more irregular aggregates, indicating morphological evolution with partial doping. EDS maps confirm homogeneous spatial distribution of Cu, O, and Fe, with no evidence of Fe-rich secondary phases at the resolution of the technique. 154

Figure 5.3.3.1:Raman spectra of pure CuO (C0) and Fe-doped CuO samples (CF1 and CF2). All samples exhibit the characteristic monoclinic CuO vibrational modes at ~298 cm^{-1} (A_g), ~345 cm^{-1} (B_{1g}), and ~627 cm^{-1} (B_{2g}). The slight blue shifts and intensity variations with Fe incorporation indicate lattice distortion and changes in local symmetry resulting from the substitutional partial doping of Fe ions within the CuO lattice. A slight blue shift and FWHM modulation of the A_g mode with partial Fe doping reflect changes in local bond strength and lattice disorder induced by substitutional Fe. 155

Figure 5.3.3.2: FTIR spectra of pure CuO (C0) and Fe-doped CuO samples (CF1 and CF2). The characteristic Cu-O vibrational bands observed at ~474, 530, and 594 cm^{-1} correspond to metal–oxygen stretching modes of monoclinic CuO. The inset highlights these absorption peaks, where slight shifts and intensity variations upon Fe incorporation indicate modifications in the Cu-O lattice environment and local bonding symmetry due to Fe substitution. 156

Figure 5.3.4.1: Tauc plots $[F(R)h\nu]^2$ versus photon energy for pure CuO (C0) and Fe-doped CuO samples (CF1 and CF2), showing the band gap variations. The estimated optical band gaps increase from ~1.435 eV (C0) to ~1.5 eV (CF1) and ~1.63 eV (CF2), indicating that Fe incorporation widens the apparent band gap through combined band-structure modification and altered defect chemistry. The inset shows the extended optical absorption edge in the visible region. 159

Figure 5.3.5.1: N_2 adsorption-desorption isotherm, and BJH pore-size distributions (insets)

for C0, CF1, and CF2. Partial Fe doping markedly increases the specific surface area and pore volume from C0 to CF1, followed by a moderate decrease in CF2, while all samples retain textural/interparticle pore features. These textural changes provide additional accessible active sites but are not the sole factor governing the observed photocatalytic trends. 160

Figure 5.3.6.1: The XPS survey scans of all the samples, representing no impurity except carbon contamination from the atmosphere (Adventitious carbon) located at a binding energy (BE) of 284.8 eV. 163

Figure 5.3.6.2: High-resolution XPS spectra of (left) Cu 2p and (right) O 1s regions for pure CuO (C0, top) and Fe-doped CuO (CF1, CF2, bottom). The Cu 2p spectra show Cu^{2+} main peaks with shake-up satellites characteristic of CuO, along with deconvoluted contributions associated with variations in final-state screening and Cu–O covalency (~933 eV), rather than definitive bulk Cu^{+}/Cu^{0} formation. The O 1s spectra are resolved into lattice oxygen (O_L), a defect/chemisorbed/oxyhydroxide-related component near 530.7 eV, and adsorbed water at ~532.8 eV; their relative fractions evolve with Fe content, evidencing Fe-induced changes in defect oxygen and surface adsorption environments. 164

Figure 5.3.6.3: High-resolution XPS spectra of the Fe 2p region for Fe-doped CuO samples CF1 and CF2. The Weak Fe $2p_{3/2}$ and Fe $2p_{1/2}$ features around 711–712 eV and 724–725 eV, partially overlapping with Cu Auger lines, confirm successful incorporation of Fe species into the CuO lattice at low concentrations. The line shape is consistent with predominantly Fe^{3+} in an oxide environment, although the limited signal-to-noise precludes a fully quantitative assessment of Fe valence states. 165

Figure 5.3.7.1a: Represents the reduction of absorbance of the MB dye with time (a, b, c), while the fitted rate constant is obtained from the graph (d). 167

Figure 5.3.7.2: (a) the relative concentration changes of the dye molecules inside the solution over time, showing (b) the degradation percentage of all the samples, in the dark as well as in the presence of light. While (c) shows the scavengers test confirming that the majority of the degradation reactions are contributed from the IPA scavenged $OH^{\cdot}$ radicals, and (d) a recyclability test to show not much degradation in terms of efficiency for three repeated cycles, which were

conducted using the CF2 sample. 169
Figure 5.3.7.3: Degradation percentage of MB dye with increasing catalyst loading. As observed from 0.5 mg/mL to 1 mg/mL, the degradation of MB increases from 97% to 99%, then decreases to 97.5% for a catalyst with 1.5 mg/mL. 170
Figure 5.3.7.1b: Schematic illustration of bandedge positions of pure and Fe-doped CuO for Enhancement in the degradation process. Note that the band gap energy (eV) is estimated from the Kubelka-Munk function and the Tauc plot (Figure 5.2.4.1). The NHE scale is referred to as pH 0. 172
Figure 6.3.2.1: (a) Linear sweep voltammetry curves of C0, CF1, and CF2 in 1 M KOH. (b) Corresponding Tafel plots extracted from the linear kinetic region. Moderate Fe substitution (CF1) exhibits reduced overpotential and lower Tafel slope relative to pristine CuO, while higher Fe loading (CF2) results in partial kinetic deterioration, indicating a promoter–inhibitor crossover. 186
Figure 6.3.2.2: (a–c) Cyclic voltammograms recorded in the non-Faradaic potential region at varying scan rates (20-100 mV s^{-1}) for (a) pristine CuO (C0), (b) CF1 (x = 0.0156), and (c) CF2 (x = 0.0312) in 1 M KOH. (d) Corresponding double-layer capacitance (C_{dl}) plots obtained from the linear relationship between capacitive current density and scan rate, used to estimate the electrochemically active surface area (ECSA). 187
Figure 6.3.3.1: Nyquist plots of pristine CuO (C0) and Fe-substituted samples CF1 (x = 0.0156) and CF2 (x = 0.0312) measured at 0.65 V vs Hg/HgO in 1 M KOH. The impedance response exhibits two distinguishable frequency-dependent features across the catalyst series. Moderate Fe substitution (CF1) shows a reduced overall semicircle relative to pristine CuO, indicating lower kinetic resistance, whereas higher Fe loading (CF2) displays an increased low-frequency contribution, suggesting redistribution of oxidation-side kinetic limitations. 189
Figure 6.3.3.2: Nyquist plot of the electrochemical impedance spectroscopy (EIS) data fitted using an equivalent circuit consisting of a series resistance (R1) and three parallel resistances (R) - constant phase element (CPE) elements. The symbols represent the experimental impedance data, while the solid red line corresponds to the fitted response. The series resistance (R_1) accounts for the solution and contact resistance. In contrast, the three R-CPE elements

describe charge transfer, interfacial processes, and low-frequency contributions to surface-reaction and mass-transport-coupled processes. 191
Figure 6.3.3.3: Bode plots (|Z| vs. frequency and phase angle vs. frequency) for three different samples, measured over the same frequency range. The symbols represent the experimental impedance data, while the solid red line corresponds to the fitted response. 191
Figure 6.3.3.4: DRT spectra derived from electrochemical impedance measurements of pristine CuO (C0), moderately Fe-substituted CuO (CF1), and higher Fe-loaded CuO (CF2) recorded at 0.65 V vs Hg/HgO in 1 M KOH. Distinct relaxation regimes are observed across high-, intermediate-, and low-frequency domains. Moderate Fe substitution (CF1) suppresses interfacial relaxation intensity relative to C0, while higher Fe loading (CF2) exhibits a pronounced intermediate-frequency relaxation contribution, consistent with the redistribution of impedance components identified through equivalent circuit analysis. 193
Figure 6.3.5.1: High-resolution XPS spectra of (left) Cu 2p and (right) O 1s regions for pristine CuO (C0), moderately Fe-substituted CuO (CF1), and higher Fe-loaded CuO (CF2). Deconvolution reveals systematic variation in defect- or ligand-hole-associated oxygen species (O_D) and satellite screening features upon Fe substitution. The evolution of O_D/O_L ratios correlates with impedance-derived redistribution of interfacial (R_2) and surface-reaction (R_3) resistance components. 196
Figure 6.3.5.2: Calculated free energy diagram for alkaline OER on pristine CuO and Fe-substituted CuO (111) surfaces at U = 0 V. Moderate Fe substitution lowers the free energy barrier of the potential-determining step, whereas higher Fe loading strengthens adsorption of oxygenated intermediates and increases the thermodynamic penalty for intermediate turnover. 199
Figure 6.3.5.3: Spin-resolved projected crystal orbital Hamilton population (−pCOHP) analysis for oxygen-intermediate adsorption on Cu and Fe catalytic sites. Integrated crystal orbital Hamilton population (ICOHP) values indicate significantly stronger Fe–O covalent interactions relative to Cu–O bonding. Enhanced Fe–O covalency at higher substitution levels supports the DFT-predicted over-stabilization of oxygenated intermediates and correlates with

the experimentally observed increase in surface-reaction resistance (R_3). 201
Figure 6.3.5.4: Planar-averaged electrostatic potential and calculated work function for pristine and Fe-substituted CuO surfaces. Moderate Fe incorporation reduces the work function, indicating improved electronic communication across the catalyst–electrolyte interface and supporting the experimentally observed reduction in interfacial resistance (R_2). 203

LIST OF TABLES

Table 2.2.2.1: Laser sources of Raman spectroscopy with wavelength. 51

Table 3.3.4.1: shows the bandgap and Urbach energy of all the samples. 86

Table 3.3.6.1: shows the specific surface area, total pore volume, and average pore diameter of all the samples. 90

Table 3.3.7.1: shows the hydrodynamic diameter and ξ-potential of all the samples in DI water. 93

Table 3.4.1.1: Irradiation time, degradation percentage, calculated rate constants, and linear correlation coefficients for different concentrations of H_2O_2. 99

Table 3.4.2.1a: Represents the degradation percentage, calculated rate constants, and the corresponding values of R^2 under direct sunlight irradiation of 30 min for all three dyes. 104

Table 3.4.2.1b: Represents the standard EVB and ECB values for different samples. 105

Table 3.4.2.2: Represents various thermodynamic parameters obtained using Arrhenius Theory and Transition State Theory for all the chemical reactions. 107

Table 3.5.2.1: Represents the leached amount of Cu^{2+} and Al^{3+} after the photocatalytic reaction. 113

Table 3.5.2.2: Literature comparison with the present work. 114

Table 4.3.1: summarizes the data obtained from the EDX analysis, which indicates the elemental composition of the prepared nanosheets. 124

Table 4.4.1: Irradiation time, degradation percentage, calculated rate constants, and linear correlation coefficients at different temperatures for MB and RhB dyes. 131

Table 4.4.2: Degradation percentage, rate constants, and corresponding values of R^2 under direct sunlight irradiation of 70 min for both dyes. 134

Table 4.5.1: All the thermodynamic parameters associated with Arrhenius's Theory and Transition State Theory of the chemical reaction with copper oxide nanosheets. 137

Table 4.6.1: A comparative study of the photocatalytic properties of CuO nanostructures for the degradation of various organic dyes, including the present study. 141

Table 5.3.5.1: Representation of specific surface area, total pore volume, and average pore diameter for all the samples. 160

Table 5.3.7.1: represents the standard EVB and ECB values for different samples. 171

Table 5.3.7.2: Literature comparison table from existing references with the present work 177
Table 6.3.3.1: Fitted electrochemical impedance spectroscopy (EIS) parameters for C0, CF1, and CF2 catalysts measured at 0.65 V vs Hg/HgO in 1 M KOH using an equivalent circuit comprising three parallel R-CPE elements connected in series with the solution resistance, representing high-, mid-, and low-frequency processes, respectively. 192
Table 6.3.5.1: Correlation between surface electronic descriptors derived from XPS and impedance-extracted kinetic parameters for pristine CuO (C0) and Fe-substituted samples (CF1 and CF2) measured at 0.65 V vs Hg/HgO in 1 M KOH. The table highlights the non-monotonic relationship between dopant-induced electronic modulation (O_D/O_L ratio and Cu 2p satellite-to-main peak intensity ratio) and redistribution of interfacial (R_2) and surface-reaction (R_3) resistive components, illustrating the promoter–inhibitor crossover in alkaline OER. 198
Table 6.3.5.2: Integrated ICOHP Values for Metal–Oxygen Interactions. 201

NOMENCLATURE

Symbol	Meaning	Units
A	Arrhenius pre-exponential factor	min^{-1}
k_{app}	Apparent rate constant	min^{-1}
E_a	Activation energy	kJ mol^{-1}
R	Universal gas constant (8.314)	J K^{-1} mol^{-1}
T	Absolute temperature	K
$\Delta^{\ddagger}H°$	Standard enthalpy of activation	kJ mol^{-1}
$\Delta^{\ddagger}S°$	Standard entropy of activation	J mol^{-1} K^{-1}
$\Delta^{\ddagger}G°$	Standard Gibbs free energy of activation	kJ mol^{-1}
E_g	Optical band gap energy	eV
E_U	Urbach energy	eV
α	Absorption coefficient	cm^{-1}
η	Overpotential	V
j	Current density	mA cm^{-2}
J_0	Exchange current density	mA cm^{-2}
Z	Electrochemical impedance	Ω

Symbol	Meaning	Units
f	Frequency	Hz
R_s	Solution (ohmic) resistance	Ω
R_{ct}	Interfacial charge-transfer resistance	Ω
R_1	High-frequency resistance component	Ω
R_2	Interfacial kinetic resistance component	Ω
R_3	Surface-reaction resistance component	Ω
C_{dl}	Double-layer capacitance	F
CPE	Constant phase element	$F\ s^{n-1}$
$ECSA$	Electrochemically active surface area	cm^2
TOF	Turnover frequency	s^{-1}
e^-	Electron	—
h^+	Hole	—
$\bullet OH$	Hydroxyl radical	—
$O_2\bullet^-$	Superoxide radical	—
V_{Cu}	Copper vacancy	—
V_O	Oxygen vacancy	—

Symbol	Meaning	Units
O_i	Oxygen interstitial	—
Cu_i	Copper interstitial	—

ACRONYMS

Acronym	Expansion
AOPs	Advanced Oxidation Processes
ROS	Reactive Oxygen Species
HER	Hydrogen Evolution Reaction
OER	Oxygen Evolution Reaction
PCET	Proton-Coupled Electron Transfer
LOM	Lattice Oxygen Mechanism
AEM	Adsorption–Evolution Mechanism
CV	Cyclic Voltammetry
LSV	Linear Sweep Voltammetry
EIS	Electrochemical Impedance Spectroscopy
DRT	Distribution of Relaxation Times
CP	Chronopotentiometry

Acronym	Expansion
CA	Chronoamperometry
XRD	X-ray Diffraction
XPS	X-ray Photoelectron Spectroscopy
FTIR	Fourier Transform Infrared Spectroscopy
UV–Vis DRS	Ultraviolet–Visible Diffuse Reflectance Spectroscopy
SEM	Scanning Electron Microscopy
FESEM	Field Emission Scanning Electron Microscopy
TEM	Transmission Electron Microscopy
HRTEM	High-Resolution Transmission Electron Microscopy
SAED	Selected Area Electron Diffraction
EDX	Energy-Dispersive X-ray Spectroscopy
BET	Brunauer–Emmett–Teller (surface area method)
DLS	Dynamic Light Scattering

Acronym	Expansion
ICP-OES	Inductively Coupled Plasma–Optical Emission Spectroscopy
MB	Methylene Blue
RhB	Rhodamine B
MO	Methyl Orange
IPA	Isopropanol
AO	Ammonium Oxalate
BQ	p-Benzoquinone
PTA	Terephthalic Acid
TAOH	2-Hydroxyterephthalic Acid

Chapter 1 Introduction

Abstract: *This chapter introduces two interconnected global challenges: the growing demand for sustainable energy conversion and the persistent problem of environmental pollution arising from industrial effluents. It highlights the limitations of fossil-fuel–based technologies and conventional wastewater treatment methods, underscoring the need for advanced catalytic strategies that operate efficiently under mild, sustainable conditions. In this context, solar-driven photocatalysis and electrochemical energy conversion are discussed as promising approaches for pollutant degradation and renewable energy technologies.*

The chapter emphasizes the role of transition-metal oxides as robust, earth-abundant catalytic materials, with particular focus on copper oxide (CuO). CuO is introduced as a charge-transfer, strongly correlated oxide, characterized by strong Cu 3d-O 2p hybridization, localized electronic states, and polaronic charge transport. These features render CuO an ideal model system for investigating how defect chemistry, dopant valency, morphology, and charge-transport limitations govern catalytic performance. Rather than treating activity enhancement as a universal goal, the chapter frames photocatalytic and electrocatalytic processes in CuO as constrained by reaction-specific kinetic bottlenecks, including charge separation, transport, redox accessibility, and interfacial charge-transfer.

The chapter concludes by defining the scope, research questions, and objectives of the thesis, which aims to develop a unified, bottleneck-oriented framework for understanding and optimizing CuO-based catalysts across photocatalytic and electrochemical reactions. This framework establishes the conceptual foundation for the subsequent chapters, which systematically examine defect-, morphology-, and valency-controlled strategies for environmental remediation and energy conversion, with hydrogen evolution positioned as a future extension of the present work.

1.1. Motivation and Background

The twenty-first century faces two interlinked global challenges that pose significant threats to sustainable development: the growing energy crisis and the escalating environmental pollution problem [1]. Rapid industrialization, urbanization, and population growth have drastically increased the demand for energy and clean water, while simultaneously intensifying greenhouse gas emissions and water contamination. These challenges, if left unaddressed, will have profound consequences on climate stability, human health, and socioeconomic development [2], [3], [4].

1.1.1. Global Energy Demand and the Role of Fossil Fuels

Energy is the backbone of modern society, powering industries, transportation, agriculture, and communication networks. According to recent reports by the International Energy Agency (IEA), global primary energy consumption has increased steadily over the past five decades, with fossil fuels, primarily coal, oil, and natural gas, accounting for more than 80% of the total energy supply [5]. Although fossil fuels have enabled unprecedented technological progress and economic growth, their extensive use has also led to unsustainable carbon emissions [6].

The combustion of fossil fuels releases large quantities of carbon dioxide (CO_2), the most significant greenhouse gas contributing to global warming. Other pollutants, such as sulfur oxides (SO_x), nitrogen oxides (NO_x), and particulate matter, are also emitted, contributing to acid rain, smog formation, and respiratory illnesses [2], [7]. Moreover, fossil fuel reserves are finite and unevenly distributed globally, leading to volatile market fluctuations and concerns about energy security. The global community, therefore, faces a dual imperative: to ensure reliable access to energy while transitioning to clean, renewable, and sustainable energy sources [8].

1.1.2. Climate Change and the Urgency of Carbon Neutrality

The Intergovernmental Panel on Climate Change (IPCC) has repeatedly emphasized the urgent need to limit the global temperature rise to below 1.5°C relative to pre-industrial levels to mitigate the most severe impacts of climate change [9]. As illustrated in Figure 1.1.2.1, human-induced warming had already reached approximately 1 °C by 2017, with the observed temperature trend closely tracking the projected trajectory of anthropogenic forcing. At the

current warming rate, global temperatures are expected to surpass the 1.5 °C threshold as early as the early 2030s, underscoring the narrowing window for effective climate action. The shaded uncertainty envelope depicted in the figure represents the range of possible future pathways consistent with limiting warming to 1.5 °C; however, achieving these pathways requires rapid, deep, and sustained reductions in global carbon emissions. Such reductions cannot be achieved within the current fossil-fuel-dependent energy framework and therefore necessitate an accelerated transition toward low-carbon, renewable, and sustainable energy systems, supported by advanced materials and next-generation catalytic technologies.

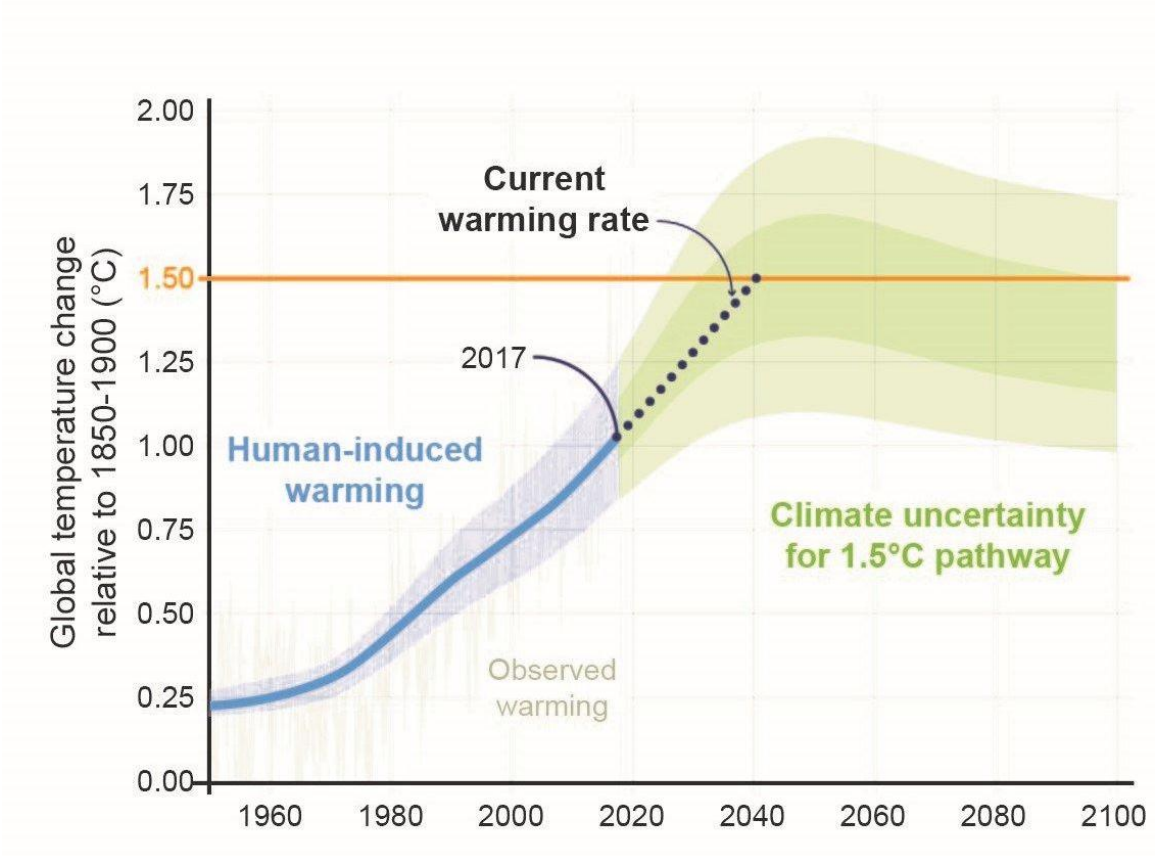


Figure 1.1.2.1: Global temperature change relative to 1850–1900 showing observed human-induced warming to ~1 °C by 2017, projected crossing of 1.5 °C in the early 2030s, and uncertainty ranges for 1.5 °C-limited pathways. Reprinted from Ref. [9], with permission from IPCC.

Renewable energy sources, including solar, wind, hydro, and biomass, have gained increasing attention. Among these, solar energy is the most abundant, with the Earth receiving

approximately 173,000 terawatts (TW) of solar energy continuously-more than 10,000 times the world's current energy consumption [1]. As illustrated in Figure 1.1.2.2, the annual average solar irradiance distribution varies across geographical regions, yet even the lowest-irradiance zones receive orders of magnitude more solar energy than required for local consumption [10]. Effectively harnessing this vast resource, however, requires advanced technologies capable of converting intermittent solar radiation into storable and dispatchable forms of energy, including electricity and solar-derived fuels. Conventional photovoltaic technologies have achieved substantial progress, but their intermittent nature and reliance on external infrastructure for energy storage limit broader deployment. This challenge has catalyzed intensive global research into solar-driven catalytic processes, particularly photocatalysis, electrocatalysis, and photoelectrochemical (PEC) conversion. These approaches utilize semiconducting materials to absorb sunlight, generate charge carriers, and drive chemical transformations that store solar energy in the form of chemical bonds. A prominent example is the photocatalytic or PEC splitting of water to generate hydrogen, a clean and high-energy-density fuel that is central to emerging carbon-neutral energy systems and the broader hydrogen economy [11].

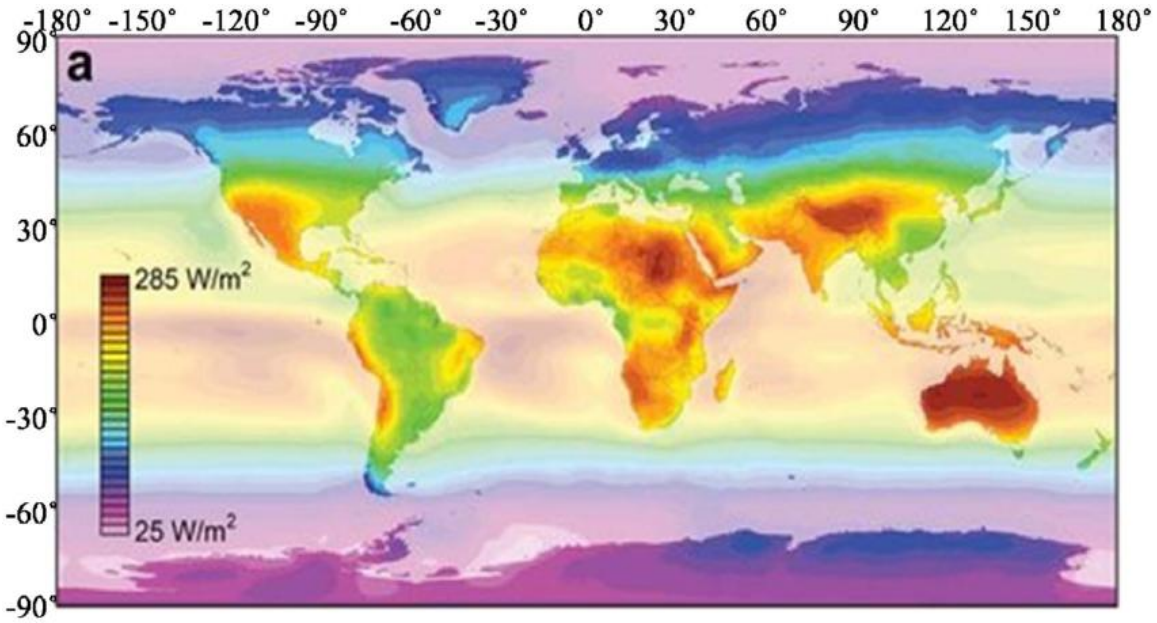


Figure 1.1.2.2: Annual average solar irradiance distribution over the surface of the Earth. Reprinted from Ref. [10], under the terms of the CC BY license.

1.1.3. Hydrogen as a Clean Energy Carrier

Hydrogen is widely recognized as a clean, sustainable, and high-energy-density fuel with the potential to decarbonize multiple sectors, including transportation, the chemical industry, and power generation. The energy content of hydrogen is ~120 MJ/kg, nearly three times higher than that of conventional fossil fuels, such as gasoline [12]. Moreover, hydrogen combustion or fuel cell utilization produces only water as a by-product, making it an environmentally benign fuel [13].

The global hydrogen economy is rapidly evolving as governments and industries recognize hydrogen's potential to serve as a unifying platform for deep decarbonization across power generation, transportation, and industrial sectors. More than 40 national hydrogen strategies have been announced in the past decade, with major economies, including the European Union, Japan, South Korea, Australia, the United States, and India, committing substantial investments toward the development of hydrogen infrastructure, production capacity, and international supply chains. These initiatives collectively aim to scale global hydrogen production to hundreds of millions of tonnes annually by mid-century, a transformative shift that underscores hydrogen's anticipated role in achieving global carbon neutrality targets [14].

Hydrogen's appeal lies in its versatility. It can be used in fuel cells for clean electricity generation; blended with or substituted for natural gas in existing pipelines; synthesized into green ammonia and methanol for long-distance trade; or employed as a reductant in green steel and other industrial processes traditionally reliant on fossil fuels. Furthermore, hydrogen offers a practical solution for long-duration and seasonal energy storage, a crucial function that complements the intermittency of renewable energy sources, such as solar and wind.

Currently, most industrial hydrogen is produced through steam methane reforming (SMR), a fossil-fuel-based process that emits significant amounts of CO_2 [15]. To realize a truly sustainable hydrogen economy, the global energy system must transition from carbon-intensive hydrogen (grey and blue hydrogen) toward green hydrogen, produced through renewable and environmentally benign pathways. Among emerging alternatives, Water splitting, driven either by solar energy (photocatalysis) or by renewable electricity (electrocatalysis), provides an attractive route to green hydrogen [16], [17]. The overall water splitting reaction can be expressed as:

$$2H_2O \rightarrow 2H_2 + O_2$$

This process involves two electrochemical half-reactions: the hydrogen evolution reaction (HER) at the cathode and the oxygen evolution reaction (OER) at the anode. Although HER is a relatively simple two-electron reduction, OER is a sluggish four-electron oxidation involving multiple proton-coupled electron transfer steps, making it the kinetic bottleneck of water splitting systems. Overcoming these kinetic limitations, while simultaneously reducing system cost and improving long-term stability, represents a core challenge for achieving economically viable green hydrogen production.

These scientific and engineering barriers are compounded by broader infrastructural challenges related to hydrogen storage, transportation, and large-scale deployment. Addressing these issues requires advanced catalytic materials capable of efficiently driving HER and OER under mild conditions using earth-abundant elements.

1.1.4. Environmental Pollution and Water Contamination

In addition to the energy crisis, the world faces the pressing issue of environmental pollution, particularly the contamination of freshwater resources. Industrial activities such as textile dyeing, leather tanning, paper production, and pharmaceutical manufacturing release enormous quantities of wastewater laden with organic dyes, heavy metals, and toxic compounds [7], [18], [19], [20]. Again, dyes are broadly classified based on their source of materials (natural or synthetic), their chemical structure (e.g., azo, anthraquinone, phthalocyanine, and triarylmethane types), or their mode of application (e.g., reactive, direct, acid, basic, disperse, vat, mordant, and sulfur dyes). Natural dyes are often categorized based on chemical structures like Indigoid, Flavonoid, and Tannin-based dyes, while synthetic dyes can also be classified by the charge they carry (anionic, cationic, or nonionic) or the resulting color produced in solution (such as red, yellow, orange, black, brown, violet, blue, and green synthetic dyes). Although the textile industry is one of the largest consumers globally, dyes and colorants are ubiquitous essentials applied in a vast array of sectors, including food, cosmetic formulations, leather processing, paper and paint manufacturing, and plastic production. Specific applications include the use of Acid dyes as synthetic food colors, Basic dyes in the coloring of paper and ink, and Direct dyes functioning as pH indicators and biological stains [21]. Figure 1.1.4.1. shows various categories of dyes and their possible industrial applications [18].

Among these, synthetic dyes such as methylene blue (MB), rhodamine B (RhB), and methyl orange (MO) are of particular concern due to their chemical stability and resistance to biodegradation. These specific pollutants represent major dye categories: MB and RhB are classified as cationic dyes, while MO is an anionic azo compound. Azo dyes, like MO, account for 60–70% of dyes manufactured and are notably poisonous, carcinogenic, and resistant to standard degradation techniques due to their high stability. Furthermore, specific health threats are associated with these compounds: RhB is identified as a chronic neurotoxin and is carcinogenic to humans and animals, and exposure to MB is linked to symptoms like vomiting, nausea, and cardiac complications. The chemical structures of synthetic dyes typically contain chromophoric groups for intense color and auxochromic groups that enhance solubility, making them difficult to remove using traditional techniques. The recalcitrance of these compounds means that they often enter the environment and accumulate physiologically along the food chain [18].

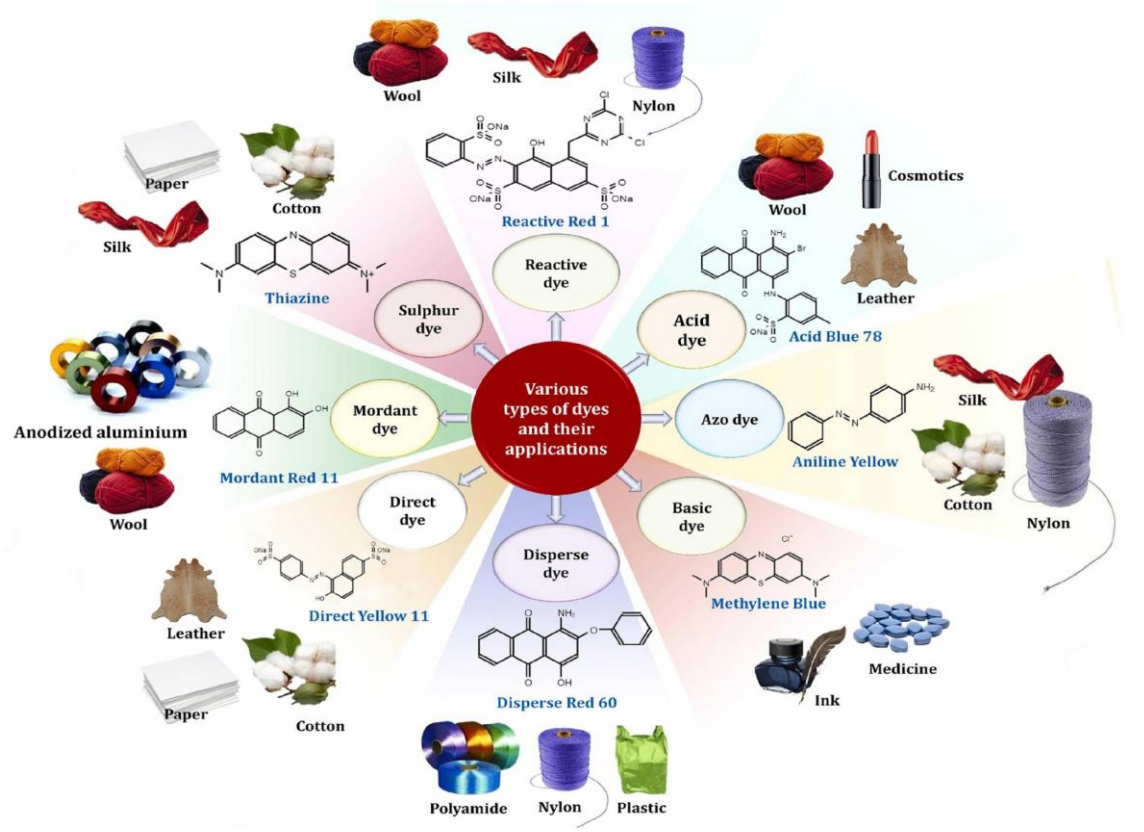


Figure 1.1.4.1: Various categories of dyes and their possible industrial applications. Reprinted from Ref. [18], under the terms of the CC BY license.

Even at low concentrations, dyes impart intense coloration to water, reducing light penetration and disrupting photosynthesis in aquatic ecosystems. The visible natural issue associated with dyes is their ability to absorb and reflect sunlight into water. This prevents light from entering the photic zone of the aquatic environment. The resulting decline in the rate of photosynthesis in aquatic flora, including algae and aquatic plants, has significant ecological consequences. Dyes, along with pigments and organic matter, also contribute to the deterioration of water quality, including objectionable colors and odors, and increase the biochemical oxygen demand (BOD) and chemical oxygen demand (COD). Furthermore, the discharge of organic matter, including dyes and pigments, can lead to under-oxygenation in stagnant aquatic environments, as bacteria require oxygen to decompose 7–8 mg of organic matter per liter of water. This high concentration of textile dyes in water consequently depletes oxygen levels. These effects collectively disrupt the oxygen transfer mechanism at the air-water interface, hindering the natural self-purification capacity of water bodies. Dyes can be detected by the naked eye even at a concentration of 5 mg/L, and synthetic dyes are highly stable, yielding a strong colored solution even at concentrations below 1 mg/L. The high concentration of solids containing dyes in industrial effluents, coupled with the lack of dissolved oxygen, impairs the growth and physiological responses of aquatic fauna and flora. Additionally, dyes, such as Disperse dyes, have the potential to bio-accumulate in algae and higher plants [21]. The ultimate consequence is an imbalance in the environment, which threatens the survival of aquatic life and various species. Figure 1.1.4.2 shows ecotoxicological impacts of dye-containing textile wastewater on

the environment and living microorganisms [18].

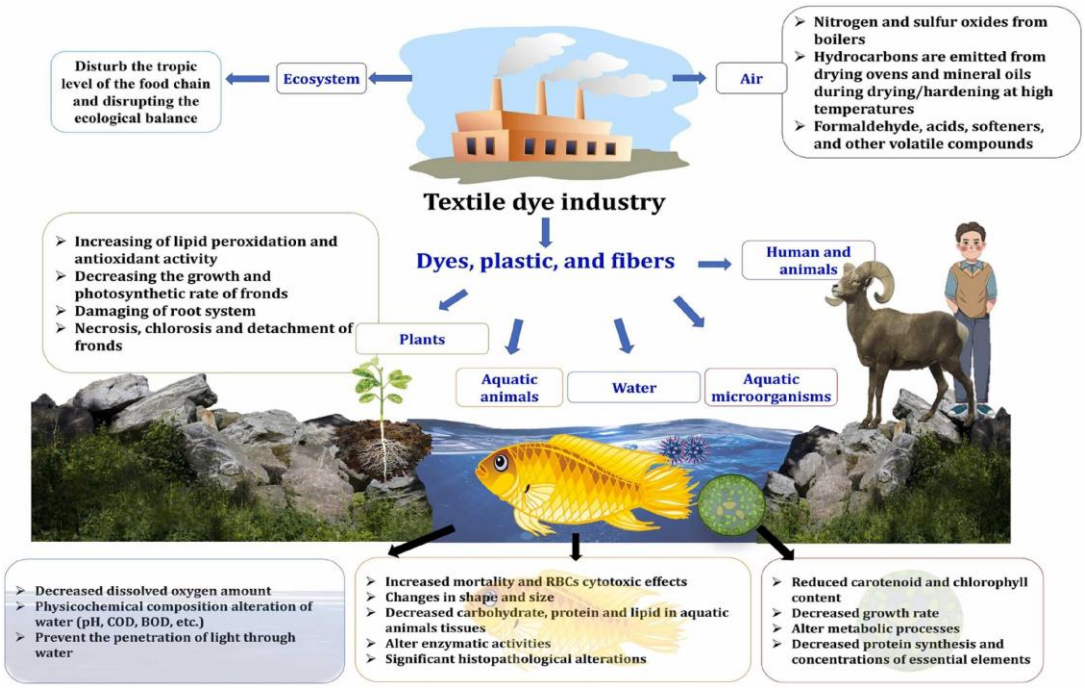


Figure 1.1.4.2: Ecotoxicological impacts of dye-containing textile wastewater on the environment and living microorganisms. Reprinted from Ref. [18], under the terms of the CC BY license.

Many dyes and their degradation by-products are toxic, carcinogenic, or mutagenic, posing significant risks to human health. These substances generate dysfunction in the kidneys, digestive system, brain, and skin, and they can reduce food intake capacity, growth, and fertility rates in mammalian cells. Specifically, azo dyes account for 60-70% of the synthetic dyes manufactured and are notably poisonous, carcinogenic, and resistant to standard degradation methods. When metabolized, azo dyes can produce toxic amino acids or carcinogenic aromatic amines, and those derived from benzidine are linked to human bladder cancer. Certain specific dyes pose serious threats: RhB is identified as a chronic neurotoxin and is carcinogenic to both humans and animals; Crystal Violet is a potent mutagen and carcinogen; and Malachite Green is a significant threat due to its potential teratogenic, carcinogenic, and mutagenic properties. Furthermore, exposure to textile dyes and chemical finishing agents, such as formaldehyde (HCHO) used in finishing, can cause various diseases, including dermatitis, skin and eye irritation, and complications in the central nervous system (CNS). Acute exposure to MB, for

instance, can cause vomiting, nausea, necrosis of tissue, methemoglobinemia, and cardiac complications. Beyond the dyes themselves, textile wastewater frequently contains toxic heavy metals, such as lead and mercury, which cause human disease; high exposure to mercury is carcinogenic to humans and can permanently damage the nervous system, kidneys, brain, and fetuses, while exposure to chromium is carcinogenic [22]. Finally, secondary toxicological hazards arise during water purification, as long-term exposure to chlorination byproducts (trihalomethanes) is associated with bladder, colon, and colorectal cancers. Figure 1.1.4.3 shows the negative impacts of textile dyes on human health, from dermatitis to the central nervous system [18].

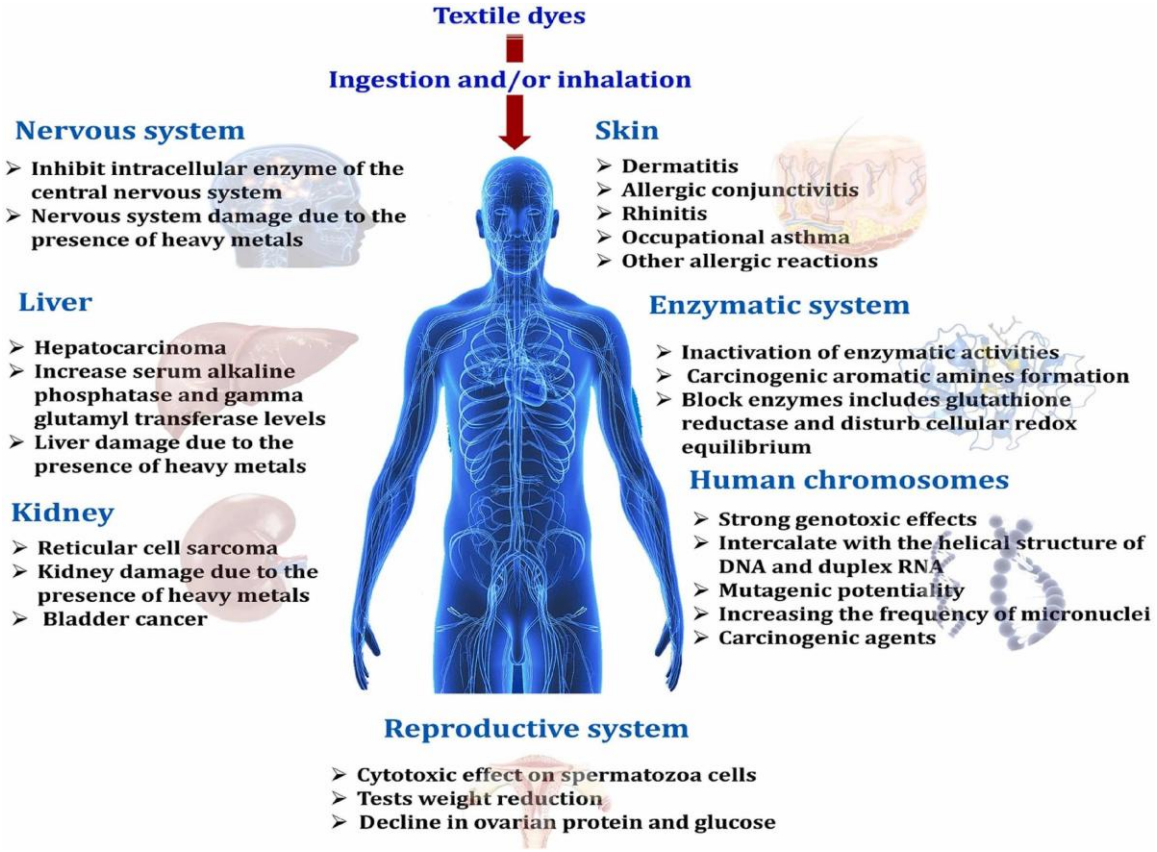


Figure 1.1.4.3: Negative impacts of textile dyes on human health, from dermatitis to the central nervous system. Reprinted from Ref. [18], under the terms of the CC BY license.

Conventional wastewater treatment methods, such as coagulation, adsorption, and biological processes, are often insufficient for completely removing these pollutants [23]. Consequently, Advanced Oxidation Processes (AOPs) are crucial chemical approaches employed to treat dye-

containing wastewater, relying on the *in-situ* generation of hydroxyl radicals (OH·), a powerful oxidizing agent capable of removing dyes quickly under harsh conditions without generating sludge [24]. Figure 1.1.4.4 shows the Classification of AOPs used in water and wastewater treatment, categorized by chemical-based, energy-based (UV light, mechanical, electrical, thermal), and hybrid systems. Each category includes common process examples such as ozonation, photolysis, ultrasound, electrochemical oxidation, and photo-electrocatalysis [24].

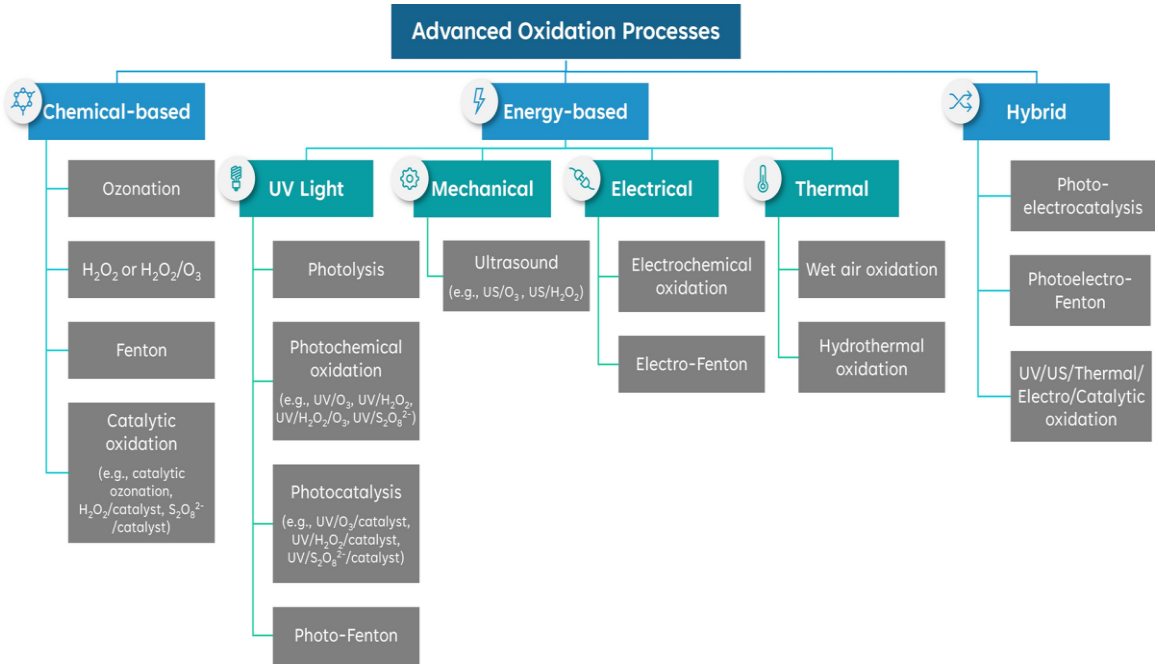


Figure 1.1.4.4: Classification of AOPs for water and wastewater treatment into chemical-based, energy-based, and hybrid systems, with examples including ozonation and photo-lysis. Reprinted from Ref. [24], with permission from Springer.

Among these AOPs, the Fenton process and photo-Fenton processes are two of the most widely used methods for degrading organic pollutants, such as dye molecules. The Fenton method operates by using a mixture of Fenton's reagent (H_2O_2) and soluble iron (II) salt (Fe^{2+}), initiating the degradation by producing radicals through the reaction $Fe^{2+} + H_2O_2 \rightarrow OH\cdot + Fe^{3+} + OH^-$. Despite their efficiency in rapidly degrading dyes, the Fenton process presents significant disadvantages, including high costs, dependence on pH levels, and the potential for producing toxic by-products. To mitigate these drawbacks, Fenton-like degradation processes have been developed, extending the concept of catalytic degradation to materials beyond traditional iron. Additionally, the photo-Fenton-like Electro-Fenton approach, which is

considered a widely advanced oxidation method, is distinguished by the absence of toxic byproducts and promotes environmental preservation.

Critically, both wastewater treatment and hydrogen production are currently energy-intensive. A unified catalytic approach capable of driving both oxidation (pollutant degradation) and evolution (water splitting) reactions using solar or chemical energy is required to lower this energy footprint.

1.2. Fundamentals of Photocatalysis and Electrocatalysis

Importantly, not all oxide semiconductors operate within a simple band-like transport framework. Several transition-metal oxides, including CuO, belong to the class of charge-transfer or strongly correlated oxides, where the ligand–metal energy separation (Δ) is smaller than the on-site Coulomb repulsion (U). In such systems (Δ < U), photogenerated holes preferentially reside on oxygen 2p orbitals rather than metal 3d states, leading to ligand-hole–associated oxygen-centred hole states and intrinsically localized charge carriers. As a result, charge transport proceeds predominantly via thermally activated small-polaron hopping, rather than conventional band conduction. This distinction has profound consequences for photocatalytic and electrocatalytic reaction kinetics and motivates a bottleneck-oriented analysis of catalytic performance rather than a purely band-edge-based description.

The conversion of solar or electrical energy into chemical fuels relies fundamentally on the interaction between semiconducting materials, light, and electrochemical interfaces. Photocatalysis and electrocatalysis are two complementary approaches within the broader field of solar-to-fuel conversion. Understanding their underlying principles is essential for rational catalyst design, especially when employing transition metal oxides (TMOs) as multifunctional materials for both environmental remediation and energy applications. This section outlines the core physicochemical principles governing photocatalytic and electrocatalytic processes, providing a foundation for the development of advanced CuO-based catalysts explored in this thesis.

1.2.1. Photocatalysis

Photocatalysis is a process in which a semiconductor material accelerates chemical reactions under light illumination without undergoing permanent chemical change itself. The

phenomenon was first widely reported in a 1972 study by Fujishima and Honda, who demonstrated photocatalytic water splitting on TiO_2 electrodes [25]. Since then, semiconductor photocatalysis has been extensively explored as a sustainable route for both environmental remediation and solar-to-chemical energy conversion [26].

When a semiconductor photocatalyst is irradiated with photons of energy equal to or exceeding its band gap (E_g), it undergoes electronic excitation that forms the basis of all photocatalytic reactions. This process begins with photon absorption, in which a valence band (VB) electron gains sufficient energy to overcome the band gap and transition into the conduction band (CB). The resulting electronic transition generates a mobile conduction-band electron (e^-) and a corresponding positively charged hole (h^+) in the VB. This fundamental excitation process can be represented as:

$$\text{Semiconductor} + h\nu \rightarrow e^- (\text{CB}) + h^+ (\text{VB})$$

The overall efficiency of photocatalysis depends on three interrelated steps:

1.2.1.1 Photon Absorption and Charge Generation

The absorption of photons leads to the creation of electron-hole pairs. The number of carriers generated depends on the semiconductor's absorption coefficient, band structure, and defect density. Materials with narrower band gaps (e.g., CuO, Fe_2O_3) can harvest visible light more effectively than wide-band-gap materials like TiO_2.

1.2.1.2 Charge Separation and Migration

Once generated, charge carriers must migrate from the bulk of the semiconductor to its surface without undergoing recombination. Recombination, either radiative (photon emission) or non-radiative (phonon dissipation), is a major intrinsic loss pathway that drastically reduces photocatalytic efficiency. Effective charge separation is influenced by: Crystal structure and intrinsic defects, Band bending at semiconductor–electrolyte interfaces, Built-in electric fields, and Dopant-induced trap states assisting charge mobility. Thus, nano-structuring and doping are therefore widely used strategies to enhance carrier mobility and suppress recombination.

In correlated oxides such as CuO, these steps are strongly influenced by localized trap states and thermally assisted polaronic detrapping/hopping, making charge delivery to the surface a

central kinetic bottleneck examined throughout this thesis.

1.2.1.3 Interfacial Surface Reactions

When electrons and holes reach the surface, they participate in reduction and oxidation reactions, respectively. These reactions occur at the semiconductor-electrolyte interface, where carriers transfer to adsorbed molecules [27]. For example:

- Reduction reactions by electrons: $O_2 + e^- \rightarrow \cdot O_2^-$
- Oxidation reactions by holes: $H_2O + h^+ \rightarrow \cdot OH + H^+$

Because electrons and holes possess specific redox potentials determined by the band-edge positions, only reactions whose redox potentials lie within the semiconductor's energetic window can proceed.

1.2.1.4 Generation of Reactive Oxygen Species (ROS)

Through a cascade of interfacial reactions, photogenerated carriers generate a suite of reactive oxygen species (ROS) that play central roles in pollutant degradation and advanced oxidation processes. The major ROS include Hydroxyl radicals (•OH), which are generated through hole oxidation of water or hydroxide ions: $H_2O + h^+ \rightarrow \bullet OH + H^+$, $OH^- + h^+ \rightarrow \bullet OH$. Thus •OH is one of the most powerful oxidants ($E^0 \approx +2.7$ V), capable of non-selectively degrading dyes, pharmaceuticals, and organic pollutants. Similarly, Superoxide radicals($\bullet O_2^-$) are formed when CB electrons reduce dissolved oxygen: $O_2 + e^- \rightarrow \bullet O_2^-$. These radicals can further participate in secondary reactions, yielding H_2O_2 or •OH. In addition, Hydrogen peroxide (H_2O_2) is often generated through the dismutation of superoxide: $2\bullet O_2^- + 2H^+ \rightarrow H_2O_2 + O_2$, which can undergo further reduction or oxidation to generate additional radicals. In the end, Singlet oxygen ($^1O_2$) can also be produced via energy transfer processes involving $\bullet O_2^-$ or excited semiconductor states.

1.2.1.5 Role of ROS in Photocatalytic Degradation

As discussed earlier, Industrial dyes are widely used in textiles, leather, and pharmaceuticals, and are resistant to biodegradation. Photocatalysts utilize light to generate ROS that mineralize dyes into CO_2 and H_2O [26]. The synergy between different radicals, combined with the semiconductor's surface acidity/basicity, morphology, and defect chemistry, governs the

overall photocatalytic performance. These species are highly reactive and can oxidize organic pollutants, enabling photocatalytic degradation and environmental purification. Figure 1.2.1.5.1 illustrates a visual mechanism of heterogeneous photocatalysis for the breakdown of micropollutants [28]

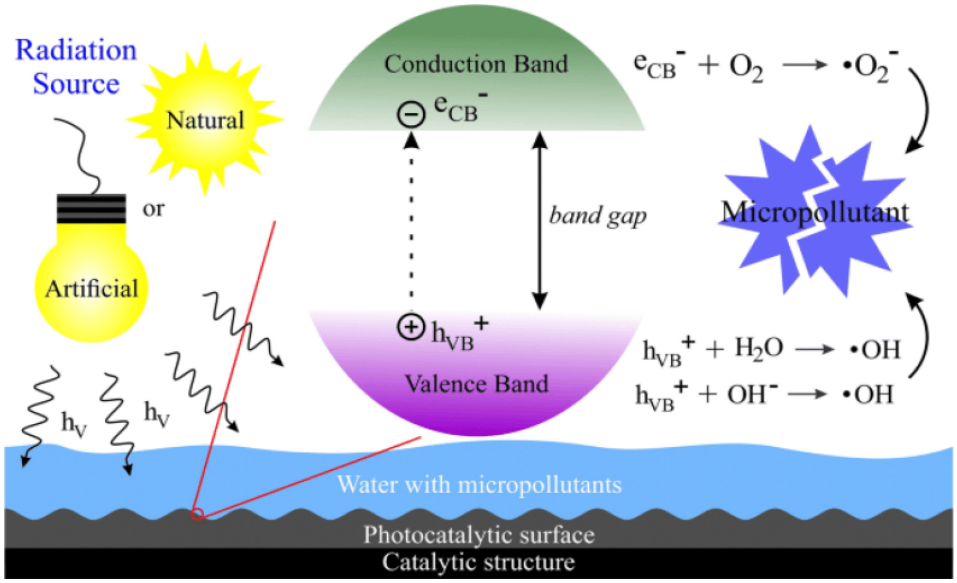


Figure 1.2.1.5.1: The mechanism of heterogeneous photocatalysis for the breakdown of micropollutants. Reprinted from Ref. [28], with permission from Springer.

1.2.2 Electrocatalysis

Electrocatalysis involves accelerating electrochemical reactions at the interface between an electrode and an electrolyte under an externally applied potential [29]. In the context of clean energy production and storage, electrocatalytic water splitting is a cornerstone technology because it converts renewable electricity into hydrogen fuel with high efficiency and zero direct emissions [30]. The process consists of two half-reactions: the hydrogen evolution reaction (HER) at the cathode and the oxygen evolution reaction (OER) at the anode. Despite its apparent simplicity, water splitting is limited by slow interfacial reaction kinetics, the requirement for significant overpotentials, and catalyst degradation under operational conditions [31]. Understanding the mechanistic underpinnings of HER and OER is therefore essential for designing advanced electrocatalysts such as transition metal oxides [32].

1.2.2.1 Concepts in Electrocatalysis

Electrocatalysis is governed by a combination of thermodynamic and kinetic factors. The thermodynamic driving force for an electrochemical reaction is defined by electrode potentials, whereas the kinetic rate is determined by: (i) Adsorption strength of intermediates (ii) Electron transfer rates across the electrode–electrolyte interface, (iii) Intrinsic conductivity of the catalyst, (iv) Surface structure, morphology, and defect density, (v) Mass transport of reactants and products, (vi) Interfacial electric double-layer structure.

These factors manifest in measurable quantities such as overpotential, Tafel slope, charge-transfer resistance, and turnover frequency, which serve as key descriptors for evaluating catalyst performance.

1.2.2.2 Hydrogen Evolution Reaction (HER) Mechanism

HER is a two-electron reaction in which water molecules (in alkaline media) or protons (in acidic media) are reduced to produce molecular hydrogen [33]. In alkaline electrolytes (discussed here for completeness; OER is the electrocatalytic focus of this thesis), water serves as the proton donor. The HER mechanism consists of the following elementary steps:

- Volmer Step – Electrochemical Adsorption: $H_2O + e^- \rightarrow H^* + OH^-$

Water dissociates on the catalyst surface, forming adsorbed hydrogen atoms (H*) and hydroxide ions. This step is often the rate-determining step (RDS) for catalysts with weak water-dissociation ability.

- Heyrovsky Step – Electrochemical Desorption: $H^* + H_2O + e^- \rightarrow H_2 + OH^-$

An adsorbed hydrogen atom combines with an electron and another water molecule to produce hydrogen gas.

- Tafel Step – Chemical Recombination: $H^* + H^* \rightarrow H_2$

Two surface-bound hydrogen atoms recombine to form H_2 without further electron transfer.

HER Pathway Determination

The kinetic fingerprint of HER is typically represented by the Tafel slope [34], which reveals

the dominant reaction pathway:

- ~120 mV dec^{-1} → Volmer step limited
- ~40 mV dec^{-1} → Heyrovsky step limited
- ~30 mV dec^{-1} → Tafel step limited

Efficient electrocatalysts reduce the energy barrier for both water dissociation (Volmer step) and hydrogen desorption (Tafel/Heyrovsky steps). For this reason, catalysts like CuO can be modified to improve charge delivery and interfacial kinetics; in this thesis, Fe-modified CuO is examined in detail for alkaline OER, while Li/Zn–CuO for HER is treated as a future extension.

1.2.2.3 Oxygen Evolution Reaction (OER) Mechanism

OER is a more complex four-electron, four-proton oxidation reaction that produces molecular oxygen. It typically occurs in alkaline media through a sequence of proton-coupled electron transfer (PCET) steps involving the formation of high-valence metal–oxygen intermediates [35].

The overall alkaline OER reaction is:

$$4OH^- \rightarrow O_2 + 2H_2O + 4e^- \quad (E^0 = +1.23 \text{ V vs. RHE})$$

The mechanistic steps on a metal oxide catalyst (M) can be described as:

- Hydroxyl Adsorption: $M + OH^- \rightarrow M–OH + e^-$
- Oxide Formation: $M–OH + OH^- \rightarrow M–O + H_2O + e^-$
- O–O Bond Formation: $M–O + OH^- \rightarrow M–OOH + e^-$
- Oxygen Release: $M–OOH + OH^- \rightarrow O_2 + M + H_2O + e^-$

Rate Determination and Challenges

Unlike HER, OER requires breaking and forming multiple chemical bonds (M–O, M–OH, M–OOH), making it intrinsically sluggish [36]. The high energy barrier for O–O Bond formation results in large kinetic overpotentials, often exceeding 300–400 mV for practical catalysts [37].

Therefore, an ideal OER catalyst must: (i) stabilize key intermediates without over-binding them, (ii) possess optimal M–OH, M–O, and M–OOH adsorption energies, (iii) offer high conductivity for rapid electron transport, and (iv) resist oxidative degradation at high potentials.

TMOs, especially those involving Ni, Fe, Co, or Cu, are excellent candidates because they can cycle between multiple oxidation states (e.g., $Cu^{2+} \leftrightarrow Cu^{3+}$) and form active oxyhydroxide species under anodic bias [38].

1.2.2.4 Electrocatalytic Performance Descriptors

Quantitative assessment of HER and OER catalysts typically involves several key parameters [39]:

1.2.2.4.1 Overpotential (η)

The overpotential serves as an essential parameter for evaluating the performance of materials in hydrogen evolution reactions (HER) and oxygen evolution reactions (OER). In theory, a reaction should occur when the applied potential matches the equilibrium potential. However, in real-world applications, applied potential often surpasses the equilibrium value. As a result, the extra potential needed to drive an electrochemical reaction beyond its thermodynamic level is termed the overpotential. This understanding of overpotential is crucial for improving the efficiency of electrochemical processes.

Over potential = [Electrode potential – Equilibrium potential]

Additional potential is required beyond the thermodynamic voltage (1.23 V for overall water splitting). In the case of the OER, η is commonly specified at a current density of j = 10 mA cm^{-2}. This value aligns closely with what is anticipated in an integrated solar-to-fuel device operating at 10% efficiency under one sun illumination. Typically, overpotential is measured in millivolts (mV), with lower η values indicating greater electrocatalytic activity. It's important to note that η is positive for anodic reactions and negative for cathodic reactions. This relationship provides valuable insights into the efficiency of the electrochemical processes involved.

1.2.2.4.2 Tafel Slope

Indicates reaction kinetics and the rate-determining step. The Tafel Equation, named after Julius Tafel, provides information about reaction kinetics. It is used to compare the OER activity performance of different electrocatalysts. Tafel analysis can be used to calculate two important parameters: Tafel Slope and Exchange Current Density, and the rate-determining step. Julius Tafel investigated that the fundamental logarithm law is obeyed between the current density and the electrochemical overpotential, which is termed as Tafel Equation and can be written as

$$\eta = a + b\log j$$

where j, η, and a, b represents the current density, overpotential, and empirical coefficient, respectively.

1.2.2.4.3 Exchange Current Density (j_0)

Represents intrinsic catalytic activity independent of overpotential.

1.2.2.4.4 Electrochemical Active Surface Area (ECSA)

Estimated via double-layer capacitance (C_{dl}), reflects accessible catalytic sites.

1.2.2.4.5 Charge-Transfer Resistance (R_{ct})

Measured from electrochemical impedance spectroscopy (EIS); lower R_{ct} indicates faster interfacial electron transfer.

1.2.2.4.6 Turnover Frequency (TOF)

Moles of reactant converted per active site per unit time, directly measuring catalytic efficiency.

1.2.2.4.7 Stability Metrices

Chronopotentiometry (CP) and chronoamperometry (CA) reveal structural and electrochemical durability.

1.2.2.5 Relevance to Transition Metal Oxides

Transition metal oxides are excellent electrocatalysts because they: (i) Exhibit rich redox chemistry (multiple oxidation states), (ii) Possess strong metal-oxygen covalency, (iii) Form active oxyhydroxide phases under operating conditions, (iv) Allow defect engineering to tune adsorption energetics, (v) Are stable and low-cost, (vi) Can be doped or combined into mixed oxides and composites.

For CuO-based catalysts, HER activity can be significantly enhanced through aliovalent (e.g., Li^{+}) and Isovalent (e.g., Zn^{2+}) doping, which improves conductivity and modifies hydrogen binding energy. Similarly, Fe- or Co-modified CuO can promote OER by stabilizing high-valent M–OOH intermediates.

1.2.3 Transition Metal Oxides as Catalysts

Transition metal oxides (TMOs) constitute one of the most versatile and widely explored classes of catalytic materials for both photocatalytic and electrocatalytic processes [40], [41], [42], [43]. Their remarkable catalytic behavior stems from the unique electronic structures of transition metals, which possess partially filled d orbitals capable of engaging in multi-electron redox reactions, forming variable oxidation states, and enabling strong metal–oxygen interactions. These features make TMOs valuable in applications ranging from environmental remediation and pollutant degradation to water splitting, CO_2 reduction, and energy storage [44].

In the context of photocatalysis and electrocatalysis, TMOs such as CuO, Fe_2O_3, Co_3O_4, MnO_x, NiO_x, TiO_2, and mixed metal oxides exhibit a desirable balance of earth abundance, low cost, chemical tunability, and functional stability, making them highly attractive for sustainable catalysis and large-scale deployment [45], [46], [47], [48], [49], [50], [51].

1.2.3.1 Electronic Structure and Redox Flexibility

The catalytic behaviour of TMOs is primarily governed by the interaction between transition metal d orbitals and oxygen p orbitals. This interaction gives rise to: (i) Variable oxidation states (e.g., $Mn^{2+}/Mn^{3+}/Mn^{4+}$, Fe^{2+}/Fe^{3+}, Cu^{+}/Cu^{2+}), (ii) Mixed valency enabling rapid electron transfer, (iii) Strong metal–oxygen covalency, influencing band structure, and (iv) Charge

compensation through intrinsic defects, including oxygen vacancies and metal interstitials.

Because catalytic reactions such as HER, OER, and ROS formation require multi-electron processes, the ability of TMOs to reversibly switch oxidation states is essential. For example: (i) Fe^{3+}/Fe^{2+} cycles facilitate Fenton-like reactions in photocatalysis, (ii) Co^{3+}/Co^{4+} and Ni^{2+}/Ni^{3+} transitions enable the formation of active oxyhydroxide species during OER, and (iii) Cu^{2+}/Cu^{+} redox shuttling enhances electron transfer and ROS generation in visible-light photocatalysis.

This redox flexibility distinguishes TMOs from noble metals and wide-band-gap semiconductors, enabling them to serve as dual-function photocatalysts and electrocatalysts.

1.2.3.2 Defect Chemistry and Catalytic Function

The presence of intrinsic and extrinsic defects plays a decisive role in determining the catalytic activity of TMOs. Important defect types include Oxygen vacancies (V_O), Metal vacancies (V_M), Interstitial metal ions (M_i), and Substitutional dopants (M'_M). These defects influence catalytic behaviour through:

(a) Modulation of Electronic Structure

Defects introduce localized states within the bandgap, which can enhance (i) visible-light absorption, (ii) improve charge separation, and (iv) facilitate electron transport

(b) Enhancement of Active Site Density

Defect-rich surfaces provide additional adsorption sites for (i) H_2O, OH^-, and oxygen intermediates during OER, (ii) H* intermediates during HER, and (iii) O_2 and organic molecules during photocatalysis

(c) Improved Conductivity

Redox-active defects (e.g., V_O in CuO) enhance small-polaron hopping and promote rapid charge transport, which is crucial for electrocatalysis.

(d) Promotion of Reaction Intermediates

Defective TMOs stabilize key intermediates such as: (i) M–OH, M–O, and M–OOH in OER,

(ii) H*, OH*, and O_2* in HER and ORR, and (iii) ROS precursors (superoxide, hydroxyl radicals) in photocatalysis

Thus, defect engineering is central to optimizing TMO catalysts.

1.2.3.3 Band Structure and Photocatalytic Properties

TMOs possess a diverse range of band gaps (from ultranarrow ~1.2 eV for CuO to wide >3.2 eV for TiO_2), enabling broad applicability under both UV and visible illumination.

Key advantages include: (i) Strong d–p hybridization, facilitating visible-light absorption, (ii) Band-edge tunability through doping, defects, and heterojunction design, (iii) Compatibility with Z-scheme and S-scheme architectures, enhancing charge separation, (iii) Stability under photo-corrosive environments compared to metal sulphides or nitrides.

Band alignment plays a critical role in determining whether the semiconductor can drive specific reactions. For example: (i) The CB edge must be more negative than 0 V vs. NHE for H^+/H_2 reduction, (ii) The VB edge must be more positive than +1.23 V vs. NHE for water oxidation or •OH generation.

Many TMOs (CuO, Fe_2O_3, Co_3O_4) satisfy these criteria for visible-light–driven ROS formation and photocatalytic degradation.

1.2.3.4 Electrocatalytic Activity of TMOs

Transition-metal oxides (TMOs) are widely investigated as electrocatalysts owing to their chemical robustness, earth abundance, and rich redox chemistry, particularly under alkaline conditions. In many oxide systems, electrocatalytic activity emerges not from metallic conductivity but from the ability of the oxide lattice and surface to reorganize electronically and structurally under applied bias. TMOs can sustain harsh electrochemical environments, undergo reversible surface reconstruction, and provide coordinatively unsaturated metal–oxygen sites that participate directly in electrochemical reactions.

A defining feature of oxide electrocatalysts is their propensity to form hydroxylated or oxyhydroxide-like surface states under anodic polarization, which often act as the catalytically active phase during oxygen evolution reaction (OER). In this context, adsorption and

transformation of oxygenated intermediates are governed by surface electronic structure, redox accessibility, and charge-transfer kinetics rather than bulk conductivity alone. These attributes make TMOs particularly suitable platforms for probing reaction-specific kinetic bottlenecks in alkaline electrocatalysis.

Despite these advantages, TMOs also exhibit inherent limitations that constrain electrocatalytic performance. Many oxides, including CuO and Fe_2O_3, possess low intrinsic electrical conductivity due to localized charge carriers and polaronic transport. Strong carrier localization can lead to sluggish interfacial charge transfer, while excessive defect densities may promote recombination or deep trapping. In addition, non-optimal binding energies of reaction intermediates can limit OER kinetics, and prolonged operation under extreme redox conditions may induce surface restructuring or degradation.

Consequently, performance enhancement in TMO electrocatalysts relies on targeted electronic and structural modulation, rather than simple surface area maximization. Strategies such as dopant-valency control, defect engineering, and morphology regulation are employed to tune redox accessibility, charge-transfer resistance, and surface reaction pathways. In this thesis, such strategies are examined within a bottleneck-oriented framework, with particular emphasis on disentangling transport-limited and surface-reaction-limited regimes using electrochemical and impedance-resolved diagnostics.

1.3. CuO as Catalyst

Copper (II) oxide (CuO) is an earth-abundant, p-type transition metal oxide that has emerged as a versatile catalyst for visible-light-driven photocatalysis, Fenton-like oxidation, and alkaline electrocatalysis [52]. Its suitability stems from the interplay of its monoclinic crystal structure, narrow band gap, rich defect chemistry, and Cu^{2+}/Cu^{+} redox flexibility, all of which contribute to its optoelectronic and catalytic behavior [53].

1.3.1. Crystal Structure, Electronic Configuration, and Crystal Field Effects

CuO crystallizes in the monoclinic tenorite phase (space group C2/c), where each Cu^{2+} ion is coordinated by four oxygen atoms in an almost square-planar arrangement, with two elongated axial Cu-O bonds resulting from Jahn-Teller distortion. Owing to the strong Cu 3d–O 2p covalency and the $\Delta < U$ electronic configuration, holes in CuO exhibit significant ligand

character, giving rise to oxygen-centred hole states that govern both photocatalytic oxidation reactions and surface redox accessibility. In this geometry, the Cu 3d orbitals experience a D_{4h}-type crystal field splitting, in which the energy ordering follows: $d_{x^2-y^2} > d_{xy} \approx d_{z^2} > d_{xz} \approx d_{yz}$ [54], [55].

Cu^{2+} ($3d^9$), therefore, has a single unpaired electron in the high-energy $d_{x^2-y^2}$ orbital, which overlaps strongly with the O 2p orbitals lying in the basal plane [56]. This hybridization produces a narrow, strongly correlated valence band that governs the p-type semi-conductivity of CuO via small-polaron hopping [57], [58]. Therefore, thermal energy (kT) plays a non-trivial role in 'detrapping' carriers, a phenomenon investigated in this thesis (Chapter 4). The conduction band is mainly composed of Cu 4s and O 2p antibonding states. The resulting narrow band gap enables visible-light absorption and photogenerated charge separation, explaining CuO's success as a photocatalyst. However, the localized nature of Cu 3d electrons results in high effective masses and limited carrier mobility, constraining electrochemical performance. In catalysis, the $d_{x^2-y^2}$ orbital also controls the adsorption of reaction intermediates through metal-oxygen or metal-hydrogen bonds [59], [60]. Fine-tuning its occupancy and energy relative to the O 2p band is thus a key strategy to optimize the adsorption-desorption balance described by the Sabatier principle [61], [62]. Controlled doping of CuO modifies this delicate balance by altering the crystal field, lattice strain, and charge-carrier concentration [63], [64].

1.3.2 Structure and Electronic Properties

CuO is a narrow-bandgap semiconductor, with reported values ranging from ~1.2 to 1.9 eV, depending on the synthesis route, particle size, and morphology [65]. The band structure of CuO allows strong absorption of visible light, which constitutes approximately 45% of solar radiation, making it an attractive source for solar energy harvesting. Unlike its counterpart Cu_2O (cuprite), which has a cubic structure and a wider bandgap (~2.1 eV), CuO is more suitable for visible-light-driven photocatalysis [66].

CuO is intrinsically a p-type semiconductor due to the presence of copper vacancies (V_{Cu}) that act as acceptor states. This p-type conductivity enhances hole-driven oxidation reactions, which are particularly important in the photocatalytic degradation of organic pollutants and in the oxygen evolution reaction (OER) during electrochemical water splitting [67]. The absorption

coefficient of CuO in the visible region is on the order of 10^5 cm^{-1}, further demonstrating its potential for light-driven processes [68].

Unlike conventional semiconductors (e.g., TiO_2), where charge carriers are delocalized in bands, CuO behaves as a charge-transfer insulator with a ground state of $d^9\underline{L}$ (where $\underline{L}$ denotes a ligand hole). This means that photogenerated holes are not just 'missing electrons' but are physically localized on the oxygen lattice (O 2p orbitals). Consequently, the catalytic rate is often limited not by surface adsorption, but by the rate of polaronic hopping required to deliver these localized charges to the active site. This thesis posits that overcoming this 'delivery bottleneck' is as critical as tuning the surface energy.

1.3.3 Defects and Conduction Mechanisms

Defect chemistry plays a central role in governing the electronic structure, charge transport, and catalytic behaviour of CuO. As a charge-transfer, strongly correlated oxide, CuO does not conform to a simple band-like semiconductor model; instead, its functional properties emerge from the interplay between localized electronic states, defect-induced trapping, and thermally activated charge transport. Intrinsic point defects such as copper vacancies (V_{Cu}), oxygen vacancies (V_O), and interstitials modify the Cu–O electronic network and strongly influence carrier localization and surface redox accessibility [56], [69].

Copper vacancies (V_{Cu}), which are preferentially stabilised under oxygen-rich conditions, act as acceptor-type defects and contribute to the intrinsic p-type conductivity of CuO. Rather than simply increasing hole concentration, V_{Cu} promotes the formation of oxygen-centred, ligand-hole–associated states, which are particularly relevant for oxidation reactions at the catalyst surface. These defects, therefore, influence both bulk charge compensation and surface redox chemistry.

Oxygen vacancies (V_O), typically generated under oxygen-poor synthesis conditions, introduce localized donor-like states that can act as electron traps. Moderate concentrations of V_O may prolong carrier lifetimes by suppressing immediate recombination; however, excessive oxygen vacancy densities can localize carriers too strongly, giving rise to deep trapping sites that function as recombination centres and impede effective charge delivery to surface reaction sites.

Interstitial oxygen (O_i) may also contribute to p-type behaviour by compensating excess electrons and stabilising hole-rich local environments, further modifying the balance between localized and delocalized charge states within the Cu–O lattice.

Charge transport in CuO is therefore dominated by small-polaron hopping, in which charge carriers (electrons or holes) are localized on Cu–O units and migrate between adjacent lattice sites via thermally activated detrapping and hopping processes, rather than extended band conduction [57]. Although this transport mechanism results in lower intrinsic mobility compared to conventional semiconductors, it plays a critical role in catalytic systems by governing charge delivery to surface reaction sites. Therefore, defects in CuO do not merely introduce additional electronic states but fundamentally regulate detrapping barriers, hopping probabilities, and interfacial charge accessibility, thereby defining the dominant reaction-specific kinetic bottlenecks under photonic, thermal, or electrochemical driving forces.

Furthermore, the redox accessibility of the Cu–O network, particularly when modified by redox-active dopants, can influence interfacial charge transfer under electrochemical bias. In this thesis, such redox flexibility is examined explicitly in the context of Fe-substituted CuO for alkaline oxygen evolution reaction (OER), where charge transfer and surface reaction kinetics become dominant bottlenecks. Hydrogen evolution reactions are treated as a future extension of this framework [70].

1.3.4 Catalytic Applications of CuO

(a) Photocatalysis and Photo-Fenton Processes

CuO effectively generates reactive oxygen species (ROS) under visible light: •OH through VB-hole oxidation, $\bullet O_2^-$ from CB-electron reduction, H_2O_2 through sequential electron transfer, •OH/•OOH via Cu^+-mediated H_2O_2 activation.

These species collectively mineralize organic dyes and persistent pollutants. In your dye-degradation studies, CuO-based materials operated efficiently even under low-power illumination and demonstrated performance boosts when interfaced with other semiconductors or halide-containing domains.

(b) Electrocatalysis (HER and OER)

CuO participates in both reactions of alkaline water splitting:

- HER: CuO requires defect engineering or dopants to optimize H* binding and improve conductivity.
- OER: CuO can form CuOOH-like intermediates under anodic bias, enabling multi-step oxygen evolution.

Although pristine CuO shows modest performance, targeted modification (through dopants, vacancies, and composites) significantly enhances reaction kinetics.

1.3.5 Limitations of Pristine CuO

Despite its advantageous properties, pristine CuO suffers from inherent drawbacks that limit its performance in photocatalysis and electrocatalysis:

- Rapid electron–hole recombination: Narrow bandgap materials often exhibit high recombination rates, reducing photocatalytic efficiency.
- Poor electrical conductivity: Small-polaron conduction restricts long-range charge transport, limiting electrochemical performance.
- Photo corrosion and instability: CuO tends to degrade under extended illumination or in strong oxidative conditions, compromising durability.
- Limited band alignment: The conduction band position of CuO lies close to the H^+/H_2 reduction potential, limiting its ability to drive proton reduction effectively without external bias or modification.

1.3.6 Strategies for Performance Enhancement

Doping (Crystal-Field and Defect Control)

Doping plays a critical role in tailoring the catalytic behavior of CuO because substituent ions such as Fe^{3+}, Zn^{2+}, Li^+, or Al^{3+} can subtly reshape the local ligand environment around Cu^{2+} and modulate the underlying crystal-field landscape [71]. By altering the octahedral and tetragonal components of the crystal-field splitting (Δ_{oct} and $\Delta_{tetragonal}$), dopants influence the energetic ordering and hybridization strength of the Cu 3d–O 2p orbitals, thereby adjusting the electronic structure that governs catalytic reactivity. These

modifications often stabilize alternative Cu oxidation states, including enhanced Cu^{+} character and oxygen-centred hole states, which participate in redox-mediated reaction pathways. At the same time, dopants can relieve polaron localization and enhance carrier mobility by introducing controlled lattice distortions or beneficial defect states, enabling faster charge transport to reactive surface sites. Collectively, these crystal-field and defect-driven changes result in more favorable adsorption energies for key catalytic intermediates, ultimately enhancing both photocatalytic and electrocatalytic performance.

Morphology and Surface Engineering

Morphology and surface engineering offer additional and highly effective means of optimizing the catalytic behavior of CuO by tailoring the material's interaction with light, reactants, and charge carriers. Controlling the size, shape, and dimensionality of CuO, whether as nanosheets, nanowires, hollow spheres, or thin films, directly influences surface area, facet exposure, and the density of undercoordinated sites, all of which govern catalytic activity. Nano structuring generally shortens carrier diffusion distances and increases the probability that photogenerated or electrochemically injected charges reach reactive sites before recombination occurs. At the same time, surface engineering strategies such as introducing oxygen-rich terminations, tuning surface hydroxylation, or creating defect-rich interfaces further enhance adsorption, activation, and conversion of catalytic intermediates. These modifications not only improve mass transport and reaction kinetics but also enhance the stability of CuO under operational conditions. Collectively, carefully engineered morphologies and tailored surface chemistries allow CuO-based catalysts to achieve superior performance across both photocatalytic and electrocatalytic applications.

From the above discussion, it becomes evident that the catalytic performance of CuO-based systems cannot be universally optimized by a single descriptor such as surface area, band gap, or conductivity. Instead, different reactions like photocatalytic degradation, photo-Fenton-like oxidation, hydrogen evolution, and oxygen evolution are limited by distinct reaction-specific bottlenecks, including charge separation, polaronic transport, redox accessibility, and interfacial reaction kinetics. Rational catalyst design therefore, requires identifying and selectively mitigating the dominant bottleneck for each reaction pathway, a concept that underpins the unified catalytic framework developed in this thesis.

1.4. Scope and Objectives of the Thesis

In the context of this thesis, a *catalytic bottleneck* is defined as the dominant elementary step or physicochemical constraint that limits the overall reaction rate under a given set of driving conditions (light, temperature, or applied potential). This bottleneck may arise from limitations in charge generation, charge transport, interfacial charge transfer, surface redox turnover, or coupled mass transport processes. Importantly, the bottleneck is reaction-specific and condition-dependent rather than an intrinsic and immutable material property.

1.4.1. Scope

Building on the above rationale, this thesis is guided by the central hypothesis that a single, earth-abundant CuO platform, when rationally engineered through dopant-valency-controlled defect chemistry and morphology modulation, can be used to identify and selectively mitigate reaction-specific catalytic bottlenecks across environmental and energy conversion processes. In charge-transfer oxides such as CuO, catalytic performance is frequently limited not by adsorption alone, but by the ability to deliver charge to surface reaction sites through charge separation, detrapping/polaronic transport, redox accessibility, and interfacial charge-transfer kinetics under different driving forces (light, temperature, and potential).

Accordingly, the thesis focuses on four core studies: (i) aliovalent, non-redox Al^{3+} substitution to electronically modulate the Cu–O network and enhance photocatalytic/photo-Fenton-like oxidation without relying on redox dopants; (ii) CuO nanosheets to isolate morphology and temperature-assisted charge-transport effects; (iii) redox-active Fe substitution to enable photo-Fenton-like dye degradation through altered surface redox pathways; and (iv) extension of Fe-doped CuO to alkaline OER, where impedance-resolved analysis is used to distinguish interfacial and surface-reaction bottlenecks. Investigations on Li/Zn-modified CuO toward alkaline HER are treated as ongoing/future work and are not considered core thesis chapters.

In line with the above hypothesis, the present work is structured around three overarching research questions

RQ1: How does aliovalent, non-redox Al^{3+} substitution and defect modulation in CuO influence charge separation, redox accessibility, and photo-(Fenton-like) oxidation performance under low-power visible light or sunlight?

RQ2: To what extent can morphology and dimensionality (CuO nanosheets) and temperature-assisted detrapping/polaronic hopping govern light-driven kinetics, and how do these transport factors differ from dark adsorption behaviour?

RQ3: How does redox-active Fe substitution alter reaction pathways and bottlenecks across photo-Fenton-like dye degradation and alkaline OER, and can a unified, reaction-specific bottleneck framework be established using structural/electronic descriptors and impedance-resolved kinetics?

1.4.2. Objectives

The specific objectives of this thesis are therefore to:

- Synthesize and systematically characterize baseline CuO, Al-substituted CuO, and morphology-controlled CuO nanostructures, and establish how defect chemistry, localized electronic (trap) states, and surface states govern light-driven charge separation, transport, and photocatalytic activity under low-power visible light and sunlight.
- Elucidate photo-Fenton-like oxidation pathways in CuO-based systems, distinguishing between ligand-hole-associated electronic modulation (Al^{3+} substitution) and redox-active dopant effects (Fe^{3+}/Fe^{2+} cycling), and identify the dominant kinetic bottlenecks controlling reactive oxygen species generation and dye degradation.
- Isolate the role of morphology and dimensionality by investigating CuO nanosheets and quantify how temperature-assisted detrapping and polaronic charge transport influence photocatalytic kinetics relative to dark adsorption behaviour.
- Develop and evaluate Fe-doped CuO electrocatalysts for alkaline oxygen evolution reaction (OER) and employ electrochemical analysis and impedance-resolved diagnostics to disentangle interfacial charge-transfer limitations, surface-reaction kinetics, and dopant-concentration-dependent activity trends.
- Construct a unified, reaction-specific bottleneck framework that correlates dopant valency, localized electronic descriptors, surface chemistry, and kinetic resistances,

thereby deriving design rules for bottleneck-targeted optimization in CuO-based oxide catalysts.

(Future extension) Position ongoing Li/Zn-modified CuO studies for alkaline HER as an extension of the same bottleneck framework, without including them as core thesis chapters.

1.5. Structure of the Thesis

This thesis is organized into seven chapters, each contributing to the development of a reaction-specific, bottleneck-oriented framework for understanding and optimizing CuO-based oxide catalysts for environmental remediation and energy conversion.

Chapter 1: Introduction

This chapter introduces the global challenges associated with sustainable energy production and water pollution and outlines the role of photocatalysis and electrocatalysis in addressing these challenges. The fundamental principles governing catalytic processes in transition-metal oxides are discussed, with particular emphasis on CuO as a charge-transfer, strongly correlated oxide exhibiting localized electronic states and polaronic charge transport. The scope, research questions, and objectives of the thesis are defined, establishing the conceptual basis for a bottleneck-oriented analysis of catalytic performance.

Chapter 2: Experimental Methods and Characterization Techniques

This chapter describes the synthesis routes and experimental methodologies employed throughout the thesis. It details the preparation of CuO-based materials using sol–gel and hydrothermal approaches, electrode fabrication protocols, and the suite of structural, morphological, optical, surface, and electrochemical characterization techniques used to probe structure–property–bottleneck relationships across photocatalytic and electrocatalytic systems.

Chapter 3: Aliovalent Al^{3+} Substitution in CuO: Defect-Driven and Ligand-Hole-Associated Photo-Fenton-Like Photocatalysis

This chapter investigates aliovalent, non-redox Al^{3+} substitution in CuO as a controlled strategy to modulate the Cu–O electronic network and localized electronic states without introducing additional redox pathways. The effects of Al incorporation on lattice structure, defect

chemistry, electronic screening, and surface properties are systematically examined, and their influence on photo-(Fenton-like) oxidation of organic pollutants under low-power visible light and natural sunlight is analyzed. This chapter establishes a baseline understanding of defect-driven, ligand-hole-associated photocatalysis in CuO.

Chapter 4: CuO Nanosheets: Morphology-Controlled and Temperature-Assisted Charge Transport in Photocatalysis

This chapter isolates the role of morphology and dimensionality by examining two-dimensional CuO nanosheets synthesized via a hydrothermal route. By decoupling morphological effects from chemical doping, the chapter demonstrates how enhanced exposed facets, shortened charge-migration lengths, and temperature-assisted detrapping and polaronic hopping govern light-driven photocatalytic kinetics. The interplay between transport-limited charge delivery and surface reaction steps is critically evaluated.

Chapter 5: Redox-Active Fe-Substituted CuO: Photo-Fenton-Like Oxidation and Reaction-Pathway Switching

This chapter explores the introduction of redox-active Fe into the CuO lattice to enable photo-Fenton-like degradation of organic dyes. The synergistic roles of Fe^{3+}/Fe^{2+} redox cycling, defect chemistry, and surface oxygen species in reactive oxygen species generation and pollutant degradation kinetics are elucidated under visible-light irradiation. The results highlight a distinct bottleneck-mitigation pathway compared to non-redox Al substitution and morphology-driven approaches.

Chapter 6: Resolving Oxidation-Side Catalytic Bottlenecks in Alkaline Oxygen Evolution Using Fe-Substituted CuO

This chapter extends the defect-engineered Fe-substituted CuO system to alkaline electrochemical oxygen evolution reaction (OER). Electrochemical measurements, impedance spectroscopy, and theoretical analysis are combined to resolve interfacial charge-transfer processes, surface-reaction kinetics, and dopant-concentration-dependent bottlenecks under applied bias. The findings demonstrate how dopant valency and electronic structure govern electrocatalytic performance in CuO-based oxides.

Chapter 7: Conclusions and Outlook: Reaction-Specific Bottleneck Engineering in CuO-Based Oxides

This chapter summarizes the key findings and unifying insights derived from the thesis, emphasizing the emergence of a reaction-specific bottleneck framework for CuO-based catalysts. The broader implications of this framework for other correlated oxide systems are discussed, and potential future research directions are outlined, including ongoing investigations on Li- and Zn-modified CuO for alkaline hydrogen evolution as a natural extension of the present work.

Chapter 2 Experimental Methods and Characterization Techniques

Abstract: *This chapter outlines the experimental procedures employed for the synthesis, processing, and characterization of CuO-based materials investigated in this thesis. Emphasis is placed on reproducibility, compositional control, and scalability of the adopted synthesis routes. Pristine and transition-metal-doped CuO materials were synthesized using sol–gel and hydrothermal methods under carefully controlled conditions. A comprehensive suite of complementary techniques was employed to elucidate structure-property relationships relevant to photocatalytic and electrochemical performance. The physicochemical properties of the as-synthesized materials were systematically examined using X-ray diffraction (XRD), field-emission scanning electron microscopy (FE-SEM), energy-dispersive X-ray spectroscopy (EDX), Fourier-transform infrared spectroscopy (FTIR), and Raman spectroscopy. Optical properties, including band-gap energy, were analyzed using UV–visible diffuse reflectance spectroscopy (DRS). Detailed morphological, crystallographic, and elemental analyses were performed using electron microscopy (TEM), selected area electron diffraction (SAED), and associated elemental mapping. Specific surface area and pore size distribution were evaluated using the Brunauer–Emmett–Teller (BET) method. Dynamic light scattering (DLS) and zeta-potential measurements were used to assess hydrodynamic particle size and surface charge in aqueous suspension.*

Photocatalytic activity was evaluated through the degradation of aqueous dye solutions under (i) low-power visible-light, (ii) low-power UV lights, as well as (iii) direct sunlight irradiation following adsorption–desorption equilibrium in the dark. Reaction progress was monitored using UV–visible spectroscopy, and degradation kinetics were analyzed using pseudo-first-order models. In addition, electrode fabrication procedures and electrochemical characterization techniques, including linear sweep voltammetry, cyclic voltammetry, electrochemical impedance spectroscopy, chronopotentiometry, and chronoamperometry, are described in detail. Collectively, this chapter establishes the experimental framework for interpreting the structure–performance relationships discussed in the subsequent chapters.

2.1. Experimental Methods

2.1.1. Materials and Reagents

All chemicals were of analytical grade and used as received without further purification. Copper precursors, dopant salts (Al^{3+}, Fe^{3+}, and other transition-metal sources), complexing agents, solvents, and oxidants were procured from commercial suppliers. Deionized water with a resistivity of 18.2 MΩ.cm was used throughout all synthesis and experimental procedures.

2.1.2. Synthesis of CuO-Based Materials

CuO-based materials investigated in this thesis were synthesized using scalable wet-chemical routes, primarily sol–gel and hydrothermal methods, selected to ensure compositional homogeneity, reproducibility, and precise control over dopant concentration and morphology.

2.1.2.1. Sol-Gel synthesis of CuO

The sol-gel process is a versatile wet-chemical synthesis technique that enables the homogeneous formation of metal and perovskite oxides at comparatively low temperatures. It offers excellent control over composition, stoichiometry, and microstructure while remaining cost-effective relative to conventional high-temperature solid-state routes. Owing to its tunability, the sol-gel method is widely used to produce ceramic materials, functional oxide powders, and thin-film intermediates. The process involves generating a stable and uniform sol from molecular precursors, followed by controlled hydrolysis and condensation to form a three-dimensional gel network. Subsequent removal of the solvent and organic residues through drying and thermal treatment yields the final oxide material with tailored structural and morphological characteristics.

Pure CuO nano powders were synthesized using a sol–gel combustion route. Stoichiometric quantities of CuO precursor were first dissolved in dilute nitric acid under continuous stirring at room temperature, forming a clear pale-blue solution. Once complete dissolution and homogenization were achieved, a mixture of citric acid and ethylene glycol (in a 1:2 molar ratio) was introduced into the cationic solution. This organic pair acted as a gelling and complexing system, where citric acid coordinated with Cu^{2+} ions while ethylene glycol promoted polymer chain formation, effectively trapping the metal ions within a uniform

polymeric network. The resulting solution was heated on a hot plate for approximately 6 hours until a viscous gel was obtained. Subsequent dehydration and self-combustion of the gel in air produced fine black CuO precursor powders. These powders were then subjected to thermal treatment at 450 °C for 6 hours to remove nitrates and residual carbonaceous species, followed by grinding and final annealing at 600 °C for 2 hours to enhance crystallinity. The resulting CuO nano powders were finely ground before being used for structural characterization and photocatalytic dye degradation studies. A schematic of the different stages in the sol-gel process is shown in Figure 2.1.2.1.

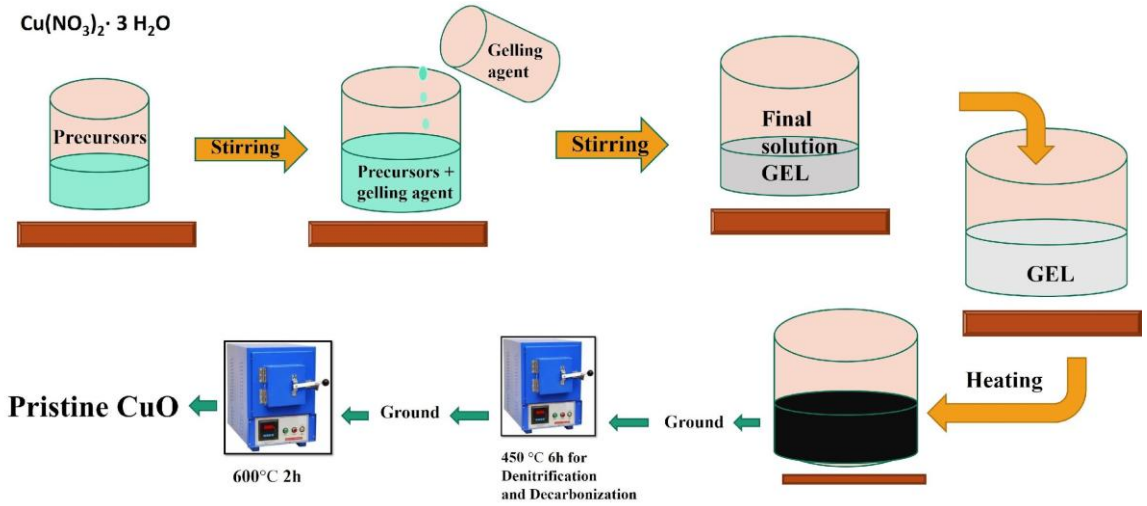


Figure 2.1.2.1: Schematic of sol-gel synthesis of Pristine CuO.

2.1.2.2. Sol-Gel synthesis of Al^{3+} doped CuO

$Cu_{1-x}Al_xO_{1+\delta}$ powders were synthesized via a sol-gel synthesis method. The samples are represented as C0 (x= 0), CA1 (x = 0.0156), CA2 (x = 0.0234), CA3 (x = 0.0312). The precursors used for the synthesis of samples were copper (II) oxide (CuO, 99.97%, Alfa Aesar) and Aluminum nitrate nonahydrate ($Al(NO_3)_3 \cdot 9H_2O$, 99.98%, Alfa Aesar). Stoichiometric ratios of CuO were dissolved in dilute nitric acid (HNO_3). After constant stirring, a pale blue solution formed at room temperature. To this solution, a calculated amount of aluminum nitrate crystallites was added and stirred vigorously. After the homogenous mixing of the precursors, a calculated amount of citric acid and ethylene glycol was added in a 1:2 ratio to the cationic solution under vigorous stirring. The citric acid and glycerol combination acted as a gelling agent by forming polymeric chains [72]. The homogeneous distributions of cations get attached

to the polymeric chains, and thereby, the homogeneity of the cations can be frozen. The polymers also act as fuel when burnt in the presence of air or oxygen. The resultant solution is heated in a hot plate for ~ 6 hours to obtain the gel. The gels were dehydrated and then burnt in the air to obtain black powders. The obtained black powders were denitrified and decarbonized by heating at 450 ^{0}C for 6 hours. The samples obtained are ground well and annealed at 850 ^{0}C for 2 hours. The obtained powders were ground again, and all the characterizations and photocatalytic dye degradation experiments were done [Figure 2.1.2.2].

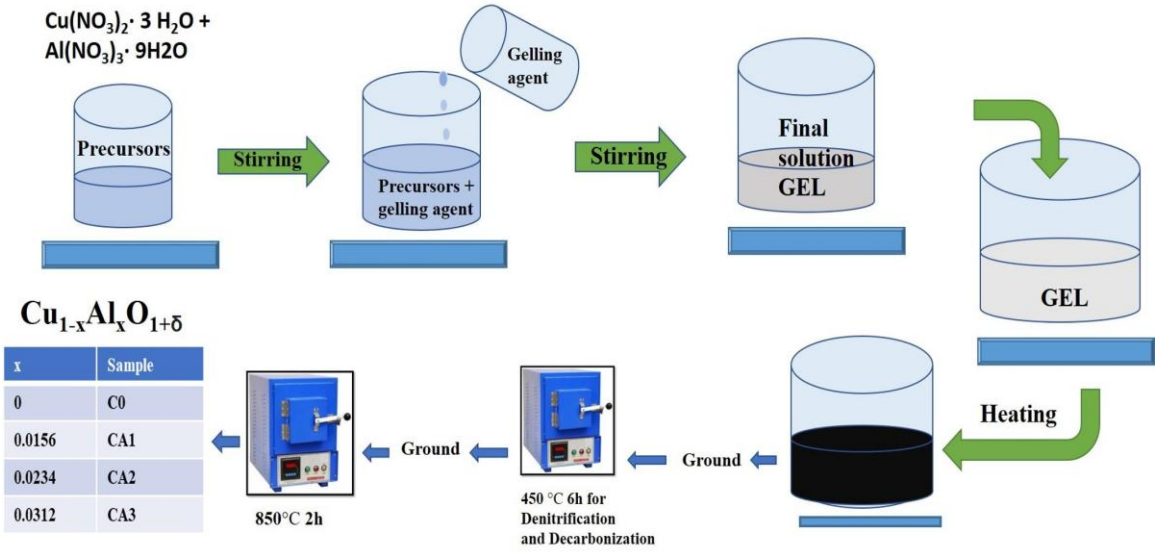


Figure 2.1.2.2: Schematic of sol-gel synthesis of Al^{3+} doped CuO

2.1.2.3. Sol-Gel synthesis of Fe^{3+} doped CuO

$Cu_{1-x}Fe_xO_{1\pm\delta}$ (CFO) nanopowders were prepared using a sol-gel synthesis route. The samples are named C0 (x = 0), CF1 (x = 0.0156), and CF2 (x = 0.0312). The precursors used for the synthesis of samples were copper (II) oxide (CuO, 99.97%, Alfa Aesar) and iron nitrate nonahydrate [Fe $(NO_3)_3.9H_2O$, 99%, Alfa Aesar]. Stoichiometric ratios of CuO were dissolved in dilute nitric acid (HNO_3). Dilution was obtained using deionized water (DIW, 18.2 mega-ohm-cm). Under constant stirring, a pale, blue-colored solution was formed at room temperature. A calculated amount of iron nitrate crystallites was added to this solution and stirred vigorously to obtain a homogeneous solution of the Cu and Fe ions. The calculated amount of citric acid and ethylene glycol was taken in a beaker in a 1:2 ratio, and DIW was added to dissolve the solution. The solution, when heated, forms monomers. This monomeric

solution was then added to the cationic solution under vigorous stirring and heating. The monomers got attached to the precursor cations, and upon further heating, formed polymeric chains with the cations attached homogeneously. The water content gradually evaporated through continuous heating for ~ 6 hours, resulting in a gel-like dehydrated state. The polymers in the polymeric gel act as a holding agent of homogeneity, as well as fuel upon further heating when burned in the air. The gels were converted to black powders that were denitrified and decarbonized by heating at 450°C for 6 hours. The black nanopowders (nps) were ground and annealed at 600°C for 2 hours to further remove traces of residual carbon and nitrogen. The obtained nps were ground again and are the final CFO samples [Figure 2.1.2.3].

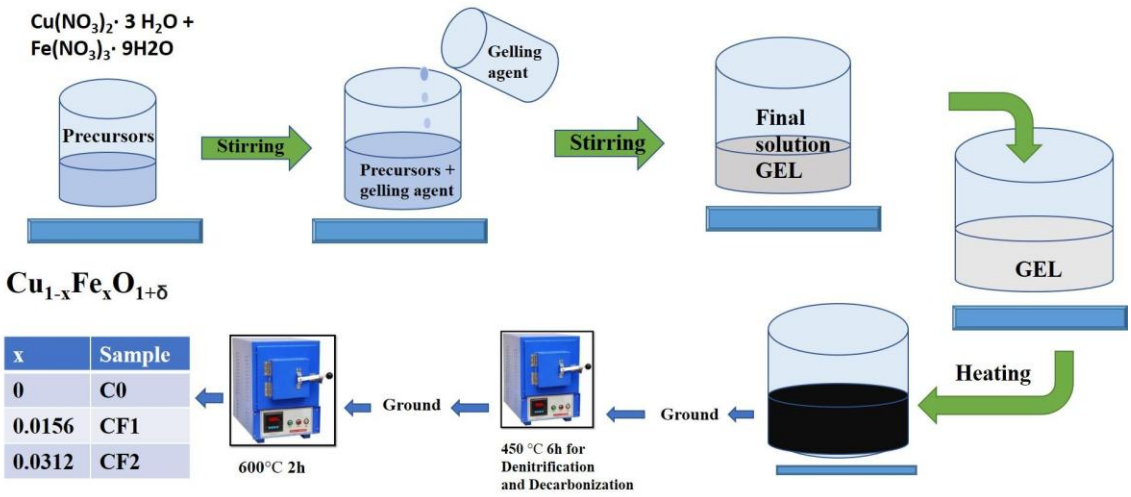


Figure 2.1.2.3: Schematic of sol-gel synthesis of Fe^{3+} doped CuO.

2.1.2.4. Sol-Gel synthesis of Li- and Zn-doped CuO

Li- and Zn-doped CuO materials were synthesized using the same sol–gel method analogous to the procedure employed for Fe-doped CuO to ensure consistency across dopant systems. The compositions were formulated as $Cu_{1-x}Li_xO_{1-\delta}$ (x = 0, 0.0078, 0.0156, 0.0234, and 0.0312) and Cu_{1-x} Zn_xO (x = 0, 0.0078, 0.0156, 0.0234, and 0.0312).

In a typical synthesis, stoichiometric amounts of copper precursor and the corresponding lithium or zinc dopant salts were dissolved in dilute nitric acid under continuous magnetic stirring to obtain a clear and homogeneous cationic solution. Deionized water was used as the solvent medium. Separately, citric acid and ethylene glycol were dissolved in deionized water

and mixed in a 1:2 molar ratio to act as chelating and polymerizing agents. This solution was heated under stirring to initiate monomer formation and subsequently added to the cationic precursor solution.

Upon further heating, the metal ions were uniformly chelated within the growing polymeric network, ensuring molecular-level homogeneity. Continuous heating led to gradual solvent evaporation and the formation of a viscous gel. The resulting gels were dried and subjected to thermal decomposition in air at 450 °C for 6 h to remove organic constituents and nitrate residues. The obtained black precursor powders were subsequently ground and annealed at 600 °C for 2 h to achieve phase-pure monoclinic CuO with substitutional incorporation of Li^{+} or Zn^{2+} ions.

After annealing, the powders were reground to obtain fine, homogeneous samples and were used for subsequent structural, optical, and electrochemical characterization. Details of dopant-dependent optimization and performance evaluation are discussed in the corresponding chapters.

2.1.3. Hydrothermal synthesis of CuO

Hydrothermal synthesis is a solution-based crystal growth technique conducted in sealed, high-pressure vessels (autoclaves), enabling the formation of metal oxides and composite nanomaterials under controlled temperature and pressure conditions. This method provides precise control over nucleation and growth kinetics, enabling the production of highly crystalline materials with well-defined morphologies, such as nanorods, nanosheets, and hierarchical architectures. Compared to conventional high-temperature solid-state routes, hydrothermal synthesis operates at relatively low temperatures while promoting uniform dopant incorporation, defect engineering, and phase purity. The process typically involves dissolving or dispersing precursor salts in an aqueous medium, adjusting the pH and adding additives to direct growth, and subjecting the mixture to elevated temperatures, where supersaturation drives crystallization. Upon cooling, the resulting precipitates are collected, washed, and dried to yield nanostructured materials tailored for catalytic, electrochemical, and photocatalytic applications.

Pure CuO nanosheets were synthesized using a facile hydrothermal synthesis route. To detail the synthesis procedure, 3 g of copper chloride ($CuCl_2 \bullet 2H_2O$: 99.9% purity, Alfa Aesar, India)

was dissolved in 80 mL of deionized water (DIW, 18.2 mega-ohm-cm). Again, 1.6 g of Sodium hydroxide (NaOH: 99.9% purity, Alfa Aesar, India) was added to the previous $CuCl_2$ solution and mixed vigorously by stirring for 60 min. Thus, the addition of NaOH in 80 ml of DIW makes 0.5M NaOH present in the total solution. This solution was thereafter transferred to a 150-mL Teflon-lined autoclave and maintained at 120 °C for 24 hours. After that, the solution was cooled naturally to room temperature. Then the residuals were filtered and washed repeatedly with distilled water and ethanol to remove the impurities and then dried in a hot air oven at 60 °C overnight for 12 hours [Figure 2.1.3.1]. The nanosheets were formed after this treatment, which was characterized structurally and electrochemically, and further used in photocatalytic applications.

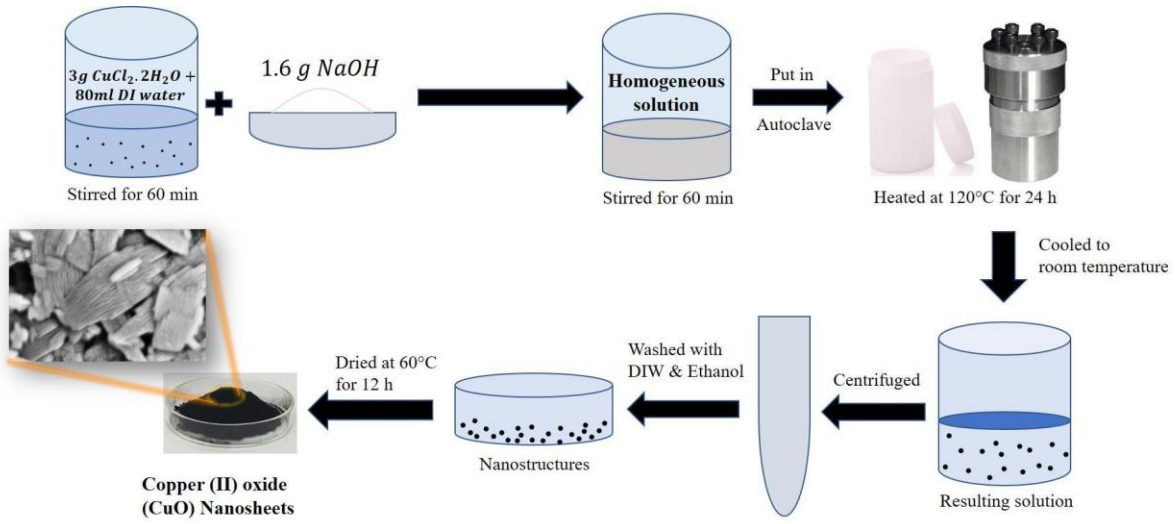


Figure 2.1.3.1: Schematic of the Synthesis Procedure of Copper Oxide Nanosheets. Reprinted from Ref. [73]

2.1.4. Photocatalytic and Photo-Fenton-like Experiments

Photocatalytic activity was evaluated using aqueous dye solutions as model organic pollutants under light irradiation. In a typical experiment, a known mass of photocatalyst was dispersed in the dye solution and magnetically stirred to ensure uniform suspension. Prior to illumination, the suspension was stirred in the dark for a fixed duration to establish adsorption–desorption equilibrium between the catalyst surface and dye molecules.

Illumination was provided using low-power ultraviolet or visible-light sources, or natural

sunlight, depending on the study. Details of the irradiation source (wavelength range, intensity, and geometry) specific to each study are provided in the corresponding chapter to avoid repetition. The two common light sources, the spectrum low-power LED and low-power UV light, are given in Figure 2.1.4.1 and Figure 2.1.4.2, respectively.

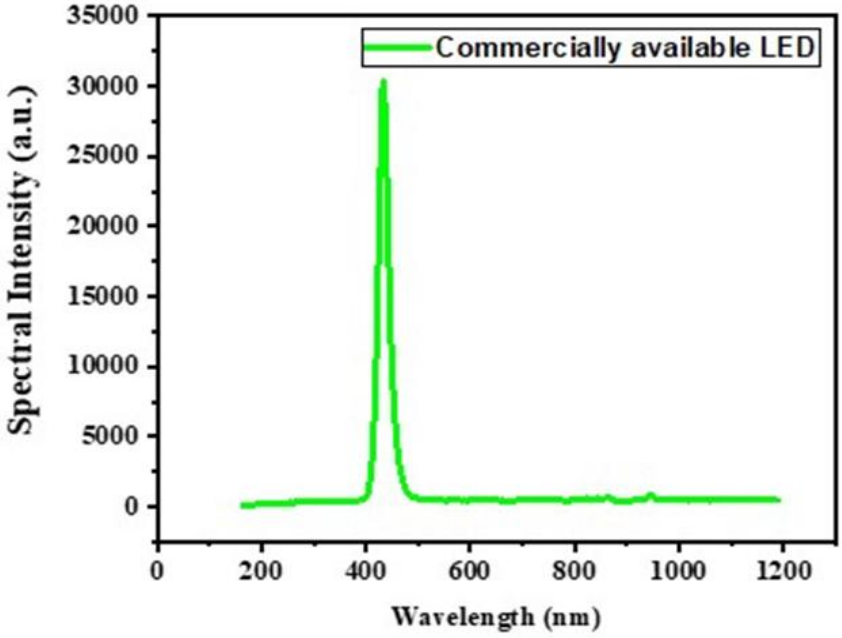


Figure 2.1.4.1: Spectrum of the commercially available household LED light used.

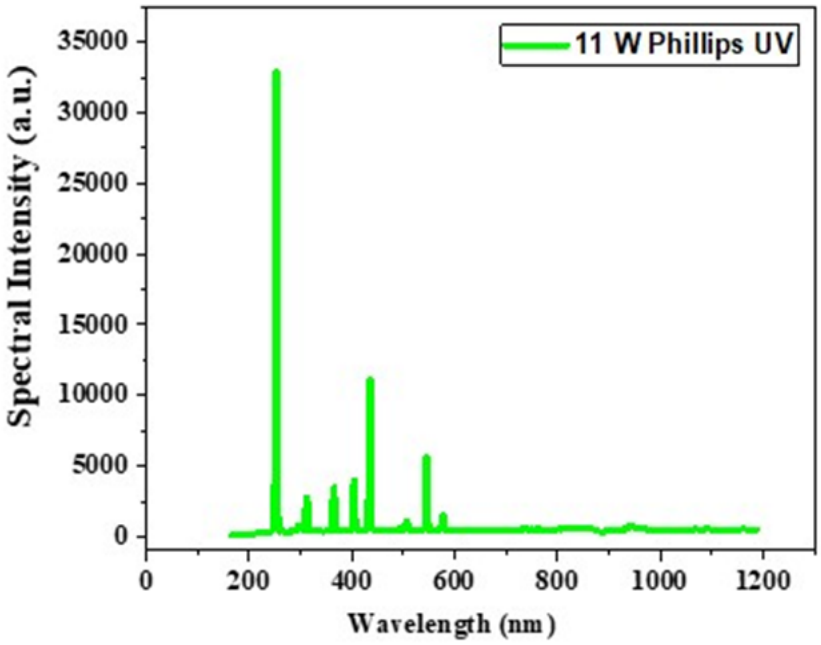


Figure 2.1.4.2: Spectrum of the 11 W Phillips light used.

During irradiation, aliquots were withdrawn at regular time intervals, centrifuged to remove catalyst particles, and analyzed using UV–visible spectroscopy. Reaction progress was monitored by tracking the temporal evolution of the characteristic absorption peak of the dye.

Photocatalytic degradation efficiency was calculated from absorbance changes as a function of irradiation time. Kinetic analysis was performed using pseudo-first-order reaction models, and apparent rate constants were extracted from linear fits. All experiments were conducted at least in triplicate to ensure reproducibility, and average values with appropriate uncertainty were reported.

For photo-Fenton-like studies, hydrogen peroxide was added as an oxidizing agent at controlled concentrations. Radical scavenger tests and catalyst reusability studies were performed where applicable to probe degradation pathways and catalyst stability. Mechanistic interpretation, reactive species identification, and comparative performance analysis are discussed in the respective results chapters.

Where required, temperature-controlled experiments and oxidant-assisted (photo-Fenton-like)

protocols were employed to decouple adsorption thermodynamics, charge-carrier activation, and redox accessibility; detailed analyses are presented in the corresponding chapters.

Where required, temperature-controlled experiments and oxidant-assisted (photo-Fenton-like) protocols were employed to decouple adsorption thermodynamics, charge-carrier activation, and redox accessibility; detailed analyses are presented in the corresponding chapters.

2.1.5. Electrode Preparation

For electrochemical measurements, catalyst inks were prepared by dispersing the synthesized powders in a mixture of solvent and polymer binder. The inks were ultrasonicated to ensure homogeneity and deposited onto conductive substrates using drop-casting. The coated electrodes were dried under ambient conditions prior to testing. Electrolyte composition, reference electrodes, and reaction-specific conditions are specified in the corresponding electrochemical chapters.

2.2. Physicochemical Characterization Techniques

A comprehensive suite of advanced physicochemical characterization techniques was employed to thoroughly investigate the physical properties, such as phase, symmetry, thermal behavior, particle size, surface morphology, atomic arrangement, and chemical features such as stoichiometry, elemental oxidation states, chemical environment, *etc.,* of the synthesized material. Powder X-ray Diffraction (XRD), having Cu-Kα radiation with wavelength λ = 1.542 Å, was used to analyze the phase purity, crystalline structure, and lattice parameters. Field Emission Scanning Electron Microscopy (FESEM) integrated with Energy Dispersive X-ray Spectroscopy (EDS) was used to explore the particle and surface morphology, particle size distribution, elemental homogeneity, and empirical stoichiometry. Raman spectroscopy analysis was used to study the bonding nature and the vibrational features. High-resolution imaging, atomic structural arrangements, lattice interplanar spacing, and structural details at the atomic level in the nanoscale range were understood through Transmission Electron Microscopy (TEM), High-Resolution TEM (HRTEM), and Selected Area Electron Diffraction (SAED) patterns. The chemical states and oxidation environments of the elements in the cathode material were investigated through X-ray Photoelectron Spectroscopy (XPS). A brief discussion of these advanced techniques is given in the following subsections.

2.2.1. X-Ray Diffraction (XRD)

XRD is a widely used, versatile non-destructive characterization tool that is commonly used to study the structure and phase characteristics of crystalline materials. This can be applied in determining the type and quantity of the phases present in the sample, unit cell parameters, crystal structure, crystalline texture, crystalline size, macro stress, and micro strain, etc. [Figure 2.2.1.1].

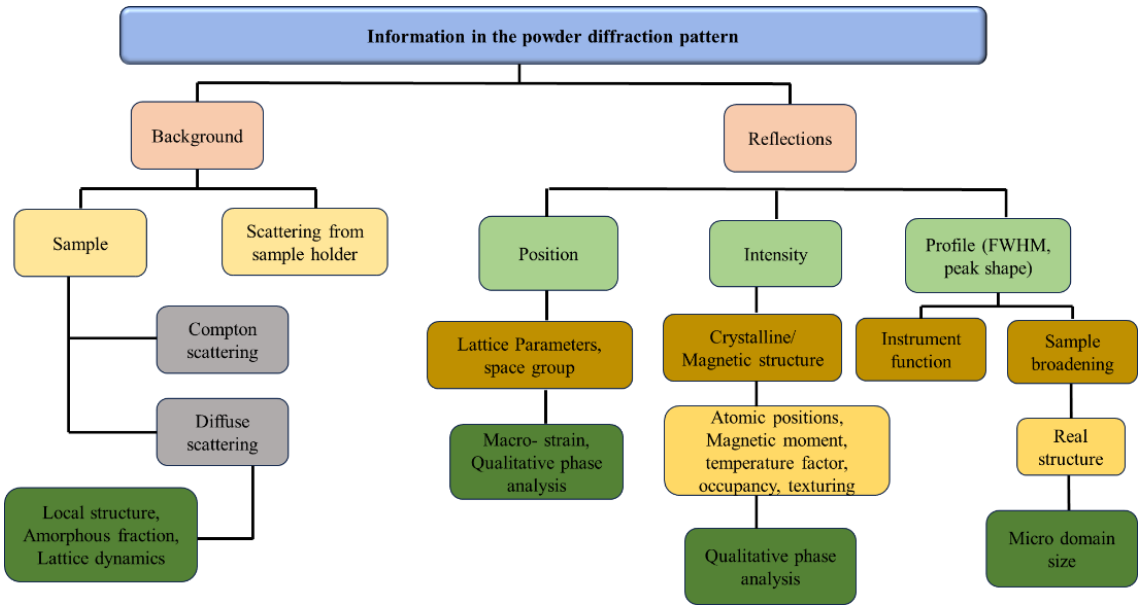


Figure 2.2.1.1: Flow chart of the different information obtained from the powder diffraction.

X-rays, electromagnetic waves with wavelengths on the order of a few angstroms, closely match the interatomic spacing of crystals. X-rays interact with their atoms when directed at a crystal, causing them to scatter. This scattering results in constructive interference, producing a distinctive pattern called an X-ray diffraction (XRD) pattern.

Bragg's condition

This law was proposed by W. L. Bragg in 1921 and is the fundamental condition of X-ray diffraction. When X-rays with wavelength "λ" strike a material at an incident angle θ, they diffract through the crystal lattice's parallel planes. Constructive interference between these diffracted rays occurs under the conditions described by Bragg's Law:

$$n\lambda = 2\ d\ sin\theta$$

where d is the interplanar spacing, θ is the incidence angle, n is an integer representing the order of diffraction, and λ stands for the wavelength of the incident light. When this criterion is met, a peak appears in the diffraction pattern at a specific angle [Figure 2.2.1.2].

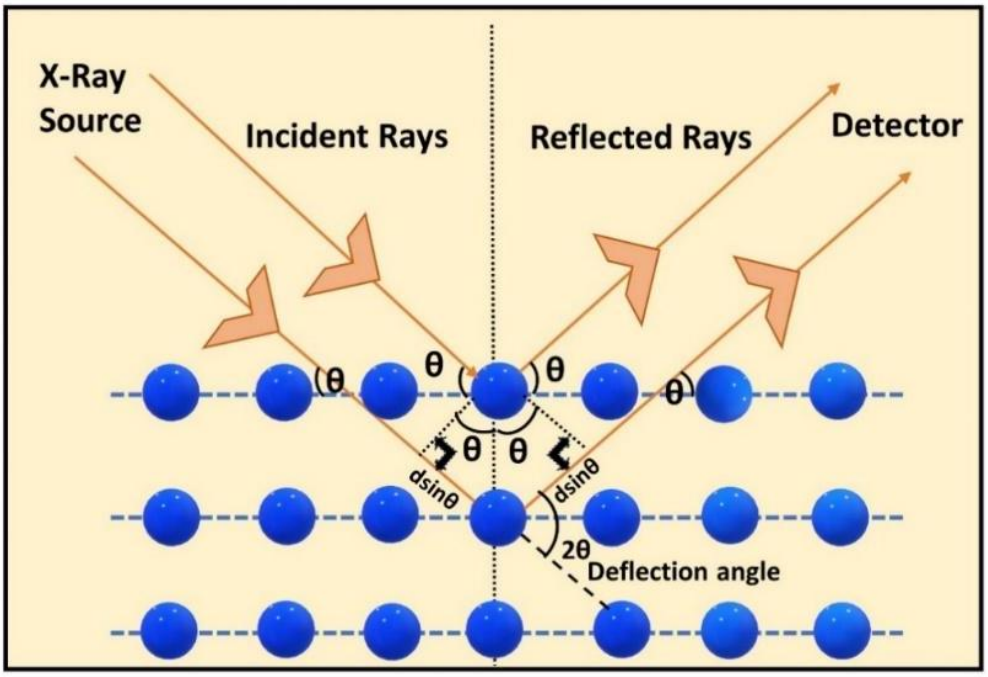


Figure 2.2.1.2: Schematic representation of X-ray diffraction in a crystal.

Experimental Setup:

The X-ray diffraction pattern was recorded for all the prepared samples using a Bruker D2 Phaser benchtop X-ray powder diffraction instrument. The instrument consists of an X-ray source, goniometer, sample stage, detector, and software.

a. The X-ray source consists of a copper anode (Cu) to generate an X-ray of wavelength Cu $K\alpha_1$: 1.5406 Å, Cu $K\alpha_2$: 1.5444 Å, with an operating current and voltage of 10 mA and 30kV, respectively. The X-ray tube features a beryllium window, which allows X-rays to escape outward. Moreover, the tube is partially encased in dense absorbing materials, such as lead, effectively preventing X-rays emitted in other directions from penetrating beyond the device's confines.
b. The goniometer controls the rotating platform of the instrument. It helps the sample holder to be precisely positioned at different angles relative to the incident X-ray (scattering angles (2θ) from 3° to 160°).

c. The samples are placed in the sample stage. Various sample holders are provided based on the type and amount of sample, including powder, film, and moisture-sensitive samples.
d. The detectors collect the diffracted X-rays from the sample. These are typically Si-strip detectors (1D LYNXEYE) capable of high-resolution data acquisition.
e. The control unit helps with the interface for operating the instrument. It allows the set of experimental parameters (2θ range, acquisitions, time, and step size) and initiates data acquisition. The software for Bruker is DIFFRAC.SUITE for instrument control and visualization of results.
f. This instrument uses Bragg-Brentano geometry to envisage sample preparation issues like particle size or preferential orientation [Figure 2.2.1.3]. In this case, the detector and the source move at the same rate while the sample holder is fixed (θ-θ geometry).

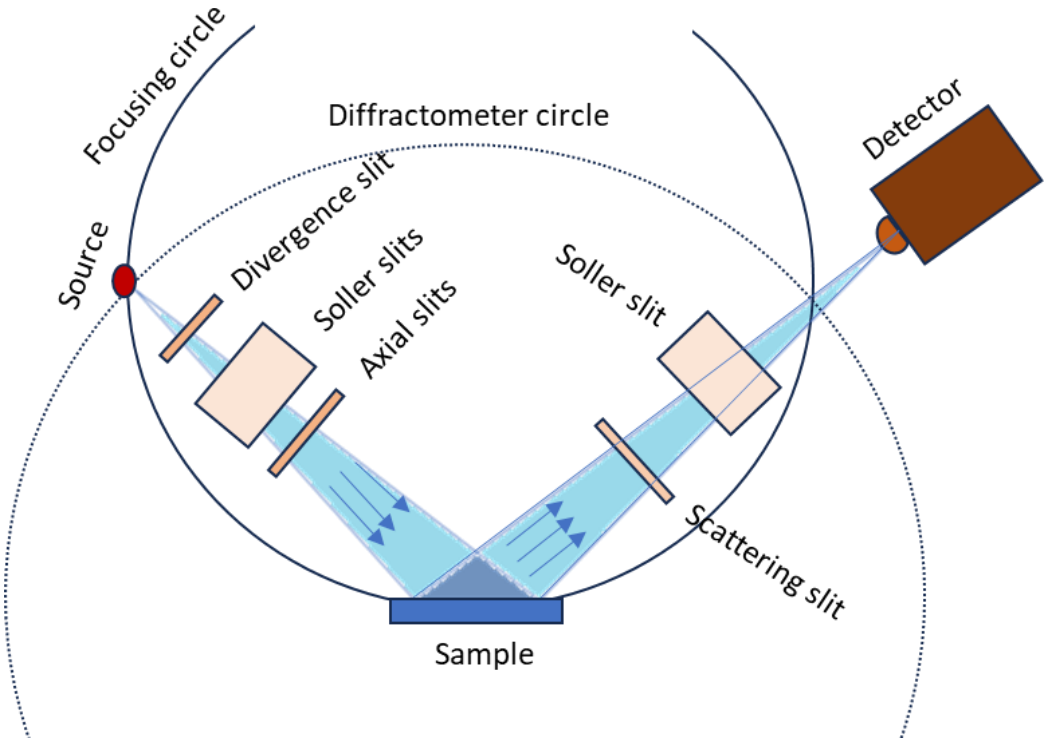


Figure 2.2.1.3: Schematic diagram of the Bragg Brantano geometry.

Structural Analysis using Rietveld Refinement

The XRD pattern obtained requires a systematic and careful analysis to extract information such as phase purity, interplanar spacing, lattice parameters, density, atomic positions, strain, bond lengths, and angles [Figure 2.2.1.4]. This analysis is performed using

the Rietveld refinement method. Hugo M Rietveld first proposed this method; the basic concept is to fit between observed and calculated diffraction intensities through least squares optimization [74], [75]. It is a full pattern-fitting approach. This process is possible for already-known materials with a pre-existing structure. It cannot be used for solving the crystal structure. The results of refinement contain information about cell parameters, anisotropy, atomic displacements, crystallite size, strain, and other relevant details. This also helps with the quantitative analysis of the weight percentage of different phases present in the sample.

There are various software options available for refinement, including MAUD, TOPAS, GSAS-II, and FullProf, among others. The calculated pattern of the structure is typically represented in a Crystallographic Information File (CIF). The Crystallography Open Database (COD) contains numerous CIF files that can be downloaded. Depending on the phases present in the sample, CIF information can be downloaded from COD. The experimental XRD pattern should be measured with a long scan rate and proper sample preparation. Both the experimental and calculated patterns, background, peak profile, and other relevant information need to be provided as input to the refinement software, allowing it to start refining the parameters corresponding to the instrument, sample, structure, and other relevant details.

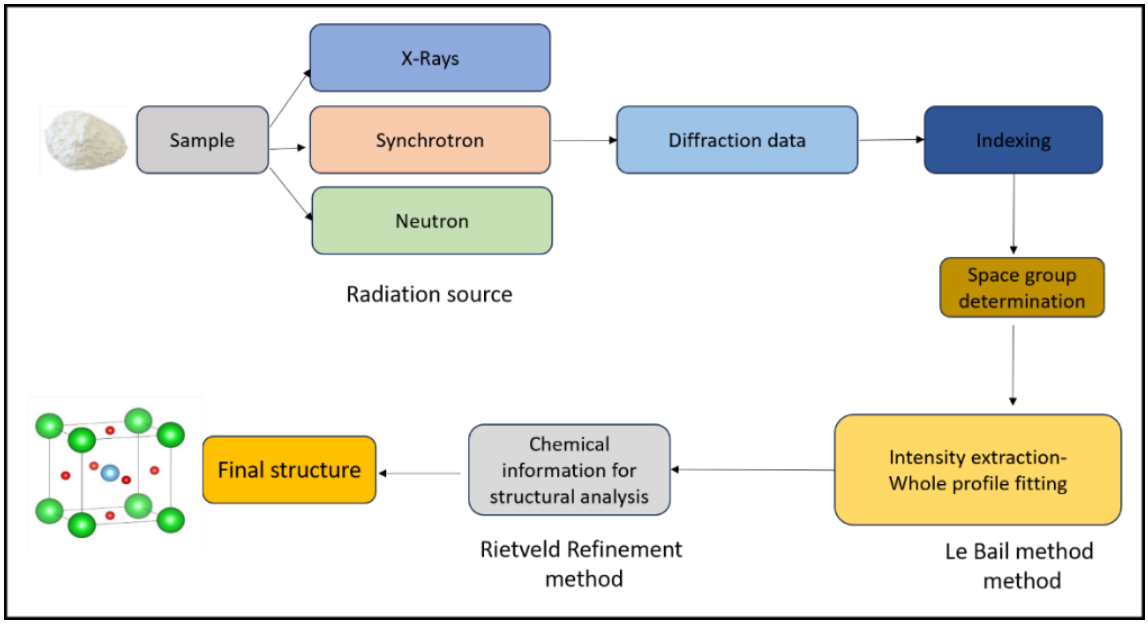


Figure 2.2.1.4: Flow chart of steps in the process of structural analysis from Powder Diffraction Data.

The residual difference (R) between the theoretical and measured results determines the quality of the refinement. Small values of R correspond to better fitting and more accurate crystal structure analysis. The commonly used R values are the Residual variance factor (R_p) and the weighted residual variance factor (R_{wp}), which are defined as follows [76].

$$R_p = \sum_i [Y_{Oi} - Y_{Ci}] / \sum_i [Y_{Oi}]$$

The most important and reliable parameters to judge the fitting qualities are weighted patterns:

$$R_{wp} = \left\{ \{ \sum_i w_i [y_{Oi} - y_{Ci})]^2 / \sum_i w_i [{y_{Oi}}^2] \}^{1/2} \right\}$$

The measured XRD intensity is Y_{oi}, the calculated intensity is Y_{ci} at point i, and w_i is the statistical weight factor. The change of R_{wp} towards a lower value indicates the refinement direction towards better fitting refinement results. The ratio of R_p to R_{wp} value is the goodness of fit χ^2. In general, χ^2 value close to 1 and an R_{wp} value close to 10 % or less is a good fit, and refined parameters are considered reliable. However, refinement cannot be completely relied on the R_{wp} value; sometimes there will be pseudo-convergence phenomena. Hence, along with the χ^2 and R_{wp} value, the chemical parameters of the refinement structure model, such as atomic coordinates, atomic proportions, etc., should be physically possible. Apart from all these factors visual assessment of the fitting of the experimental and theoretical model is also important.

As mentioned, a Bruker D2 phaser XRD instrument [Figure 2.2.1.5] with Cu Kα (λ = 1.54 Å) radiation was employed and operated at an applied voltage of 30 kV and current of 10 mA using Bragg Brentano geometry with a θ-θ goniometer. A silicon XRD sample holder is used, and the 2θ range is from 20° to 80° with a step size of 0.02° and a scan time of 0.6 seconds. GSAS-2 is used for the Rietveld refinement process, and the refined CIF file is analysed and plotted in Visualisation of Electronic and Structural analysis (VESTA) and Mercury software.

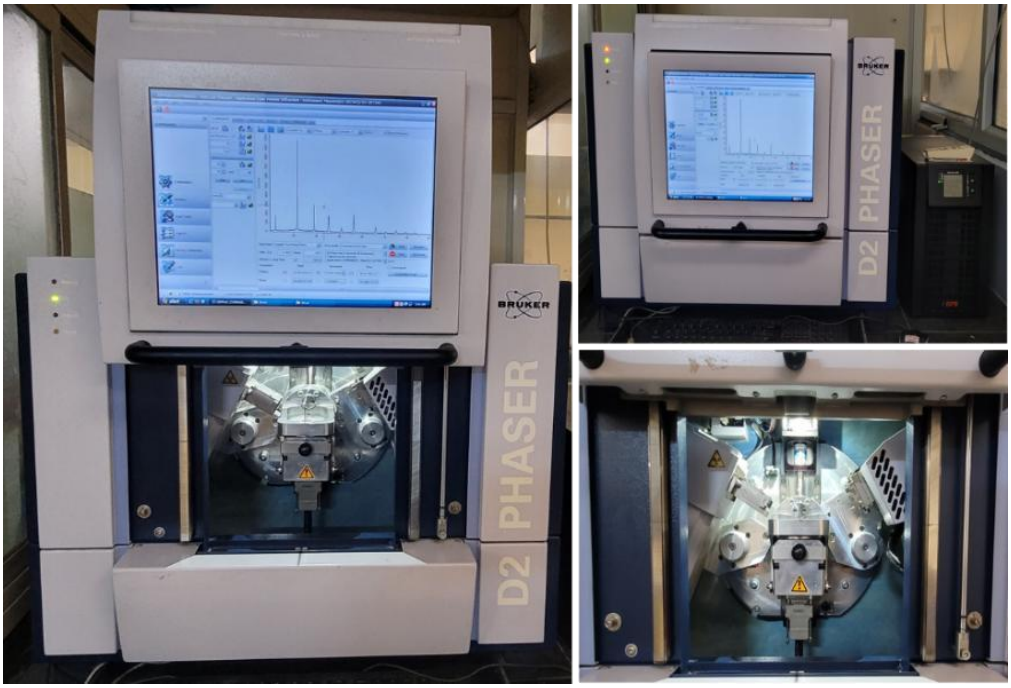


Figure 2.2.1.5: Picture of D2 PHASER XRD.

2.2.2. Raman Spectroscopy

When light incident on a material, energy is transferred between the incident radiation and the material, leading to inelastic scattering. The scattered light can provide information about the vibrational state of matter. Raman spectroscopy is the study of inelastic scattering of light. Raman scattering is named after Indian physicist Chandrasekhara Venkata Raman, who discovered it in 1928. He used mercury lamps as a monochromatic source of photons and a photographic plate to record spectra; he won the Nobel prize in physics in 1930 for the discovery of the Raman effect.

A monochromatic light source is focused on a sample, and the radiation scattered from the sample is observed. The process of elastic scattering in which most of the light scattered retains the same energy as the incident light is called Raleigh scattering. A small fraction of light is scattered with different energy than that of the incident energy due to inelastic scattering, known as Raman scattering. The scattered light consists of the Raleigh line, which is a strong line having a frequency equal to that of the incident light. Weak lines of higher frequency, higher than the exciting line, are anti-Stokes lines, and weak lines of lower frequency than the exciting lines are called Stokes lines. The schematic representation of Raman scattering is

shown in Figure 2.2.2.1.

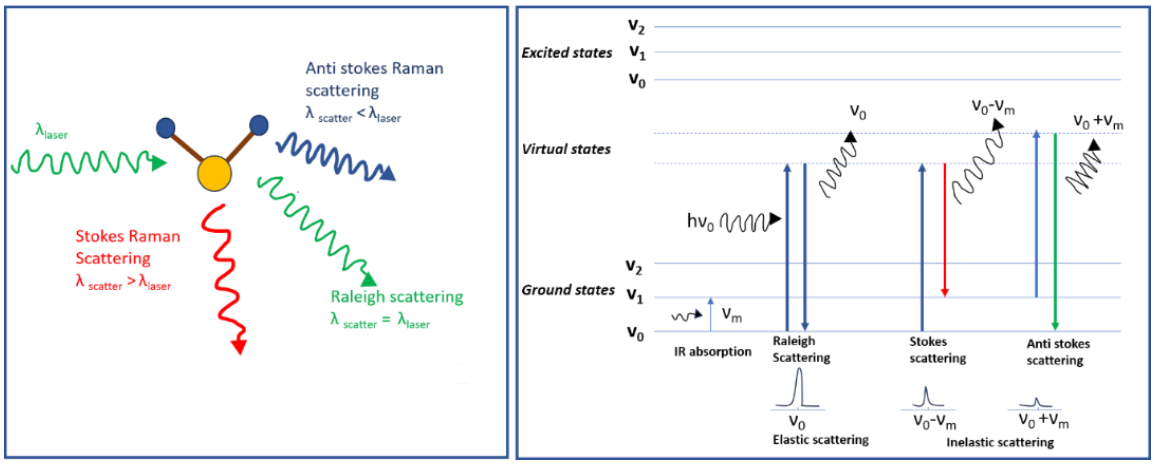


Figure 2.2.2.1: (a) Schematic of the different lines in Raman scattering, (b) Energy excitation diagram of different Raman lines.

The interaction between the electron cloud of the sample and monochromatic light induces changes in the vibrational state, generating the Raman mode. Group theory provides selection rules based on symmetry considerations to identify the Raman-active modes. A Raman spectrometer consists of a Laser source, a sample illumination system, and a spectrometer. Details of all the components are shown in Figure 2.2.2.2.

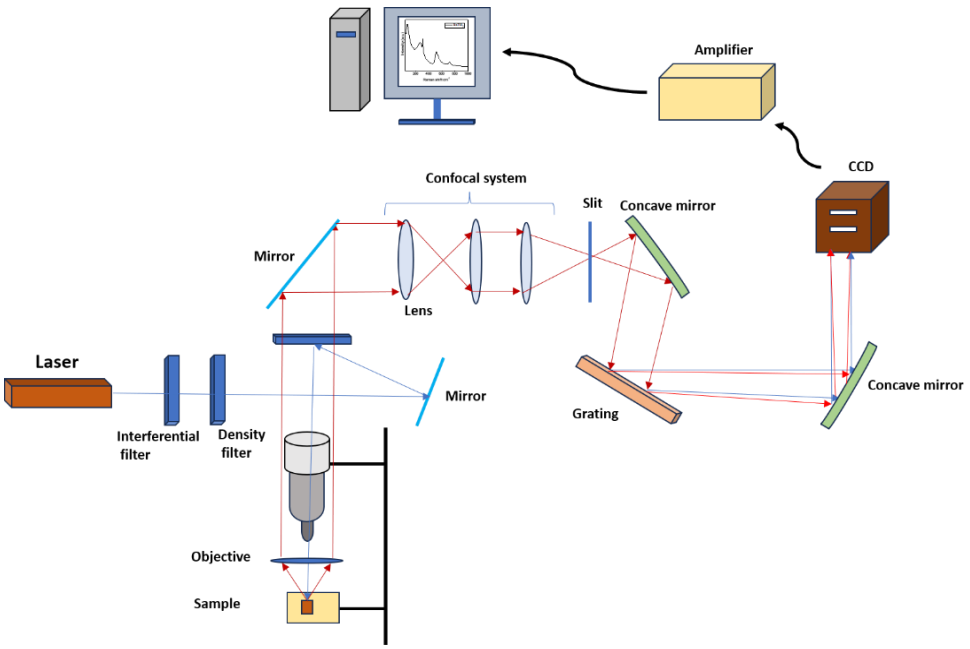


Figure 2.2.2.2: Block diagram of the instrumentation of the Raman spectrometer.

2.2.2.1. Laser Source

A mercury arc lamp with a 435.8 nm line from a coiled low-pressure source was used as a light source in Raman spectrophotometers until the 1960s [77]. Laser sources became available in the late 1960s and completely replaced the mercury lamp. These laser sources provide a stable and intense beam of radiation. The table provides a list of different sources of lasers used for different wavelength regions.

Table 2.2.2.1: Laser sources of Raman spectroscopy with wavelength.

Laser	Wavelength (nm)
Argon ion	488 or 514.5
Krypton ion	530.9 or 647.1
Helium Neon	632.8
Near IR diode	785
Nd-Yag Laser	1064

2.2.2.2. Sample illumination system

In Raman spectroscopy, there is no need for a separate sample holder; the sample can be placed on a glass plate, and a very small sample can be investigated. The laser beam is focused on the sample by means of different lenses, and the calibration is done by using a Si film. The measurement is done on back-scattered geometry in which the sample is irradiated with a laser beam, and the scattered light is collected and focused back on the detector, typically at a 180° angle.

2.2.2.3. Spectrometer

One of the great challenges in the Raman spectrometer is to remove the Rayleigh signal. Thus, the most critical component in a Raman spectrometer is the filter that damps the Rayleigh scattered light. For this, either a notch, edge pass, or bandpass filters are used, depending upon

the laser wavelength. The Rayleigh line is filtered out using a suitable filter, while the rest of the scattered light is dispersed onto a detector. A charge-coupled device (CCD) is used as the detector in the Raman spectrometer. A CCD is a silicon-based multichannel array detector of the UV, Visible, and near-infrared region. The high sensitivity of the CCD makes it suitable to detect weak Raman signals, and the entire Raman spectrum can be detected in a single acquisition through multi-channel operation.

CCD detector contains 1D or 2D arrays of millions of individual detector elements (Pixels). Each of these elements interacts with light and builds up charge. The scattered light is dispersed with a diffraction grating, and the dispersed light will fall on the long axis of the CCD array. Each element in the detector will detect the light from the different spectral regions. The charge registered will be more as the interaction is longer and the light is stronger. After the measurement, each charge reading is measured. CCDs require cooling for their proper operation in spectroscopy. Typically, this is done using Peltier cooling or liquid nitrogen cooling [78].

In this thesis, a Make: Jobin Yvon Horibra Model with LABRAM-HR visible (400−1100 nm) having Spectral Range: 5−4000 cm^{-1}, Excitation Laser Sources: He-Ne (632.8 nm) and Argon (488 nm), Detector: CCD detector, Spectral resolution: ~1 $cm^{-1,}$ Optics: A high-stability confocal Microscope was used [Figure 2.2.2.3].

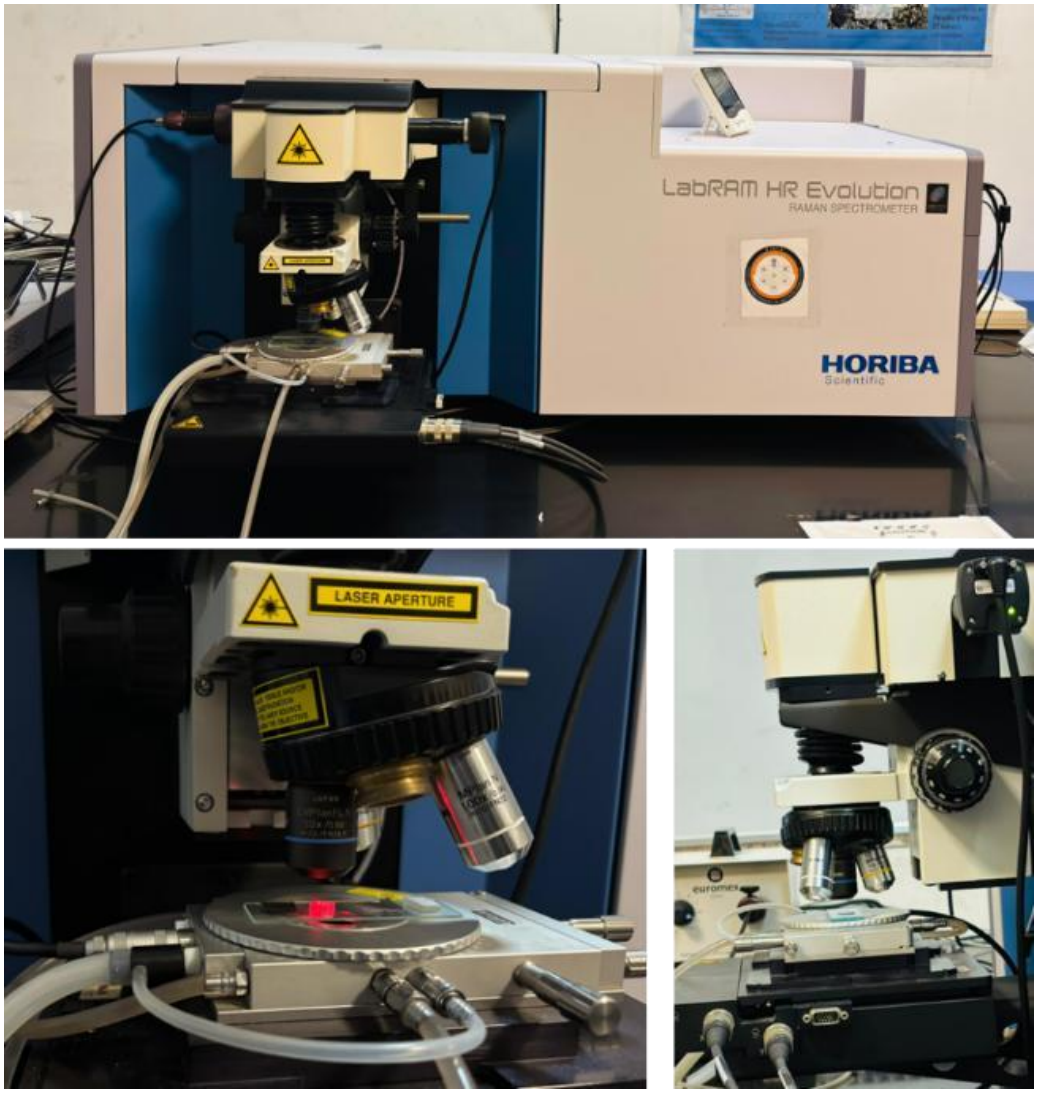


Figure 2.2.2.3: Raman spectrometer.

2.2.3. Fourier Transform Infrared (FT-IR) Spectroscopy

In the present thesis, the FT-IR spectra for all samples were recorded using a Perkin Elmer (Model Spectrum 400) FT-IR spectrometer.

Fourier Transform Infrared (FT-IR) Spectroscopy is a powerful analytical technique widely used in chemistry, materials science, and related fields to identify and study the chemical composition and structure of materials. This method relies on the interaction between infrared radiation and matter, providing valuable information about molecular vibrations and chemical bonds within a sample [79], [80]. The fundamental principle of FT-IR spectroscopy is that molecules absorb specific frequencies of infrared radiation that correspond to their

vibrational modes. When exposed to infrared radiation, a sample selectively absorbs certain wavelengths, resulting in characteristic absorption patterns. These patterns, known as spectra, serve as unique "fingerprints" for different molecules and chemical structures. Unlike traditional dispersive infrared spectroscopy, which measures absorption at individual wavelengths sequentially, FT-IR employs an interferometer to collect data simultaneously across a wide range of wavelengths. This approach offers several advantages, including improved speed, sensitivity, and signal-to-noise ratio.

The core component of an FT-IR spectrometer is the Michelson interferometer, which consists of a beam splitter, a fixed mirror, and a moving mirror. The infrared radiation from the source is split into two beams by the beam splitter. One beam is reflected off the fixed mirror, while the other is reflected off the moving mirror. As the moving mirror oscillates, it creates an optical path difference between the two beams, resulting in constructive and destructive interference when they recombine.

The recombined beam passes through the sample, where specific wavelengths are absorbed based on the sample's molecular composition. The transmitted light is then detected, and the resulting signal is referred to as an interferogram. This interferogram contains information about all wavelengths measured simultaneously, but is not directly interpretable as a spectrum. To convert the interferogram into a meaningful spectrum, a mathematical operation called the Fourier transform is applied. This transformation converts the time-domain signal (interferogram) into a frequency-domain spectrum, which displays the intensity of absorption as a function of wavenumber (reciprocal of wavelength). The resulting spectrum provides detailed information about the chemical bonds and functional groups present in the sample.

FT-IR spectroscopy offers numerous advantages over traditional infrared techniques. The simultaneous collection of data across all wavelengths (multiplex advantage) results in faster measurements and improved signal-to-noise ratios. Additionally, the use of a laser to control mirror movement (Connes' advantage) ensures precise wavelength calibration, enhancing spectral accuracy and reproducibility. This technique can be applied to a wide range of sample types, including solids, liquids, and gases. Various sampling methods, including transmission, attenuated total reflectance (ATR), and diffuse reflectance, enable the analysis of diverse materials. FT-IR is particularly useful for identifying organic compounds, as it can detect characteristic vibrations of functional groups, such as C-H, O-H, N-H, and C=O bonds [81].

2.2.4. Field Emission Scanning Electron Microscope (FE-SEM)

A microstructure image of the materials is captured by FE-SEM. The morphology, surface structure, thickness, and particle size can be analyzed from FE-SEM. An electron beam is used for imaging the material. FESEM utilizes a field emission gun that produces a high-brightness, narrow, and coherent electron beam, enabling imaging resolutions as low as ~1.5 nm at magnifications of up to 300,000×. It operates at low accelerating voltages of approximately 0.5–30 kV, which helps reduce sample charging and minimize the need for conductive coatings. When high-energy electrons impinge on the sample, various types of electrons, including secondary, Auger, primary, and backscattered electrons, as well as X-rays, are generated depending on the depth of electron matter interaction [Figure 2.2.4.1].

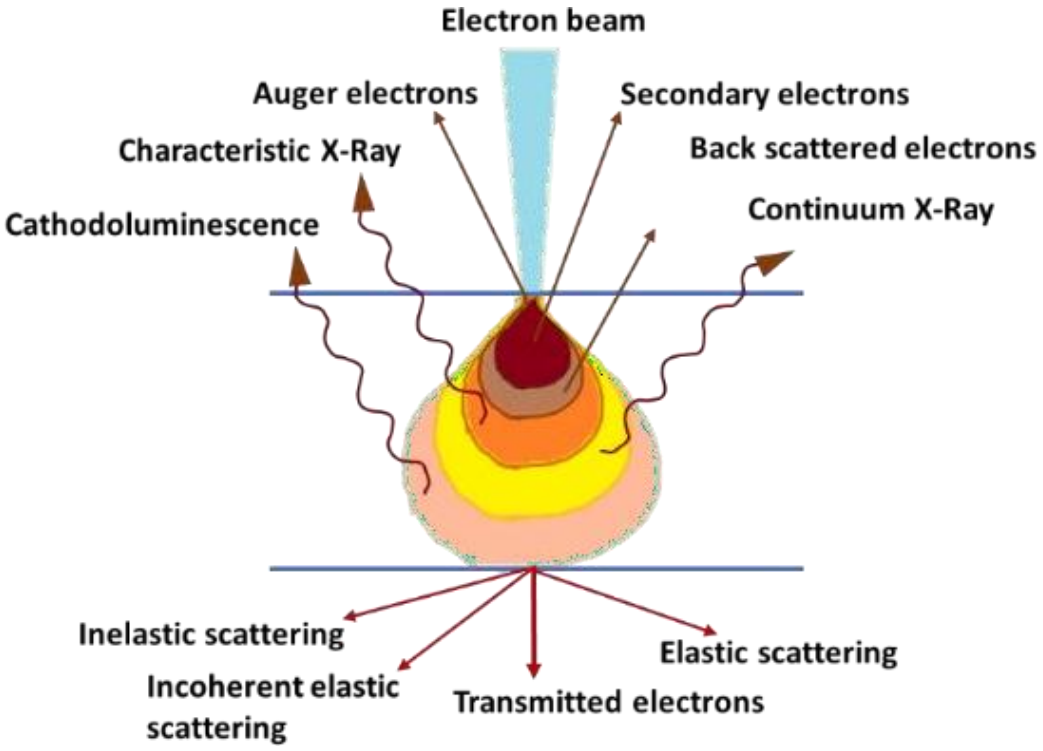


Figure 2.2.4.1: Schematic of the different kinds of radiation emitted when high-energy electrons impinge on the sample.

- **Secondary electrons (SE)**

When the impinging electrons interact with a few nanometres of the sample, secondary electrons are generated. SE electrons undergo inelastic interaction between the beam and the

sample. It is sensitive to surface structure and provides topographic information.

- **Secondary Backscattered electrons (BSE)**

Backscattered electrons are primary electrons that are back-reflected by the atoms in the sample. Back-scattered electrons are generated from a wide region within the interaction volume. These are high-energy electrons, scattered from deep inside the sample rather than the region of origin of SE (a few microns below the surface). This will provide compositional information about the sample. Backscattered electrons are reflected after elastic interactions between the beam and the sample. BSE shows high sensitivity to atomic numbers. As the atomic number of elements in a material increases, the BSE image of that element becomes brighter compared to a lower atomic number element in the same material. Hence, this technique can be utilized for chemical phase distribution.

- **X-rays**

When electrons incident on the sample, characteristic X-rays are produced below the depth of the origin of BSE. These X-rays give information about the elemental composition.

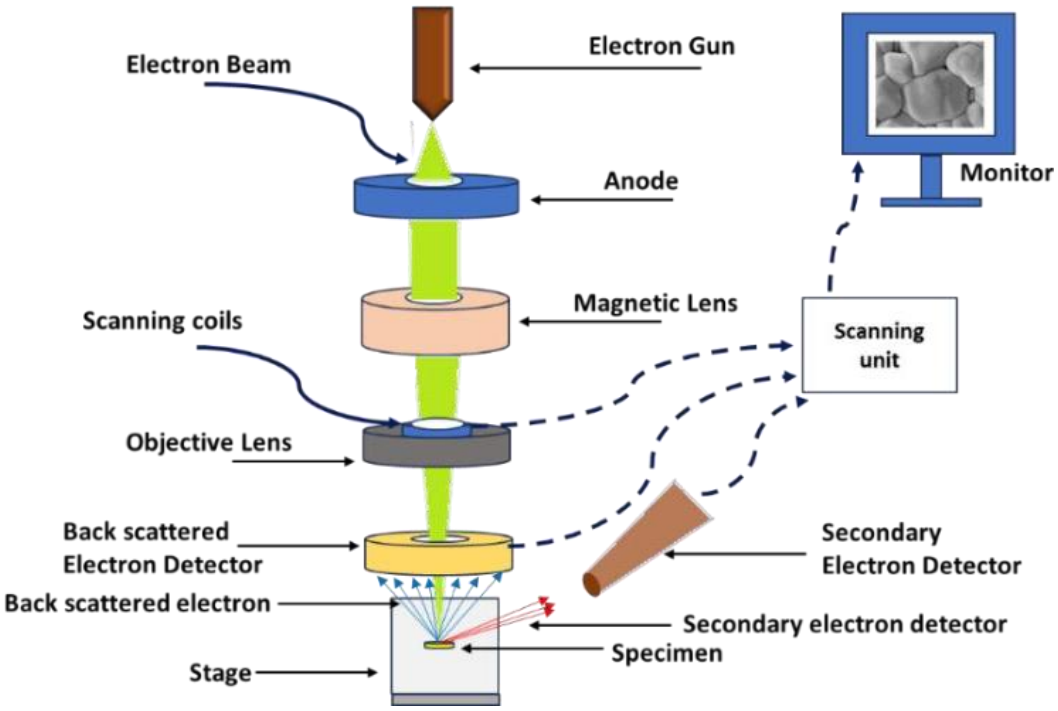


Figure 2.2.4.2: Block diagram of the FE-SEM.

FE-SEM needs a vacuum environment to avoid the disturbance of the electron beam, SE, and

BSE by the gas molecules. The electron gun of an SEM consists of a field-emission cathode that can provide spatial resolution and minimize sample charging effects. FESEM yields a less electrostatically distorted, clearer image with high magnification. Figure 2.2.4.2 shows the block diagram of the different parts of the FE-SEM instrument.

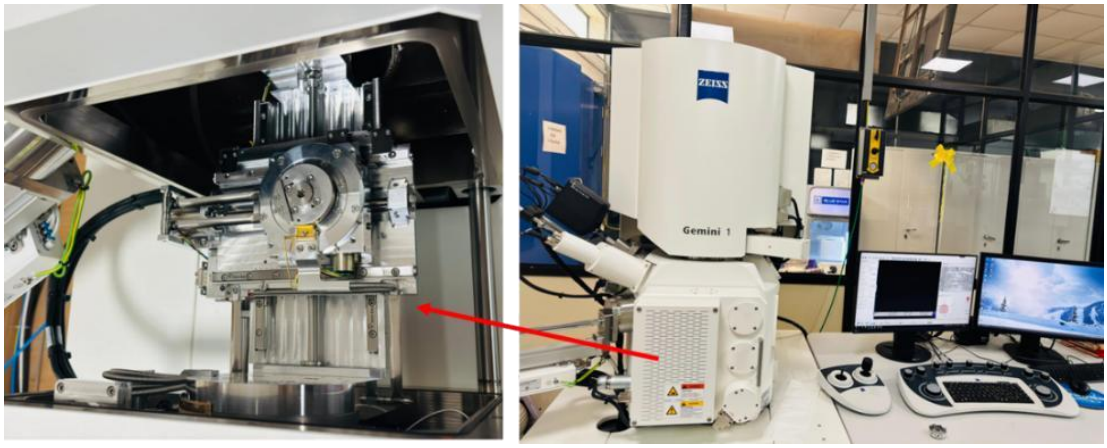


Figure 2.2.4.3: FE-SEM Instrument used.

System specifications:

Make: Zeiss

Model: Gemini SEM 360 [Figure 2.2.4.3]

Magnification: 8 – 2,000,000

Probe current: 3 pA - 20 nA

Resolution: 0.7 nm @15 kV

Maximum field of view: 5 mm at 5 kV and WD = 8.5 mm.

2.2.5. TEM, High Resolution TEM (HRTEM), and SAED

The primary distinction between Scanning Electron Microscopy (SEM) and Transmission Electron Microscopy (TEM) lies in their imaging mechanisms. SEM generates images by detecting electrons reflected or knocked off the sample's surface. In contrast, TEM utilizes electrons that pass through the sample, known as transmitted electrons, to produce an image. Consequently, TEM offers valuable insights into the internal structure of the specimen (crystal structure, morphology, and stress state information) [82].

High resolution and a shorter wavelength of electrons increase the microscope resolution when

accelerated through a strong magnetic field. Since electrons can have a significantly shorter wavelength (approximately 100,000 times smaller) than visible light when accelerated through a strong electromagnetic field, this increases the microscope's resolution by several orders of magnitude. Ultimately, by using a TEM, we can see the columns of atoms present in crystalline samples and the molecular machinery inside cells. It allows visualization and analysis of specimens in the realms of micro space (1 micrometer = 1μm = 10^{-6} m) to nano space (1 nanometer = 1 nm = 10^{-9} m).

TEM creates a bright-field image of a sample using a beam of highly energetic electrons. While transmitting through the sample, electrons will be scattered or diffracted at the potentials of the atom, thereby changing the phase of the electron wave. The transmitted electrons are collected onto a phosphorescent screen or through a camera. The regions where electrons do not pass through appear darker, and the unscattered electron region shows a brighter image. There is a range of grey in between these two regions, depending on the interaction of electrons and scattering within the sample. This image can provide direct and highly resolved information about the sample under investigation. TEM provides information on the size, shape, and structure of nanomaterials. It can examine defects, grain structures, and layer thicknesses in microelectronic devices, aiding in quality control and the development of new materials.

2.2.5.1. Instrumentation

The main components of the Source of electrons, electron gun, Electron beam, Electromagnetic lenses, Vacuum chamber, two condenser lenses, Objective and Intermediate lens, Sample holder and stage, (Imaging Device) Phosphor or fluorescent screen, Computer [Figure 2.2.5.1].

There are two common ways to produce electrons: thermionic emission and cold field emission. With thermionic emission, a tiny tip, often made from tungsten, a LaB6 crystal, or a special ZrO/W Schottky emitter, is heated up by running an electric current through it. The heat provides the electrons with sufficient energy to escape from the surface. At the same time, a high voltage between this electron source (the cathode) and a nearby plate (the anode) creates an electric field that helps steer and speed up the electrons. On the other hand, cold field emission doesn’t need any heating. Instead, it uses an extremely sharp tungsten tip at room temperature. When a strong electric field is applied, electrons can “tunnel” out of the metal, escaping without any extra heat. These sources have a high yield of electrons and a low

chromatic aberration, allowing imaging at atomic resolution [83].

Electromagnetic lenses consist of a large bundle of insulated copper wire windings, a soft iron core, and a pole piece. A magnetic field is induced by the current in the winding and reaches its main strength at the pole piece of the lens. The accelerated electrons entering the magnetic field are deflected by Lorentz forces.

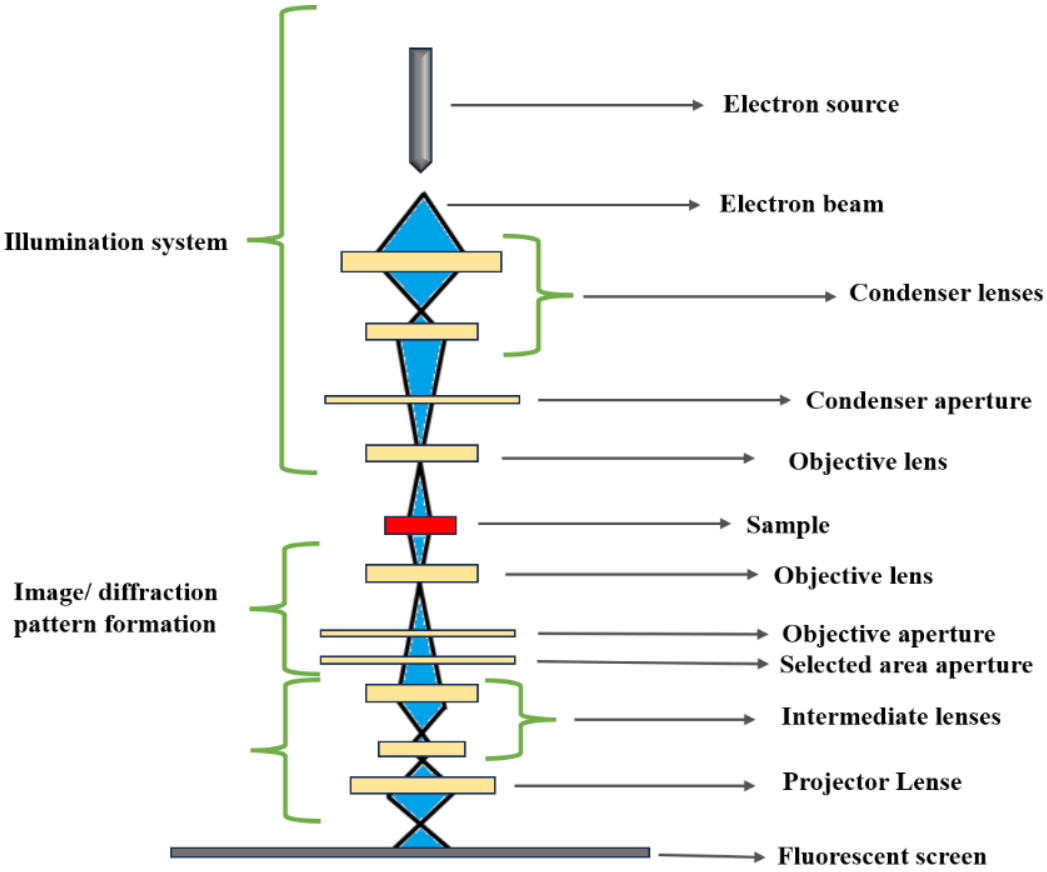


Figure 2.2.5.1: Block diagram of the TEM instrument.

The condenser lens system controls the diameter of the beam. The first condenser lens, which is strong, shrinks the image of the electron source down to about one hundredth of its original size. This creates a tiny, focused spot called the "crossover," which is much clearer and more precise than the larger tip of the filament. Then, the second condenser lens, which is slightly weaker, takes that small image and projects it onto the sample, making it roughly twice as large. Overall, this means the source is reduced in size by about fifty times. This lens also helps control how much the light spreads out on the screen. There is also a condenser aperture located just below or between these lenses, which serves to narrow and shape the electron

beam, as well as adjust its brightness. Objective lenses focus the electron beam through the specimen, and the intermediate lens helps to magnify the image or diffraction pattern.

The electron column does not offer a lot of space for the sample. The sample should be thin so that the electrons can penetrate the specimen to produce the image. Thin sections of the sample are mounted on copper grids, which are available in a wide variety of materials and mesh sizes. The grids with the sections on top are attached to a holder and introduced into the TEM goniometer through a vacuum lock. The goniometer is the mechanical setup that enables highly precise and stable control of the specimen holder during imaging.

When using a TEM to examine a sample, there are two primary modes of operation: Image mode and Diffraction mode. In Image mode, the microscope uses lenses and apertures to control the electron beam that hits the sample. The electrons that pass through are then focused and magnified to create an image on the screen, revealing details such as the size of grains or any defects in the material's structure. Diffraction mode works slightly differently; it produces a pattern on a fluorescent screen based on how the electrons scatter after interacting with the sample. This pattern is similar to X-ray diffraction and is known as a Selected Area Electron Diffraction (SAED) pattern. If the sample is a single crystal, sharp spots will appear in the pattern. However, if it is polycrystalline, the pattern will resemble rings. The crystalline structure can be analysed by this SAED pattern [83].

In electron microscopy, there are two primary methods for creating images using the objective aperture as a filter: bright-field and dark-field microscopy. In bright field mode, the image is formed by electrons that travel straight through the sample without bouncing off, while the diffracted electrons are blocked by a diaphragm. On the other hand, dark field imaging works by using those diffracted electrons to create the picture instead

TEM can image the internal structures of the material even at the nanoscale. In contrast to SEM, which reveals surface morphology, TEM enables atomic-level resolution for the direct observation of internal morphology, particle size, crystallinity, lattice defects, and phase boundaries. In TEM, a high-energy (60-300 keV) coherent electron beam is passed through an ultrathin specimen (<100 nm thick). The electrons scatter, absorb, or transmit upon interaction with the atoms of the material. Mass-thickness, diffraction, and phase differences lead to contrast based on these interactions, revealing morphological and crystallographic details such

as particle morphology, grain boundaries, and voids.

HRTEM is an upgraded version of TEM, which utilizes aberration-corrected optics to achieve sub-angstrom resolution (<0.1 nm), allowing for the direct visualization of atomic arrangements, atomic structures, and lattice fringes. HRTEM is important in determining the interplanar spacing *d*-spacing viewing dislocations [84], [85], [86]. SAED enhances the TEM imaging capability by providing crystallographic information from limited areas of interest (usually 50–500 nm in diameter). By placing a chosen area aperture in the back focal plane of the objective lens, a diffraction pattern is produced, comprising bright spots or rings corresponding to the crystal planes of the material. SAED is essential for phase identification, observing polycrystalline, nanocrystalline, or amorphous domains, and measuring the interplanar spacing (d-spacing) [87]. Figure 2.2.5.2 shows a schematic diagram of TEM. When a high-energy electron beam illuminates a thin sample, the electrons are scattered elastically or inelastically from the sample. Transmitted electrons are magnified through a sequence of electromagnetic lenses to produce an image or diffraction pattern. Either high-resolution structural information or crystallographic data is recorded, depending on the detector mode. In this thesis work, TEM analysis was performed using a JEOL JEM-2100 Field Emission TEM, operated at 200 keV. This instrument enabled atomic-scale imaging and crystallographic characterization of the synthesized materials. TEM, HRTEM, and SAED were used to examine morphology, particle connectivity, lattice ordering, *d*-spacing, and orientation analysis. Hence, the combination of TEM, HRTEM, and SAED provided full structural and crystallographic information on materials to support the rational design of long-lived, high-performance.

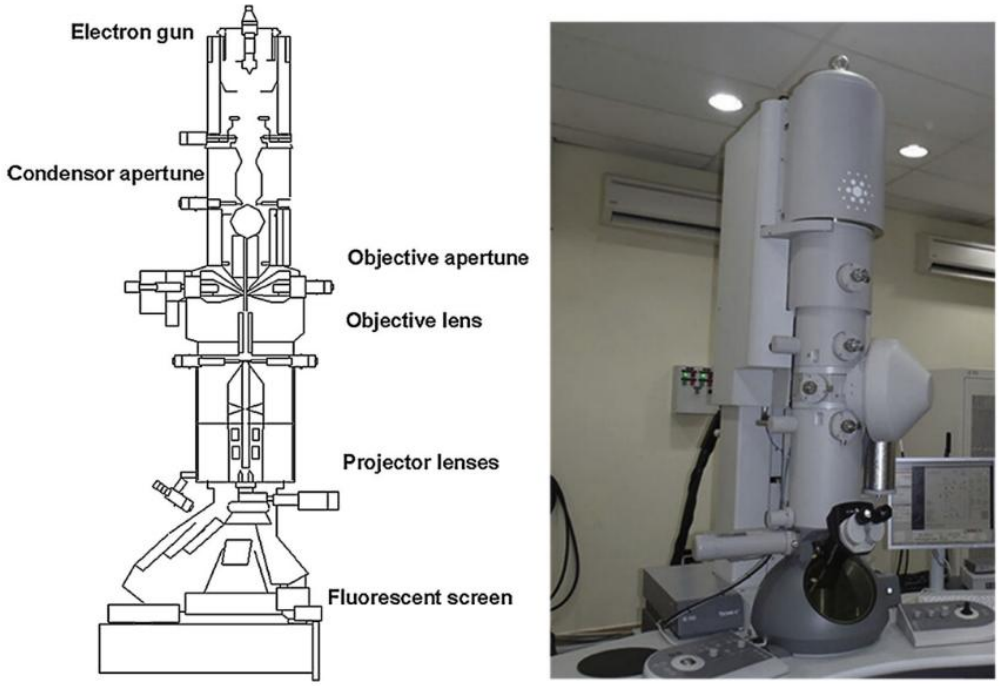


Figure 2.2.5.2: Schematic diagram of TEM.

2.2.6. UV-Vis Diffuse Reflectance Spectroscopy (UV-Vis DRS)

A reflectance spectrum is generated by measuring and analyzing the electromagnetic radiation that bounces off a surface, examining it in frequency or wavelength [88], [89]. There are two primary forms of reflection: regular or specular reflection, typically occurring on smooth, polished surfaces like mirrors, and diffuse reflection, which happens on textured or dull surfaces like powders [Figure 2.2.6.1]. Specular reflection is the reflection of incident light symmetrically with respect to the normal line, which satisfies the laws of reflection.

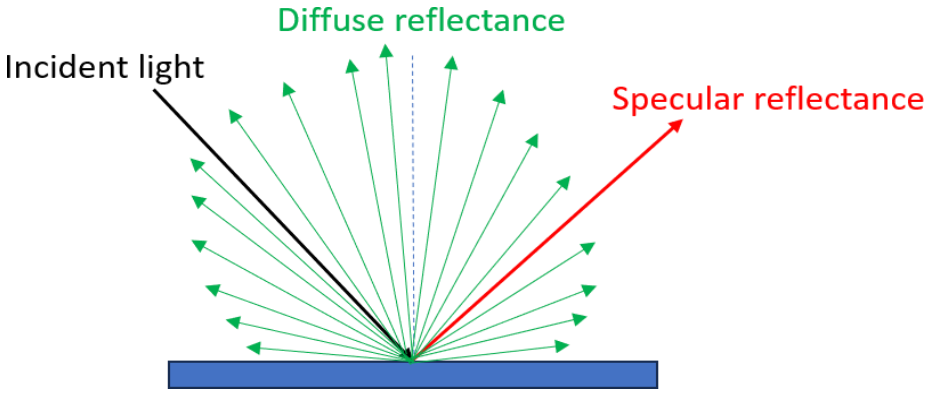


Figure 2.2.6.1: Schematic of the specular reflection and Diffuse reflectance.

The schematic shown in Figure 2.2.6.1 represents diffuse reflectance spectroscopy (DRS) measurements performed using an integrating sphere. The powdered catalyst samples predominantly exhibit diffuse scattering; therefore, the optical analysis and Kubelka–Munk transformation were based on diffuse reflectance data. Specular reflectance was not separately measured in the present study.

If the material absorbs light, the radiant flux that is transmitted through the material decreases according to Beer-Lambert's Law:

$$I(x) = I_0 e^{-kx}$$

Where I_0 is the initial radiant flux, $I(x)$ is the transmitted flux, x is the thickness of the absorbing layer, and K is the absorption (or extinction) coefficient. In powders composed of randomly oriented particles, a fraction of the incident light is reflected in multiple directions within the same hemisphere from which it originates. This behavior arises from the combined effects of reflection, refraction, diffraction, and absorption within the particulate medium and is termed diffuse reflection. Unlike specular reflection, diffuse reflection redistributes incident light in multiple directions and does not obey the classical laws of reflection. When light is incident on a crystalline powder, part of the radiation undergoes specular reflection at individual grain surfaces, while the remaining portion penetrates the particles and experiences multiple internal reflections, refractions, and absorptions. The radiation emerging from the powder after these interactions constitutes the diffuse reflected light.

Diffuse reflectance spectroscopy is widely employed to probe the optical properties of semiconducting materials, including the optical band gap (E_g), electronic disorder quantified by the Urbach energy (E_U), and defect states, using the UV-visible absorption measurements.

The most accepted model of the theory of diffuse reflectance is the Kubelka-Munk model. The Kubelka-Munk theory explores how a plane-parallel layer with a given thickness x can scatter and absorb light [90], [91]. Typically, measurements are taken on layers with sufficient thickness to ensure that further increases in thickness no longer affect the reflectance. Under such conditions, the reflectance value is known as R_∞, representing the limiting reflectance that occurs when the layer's thickness is large enough that it no longer influences the amount of reflected light and is given by:

$$\frac{K}{S} = \frac{(1 - R_\infty)^2}{2R_\infty} = F(R_\infty)$$

where F(R_∞) is known as the K-M function, K is the molar absorption coefficient, s is the scattering coefficient, and R_∞ is the relative diffuse reflectance of the sample over a standard sample.

$$R_\infty = \frac{R_{Sample}}{R_{Standard}}$$

R_∞ is proportional to the absorption coefficient of the material, α and can be written as

$$F(R_\infty) = \alpha = C\frac{(h\nu - E_g)^{1/n}}{h\nu}$$

Where C is the proportionality constant, $h\nu$ is the photon energy, and E_g is the band gap. It can be written in the form of a linear equation $(\alpha h\nu)^n = h\nu - E_g$ [92]. The Tauc plot shows the quantity $h\nu$ on the abscissa and the quantity $(\alpha h\nu)^n$ on the ordinate. Hence, a plot of $(\alpha h\nu)^n$ v/s $h\nu$ produces a straight line, and the intercept on the energy axis gives the value of the band gap of the sample.

Urbach energy, E_U, is characterised by the exponential tail observed near the band gap as a tail in the disordered crystalline material [93]. These tails are arising due to the localised states in these materials due to defects and disorder, which extend into the band gap. In the spectral region corresponding to transitions involving the tails of the electronic density of states, the spectral dependence of the absorption coefficient α is described by the Urbach equation,

$$\alpha = \alpha_0 e^{(h\nu - E_g)/E_U}$$

Where, α_0 is a constant, E_U reflects structural disorder and defects of a semiconductor [93].

Instrumentation:

The instrumentation for the UV-Vis-DRS setup is presented in Figure 2.2.6.2. The setup consists of the following components:

a) Source: A Deuterium lamp (185-400 nm) and a tungsten halogen lamp (350-1100 nm) were used to get the entire UV-Vis region.

b) Monochromator: It includes an entrance slit for dispersing light into various wavelengths and an exit slit to allow the selected wavelength band to pass through.

c) Sample Compartment: In the sample compartment, a beam from the monochromator passes through the sample in a cuvette. Solid samples can be held in place for simple transmission measurements or measured at various angles of incidence.

d) Spectrophotometer: A double-beam optical design, light from the monochromator is split into a reference beam and a sample beam using an optical element such as a rotating wheel with a mirrored segment or a beam splitter. These beams travel through separate optical paths into the sample chamber, allowing simultaneous measurement of the reference and the sample.

e) Detector: The detector converts light from the sample into an electrical signal, offering a linear response over a wide wavelength range with low noise and high sensitivity. Spectrophotometers typically use either a photomultiplier tube detector or a photodiode detector.

For the measurement, initially, the baseline correction is done by placing the standard sample white board filled with barium sulphate at the reflection position, and then the diffuse reflected light is measured by converging the scattered light in all directions through an integrating sphere.

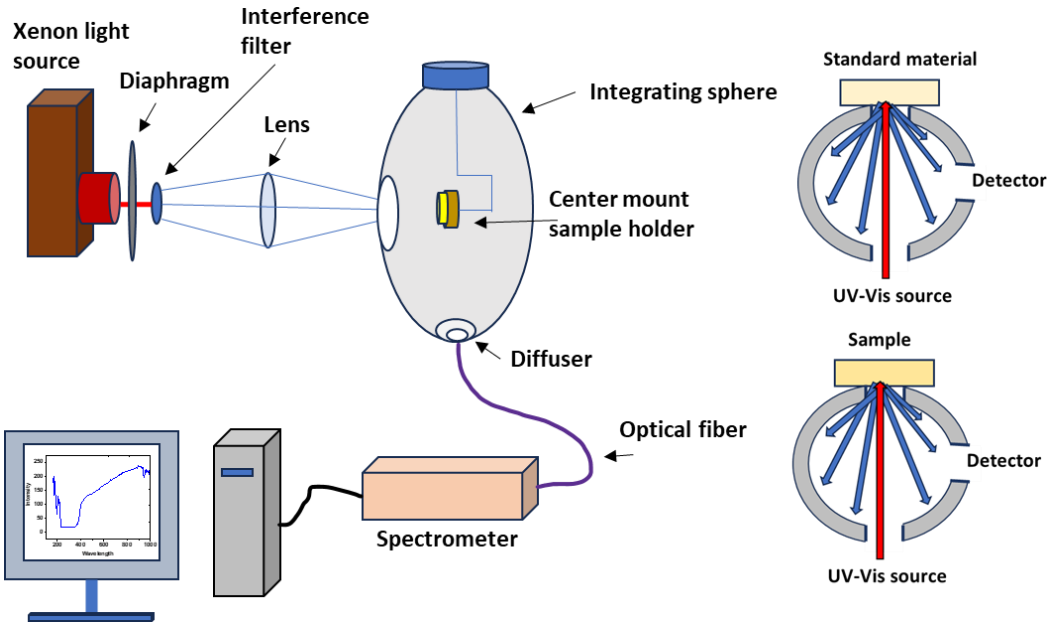


Figure 2.2.6.2: Schematic of the instrumentation of the UV-DRS.

System specifications:

Makeer: Shimadzu [Figure 2.2.6.3], Model: UV 2600i, Spectral Range: 220 nm to 1400 nm, Detector: Photo multiplier Tube



Figure 2.2.6.3: Shimadzu UV-Vis DRS spectrophotometer.

2.2.7. X-ray Photoelectron Spectroscopy (XPS)

XPS is a surface analytical tool with high sensitivity, commonly used to investigate the chemical composition, oxidation states, and electronic environments of elements on the top few nanometers of the surface of a material [94], [95], [96].

Principle of XPS:

Figure2.2.7.1 represents the working principle of XPS. X-ray Photoelectron Spectroscopy (XPS) reveals the intensity of electrons ejected from a sample surface with kinetic energy after surpassing their binding energy (B.E.) to the atom. This binding energy serves as a distinctive feature of the electronic orbitals of a specific atom [Figure2.2.7.1(a)]. When a sample is exposed to monoenergetic soft X-rays (~6 keV), electrons are emitted due to the photoelectric effect. These rays can penetrate the sample surface to a depth of a few nanometers. The total energy (hν) supplied by the X-rays is the energy of the irradiated photons. This energy is distributed in overcoming the binding energy (B.E.) of the atomic orbital from which the electron is emitted, as well as the work function (φ_{Sp}) of the material's surface. At the same time, the remaining part provides the kinetic energy (K.E.) of the ejected electrons [Figure2.2.7.1(b)]. This relationship can be expressed as

$$K.E. = h\nu - B.E. - \varphi_{Sp}$$

Consequently, the B.E. can be calculated using the equation.

$$B.E. = h\nu - K.E. - \varphi_{Sp}$$

The distinction between the work function of the sample, denoted as φ_S, and the work function of the spectrometer, denoted as φ_{Sp}, is evident.

An XPS spectrum reveals detailed information about a sample through various features. Photoelectron lines reflect the binding energies of electrons in different atomic orbitals, providing insights into the sample's elemental composition, chemical state, and electronic configuration. The spectrum also includes a background from elastic and inelastic electron scattering, with functions like Shirley, linear, and Tougaard used to fit the background. Satellite peaks arise from changes in Coulombic potential as photoelectrons pass through the valence band, indicating ions left in an excited state. Auger lines result from a three-electron process

involving the interaction of X-rays with the sample, leading to the emission of Auger electrons, typically observed as KLL, LMM, MNN, and NOO peaks. Plasmonic peaks occur when electrons near the surface oscillate collectively at a specific frequency, particularly in the presence of metallic nanoparticles, causing broadening of the photoelectron peak. Lastly, spikes in the spectrum can be caused by unwanted noise from high-voltage instruments, affecting the reliability of measurements by introducing signal loss or false counts.

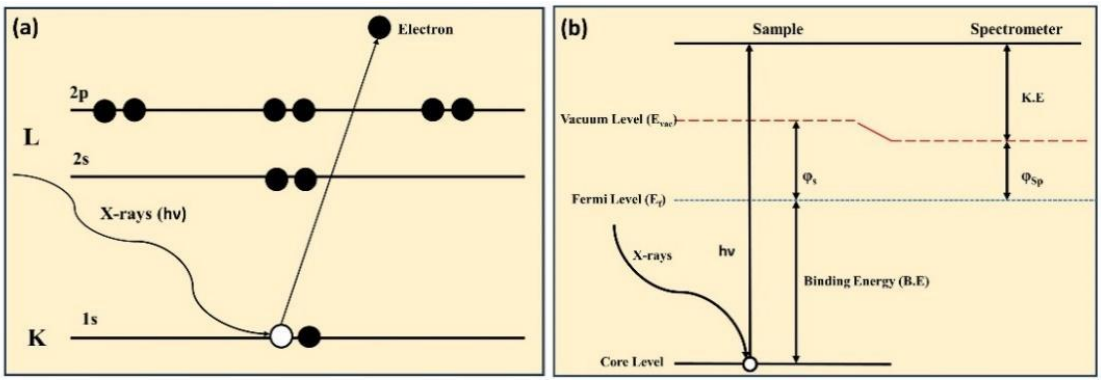


Figure 2.2.7.1: Schematic diagram representing the (a) Photoemission of X-rays from the K-shell, (b) working principle of XPS.

The basic working of XPS is shown schematically in Figure2.2.7.2. The XPS instrument comprises several key components. The X-ray source, either an X-ray tube or a synchrotron radiation source, produces X-rays with sufficient energy to excite core-shell electrons. The sample stage, equipped with an ultrahigh vacuum, holds the specimen. The electron analyzer, a hemispherical or cylindrical mirror analyzer, separates emitted photoelectrons based on their kinetic energy. The detector records the energy of these photoelectrons after they pass through the analyzer, converting the information into an XPS spectrum. Vacuum systems maintain the high vacuum conditions necessary to prevent sample contamination and ensure accurate measurements. An energy analyzer, often including a monochromator, selects the X-ray energy for precise sample excitation. Finally, data acquisition systems record and process the signal from the detector, generating XPS spectra and providing data analysis capabilities.

The advantages of this technique are getting element-specific information and chemical states. However, the main disadvantage of this technique is probing the bulk of thick samples, as the penetration depth is low, and an ultrahigh vacuum is required to run the experiment.

In this work, the XPS data were obtained using a Kratos Axis Supra instrument equipped with a monochromatic Al K_α X-ray source ($h\nu$ = 1486.6 eV) operating at a power of 150 W and under ultra-high vacuum (UHV) conditions in the range of ~10E−9 mbar. All spectra were recorded in hybrid mode, using electrostatic and magnetic lenses and an aperture slot of 300 µm × 700 µm. The wide and high-resolution spectra were acquired at fixed analyzer pass energies of 80 and 20 eV, respectively. The samples were mounted in a floating mode to avoid differential charging, and thus, all spectra were acquired using charge neutralization. The XPS spectra were deconvoluted using XPSPEAK4.1 software. The spectra were calibrated using the C-1*s* peak (Binding energy = 284.8 eV). The background extraction was done using the Tougaard function. To get a quality fitting, a combined Gaussian-Lorentzian peak shape was used for all the peaks.

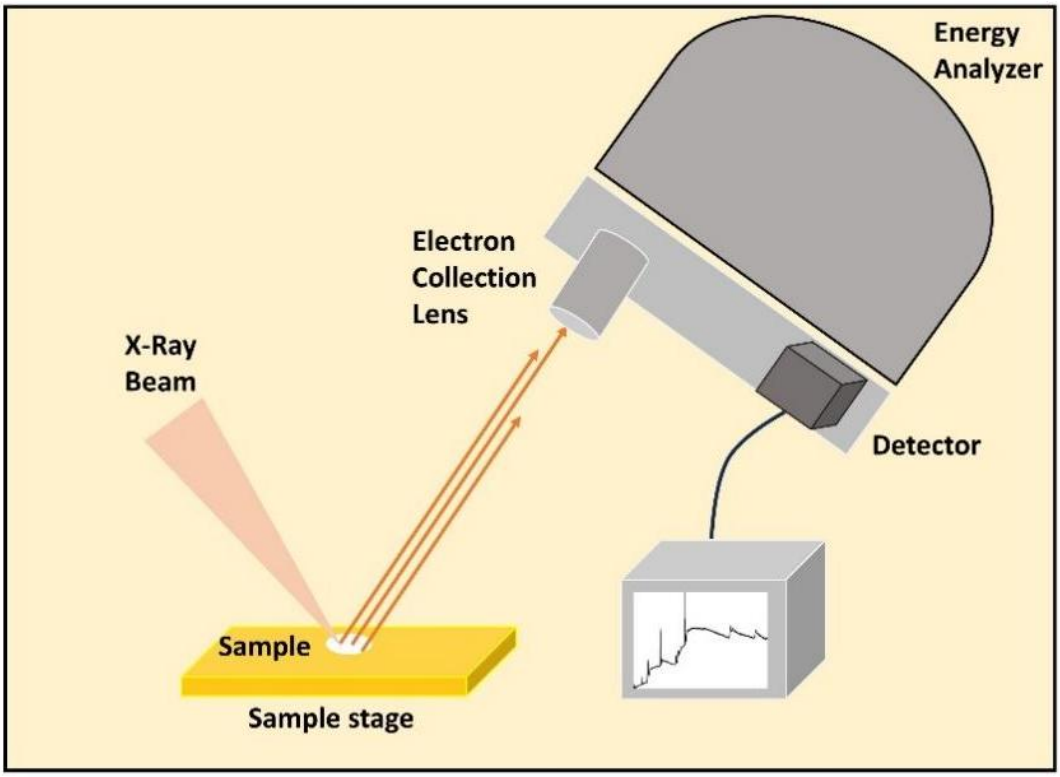


Figure 2.2.7.2: Schematic representation of the working of the XPS instrument.

2.2.8. Brunauer-Emmett-Teller (BET)

The Brunauer-Emmett-Teller (BET) surface area analysis involves measuring a material's specific surface area (m^2/g) through gas adsorption [97], [98]. In this process, an inert gas, such

as nitrogen, is continuously passed over the solid sample, or the sample is placed in a controlled gaseous environment. Due to weak van der Waals forces, small gas molecules adsorb onto the surface of the solid and its porous structures, creating a monolayer of adsorbed gas. This monolayer and the adsorption rate can then be used to determine the specific surface area of the solid sample and analyze its porosity. The BET theory extends the Langmuir adsorption model. It assumes that: (1) Gas molecules physically adsorb on a solid in layers. (2) The adsorption process is reversible. (3) The heat of adsorption for the first layer is different from that of subsequent layers, which is equal to the heat of liquefaction of the gas. The BET equation is defined as:

$$\frac{1}{v\left(\frac{P_0}{P}-1\right)} = \frac{C-1}{v_m C}\cdot\frac{P}{P_0} + \frac{1}{v_m C}$$

where v is the volume of gas adsorbed at pressure P, v_m is the volume of gas required to form a monolayer on the surface, P_0 is the gas saturation pressure, and C is the BET constant, related to adsorption energy [99]. The basic principle of the BET instrument is schematically presented in Figure 2.2.8.1. Sample preparation for BET analysis involves degassing to remove water and contaminants, which is performed under vacuum at elevated temperatures to preserve the sample's structure. Samples are placed in glass cells with glass rods to minimize dead space. These cells come in various sizes and shapes, are inserted into heating mantles, and are connected to the instrument's outgas port. After degassing, the sample cell is transferred to the analysis port and cooled using liquid nitrogen to ensure strong adsorption interactions. Nitrogen gas is introduced as the adsorbate, and the dead volume within the sample cell is calibrated with helium gas before and after each measurement since helium does not adsorb onto the sample surface. This work utilized a Quanta Chrome Autosorb iQ2 BET Surface Area & Pore Volume Analyzer.

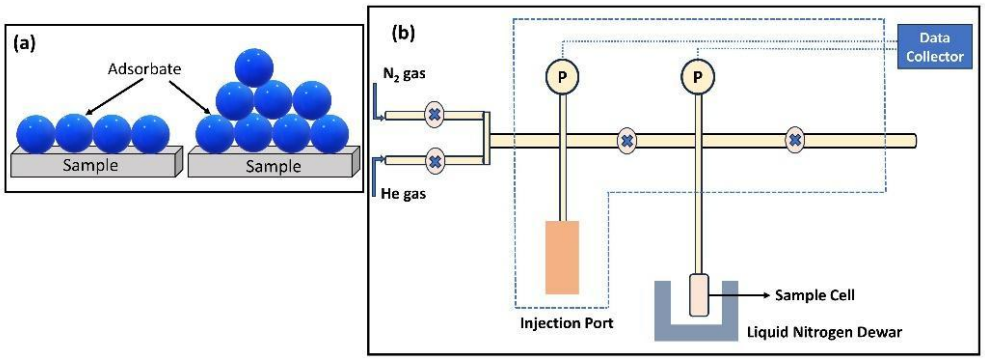


Figure 2.2.8.1: Schematic of (a) adsorption of gas molecules on the surface of the sample, considering the monolayer adsorption (left, Langmuir theory) and multilayer adsorption (right, BET theory), (b) BET instrument.

2.2.9. Dynamic Light Scattering (DLS) Measurement

Zeta potential is a key parameter that measures the electrical charge at the slipping plane surrounding a particle in a fluid, influencing the stability and behavior of colloidal systems. It is defined as the potential difference between the dispersing medium and the stationary layer of liquid attached to the dispersed particle. This potential is crucial in understanding how particles will interact in suspension, particularly in colloids, emulsions, and nanoparticles [100], [101].

In colloidal systems, a higher absolute zeta potential typically indicates greater stability, as it suggests that particles will repel each other due to their similar charges, reducing the likelihood of aggregation. Conversely, low zeta potential values suggest that particles may come together easily, leading to flocculation or sedimentation.

Zeta potential can be measured using techniques such as microelectrophoresis or dynamic light scattering. The results are essential in various fields, including pharmaceuticals, paint formulations, food science, and wastewater treatment, among others. Understanding zeta potential enables researchers and manufacturers to tailor formulations for enhanced stability, improved performance, and desired interactions within a system. Overall, zeta potential is a critical factor in predicting the stability and dynamics of colloidal and nanoparticle systems in numerous applications. The surface charge was determined by using the Anton Paar XT-500 Zetasizer.

2.2.10. Electrochemical Characterization Techniques

Electrochemical characterization was performed using a computer-controlled electrochemical workstation that integrates high-precision potentiostatic and galvanostatic control with dedicated data acquisition and analysis software. Such workstations enable systematic investigation of electrochemical reactions and interfacial processes, providing quantitative insight into charge-transfer behaviour, reaction kinetics, and electrode stability. Electrochemical workstations are extensively employed in materials science and energy-related research, including electrocatalysis, energy storage, and corrosion studies. All electrochemical measurements were performed with Metrohm Autolab (M204 multichannel potentiostat/galvanostat using Nova 2.1.4 software [Figure 2.1.10.1].

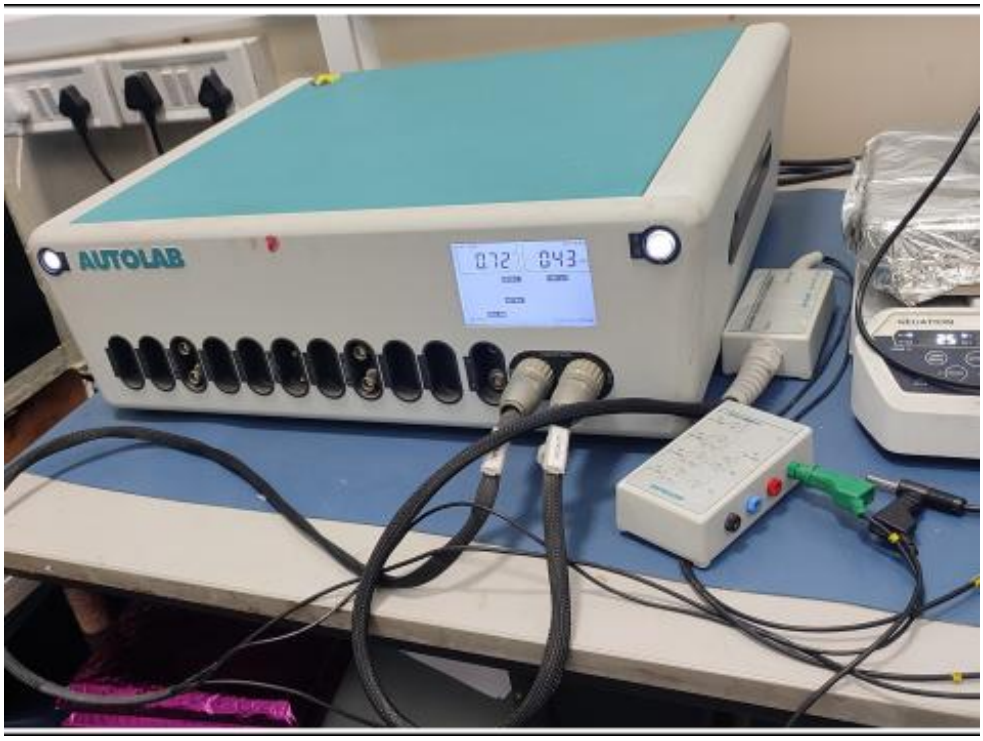


Figure 2.2.10.1: Autolab electrochemical workstation.

2.2.10.1. Cyclic Voltammetry (CV)

Cyclic voltammetry (CV) was employed to investigate the redox behaviour, electrochemical stability, and capacitive characteristics of the synthesized materials. In a typical CV measurement, the electrode potential was swept cyclically between predefined limits at

controlled scan rates. The resulting current–potential response provides information on reversible and quasi-reversible redox processes, surface oxidation–reduction behaviour, and electrochemically accessible surface states.

For electrochemically active surface area (ECSA) estimation, CV measurements were performed within a non-Faradaic potential window at multiple scan rates, and the double-layer capacitance was extracted from the linear dependence of capacitive current on scan rate.

2.2.10.2. Linear Sweep Voltammetry (LSV)

Linear sweep voltammetry (LSV) was employed to assess the electrocatalytic activity of the materials towards anodic and cathodic reactions, particularly the oxygen evolution reaction (OER). In LSV measurements, the electrode potential was swept linearly in a single direction at a fixed scan rate while recording the corresponding current response.

LSV curves were used to determine key performance metrics, including onset potential, overpotential at benchmark current densities, and reaction kinetics. All potentials were referenced to the appropriate reference electrode and converted to the reversible hydrogen electrode (RHE) scale where applicable.

2.2.10.3. Electrochemical Impedance Spectroscopy (EIS)

Electrochemical impedance spectroscopy (EIS) was employed to probe interfacial charge-transfer processes and reaction kinetics over a wide frequency range. Impedance measurements were performed at relevant applied potentials under steady-state conditions by superimposing a small sinusoidal potential perturbation (typically 5–10 mV) onto the working electrode and recording the corresponding current response [102].

The impedance data were represented as Nyquist and Bode plots, which enable the separation of electrochemical processes occurring at different characteristic time scales. In the Nyquist representation, the high-frequency intercept corresponds to the uncompensated ohmic resistance arising from the electrolyte, electrode contacts, and current collectors. Semicircular features observed in the mid-frequency region are associated with interfacial charge-transfer resistance in parallel with capacitive elements related to the electrochemical double layer. In contrast, low-frequency features reflect slower surface-reaction-controlled kinetics and mass-

transport-related processes[103].

To quantitatively interpret the impedance spectra, the experimental data were fitted using appropriate equivalent circuit models, from which parameters such as solution resistance, charge-transfer resistance, and capacitance-related elements were extracted. EIS thus provides insight into time-dependent electrochemical behaviour and enables the distinction between interfacial charge-transfer limitations and slower surface-reaction kinetics, which is particularly relevant for understanding and optimising oxygen evolution reaction (OER) performance.

2.2.10.4. Chronopotentiometry (CP)

Chronopotentiometry (CP) was employed to assess the operational stability and durability of the electrocatalysts under constant current conditions. In CP measurements, a fixed current density was applied to the working electrode, and the potential response was monitored over time.

This technique allows evaluation of catalyst stability, resistance to degradation, and potential drift during prolonged electrochemical operation, providing insight into the long-term performance of the electrode materials under OER-relevant conditions.

2.2.10.5. Chronoamperometry (CA)

Chronoamperometry (CA) was conducted to investigate the temporal stability and charge-transfer behaviour of the materials under constant potential operation. In CA experiments, the electrode potential was held at a fixed value, and the resulting current was recorded as a function of time.

CA measurements were used to evaluate transient current responses, steady-state behaviour, and the stability of electrocatalytic activity during sustained operation. This technique is particularly useful for probing reaction kinetics and electrode robustness under continuous electrochemical bias.

2.3. Chapter Summary

This chapter has outlined the experimental methods and characterization techniques employed

throughout this thesis. The integrated use of structural, optical, surface, photocatalytic, and electrochemical analyses provides a robust foundation for correlating material properties with functional performance. The methodologies described herein support the detailed results and discussions presented in the subsequent chapters.

Chapter 3 Aliovalent Al^{3+} Substitution in CuO: Defect-Driven and Ligand-Hole-Associated Photo-Fenton-Like Photocatalysis

Abstract: *This chapter investigates the synthesis, physicochemical properties, and photocatalytic performance of aliovalent Al^{3+}-doped CuO as a visible-light-active catalyst for the degradation of organic pollutants. A controlled series of $Cu_{1-x}Al_x O_{1+\delta}$ compositions was synthesized using a scalable sol–gel method to systematically examine how non-redox Al^{3+} substitution modulates the electronic structure, defect chemistry, and surface reactivity of CuO. Structural and spectroscopic analyses, including X-ray diffraction with Rietveld refinement, Raman and FTIR spectroscopy, UV–Vis diffuse reflectance, BET surface area analysis, electron microscopy, and electrokinetic measurements, reveal that moderate Al incorporation induces lattice strain, reduces crystallite size, enhances surface area, and modifies intrinsic defect populations, particularly Cu vacancies and oxygen-related states. These changes result in improved visible-light absorption and more efficient charge-carrier utilization.*

Photocatalytic activity was evaluated using methylene blue, rhodamine B, and methyl orange under household LED illumination and natural sunlight. Reaction parameters such as catalyst loading, temperature, and oxidant concentration were optimized, leading to rapid and near-complete dye degradation. Kinetic analysis confirms a pseudo-first-order kinetic model under the investigated experimental conditions, while scavenger and fluorescence studies identify hydroxyl radicals as the primary reactive species, supporting a ligand-hole-assisted, photo-Fenton-like degradation pathway. Reusability, structural stability, and leaching analyses demonstrate sustained activity with minimal secondary contamination. Overall, this chapter establishes defect-engineered Al-doped CuO as a non-redox electronic modulator, demonstrating that photocatalytic enhancement arises from mitigation of charge-utilisation bottlenecks rather than dopant-driven redox chemistry, and providing a mechanistic foundation for subsequent morphology- and redox-controlled catalytic studies.

3.1. Chapter Introduction and Scope

Building on the general background on photocatalysis, advanced oxidation processes, and CuO-based catalytic systems introduced in Chapter 1, this chapter focuses specifically on the role of aliovalent Al^{3+} substitution in CuO and its implications for visible-light-driven photocatalytic degradation of organic pollutants. While pristine CuO is an attractive photocatalyst due to its narrow band gap, p-type conductivity, and rich redox chemistry, its practical performance is often limited by inefficient charge-carrier utilisation arising from electronic localisation and rapid recombination, as well as restricted surface reactivity, and sub-optimal defect distributions. Rational modification of CuO through controlled dopant incorporation, therefore, represents an effective strategy to mitigate these intrinsic bottlenecks.

Aluminum is selected in this chapter as a non-redox-active, trivalent dopant, providing a well-defined model system to isolate the influence of charge compensation, lattice distortion, and defect redistribution without introducing additional transition-metal redox pathways. Substitution of Al^{3+} for Cu^{2+} in the CuO lattice is expected to perturb local coordination environments and induce intrinsic defects, such as copper vacancies and oxygen-related states, which directly influence optical absorption, charge transport, and surface reaction kinetics. Unlike Fe- or Co-based dopants, Al^{3+} does not participate directly in catalytic redox cycles, allowing defect- and ligand-hole-associated electronic effects on photocatalysis to be examined in a controlled manner.

In parallel, this chapter introduces the concept of photo-Fenton-like degradation within a CuO-based photocatalytic framework. Conventional Fenton and photo-Fenton processes rely on soluble iron species and operate effectively only under acidic conditions, limiting their practical applicability. In contrast, CuO-based systems can generate reactive oxygen species (ROS), predominantly hydroxyl radicals, under visible-light illumination without the need for homogeneous iron catalysts. The incorporation of Al^{3+} provides a means to tune the surface chemistry and electronic structure of CuO, thereby influencing ROS generation pathways and degradation kinetics under near-neutral conditions and low-power illumination.

The objectives of this chapter are therefore threefold. First, a systematic series of Al^{3+}-substituted CuO photocatalysts is synthesised using a scalable sol–gel route, enabling controlled variation of dopant concentration. Second, comprehensive structural, optical, and

surface characterisation is employed to establish correlations between Al incorporation, defect chemistry, and electronic structure. Third, the photocatalytic performance of the materials is evaluated using representative cationic and anionic dyes under household LED light and natural sunlight, with kinetic analysis and scavenger studies used to elucidate the dominant degradation pathways.

Overall, this chapter establishes a defect-engineering-driven, non-redox electronic modulation framework for CuO-based photocatalysis and serves as a baseline reference system for subsequent chapters that explore morphology-controlled thermal effects and redox-assisted catalytic pathways.

3.2. Synthesis and experimental methods

The synthesis of the photocatalysts investigated in this chapter and their structural, optical, and surface characterization have been described in detail in Chapter 2. This section, therefore, focuses specifically on the photocatalytic measurement parameters and testing conditions employed to evaluate the degradation performance of the materials discussed in this chapter.

The photocatalytic performance of all the samples were studied under the irradiation of visible light using a household LED (Monochromatic light having maximum intensity at 455 nm, light intensity 100 lx ≈ 0.79 Wm^{-2} i.e.1266 times smaller than AM 1.5G Sun) (Spectrum is given in Chapter 2, Figure 2.1.3.1) and under sunlight in a typical winter season at IIT Indore, India campus (22.525^0 N, 75.921^0 E) having light intensity 60000 lx ≈ 474 Wm^{-2} (2 times smaller than AM 1.5G Sun), temperature ≈ 35 °C. A 10-ppm strength stock solution of pollutant dyes was prepared by mixing 5 mg of the dyes in 500 mL of deionized water (DIW). The dyes used in this study were methylene blue (MB), methyl orange (MO), and rhodamine B (RhB). Appropriate amounts of C0, CA1, CA2, and CA3 samples were added to separate beakers containing 50 ml of each dye solution to produce a particular catalyst concentration. By varying the number of samples, the catalyst concentrations were varied for five different values: 0.2 mg/mL, 0.4 mg/mL, 0.6 mg/mL, 0.8 mg/mL, and 1 mg/mL. Initially, 0.52 mL of hydrogen peroxide (H_2O_2) (30% w/v ~ 90 mM) was added to this solution. H_2O_2 is added to enhance the photocatalytic reaction. To study the effect of H_2O_2 concentration on the catalysis reaction, the molar concentration of the H_2O_2 varied from 90 mM to 180 mM. Temperature-dependent degradation was also analyzed in the range 29 ^{0}C to 59 ^{0}C in steps of 10 ^{o}C. The

obtained mixed solutions were stirred continuously in the dark for 60 min to achieve good dispersion and adsorption equilibrium. The variations were recorded from the absorption data using a Research India UV-visible spectrophotometer. A 2 mL solution was extracted from the photo-reacted solution after each step of the degradation. The solutions were centrifuged properly, and the absorption peaks at a maximum wavelength λ_{max} = 462 nm (MO), λ_{max} = 664 nm (MB), and λ_{max} = 550 nm (RhB) of this extracted solution were studied. The photocatalytic degradation efficiency of the organic dyes was calculated using the following formula:

$$Degradation\ (\%) = (A0 - At)/A * 100$$

where A0 is the absorbance of the dye solution before the photo-irradiation, and At is the absorbance of the solution after photo-irradiation for a certain time t.

The compositions reported throughout this chapter correspond to the nominal precursor stoichiometries employed during synthesis. Although direct elemental quantification using ICP-based techniques was not performed, systematic changes observed in XRD, Raman, FTIR, and optical characterization provide evidence for successful Al incorporation into the CuO framework.

3.3. Structural, Optical, and Surface Properties

All chemicals were of analytical grade and used as received without further purification. Copper precursors, dopant salts (Al^{3+}, Fe^{3+}, and other transition-metal sources), complexing agents, solvents, and oxidants were procured from commercial suppliers. Deionized water with a resistivity of 18.2 MΩ.cm was used throughout all synthesis and experimental procedures.

3.3.1. XRD Analysis

The XRD patterns of all the samples reveal a single-phase monoclinic structure with the *C2/c* space group. Rietveld refinement using GSAS-2 software revealed modifications of the *CuO* lattice with Al^{3+} incorporation. The lattice parameters, bond angles, and bond lengths all showed reducing trends with increasing partial Al^{3+} doping concentration. However, the variations were in the range of a few picometers, which is very nominal.

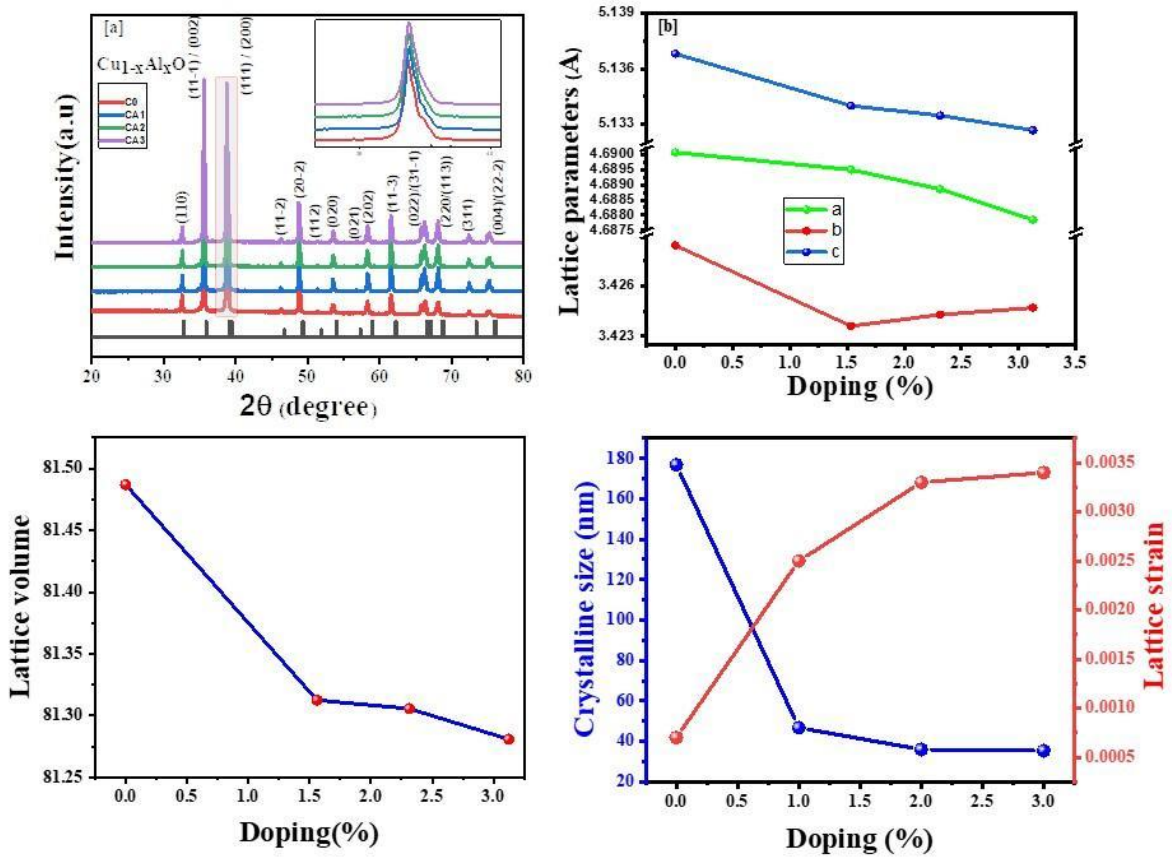


Figure 3.3.1.1: Represents (a) XRD pattern for all the samples, where the inset shows the peak shift of the highest intensity peak, (b), (c) lattice parameters and lattice volume, and (d) Crystallite size and lattice strain variation with partial doping percentage.

The Cu atom in a CuO lattice is in octahedral geometry with six O-atoms around it in a distorted octahedral form. The Cu-O bond lengths in the plane are ~1.88 Å and ~1.96 Å, respectively. However, the Cu-O distance of two O atoms perpendicular to the plane is much greater (~2.9 Å) to be considered as a bond, so an octahedral type of coordination can be ruled out. Hence, practically four O-atoms bond with a Cu atom, and hence the Cu is most likely four-coordinated in the CuO lattice [104]. Hence, the field is discussed in different lights in the literature [72]. The O atom is coordinated with four Cu atoms in the form of a distorted tetrahedron. The Al^{3+}(IV) has a much lesser radius (0.53 Å) in comparison with that of the Cu^{2+}(IV) (~0.71 Å). Hence, one can expect a shrinking of the lattice in the vicinity of the dopant Al^{3+} atom due to the smaller size of the host Cu^{2+} atom. However, the charge of Al^{3+} is more than that of the Cu^{2+} ion. So, to neutralize the charge in the lattice, various kinds of defects can

be formed in the CuO lattice. Hence, there is competition between the shrinking of the lattice due to the lesser radii of Al^{3+} incorporation, vacancy defects formed in the lattice, and the expansion of the lattice due to interstitial defects. This will result in the changes in the lattice parameters observed by XRD. In pure CuO, various intrinsic defect states exist. These can be O_i (oxygen interstitials), V_{Cu} (Cu vacancies), V_O (Oxygen vacancies), and Cu_i (Cu interstitials). These defects are formed by the following reactions:

$$O_o \rightarrow V_o^{xo} + xe^- + ½\ O_2$$

$$½\ O_2 \rightarrow V_{Cu}^{x-} + xh^o + O_o$$

$$½\ O_2 \rightarrow O_i^{x-} + xh^o$$

$$Cu_i^{x+} \rightarrow Cu_{Cu} + xh^0$$

The above symbols represent Kroger - Vink notations. The term O_o denotes an O-atom without any charge. Note that the V_{Cu} and O_i can produce free holes and are responsible for the p-type conductivity. On the other hand, the V_O and Cu_i produce electrons and hence are hole killers. The optoelectronic property of CuO is determined by the most probable reaction above. The competition for the formation of these defects is mainly related to the formation energy of these defects and the synthesis conditions. There is continuous competition between a variety of processes depending on the energy of creation of a particular defect state. Among these intrinsic defects, copper vacancies and oxygen-related acceptor states are particularly relevant, as they directly contribute to hole density and ligand-hole character in CuO, thereby influencing charge transport and photocatalytic reactivity.

The values of the lattice parameters obtained from the Rietveld analysis are presented in Figure 3.3.1.1. The lattice parameters decrease from the pure CuO lattice to the Al^{3+} doped CuO lattice. These variations in the lattice parameters are an indication of the incorporation of the Al^{3+} ions in the CuO lattice, which leads to changes in the Cu-O bond lengths. Similar structural changes due to partial Al doping have also been reported elsewhere [105], [106]. When more charge is introduced in the lattice due to Al^{3+} substitution in the lattice, there is a possibility of the formation of O_i and V_{Cu} for the charge neutralization. The unit cell volume calculated from the lattice parameters shows a decreasing trend with Al^{3+} substitution. This is an indication of an increase in vacant sites and substitutions by a smaller ion. This somewhat hints at the

increase of V_{Cu} since O_i may lead to lattice expansion.

The FWHM and the peak position of the most intense peak (11-1) were used to calculate the crystallite size and lattice strain using the Tiny Tool XRD calculator. The software calculate crystallite size using Scherer equation: $D = 0.9\lambda/(\beta*\cos(\theta))$ (where, β is FWHM of XRD peaks and D is the crystallite size) and the lattice strain from Williamson-Hall equation: $\beta_{total}(\cos(\theta)) = 0.9\lambda/D + 4\varepsilon\sin(\theta)$, [107], [108], [109] (where ε is the lattice strain and λ is the X-ray wavelength of Cu(Kα)). The incorporation of the Al^{3+} in CuO removes Vo and introduces either V_{Cu} or O_i or both. While an increase in V_{Cu} leads to compression of the lattice, an increase in Oi can lead to an expansion. A drastic increase in the lattice strain is observed from C0 to CA1. Thereafter, the strain increases gradually in CA2 and CA3. The sudden increase of lattice strain when Al^{3+} is incorporated into the CuO lattice, associated with a decrease in the cell volume, may be related to the increase of V_{Cu} rather than O_i. The newly formed V_{Cu} may leave a lot of space in the lattice, which may induce compression in the lattice. This may lead to an increase in the strain of the lattice. The anomaly in the bond lengths for the CA3 sample, for which one can see a nominal increase of the same as CA2, may be an indication of the addition of some O_i which creates further strain in the lattice due to the large size of the O-ion at an interstitial site which also results in an increase of the separation between the Cu and O atoms. Lattice strain and crystallite size have often been found to be inversely proportional to each other, as the strain restricts the long-range order. The crystallite size decreases drastically with the Al incorporation from C0 to CA1 and then slowly decreases for CA2 and CA3. This trend is well understood in the literature [110].

From analyzing the refined CIF file of the pure and doped samples, there are three sets of Cu-O bonds termed Cu-O_1, Cu-O_2, and Cu-O_3. The structure contains a distorted octahedron. The longest bond, ~2.796 Å in the C0 sample, is represented as Cu-O_3, whereas the shortest bond, ~1.9515 Å, is termed as Cu-O_1 in comparison with the nominally larger Cu-O2 bond, ~1.9640 Å. The large difference between Cu-O_3 and Cu-O_1/O_2 bonds raises the question of the octahedral environment associated with the Cu atoms [72]. The Al^{3+} incorporation leads to the reduction of Cu-O_3 distance and Cu-O_2 bond length from C0 to CA2. Thereafter, an increment is observed for CA3. The changes in Cu-O_1 are negligible compared to the other two bonds. The formation of the V_{Cu} defects may be the reason for the increase in the bond lengths of Cu-O_3 and Cu-O_2 after CA2. This trend is also observed in the variation of '*b*' lattice parameters

as well. Although a higher nominal Al concentration (x = 0.046875) was also examined, the appearance of a weak additional diffraction peak suggested the onset of secondary-phase formation; therefore, subsequent photocatalytic investigations were focused on the phase-pure compositions, among which CA1 (x = 0.015625) exhibited the optimum performance.

3.3.2. Raman spectroscopy

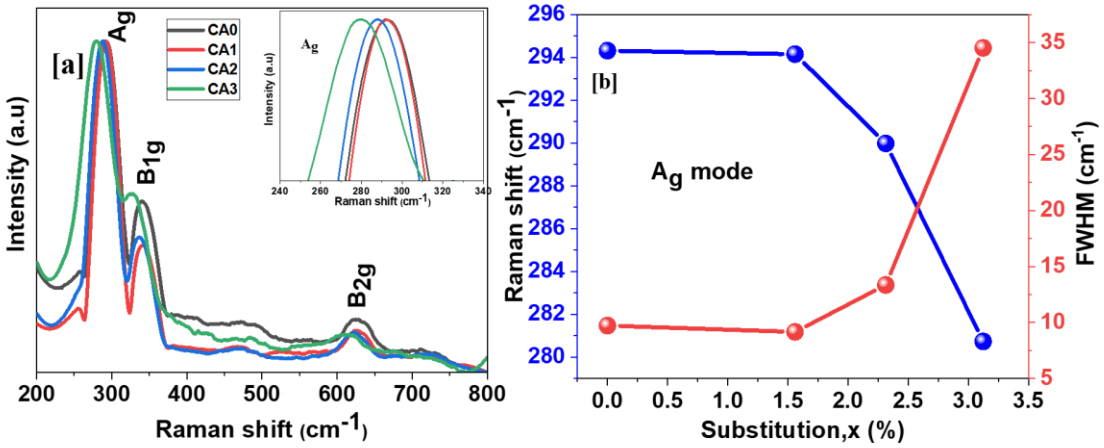


Figure 3.3.2.1: Represents (a) Raman spectra for all the samples, where the insets show the peak shift of A_g mode, (b) the Raman shifts and FWHM that were observed for A_g mode.

The monoclinic CuO is reported to have the following vibrational modes: three acoustic modes ($A_u + 2B_u$), six infrared active modes ($3A_u + 3B_u$), and three Raman active modes ($A_g + 2B_g$) [111]. The active Raman modes are contributed by vibrations of oxygen atoms [112]. The presence of these three modes in all the prepared samples confirms the single monoclinic phase. No other impurity phase or Cu_2O phase peaks are detected in these samples, consistent with XRD data. The Raman spectra of C0 Powders revealed Raman vibration at 292.3 cm^{-1} (A_g), 341.3 cm^{-1} (B_{1g}), and 626.7 cm^{-1} (B_{2g}). The A_g mode is the strongest notable mode for powder samples. Negligible shifting is observed for the CA1 sample. However, a significant shift of the A_g mode towards lower wavenumber is observed in CA2 and further for CA3. Note that the strain also increases with partial doping. However, the difference is that the strain increased drastically from 7 x 10^{-4} in C0 to 2.5 x 10^{-3} in CA1 and thereafter nominally to 3.3 x 10^{-3} in CA2 and 3.4 x 10^{-3} in CA3. However, the phonon frequency did not change much for the C0 and CA1 samples. Similar trends in FWHM and Raman shift are observed in the B_{1g} mode as

well. These changes in the A_{1g} and B_{1g} modes may be because, for CA1, the strain was due to the contraction of the lattice due to an increase in the V_{Cu} defects, while the O-lattice was not affected. The only change in the O-lattice could have been the loss of V_os, which doesn't affect the phonon energy. However, with further partial Al-doping and introduction of more O in the lattice, even after the complete annihilation of the latent V_o, the O-lattice gets affected by the increasing V_{Cu} content, which helps to compensate for the extra charges of Al^{3+}. The increasing V_{Cu} content may result in increasing lattice strain. Hence, the phonons become less energetic. The FWHM of the A_g mode does not show much change for CA1, but increases for CA2 and CA3. An increase in the FWHM of the Raman modes is an indication of an absence of long-range order in the lattice with Al^{3+}-incorporation [Figure 3.2.2.1(b)]. This, too, can be correlated to the increasing strain in the lattice. The shift towards lower wavenumber of phonon modes can also be correlated with the modification of bond strength of the Al - O bond compared to the Cu-O bond. The smaller size of Al^{3+} in Cu^{2+} size reduces the effective bond strength due to the lesser overlapping of the electron clouds, which may lead to the shift towards lower wavenumber as well.

3.3.3. FTIR Analysis

To understand the surface chemistry and the vibrational properties of the atoms, FTIR spectra of the prepared nanostructures have been recorded in the wave number range 400–4000 cm^{-1} [Figure 3.2.4.1(b)]. There are three standard Cu-O stretching modes, one A_u mode, and two B_u modes characteristic of a CuO structure. These modes are observed at 473 cm^{-1} (A_u mode along [1 0 1] direction), 538 cm^{-1}, and 595 cm^{-1} (B_u mode along [-101] direction) [113]. The effects of partial Al doping on the modes were visible. Two B_u modes were observed at 540 cm^{-1} and 595 cm^{-1} in C0, which shifted to a lower wavenumber 525 cm^{-1}, 593 cm^{-1} in CA1, and thereafter slightly shifted to a higher wavenumber 527 cm^{-1} and 594 cm^{-1} in CA3. Shifts in the FTIR modes indicate changes in the phonon energy. This can be correlated with variations in the electron density of the vibrating atom [114]. A shift in the FTIR modes is observed if there is a change in the electron density due to the absence of oxygen or copper atoms [115]. Hence, the formation or creation of defects in Al^{3+}doped CuO can be revealed by FTIR analysis. The shifts due to partial Al-doping may also be associated with changes in the surface area [116] and surface defects [117]. No additional absorption bands corresponding to secondary phases were detected in the FTIR spectra. The characteristic Cu-O vibrational modes

remain preserved across the investigated compositions, indicating that Al^{3+} incorporation does not significantly disrupt the local CuO bonding environment. The phase purity and monoclinic crystal structure of the $Cu_{1-x}Al_xO_{1+\delta}$ samples were established independently through XRD and Rietveld refinement analyses. Common peaks at 1094 cm^{-1} and 1734 cm^{-1} correspond to C-O stretching, 1220 cm^{-1} to C-O stretching, and 1376 cm-1 to C-H bending vibrations, respectively. These vibrations indicate the presence of carbonaceous content at the surface.

3.3.4. UV-Vis DRS Analysis

The UV-Vis Diffuse Reflectance Spectra were measured for all the samples in the range of 200 ~ 1000 nm. The band gap is determined from these spectra using the Kubelka-Munk function: $F(R) = (1-R)^2/2*R$ [115] where R is the diffuse reflectivity of the samples. The absorption coefficient, α, is in close proximity to the F(R) [118]. The diffuse reflectance increases drastically near the band edge. A linear region is observed near the edge [118]. Energy-dependent optical absorbance data are used to calculate the optical band gap [119]. The Tauc equation for the band gap energy determination is $(\alpha h\nu)^{1/n} = A(h\nu-Eg)$ [115]; where α is the absorption coefficient, ν is the photon's frequency, h is Planck's constant, A is a proportionality constant, and E_g is the band gap. The nature of the transition is between the conduction band (CB) and valence band (VB), determined by the power n; n = 1/2, 3/2, 2, and 3 for direct allowed, direct forbidden, indirect allowed, and indirect forbidden transitions, respectively. Doping implies the introduction of elements with different valence states and ionic sizes. This introduces lattice distortions, which can be responsible for the induction of defect states. These can modify the bandgap and also introduce states inside the gap [106]. Depending on the location of these defect states, modification of the band edges can result in tailing near the band edge. The energy associated with these states is defined in terms of the Urbach energy E_U and can be calculated from these tail regions [120]. The value of α increases exponentially with energy $E = h\nu$ and is dependent on the value of E_U: $\alpha = \alpha_o.\exp(h\nu/E_U)$ [120]; where α_o is a constant. Taking the natural logarithm of both sides, one can achieve a linear relation between ln(α) and E: $\ln[\alpha] = \ln[\alpha_o] + (E/E_U)$. An estimate of the E_U can be done with the linear fitting of the linear region in ln(α) vs E plots. The hybridization of Cu 3d and O 2p states forms both the valence and conduction bands. In the conduction band, the Cu 3d state is more dominant, and in the valence band, the O 2p state is predominant [121]. As Al^{3+} is doped in CuO, very little contribution from Al 3p states and no contribution from Al 3s states are observed. From

the band gap analysis using the Tauc method, the band gap energy was observed to continuously increase from C0 to CA3. The bandgap and Urbach energy seem to get modified with composition [Figure 3.2.4.1(a)]. The Al^{3+} ions incorporation in CuO causes a widening in the optical band gap from 1.43 eV in C0 to 1.47 eV in CA1, 1.48 eV in CA2, and 1.49 eV in CA3. On the other hand, the E_U initially increased drastically from 93 meV in C0 to 119 meV in CA1, but with further Al^{3+} incorporation, it continually decreased to 112 meV in CA2 and 102 meV in CA3. The incorporation of Al^{3+} ions in CuO causes a widening in the optical band gap from 1.43 ± 0.00246 eV (C0) to 1.47 ± 0.0008 eV (CA1), 1.48 ± 0.00145 eV (CA2), and 1.49 ± 0.00089 eV (CA3). There can be two possible explanations for this observation. Often in literature, one may find an effect of doping known as the Burnstein-Moss effect [122], [123]. This effect is observed in doped samples when hybridized states between the dopant atoms and O are formed in the conduction band, but very close to the conduction band minima. Electrons can be excited directly to these trap states, and an effective band gap appears to increase. On the other hand, compared to an undoped CuO with intrinsic latent defects like V_o and V_{Cu}, the scenario should change in Al^{3+}-doped CuO. Due to the extra positive charge of the Al^{3+} ions, it is likely that the V_o may be neutralized. Such doping can happen by replacing a Cu^{2+} ion or by filling in the void of a V_{Cu}. It has been observed that V_{Cu} states are located very near the conduction band edge, and therefore, the eradication of these states may imply a reduction in the possibility of a transition of an electron from the VB to these states. Associated with such a replacement of V_{Cu} states are the annihilation of V_o. Such a change, therefore, can in the long run regularize the lattice, thereby reducing disorder with more Al^{3+} incorporation. However, initially, the disorder may arise due to the substitution of Al^{3+} at the Cu^{2+}-site. The trend in Urbach energy, Eu, reveals such a trend. Table 3.3.4.1 shows the change in bandgap and Urbach energy that represents the disorder in the system, which can be correlated to strain inside the copper oxide structure with aluminum incorporation.

Table 3.3.4.1: shows the bandgap and Urbach energy of all the samples.

Sample	Bandgap, E_g (eV)	ΔE_g (meV) = $E_g - E_{gCuO}$	Urbach energy, E_U (meV)	Strain from XRD (10^{-3})

C0	1.43	0	93	0.7
CA1	1.47	40	119	2.5
CA2	1.48	50	112	3.3
CA3	1.49	60	102	3.4

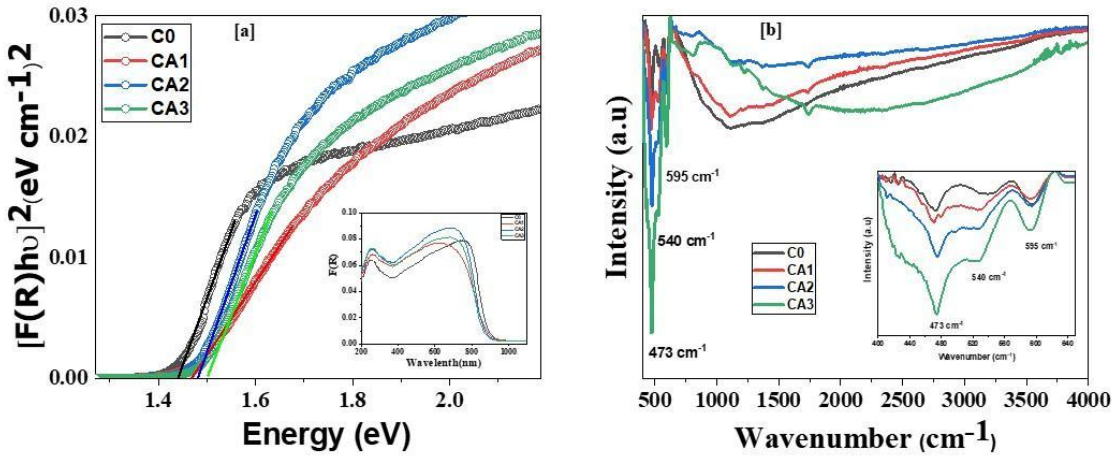


Figure 3.3.4.1: Represents (a) bandgap analysis where the insets show the corresponding F(R) as a function of wavelength, (b) the FTIR spectra, and the insets show the lower wavenumber spectra for all the samples.

3.3.5. Surface Morphology

The surface morphology was obtained for all the samples using Field Emission Scanning Electron Microscopy (FESEM). The FESEM image of all the samples is shown in Figure 3.3.5.1. The average particle size for different samples is calculated and given in Table 3.3.7.1. With the substitution, the size of the particles varies. The particle size is small for all the doped samples in comparison to the pure CuO, as calculated from FESEM images, which can be

correlated to the decreasing trend of crystallite size obtained from XRD analysis. The calculated particle sizes are given in Figure 3.3.5.2.

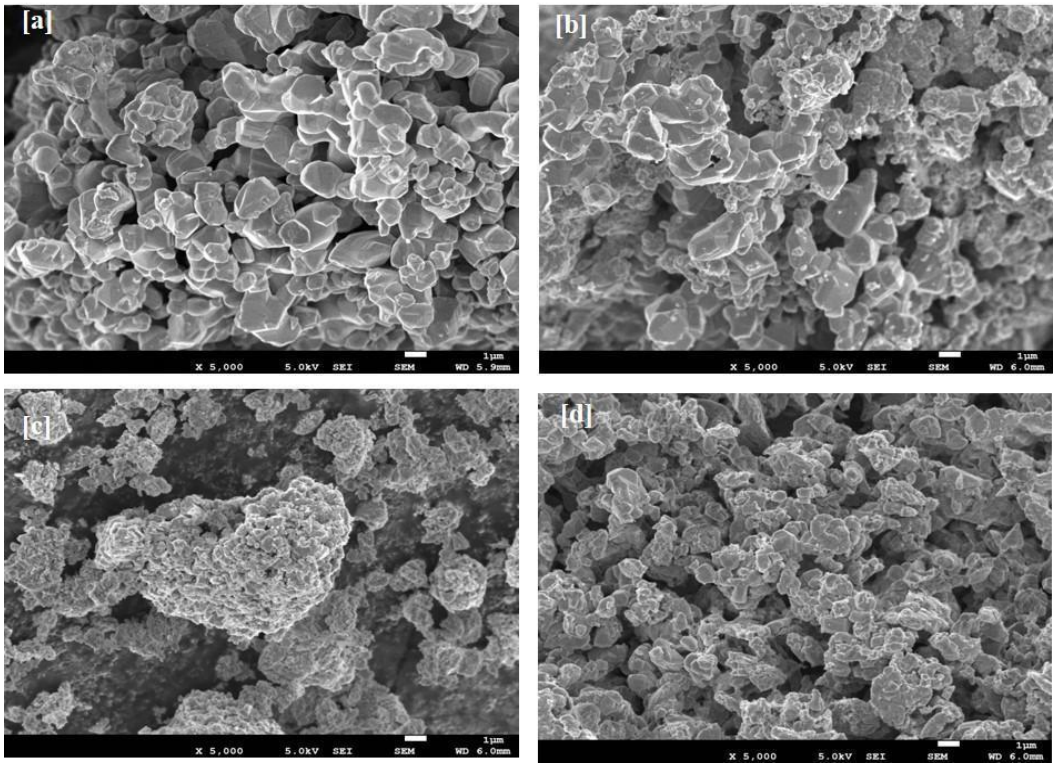


Figure 3.3.5.1: Represents FESEM image of (a) C0, (b) CA1, (c) CA2, (d) CA3.

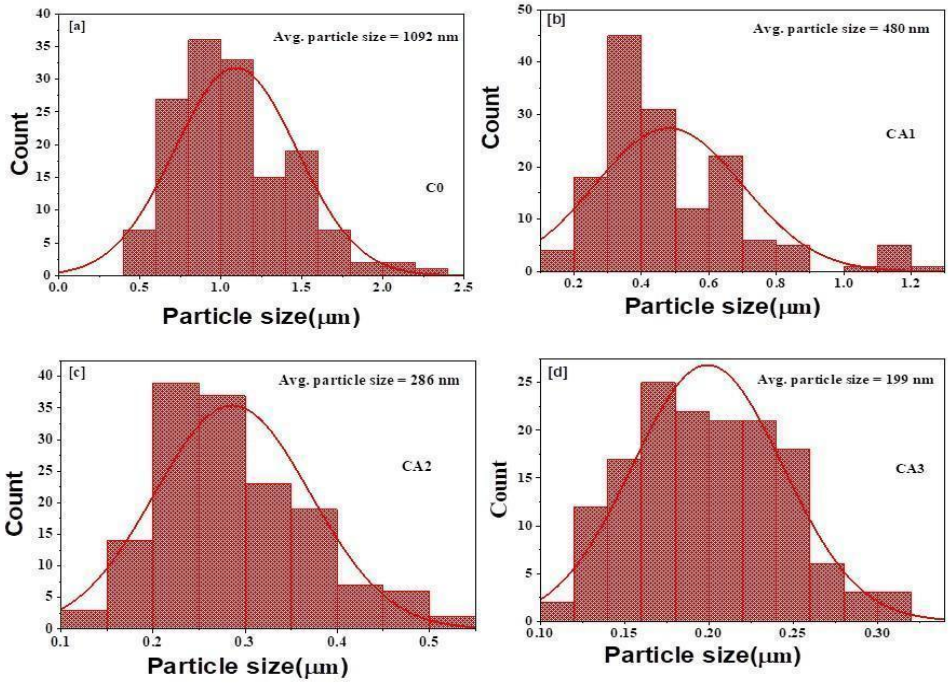


Figure 3.3.5.2: Represents (a), (b), (c), (d) calculated particle sizes using ImageJ software.

3.3.6. Surface area analysis

Brunauer-Emmett-Teller (BET) surface area analysis is the multi-point measurement of specific surface area (m^2/g) through gas adsorption analysis. The solid sample under measurement is suspended in an inert gaseous volume, or an inert gas is made to continuously flow over the solid sample. Small gas molecules adsorb to the surface of the solid substrate. A porous structure is a better material for this adsorption process as more molecules can get adsorbed due to weak van der Waals forces, forming a monolayer of adsorbed gas [124]. The rate of adsorption and the formed monomolecular layer can be used to calculate the specific surface area and the porous geometry of the solid sample. The specific surface area increases drastically from 0.4 m^2/g (C0) to 4.7 m^2/g (CA1). Then it gradually decreases to 1.4 m^2g^{-1} (CA2) and 1.3 m^2g^{-1} (CA3) samples [Figure 3.3.6.1]. This increased surface area is due to the increased porosity of the CA1 sample. Similar findings can be seen from the other reports [125], [126], [127]. This is obtained from the calculation of the pore volume of all the samples. The CA1 sample has a maximum pore volume of 0.0264 cm^3g^{-1}, and the minimum pore volume is for the C0 sample of 0.0028 cm^3g^{-1}. The values of specific surface area, total pore

volume, and the average pore diameter of all the samples are tabulated in Table 3.3.6.1. From the BET result, it is observed that for all Al^{3+} doped samples, the surface area and pore volume are larger compared to pure CuO samples. The highest surface area and pore volume are for the CA1 sample. For CA2 and CA3 samples, the surface area is less than that of CA1.

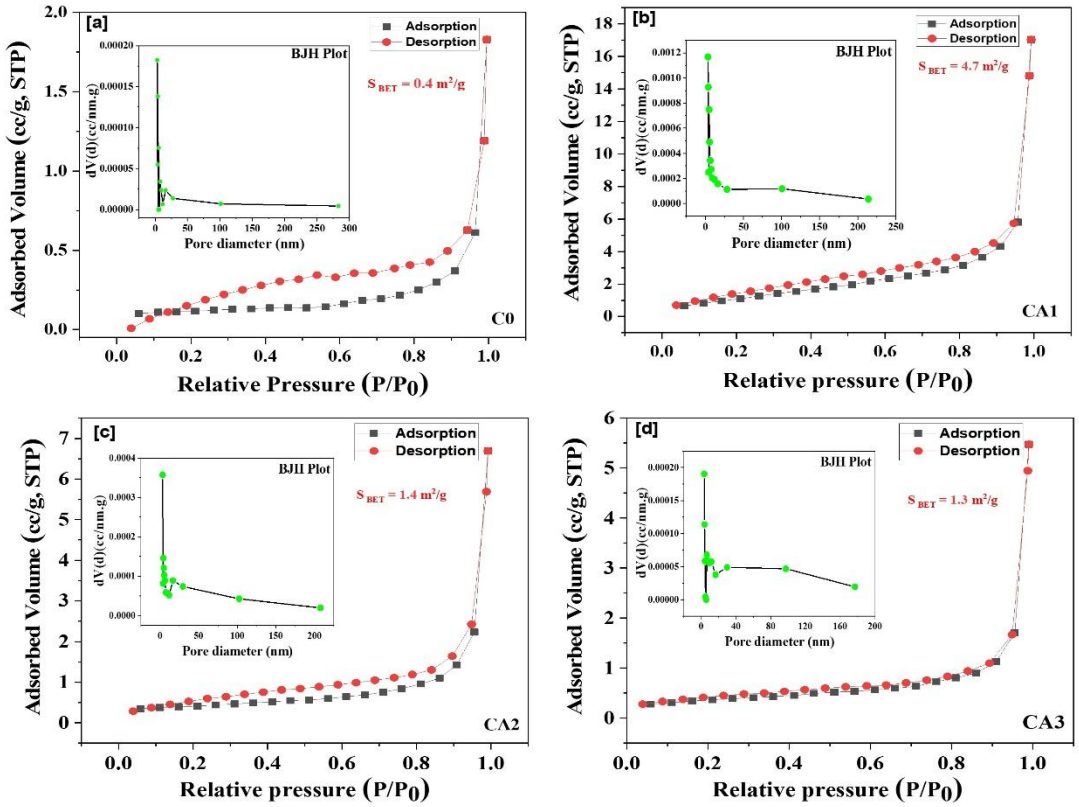


Figure 3.3.6.1: Represents (a), (b), (c), (d) N_2 adsorption/desorption isotherm, and the insets show the BJH pore size distribution.

Table 3.3.6.1: shows the specific surface area, total pore volume, and average pore diameter of all the samples.

Catalyst	Specific Surface Area (S_{BET}) ($m^2\ g^{-1}$)	Total Pore Volume (V_{pore}) ($cm^3\ g^{-1}$)	Average Pore Diameter (D_{pore}) (nm)

C0	0.4	0.0028	14.85
CA1	4.7	0.0264	11.20
CA2	1.4	0.0104	14.85
CA3	1.3	0.0085	13.51

3.3.7. Dynamic light scattering (DLS) analysis

Dynamic light scattering [DLS], also known as photon correlation spectroscopy or quasi-elastic light scattering, is a technique that primarily measures three important parameters related to the Brownian motion of macromolecules in solution that arises due to the bombardment of solvent molecules. These three parameters are the Zeta potential (V_ξ) (ξ-potential), the Hydrodynamic Size (D_h) [HDS], and the Polydispersity Index (PDI) of the samples. The motion of the nanoparticles is related to the D_h, which is the size of the cluster of nanoparticles inside a specific fluid medium. The V_ξ is an estimate of the surface charge of crystals, while the PDI is a measure of the broadness of the size distribution of the particles in a sample.

V_ξ can be employed to understand the physical stability of suspended nanoparticles in the solution [128]. If -10 mV < V_ξ < +10 mV, then particles are approximately neutral, while for Vξ > +30 mV, particles are strongly cationic, and for Vξ < -30 mV, then nanoparticles are strongly anionic [129]. A large positive or negative value of V_ξ of nanocrystals indicates good physical stability of nanosuspensions due to electrostatic repulsion of individual particles. For a range, −30 mV< V_ξ < +30 mV, the repulsive forces are generally considered to be insufficient to attain better physical colloidal stability [130]. On the other hand, a small V_ξ value can result in particle aggregation and flocculation due to the Van der Waals attractive forces acting upon them. These may result in physical instability [129]. It is the potential that is generated at the

slipping plane, where the slipping plane is the plane between the fluid layer, which is electrostatically attached to the nanoparticle. The values of V_ξ were predominantly negative for C0, which is -34.37 ± 0.6 mV, and decreased in magnitude for CA1 ~ -19.3 ± 0.1 mV, and for CA2 ~ -7.6 ± 0.3 mV (Table 3.3.7.1). Hence, the pure CuO powders having a V_ξ < -30 mV have a signature of good colloidal stability with particles separated from each other in solution. The values of V_ξ for all other Al-doped samples are in the range −30 mV< V_ξ < +30 mV. Hence, these samples cannot attain good colloidal stability. CA1 with V_ξ ~-19.3 mV seems to have a better colloidal stability than the CA2 and CA3 samples. The CA3 sample has a positive V_ξ ~ +4.58 mV as compared to the negative V_ξ recorded for the other three compositions. Note that the value of V_ξ continually increases from a high negative value, as in the case of C0, to a lesser negative value in CA1, and further in CA2, and then becomes moderately positive for CA3. The V_ξ value is an average value of the surface charge of the Powders, which is the resultant of all surface terminations of the same. Hence, surface terminations with negative O-planes are dominating in C0, while the relative amount of surface terminations with positive Cu-planes increases with increasing Al^{3+}-content. This is a remarkable result that modifies the possible surface construction due to partial Al^{3+}-doping. D_h is the effective spherical size of a molecule of the particles, which provides the same friction in the fluid as the molecule itself. D_h showed a random variation. The D_h of C0 is 2543 ± 6 nm, CA1 is 732 ± 4 nm, CA2 is 2287 ± 3 nm, and CA3 is 1678 ± 3 nm. On revisiting the crystallite and particle size, one can remember that the size in both cases decreased with increasing Al-content. In fact, the crystallite size of the pure C0 sample (177 nm) is at least three times that of the CA1 sample (47 nm). Hence, a size reduction is anticipated. Moreover, the larger negative charge of the C0 is supposed to attract more positive ions to the surface, thereby increasing the D_h. In spite of the low particle or crystallite size of CA2 and CA3, the extremely low V_ξ values for these samples may be responsible for their agglomeration, resulting in a larger D_h. The moderately smaller D_h value for CA1 may be due to a relatively higher negative charge V_ξ ~-19.3 mV than CA2 but yet being a lower flocculation or agglomeration than the CA2 sample.

For a monodisperse sample, the PDI value must be less than 0.05, whereas extremely polydisperse materials have a PDI > 0.7. If PDI is in the range, 0.08 < PDI < 0.7, then the material is said to have mid-range polydispersity, whereas samples with 0.05 < PDI < 0.08 are nearly monodisperse [131]. The C0 sample revealed a PDI value of 1, indicating a highly polydisperse nature of the sample. The PDI value of CA1 was 0.449, while that of CA2 was

0.826, and that of CA3 was 0.15. These values indicate that the Al-doped samples are of mid-range polydispersive nature. Hence, partial Al-doping helps to reduce the extremely wide distribution of the size of the samples, as in pure CuO, to a moderately lower size distribution. However, the fluctuating nature of the PDI can be correlated to the fluctuating nature of D_h, which needs to be studied further.

Hence, the decreasing crystallite/particle sizes, which can be related to the increasing strain in the increasing Al^{3+}-content in the lattice, may simultaneously affect the surface termination from a predominantly negative weightage towards a more positive one. This shift in surface charge towards moderately lower values modifies the surface capabilities of hosting the number of attached ions to themselves, thereby showing their effects on the values of D_h. Such changes in the values of average D_h may also be correlated to the size distribution of these effective particles in solution, which thereby modifies the PDI of the same. This enables one of these samples, i.e., CA1, to have a minimum D_h value and thereby be better fitted for photocatalytic activity in solution. Hence, photocatalytic correlation is important in this study.

Table 3.3.7.1: shows the hydrodynamic diameter and ξ-potential of all the samples in DI water.

Sample	Crystallite size from XRD (nm)	Particle Size from FESEM (nm)	ξ-potential (mV)	Hydrodynamic Size, D_h (nm)	PDI
C0	177	1092	-34.37 ± 0.6	2287 ± 003	1
CA1	47	482	-19.3 ± 0.1	732 ± 004	0.449
CA2	36	286	-7.61 ± 0.3	2543 ± 006	0.826

CA3	35	199	4.58 ± 0.6	1678 ± 003	0.15

3.4. Photocatalytic Performance and Kinetics

The general trend of checking photocatalytic activity is to use an expensive apparatus using a high-power (250~300W) UV/Xenon lamp or the use of direct sunlight. In this work, an attempt was made to check the photocatalytic activity of the powders for real wastewater in the presence of normal, inexpensive, commercially available household LED bulbs. Later, the same was verified with direct sunlight. The photocatalytic activity was performed for pure and Al-modified copper oxide (CuO) using three different cationic dyes (MB, RhB, and MO).

3.4.1. Photocatalysis under household LED

At normal room temperature, the photocatalytic degradation of pure CuO was found to be only 5.8% under 10 min irradiation of the visible household LED. By introducing aluminum in CuO systems, the photocatalytic degradation has increased to 16% for CA1, 10% for CA2, and 13% for CA3 within the same 10 min visible-light irradiation of LED light. Hence, it was observed that all the aluminum-doped CuO samples have a better dye degradation property than the pure CuO.

3.4.1.1. Effect of Temperature on dye degradation of Al^{3+} doped CuO

Several factors were investigated that can affect photocatalytic activities, e.g., catalyst loading, addition of external oxidizing agents, etc. Amongst these parameters, reaction temperature is of prime importance. The high-power light used creates a heating effect that increases the temperature of the solution. Hence, the temperature keeps increasing with time [132]. Higher temperature seems to increase the photocatalytic degradation of organic dyes in water [133]. However, in this study, a simple LED was used, which did not increase the temperature significantly. Under such a situation, to understand the effect of temperature and light simultaneously on photocatalytic activity needs to be verified to keep similarities between the studies. Hence, external heating was performed while irradiating the entire sample. By elevating the reaction temperature from RT to 80 °C, the photocatalytic activity increases. This

may be due to the improvement of interfacial charge transfer from solid to liquid [134]. However, reaction temperature greater than 80 °C leads to the charge carrier recombination, and it will disfavor the adsorption process of the organic compounds on the catalyst surface [135]. A reaction temperature below 80 °C favors adsorption. Whereas further decrease of reaction temperature to 0 °C leads to an increase in activation energy [136]. Hence, the temperature of 20-80 °C is considered effective for the photo mineralization of organic content. However, one must also consider the effective changes of D_h in the presence of light and higher temperatures. It is known that D_h is proportional to temperature, but one should also consider the thermodynamic rate of reaction, which increases with temperature due to the increased number of collisions between the reactive species. Hence, a continuous increase in the degradation percentage can primarily be attributed to the thermally activated nature of the process.

To do the temperature-dependent photocatalysis, the temperature of the experimental setup varied from 29 ^{0}C to 59 ^{0}C with a step size of 10 ^{0}C. The maximum dye degradation was obtained for the temperature of 59 ^{0}C. Above 59 ^{0}C, the increased temperature may favor the increased charge recombination rate and may lead to more thermodynamically affected processes. Hence, these may decrease photocatalytic activity. Also, considering the practical real-life applications, the temperature was limited to 59 ^{0}C, which can be easily available by solar light heating (40 ^{0}C to 42 ^{0}C on a winter afternoon, and ~ 50 ^{0}C on a summer afternoon). This temperature is sometimes carried by the wastewater from the textile industry itself and hence can be used as a self-treatment process [137]. Hence, the choice of 59 ^{0}C can be justified as a workable temperature for this photocatalytic study. At each fixed temperature, the light was irradiated for a fixed time duration (10 min), and the corresponding photo-degradation was measured, Figure 3.4.1.1(a). At all the fixed temperatures, the photodegradation change of relative concentration followed a pseudo-first-order chemical kinetics, and the corresponding rate constants and degradation percentage were calculated [Figure 3.4.1.1(b, c)]. The temperature-dependent enhancement observed in the present study is interpreted as a thermally assisted catalyst-mediated process. The investigated temperature range (29-59 °C) is substantially lower than that typically associated with rapid thermal decomposition of H_2O_2, and the low-power 455 nm LED source is not expected to induce significant dye photolysis in the absence of a catalyst. Furthermore, the strong dependence of degradation efficiency on catalyst composition suggests that the catalyst remains the dominant factor governing the

reaction kinetics.

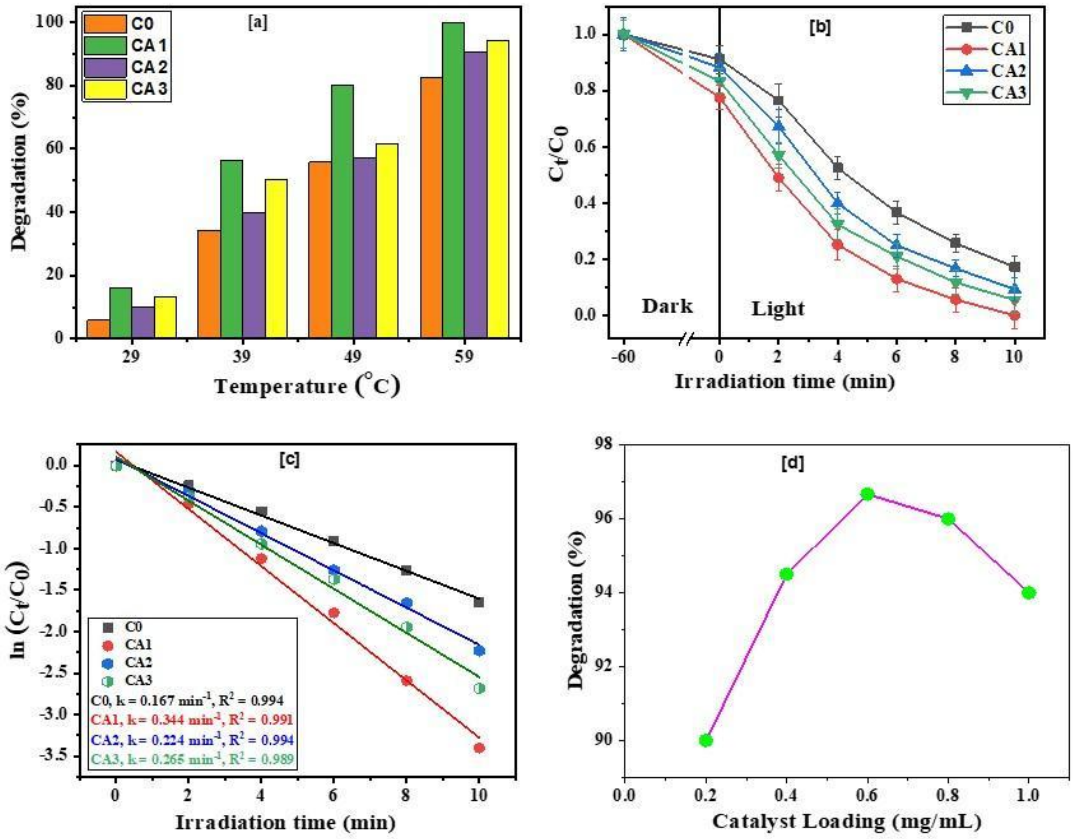


Figure 3.4.1.1: Represents (a) the degradation percentage of all the samples at different temperatures for a fixed irradiation time of 10 min, (b), (c) relative concentration and calculated rate constants, and (d) Degradation percentage of the CA1 sample as a function of catalyst concentration after a fixed visible-light irradiation time of 10 min at 59 °C. The figure was used to determine the optimum catalyst loading for subsequent photocatalytic experiments.

3.4.1.2. Comparison of Photocatalytic activity of C0 and CA1 at 59 ^{0}C:

The photocatalytic degradation has increased from 80% in C0 to 97% in CA1 within the first 10 min of visible-light irradiation. The prominent absorption band of methylene blue in the visible region, typically centred around ~664 nm, originates from the π–π* transition of the conjugated chromophoric structure of the dye. The gradual decrease in this peak intensity with irradiation time indicates disruption of the chromophore and progressive dye degradation/decolorization. Therefore, the reduction in absorbance at this wavelength was used

to estimate the relative dye concentration and calculate the apparent degradation kinetics. Hence, CA1 reveals 17% more degradation as compared to C0. This is approximately a 2-fold increment in the rate constants, ~0.167 min^{-1} in C0 to 0.344 min^{-1} in CA1.

3.4.1.3. Effect of catalyst concentration

After optimizing the CA1 sample among all the Al^{3+}doped CuO samples, the concentration of the CA1 has been optimized for enhanced photocatalytic activity. For this, different concentrations of the CA1 sample, 0.2 mg/mL, 0.4 mg/mL, 0.6 mg/mL, 0.8 mg/mL, and 1 mg/mL have been taken and used for the dye degradation at 59 ^{0}C simultaneously. As the amount of catalyst loading increases from 0.2 mg/mL to 0.6 mg/mL, the degradation of MB increased from 90% to 97% and then decreased to 96% for 0.8 mg/mL and further to 94% for 1 mg/mL catalyst loading within 10 minutes of light irradiation [Figure 3.4.1.1(d)]. With increasing catalyst amount, the number of collisions between reactants increases (a feature of heterogeneous photocatalysis), thereby the photodegradation of dye increases [138]. The formation of •OH radicals, which take part in dye degradation, will increase with the number of active sites on the photocatalyst surface. As the amount of catalyst increases beyond a certain amount, the solution becomes turbid and thus blocks the radiation for the reaction to proceed. That leads to a decrease in the percentage degradation [139]. The optimum concentration of the CA1 sample has been taken to be 0.6 mg/mL.

3.4.1.4. Effect of H_2O_2 concentration

Adding oxidizing species like hydrogen peroxide (H_2O_2) and potassium peroxydisulfate ($K_2S_2O_8$) is one of the best procedures that can increase the photocatalysis [140]. Hydrogen peroxide can play a dual role by producing •OH radicals, and it helps to increase the charge separation by accepting an electron from the conduction band.

$$H_2O_2 + e^- \rightarrow OH^- + {}^{\bullet}OH$$

$$H_2O_2 + O^{2-} \rightarrow OH^- + \bullet OH + O_2$$

Thus, the produced hydroxyl ions and hydroxyl radicals can degrade the organic dyes. H_2O_2 is formed in the process of dye degradation, and it enhances the degradation process. To further enhance the degradation of dyes, additional H_2O_2 can be added to the test solution. Addition of

this scavenger H_2O_2 encourages the formation of •OH, OH^-. To see the effect of concentration of H_2O_2 on the degradation kinetics, the concentration of H_2O_2 varies from 90 mM to 180 mM [Figure 3.4.1.2]. The temperature and catalyst (CA1) concentration were fixed at 59 ^{0}C and 0.6 mg/mL, which is the optimized concentration and temperature, respectively. As expected, the rate constants increase from 0.344 min^{-1} to 0.466 min^{-1}, then to 0.664 min^{-1} and to 0.83 min^{-1} for different H_2O_2 concentrations, i.e, for 90 mM, 120 mM, 150 mM, and 180 mM, respectively [Figure 3.4.1.2(d)]. However, further increasing the concentration of H_2O_2, the value of the rate decreased. This may be attributed to the fact that, at higher H_2O_2 concentration, there is a decrease in hydroxyl radical concentrations in the reaction medium owing to self-attenuation of hydroxyl radicals by H_2O_2, as shown in the following reactions.

$$H_2O_2 + \bullet OH \rightarrow H_2O + HO\bullet$$

$$HO\bullet + \bullet OH \rightarrow H_2O + O_2$$

All the calculated rate constants are given in Table 3.4.1.1. So, H_2O_2 can enhance the dye degradation rate and decrease the degradation time drastically. So, we optimized the concentration of H_2O_2 to 180 mM for further reactions.

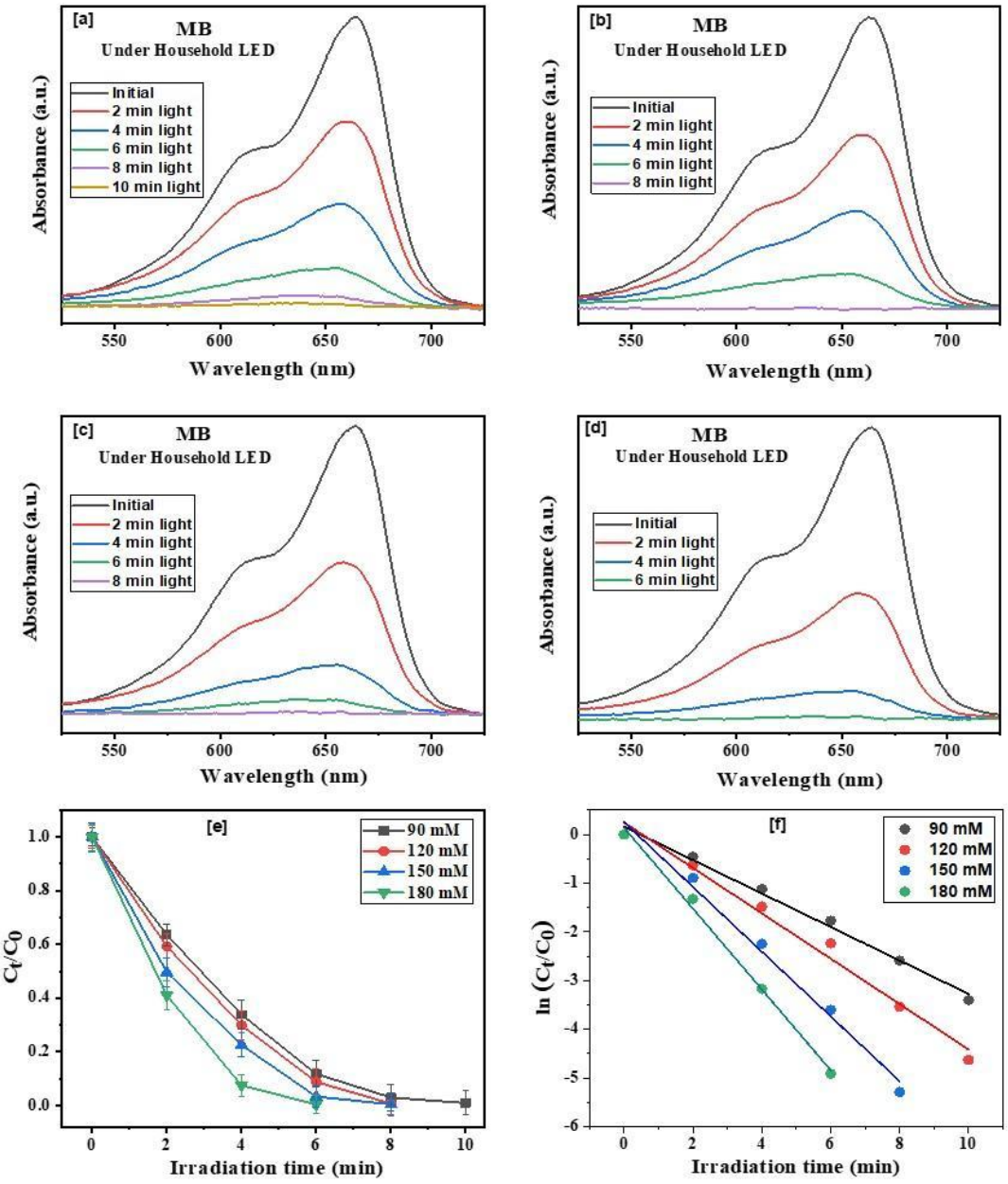


Figure 3.4.1.2: (a, b, c, d) absorbance of MB dye (d) relative concentration changes with irradiation time, (e) calculated rate constants at different H_2O_2 concentrations, i.e, 90 mM, 120 mM, 150 mM, and 180 mM, respectively, for the CA1 sample at 59 ^{0}C.

Table 3.4.1.1: Irradiation time, degradation percentage, calculated rate constants, and linear

correlation coefficients for different concentrations of H_2O_2.

H_2O_2 Concentration (mM)	Irradiation time (min)	Degradation (%)	Rate constants (min^{-1})	R^2
90	10	96.67	0.344	0.991
120	10	99.02	0.466	0.985
150	8	99.49	0.664	0.989
180	6	99.27	0.83	0.995

3.4.1.5. Photocatalytic degradation of Methyl orange (MO) and Rhodamine B (RhB)

By taking all the optimized parameters from the previous experiments, the photocatalytic degradation was also tested for two more cationic dyes, MO and RhB. The initial dye concentration was taken to be 10 ppm (10 mg/L), catalyst loading = 0.6 mg/mL, 180 mM H_2O_2. Figure 3.4.1.3 shows the relative concentration change and calculated rate constants of MO and RhB dye under household LED light.

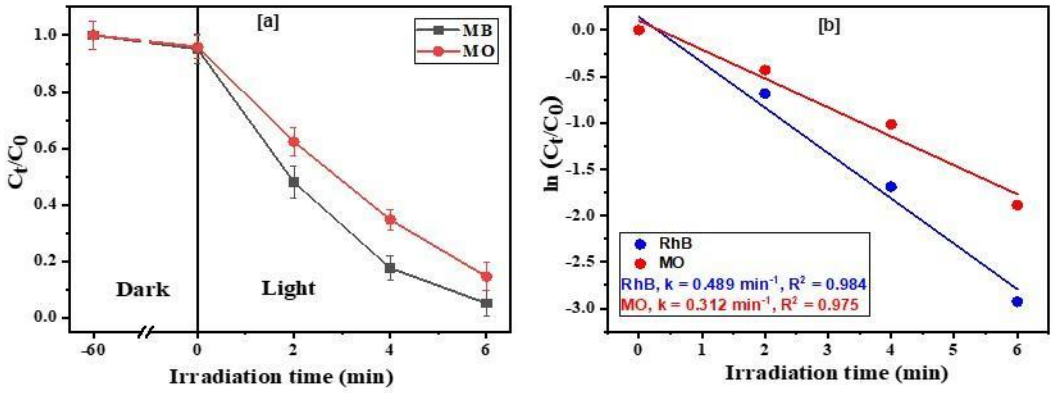


Figure 3.4.1.3: Represents (a, b) relative concentration change, and calculated rate constants of MO and RhB dye under household LED light, Initial dye conc. = 10 ppm (10 mg/L), catalyst loading = 0.6 mg/mL, 180 mM H_2O_2 at 59 ^{0}C.

3.4.2. Photocatalysis under Sunlight

To make this methodology more practical and usable with respect to the most abundant energy available on the Earth's surface, photocatalytic activity was carried out under direct sunlight without controlling the reaction temperature. The temperature of the surroundings was between 35°C and 40°C, while the intensity was 6 × 10 ^5 lx. This considers factors such as hydrodynamic changes and focuses solely on the effect of light. For this experiment, all parameters were kept constant, i.e., the initial dye concentration was set at 10 ppm (10 mg/L), the catalyst loading was 0.6 mg/mL, and the H_2O_2 concentration was 180 mM. The photocatalytic performance was taken for all three cationic dyes. Almost all the dyes degraded within 30 minutes under sunlight at a temperature of 35°C and with a light intensity 2 times smaller than AM 1.5G Sun, which is an approximate value of the intensity for artificial solar light [Figure 3.4.2.1]. It should be noted that the sunlight experiments were performed under natural outdoor conditions at IIT Indore, with an average measured solar intensity of approximately 474 W m^{-2}, which is lower than the standard 1 Sun condition (~1000 W m^{-2}). The observed photocatalytic performance, therefore, demonstrates effective catalyst activity even under sub-1 Sun irradiation. Under standardized 1 Sun illumination, higher degradation rates may be expected due to increased photon flux and enhanced generation of photogenerated charge carriers. However, the response may not be strictly linear because photocatalytic

performance is also governed by recombination processes, oxidant availability, interfacial reaction kinetics, and mass-transfer effects. Experimental validation under a calibrated solar simulator was beyond the scope of the present work and may be explored in future studies.

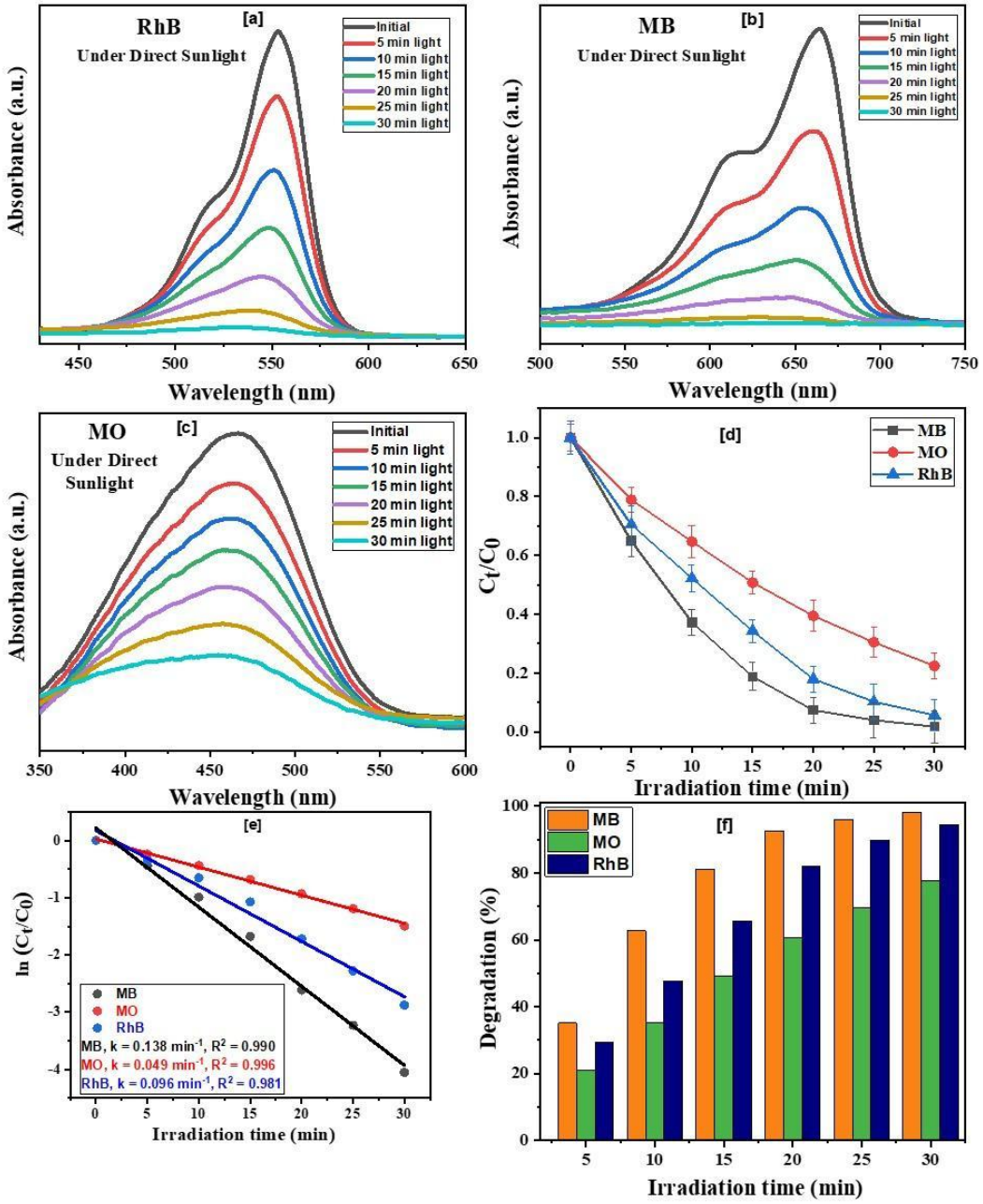


Figure 3.4.2.1a: (a), (b), (c) represent the absorbance of MB, RhB, and MO solutions, (d) relative concentration, (e) fitted rate constants, and (f) degradation percentage at different irradiation times under sunlight.

The characteristic absorption peaks of MB, RhB, and MO originate from their respective chromophoric structures responsible for visible-light absorption. The MB absorption band (~664 nm) arises from π–π* transitions within the conjugated phenothiazine structure, RhB absorption originates from the xanthene chromophore, and the MO absorption band is associated with the azo (–N=N–) chromophore. The gradual decrease in these absorption bands with irradiation time indicates destruction of the chromophoric groups and progressive degradation of the dye molecules. Consequently, the spectral evolution provides direct evidence for both decolorization and structural transformation during the photocatalytic process.

Under direct sunlight irradiation, the change in the relative concentration was observed to follow a pseudo-first-order kinetics model under the investigated experimental conditions for all three cationic dyes (MB, MO, and RhB). The degradation percentage, calculated rate constants, and the corresponding values of R^2 (the coefficient of determination) are given in Table 3.4.2.1. The coefficient of determination (R^2) was used to evaluate the quality of the pseudo-first-order kinetic fitting applied to the photocatalytic degradation data. R^2 values approaching unity indicate that the experimental degradation behavior is well described by the pseudo-first-order kinetic model. Therefore, the apparent rate constant (k) provides information regarding the degradation rate, whereas the R^2 value reflects the goodness-of-fit and statistical reliability of the kinetic analysis. The high R^2 values obtained in the present study suggest that the degradation of the investigated dyes follows pseudo-first-order kinetics under the experimental conditions employed. It should be noted that the LED-assisted and sunlight-assisted photocatalytic experiments were conducted under different operating conditions. The LED experiments were performed under optimized reaction conditions, including elevated temperature and controlled H_2O_2 concentration, whereas the sunlight experiments were carried out under ambient outdoor conditions. Therefore, the observed differences in degradation kinetics should not be interpreted solely as a consequence of illumination intensity. Instead, they reflect the combined influence of photon flux, temperature, oxidant availability, and catalyst-mediated interfacial reaction kinetics. The objective of the sunlight-assisted experiments was to evaluate the practical applicability of the optimized Al^{3+}-doped CuO photocatalyst under naturally available solar irradiation rather than to directly compare photocatalytic rates obtained under optimized laboratory LED conditions.

Table 3.4.2.1a: Represents the degradation percentage, calculated rate constants, and the corresponding values of R^2 under direct sunlight irradiation of 30 min for all three dyes.

Name of the Dyes	Degradation percentage (%)	Rate constants (min^{-1})	R^2
MB	98.3	0.138	0.990
MO	77.6	0.049	0.996
RhB	94.4	0.096	0.981

3.5. Photo-Fenton-Like Degradation Mechanism

The detailed mechanism of dye degradation is a common and well-understood mechanism for the semiconductor photocatalysis process [141]. The role of Al^{3+} in CuO can be explained with a mechanism detailed in Figure 3.4.2.1b. The potential of valence band edge (E_{VB}) and conduction band edge (E_{CB}) were measured using the formulas: $E_{VB} = X - E^C + 0.5E_g$ and $E_{CB} = E_{VB} - E_g$, where X is the Mulliken electronegativity of the photocatalyst (5.81 eV for CuO), E^e is the free electron energy (4.5 eV v_s NHE), and E_g is the band gap energy [142], [143], [144], [145]. The E_{VB} and E_{CB} values for different samples were summarized in Table 3.4.2.1b. The conduction-band and valence-band positions shown in Figure 3.4.2.1b were estimated using the Mulliken electronegativity method described above, together with the experimentally determined optical bandgap values. It can be observed that by Al^{3+}-incorporation in the copper oxide system, the band gap increased, and the corresponding valence band edge and conduction band edge changes with the change of band gap. As the standard electrode potential for $OH^-/OH^\cdot$ is about 1.9 eV, the hole, h^+, from the valence band reacts with OH^- to produce $OH^\cdot$ radicals as this pathway are more thermodynamically

favourable. Similarly, the redox potential for $OH^{\cdot}/H_2O_2$ is 0.8 eV. Hence, the *electrons* from the conduction band react with H_2O_2 to give $OH^{\cdot}$ radicals that can take part in the reactions. Then the reactive $OH^{\cdot}$ converts the organic dye molecule into less harmful by-products like CO_2 and H_2O [146], [147], [148], [149], [150], [151], [152].

Table 3.4.2.1b: Represents the standard EVB and ECB values for different samples.

Samples	E_{VB}	E_{CB}
C0	2.025	0.595
CA1	2.045	0.575
CA2	2.05	0.57
CA3	2.055	0.565

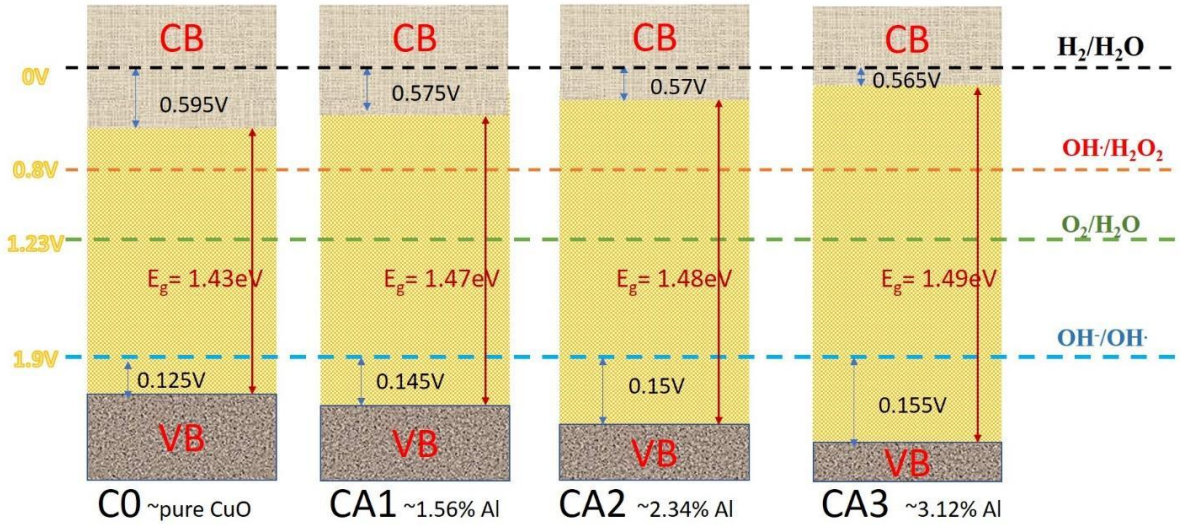


Figure 3.4.2.1b: Schematic degradation mechanism of Al^{3+}-modified copper oxide. The

conduction-band and valence-band positions shown here were estimated using the Mulliken electronegativity method described above, together with the experimentally determined optical bandgap values.

Again, the effect of increasing temperature on the photocatalytic process can be understood with the proposed mechanism and associated thermodynamic theories. The temperature dependence of photocatalysis can be explained using the Arrhenius equation. Experimentally, it was observed that the chemical reaction rate doubles or triples for every 10°C rise in temperature [153]. A minimum energy is needed, termed the activation energy (E_A), for a reaction to proceed. With increasing temperature, E_A remains unchanged. However, due to the absorbed heat, there is an increase in the kinetic energy E_K of the particles. This increase in the average E_K implies that a larger number of reactants are now having the minimum energy necessary to collide and react. An increase in temperature causes a rise in the energy levels of the molecules involved in the reaction, so the rate of the reaction increases. From the observed increase in rate constants with temperature, an Arrhenius model can be used to calculate the E_A of reaction: $k_{app} = Aexp(-E_A/RT)$, where, k_{app} is the apparent reaction rate constant (min^{-1}), A is Arrhenius factor, and R is ideal gas constant which is equal to 8.314 J/K mol and T is the temperature (K). The logarithmic form of this equation can be written as: $ln\ k_{app} = ln\ A - E_A/RT$. The value of E_A was estimated from the slope of the straight-line plot of $ln\ k_{app}$ *versus* $1000/T$ [Figure 3.4.2.2] in the temperature range 29 °C - 59 °C. Also, in a similar fashion, the transition state theory can be used to see the chemical kinetics model as well as all the related parameters that are associated with it [154], [155]. Figure 3.4.2(b) shows the Eyring plot, which is plotted by taking $ln\ (k_{app}/T)$ *versus* $1000/T$. All the related parameters are summarized in Table 3.4.2.2 The positive values of $\Delta^{\ddagger}H^{o}$ indicate that the rate-determining illuminated step is thermally activated, consistent with interfacial charge transfer and ROS generation rather than adsorption-controlled kinetics. This does not imply that dye adsorption itself is endothermic; rather, adsorption weakens with increasing temperature, while the activated surface redox step accelerates, leading to an overall increase in the apparent photocatalytic rate constant [156]. The increase in experimental temperature leads to the positive values of standard Gibbs free energy change of activation ($\Delta^{\ddagger}G° > 0$), which increased for all the samples except CA1. The large positive $\Delta^{\ddagger}G°$ at the higher temperature indicated no spontaneous processes and weak adsorption of organic pollutants on C0, CA2, and CA3. However, for the CA1 sample, the

positive values of standard Gibbs free energy change of activation ($\Delta^{\ddagger}G° > 0$) decreased [Table 3.4.2.2]. This can be explained by the fact that although the value is positive, indicating the reaction is not spontaneous, the adsorption is still better, which can be another reason for the CA1 sample to show maximum photocatalytic activity. Again, with an increase in temperature, the photocatalytic reactions compete more efficiently with electron–hole pair recombination, so the photocatalytic activity of all the samples increased with increasing temperature [157]. It should be noted that the surface character facilitates pollutant interaction without adsorption being the rate-limiting step.

The temperature dependence observed here is consistent with thermally assisted charge detrapping and hopping processes in strongly correlated CuO, rather than a transition from adsorption- to diffusion-limited kinetics.

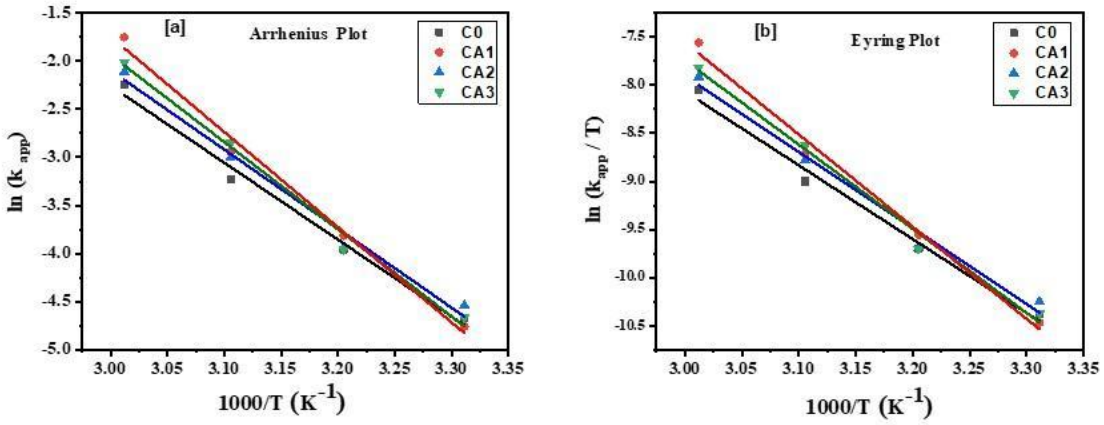


Figure 3.4.2.2: shows Arrhenius plots and Eyring plots for all the chemical reactions.

Table 3.4.2.2: Represents various thermodynamic parameters obtained using Arrhenius Theory and Transition State Theory for all the chemical reactions.

				Arrhenius Theory			**Transition State Theory**				
Chemical	**T, K**	**K_{app} in min^{-1}**	**ln (K_{app} /T) in min^{-1}**	**A (× 10^7) in**	**E_a in kJ/m**		**$\Delta^{\ddagger}H^0$ in kJ/m**	**$\Delta^{\ddagger}S^o$ in kJ/m**	**$\Delta^{\ddagger}G^o$ in kJ/mo**	**A (× 10^**	

reactions with			**K^{-1}**	**min^{-1}**	**ol.**	**R^2**	**ol.**	**ol. K**	**l.**	**11) in min^{-1}**	**R^2**
C0	302	0.0094	-10.38	4.45	66.42	0.98	63.78	-0.039	75.6	1.04	0.98
	312	0.019	-9.7						76.02	1.08	
	322	0.0397	-9						76.41	1.11	
	332	0.1058	-8.05						76.8	1.15	
CA1	302	0.0086	-10.47	2260	82.27	0.99	79.64	0.0126	75.84	1.05	0.99
	312	0.022	-9.56						75.7	1.08	
	322	0.053	-8.72						75.58	1.12	
	332	0.174	-7.56						75.46	1.15	
CA2	302	0.011	-10.25	10.4	68.35	0.98	65.71	-0.032	75.41	1.04	0.98
	312	0.019	-9.688						75.73	1.08	
	322	0.049	-8.779						76.05	1.11	

	332	0.12	-7.92						76.37	1.15	
CA3	302	0.009	-10.4	154	75.34	0.99	72.71	-0.0098	75.659	1.05	0.99
	312	0.019	-9.7						75.757	1.08	
	322	0.057	-8.63						75.855	1.12	
	332	0.134	-7.82						75.953	1.15	

3.5.1. Scavenger test

The scavenger test is usually used to quantify the number of radicals that play a major role in the photocatalytic degradation of organic dyes. This includes hydroxyl, superoxide, and holes in the study. Three different chemicals, such as isopropanol (IPA), ammonium oxalate (AO), and p-benzoquinone (BQ), were used to trap hydroxyl radicals, holes, and superoxide radicals, respectively [158]. MB, RhB, and MO dyes are degraded by chemical reactions with electrons and holes, hydroxyl, and superoxide radicals [159]. The different amounts of chemicals used are as follows: IPA (60 μL/mL), AO (0.124 mg/mL), and p-BQ (0.108 mg/mL). For the hydroxyl radical scavenger (IPA), the degradation was the least, with degradation rates of 7% for MO, 9% for RhB, and 11.4% for MB. The degradation was considerably high for the hole scavenger (AO), with degradation rates of 60% for MO, 65% for RhB, and 72.8% for MB. The most degradation was observed for the superoxide scavenger (BQ), with degradation of 65% for MO, 70% for RhB, and 78.9% for MB [Figure 3.5.2.1b]. Therefore, the presence of IPA reduces the concentration of the hydroxyl radical, which drastically reduces the degradation process. Hence, this radical appears to play a crucial role in the degradation process. Similar logic reveals the least effectiveness of the superoxide radical in degrading MO, RhB, and MB dyes.

3.5.2. Hydroxyl radicals' detection by Steady-State Fluorescence spectroscopy:

To further confirm the role of hydroxyl radicals in photocatalytic degradation with the CA1 sample, Steady-State Fluorescence was performed. The fluorescence spectra of the solutions were recorded using a Fluoromax-4p spectrofluorometer from Horiba JobinYvon (model: FM-100). All fluorescence emission spectra were analyzed using Origin Pro 2018 software. The spectral sensitivity of the instrument was taken care of. The experiment was performed by taking 100 µL of 0.1 mM of Terephthalic acid (PTA) in 50 mL Solution (0.2 mM PTA overall) containing 180 mM H_2O_2 with 0.6 mg/mL CA1 catalyst concentration at 59 ^{0}C and by illuminating the same light (Blue LED) used in photocatalytic reactions. It is widely presumed that only photoluminescent 2-hydroxyterephthalic acid (TAOH) is formed upon reaction with hydroxyl radical [160], [161]. With light irradiation, the generation of hydroxyl radicals has increased continuously, which can be observed from the increase in fluorescence spectra as evident from Figure 3.5.2.1a. Hence, both the fluorescence spectroscopy and scavengers test using Hydroxyl radical scavengers (IPA) confirmed the role of hydroxyl radical in the rapid photocatalytic degradation of organic dyes.

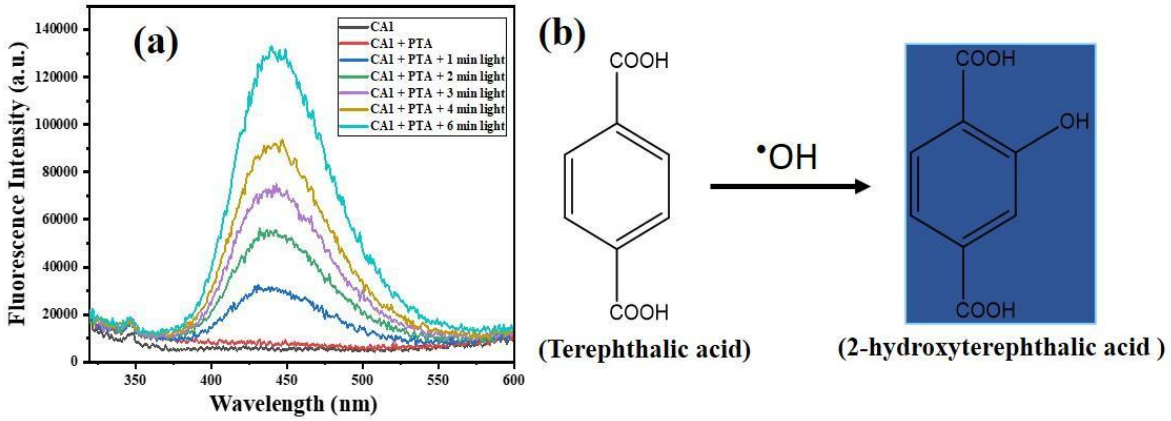


Figure 3.5.2.1a: : (a) The Fluorescence spectra of the solution after irradiating the light for a given period, (b) Conversion of Terephthalic acid to Fluorescent 2-hydroxyterephthalic acid with reacting hydroxyl radical generated from the reaction.

3.6. Stability, Reusability, and Practical Implications

Five cycles of the degradation process were run to ensure reusability and the stability of the

samples for the MO, RhB, and MB dyes. After each cycle of degradation, the samples were collected through centrifugation. It is washed with ethanol and DI water and dried. These dried samples are again used for photocatalytic dye degradation. All the experimental conditions, like temperature, amount of catalyst, etc., were kept constant. Figure 3.5.2.1b (d) shows the reusability of the prepared samples for the three dyes. It is seen that the efficiency of the prepared samples nominally decreases for the next consecutive cycles. This may be due to the loss of materials during the filtering and washing process.

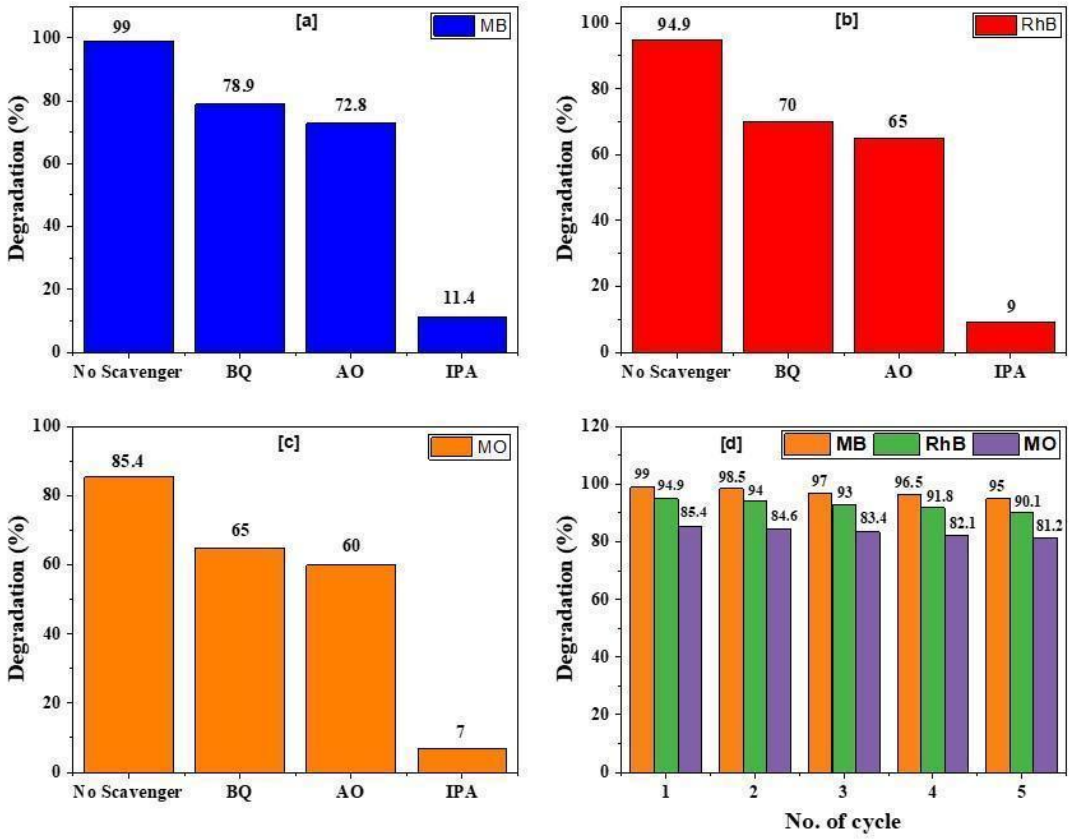


Figure 3.5.2.1b: (a), (b), (c) The scavenger test results reveal the importance of hydroxyl radical in the photodegradation process for all three dyes, (d) Assurance of re-usability of the materials for all three dyes.

To check the stability of the given catalyst, we have performed XRD [Figure 3.5.2.2] and Transmission Electron Microscopy (TEM) analysis [Figure 3.5.2.3] of the CA1 sample before and after use in the photocatalytic experiment. The lattice spacing calculated from the HRTEM

image [Figure 3.5.2.3(b, e)] is 0.273 nm, 0.253 nm, and 0.251 nm, which correspond to the (110), (002), and (11-1) planes for the CA1 sample before being used for catalysis. Similarly, the lattice spacings are calculated to be 0.253 nm and 0.251 nm, which correspond to the (002) and (11-1) planes of the CuO crystal (JCPDS Card No. 48-1548) for the CA1 sample after five repeated uses, which confirms the stability of the catalyst. The selected area electron diffraction (SAED) of the catalyst before and after use in catalysis [Figure 3.5.2.3(c, f)] also agrees with the HRTEM data corresponding to different lattice planes of CuO crystals.

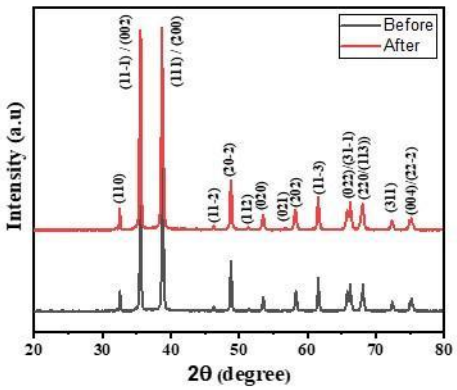


Figure 3.5.2.2:represents the XRD pattern of the CA1 sample before and after five times of repeated use for photocatalytic degradation.

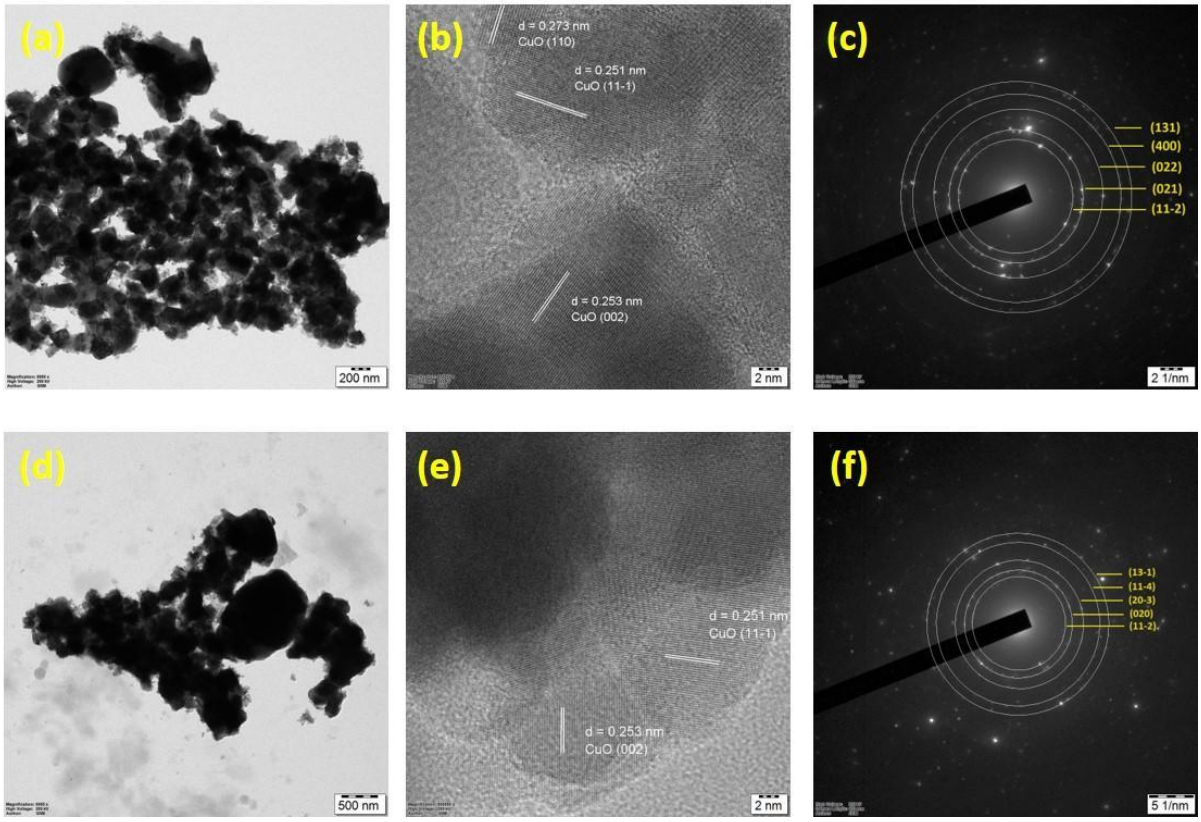


Figure 3.5.2.3: (a, b, c) are the TEM image, HRTEM Image, and SAED pattern of the Fresh CA1 sample. Similarly, (d, e, f) are the TEM image, HRTEM Image, and SAED pattern of the recycled CA1 sample, showing there is no chemical change in the material, which confirms the stability of the given material even after five times repeated use.

In addition to the above experiment, the photodegraded filtrate was also subjected to ICP-OES detection for Cu and Al leaching. As the results show, [Table 3.5.2.1], the leaching amounts of Cu and Al are 4.786 and 0.084 mg/L, which are very low. As the leaching amount is very minute, it can be considered that there is almost no difference in secondary pollution attributed to leaching, further indicating the stability of the CA1 photocatalyst even after repeated use.

Table 3.5.2.1: Represents the leached amount of Cu^{2+} and Al^{3+} after the photocatalytic reaction.

Element	**Leaching concentration (mg/L)**

Cu^{2+}	4.786 mg/L
Al^{3+}	0.084 mg/L

The sustainability of the sample can be seen by comparing the CA1 photodegradation results with the existing literature [Table 3.5.2.2]

Table 3.5.2.2: Literature comparison with the present work.

Sample	**Light, Dye (Conc.) used**	**Reaction Temp.**	**Rate constant (min^{-1})**	**Degradation (%) & time**	**Ref.**
CuO NPs	Sunlight MB, MR, and CR (2×10^{-5} mol/L)	RT	0.02059 0.02046 0.01749	MB - 93% MR - 90% CR - 85% in 120 min	[162]
Mn/Ag co-doped CuO NPs	Sunlight MB (5 ppm)	RT	0.0127	83.9% in 150 min	[163]

Ni-doped CuO NPs Fe-doped CuO NPs Zn-doped CuO NPs	500 W Xenon lamp MB (NM)	RT	NM	Ni doped: 52% Fe doped: 62% Zn doped: 63% in 60 min	[164]
CuO/ZnO NPs composite	400 W UV lamp MB MO (NM)	45 °C	MB: 0.288 MO: 0.060	MB - 99% in 15 min MO - 99% in 75 min	[165]
Al-doped CuO NPs	Household LED MB, RhB, and MO (10 ppm)	59 °C	MB: 0.83 RhB: 0.489 MO: 0.312	MB - 99.27% RhB - 94.9% MO - 85.4% in 6 min	This work
Al-doped CuO NPs	Direct Sunlight MB, RhB, and MO (10 ppm)	RT	MB: 0.138 RhB: 0.096 MO: 0.049	MB - 98.3% RhB - 94.4% MO - 77.6% in 30 min	This work

*Not Mentioned (NM)

Although Al^{3+} substitution enhances photocatalytic degradation rates, the observed decrease in dark adsorption with increasing temperature indicates that adsorption equilibrium does not govern the overall reaction rate. Instead, the monotonic increase in the apparent rate constant under illumination confirms that the dominant bottleneck lies in thermally activated interfacial redox processes and charge carrier utilization, rather than surface coverage.

In this context, Al^{3+} acts as a non-redox electronic modulator, improving Cu–O covalency, ligand-hole density, and hole mobility, thereby mitigating recombination losses intrinsic to strongly correlated CuO. This establishes that photocatalytic enhancement can be achieved without introducing additional redox centers by directly addressing the electronic bottleneck.

3.6 Chapter Summary

This chapter investigated the photocatalytic degradation of organic pollutants using aliovalent Al^{3+}-substituted CuO as a model defect-engineered oxide system. Building on the general experimental framework outlined in Chapter 2, this chapter focused on establishing clear correlations between aliovalent Al^{3+} substitution, defect chemistry, and visible-light-driven photocatalytic performance, with particular emphasis on electronic charge-utilisation bottlenecks intrinsic to CuO. The synthesis strategy enabled controlled incorporation of Al^{3+} into the CuO lattice, providing a non-redox-active electronic modulation platform to isolate defect- and ligand-hole-associated effects on photocatalytic behaviour.

Comprehensive photocatalytic measurements demonstrated that moderate Al^{3+} substitution significantly enhances degradation efficiency under both low-power LED illumination and natural sunlight when compared with pristine CuO. Systematic variation of reaction parameters, including catalyst loading, dye concentration, temperature, and oxidant dosage, revealed optimal operating conditions and confirmed reproducible performance trends. Kinetic analysis indicated pseudo-first-order degradation behavior, highlighting improved reaction rates arising from dopant-induced enhancement of charge-carrier utilisation and interfacial redox accessibility, rather than adsorption-controlled effects.

Mechanistic investigations using scavenger studies and fluorescence probing established hydroxyl radicals as the dominant reactive species governing pollutant degradation, supporting a ligand-hole-assisted, photo-Fenton-like degradation pathway intrinsic to the Al-modified CuO system. Reusability and stability assessments further demonstrated sustained

photocatalytic activity with minimal structural degradation or secondary contamination.

Overall, this chapter establishes Al^{3+}-substituted CuO as a defect-engineered, non-redox reference system for visible-light photocatalysis and provides a bottleneck-resolved mechanistic framework that underpins the subsequent chapters exploring morphology-controlled thermal effects and redox-assisted catalytic pathways.

It should be noted that the scavenger and fluorescence experiments provide qualitative evidence for the involvement of hydroxyl radicals as the dominant reactive species. However, absolute ROS generation rates or radical concentrations were not quantified in the present work. Quantitative ROS analysis using calibrated fluorescence methods or EPR/ESR spin-trapping could provide further mechanistic insight in future studies.

The strong photocatalytic performance obtained under sub-1 Sun natural irradiation conditions suggests promising applicability under practical outdoor environments, although further evaluation under standardized 1 Sun illumination would provide useful benchmarking of light-intensity-dependent performance.

Chapter 4 CuO Nanosheets: Morphology-Controlled and Temperature-Assisted Charge Transport in Photocatalysis

Abstract: *In Chapter 3, Al^{3+}-substituted CuO photocatalysts exhibited enhanced photo-Fenton-like degradation of organic pollutants under low-power illumination, where reaction temperature emerged as an influential but coupled parameter alongside dopant-induced electronic effects. To isolate and clarify the intrinsic role of temperature on photocatalytic kinetics, the present chapter focuses on undoped, morphology-engineered CuO nanosheets as a simplified model system.*

Phase-pure monoclinic CuO nanosheets were synthesized via a single-step hydrothermal route and comprehensively characterized in terms of structure, morphology, surface area, and optical properties. Photocatalytic degradation of methylene blue and rhodamine B was systematically investigated under low-power ultraviolet irradiation (11 W) and direct natural sunlight across environmentally relevant temperatures. The degradation process follows pseudo-first-order kinetics, with reaction rates showing a strong and reproducible temperature dependence. Arrhenius and transition-state analyses indicate thermally activated photocatalytic kinetics, suggesting that the rate-limiting interfacial charge-transfer and ROS-generation process benefits from increased temperature, thereby promoting improved charge-carrier utilization and reactive oxygen species generation.

By decoupling dopant effects from thermal contributions, this chapter provides mechanistic insight into temperature-assisted photocatalysis in CuO, thereby rationalizing and supporting the temperature-dependent trends observed in the Al^{3+}-doped photo-Fenton systems discussed in Chapter 3. The findings establish a coherent framework linking morphology, temperature, and photocatalytic reactivity in CuO-based materials for sustainable wastewater treatment.

4.1. Chapter Introduction and Objectives

In the preceding chapter, Al^{3+}-substituted CuO photocatalysts demonstrated enhanced photo-Fenton-like degradation of organic pollutants under low-power illumination. While dopant-induced electronic modulation played a central role, reaction temperature was also found to significantly influence degradation kinetics. However, in doped systems, thermal effects remain intrinsically coupled with compositional and redox-active contributions, making it difficult to isolate the fundamental role of temperature in governing photocatalytic reaction pathways and charge-carrier dynamics.

Temperature is known to influence several elementary steps in heterogeneous photocatalysis, including adsorption–desorption equilibria, interfacial charge transfer, reactive oxygen species (ROS) generation, and electron–hole recombination. Despite this, most photocatalytic studies rely on high-power light sources, where uncontrolled heating obscures the distinction between photonic and thermal effects. As a result, the mechanistic origin of temperature-assisted photocatalysis under low-power or solar irradiation remains insufficiently understood.

To address this limitation, the present chapter adopts a simplified, undoped CuO system with a well-defined nanosheet morphology as a model photocatalyst. By eliminating dopant-related electronic complexity and focusing on morphology-engineered CuO nanosheets, this chapter aims to decouple and systematically examine temperature-dependent effects on photocatalytic degradation kinetics. Low-power ultraviolet irradiation and direct natural sunlight are employed to maintain environmentally realistic operating conditions while enabling controlled temperature variation.

Objectives of Chapter 4

The specific objectives of this chapter are to:

- Synthesize phase-pure CuO nanosheets with controlled two-dimensional morphology using a facile hydrothermal route.
- Establish structure–property correlations through comprehensive structural, optical, surface, and colloidal characterization.
- Systematically investigate the influence of reaction temperature on photocatalytic degradation kinetics under low-power UV and natural sunlight irradiation.

- Quantify temperature-dependent reaction parameters using kinetic, Arrhenius, and transition-state analyses.
- Identify the dominant reactive oxygen species involved in temperature-assisted photocatalysis through scavenger studies.
- Provide mechanistic clarity to the temperature-dependent trends observed in Al^{3+}-doped photo-Fenton systems discussed in Chapter 3.

Through this approach, Chapter 4 establishes a clear mechanistic framework linking morphology, temperature, and photocatalytic reactivity in CuO-based systems, thereby strengthening the overall coherence of the thesis.

4.2. Synthesis and Experimental Methods

The synthesis of CuO nanosheets and all physicochemical and photocatalytic measurements were carried out following the general procedures described in Chapter 2. Any deviations or additional experimental conditions specific to this chapter are detailed below.

4.3. Structural, Optical, and Surface Properties

XRD analysis revealed a single-phase monoclinic structure of the CuO nanosheets [Figure 4.3.1(a)]. Rietveld refinement was performed on the XRD data with a CIF file #1011148 (analogous to JCPDS file #05-661), and the lattice parameters were found to be a = 4.66 Å, b = 3.41 Å, and c = 5.1 Å. The lattice stress was nominally ~0.0065, while the crystallite size was ~18.3 nm.

The monoclinic CuO exhibits the following vibrational modes: three acoustic modes ($A_u + 2B_u$), six infrared active modes ($3A_u + 3B_u$), and three Raman active modes ($A_g + 2B_g$). Displacements of oxygen atoms contribute to the active Raman modes. The Raman spectra of as-prepared nanosheets showed a Raman vibration at 296 cm^{-1} (A_{1g}), 344 cm^{-1} (B_{1g}), and 632 cm^{-1} (B_{2g}) [Figure 4.3.1(b)], confirming the single monoclinic phase. No other impurity phase, especially Cu_2O, was detected in this sample.

An increased specific surface area generally enhances photocatalytic activity by increasing the density of accessible interfacial reaction sites. Therefore, the pore size distribution and surface area are estimated from an N_2 adsorption-desorption measurement

(Brunauer-Emmett-Teller (BET) surface area analysis) [Figure 4.3.1 (c)]. A distinct hysteresis loop of type IV was observed for these nanosheets, indicating a mesoporous/ agglomeration-related porosity. The specific surface area was found to be 13.2 m^2/g. A large pore volume of 0.255 cc/g was observed in the nanosheets. Such a large value is expected to provide better surface-active sites for photocatalytic activities. The pore size distributions [inset of Figure 4.3.1 (c)] were observed in the range of 3 nm–311 nm. However, the average (mean) pore size distribution was found to be 3.419 nm, confirming the mesoporous/agglomeration-related porosity structure of the synthesized nanosheets.

The band gap was estimated from the UV-Vis DRS measurement, performed in the range of 200 nm to 1100 nm. Using the Kubelka-Munk function $F(R) = (1-R)^2 / 2*R$, the absorption coefficient was determined from the diffuse reflectivity, R, of the samples [166]. The optical band gap was estimated from the energy-dependent optical absorbance data using the Tauc method. $(\alpha h\nu)^{1/n} = A(h\nu-E_g)$; where α is the absorption coefficient, ν is the photon's frequency, h is Planck's constant, A is a proportionality constant, and E_g is the bandgap. Where n = 1/2, 3/2, 2, and 3 for direct allowed, direct forbidden, indirect allowed, and indirect forbidden transitions, respectively, which determines the nature of the transition between the conduction band (CB) and valence band (VB) [167].

There are inherent defect states in the sample, such as O_i, V_O, V_{Cu}, and Cui, among others. The energy associated with these defect states, Urbach energy (E_U), is related to the absorption coefficient in the band-tailing regions of the absorption edge and is expressed as $\alpha = \alpha o.\exp(h\nu/E_U)$, where α_o is a constant. Taking the natural logarithms of both sides of the equation, one can express the above equation as $\ln[\alpha] = \ln[\alpha_o] + (h\nu/E_U)$, which is a straight line of slope $1/E_U$. This allows one to estimate E_U from an ln(α) vs. hν plot [120].

Using the Tauc method, the bandgap of the CuO nanosheets was determined to be 1.575 ± 0.008 eV, which falls within the range of visible red to near-infrared light. The Urbach energy associated with the defect states was observed to be 205.5 ± 4 meV.

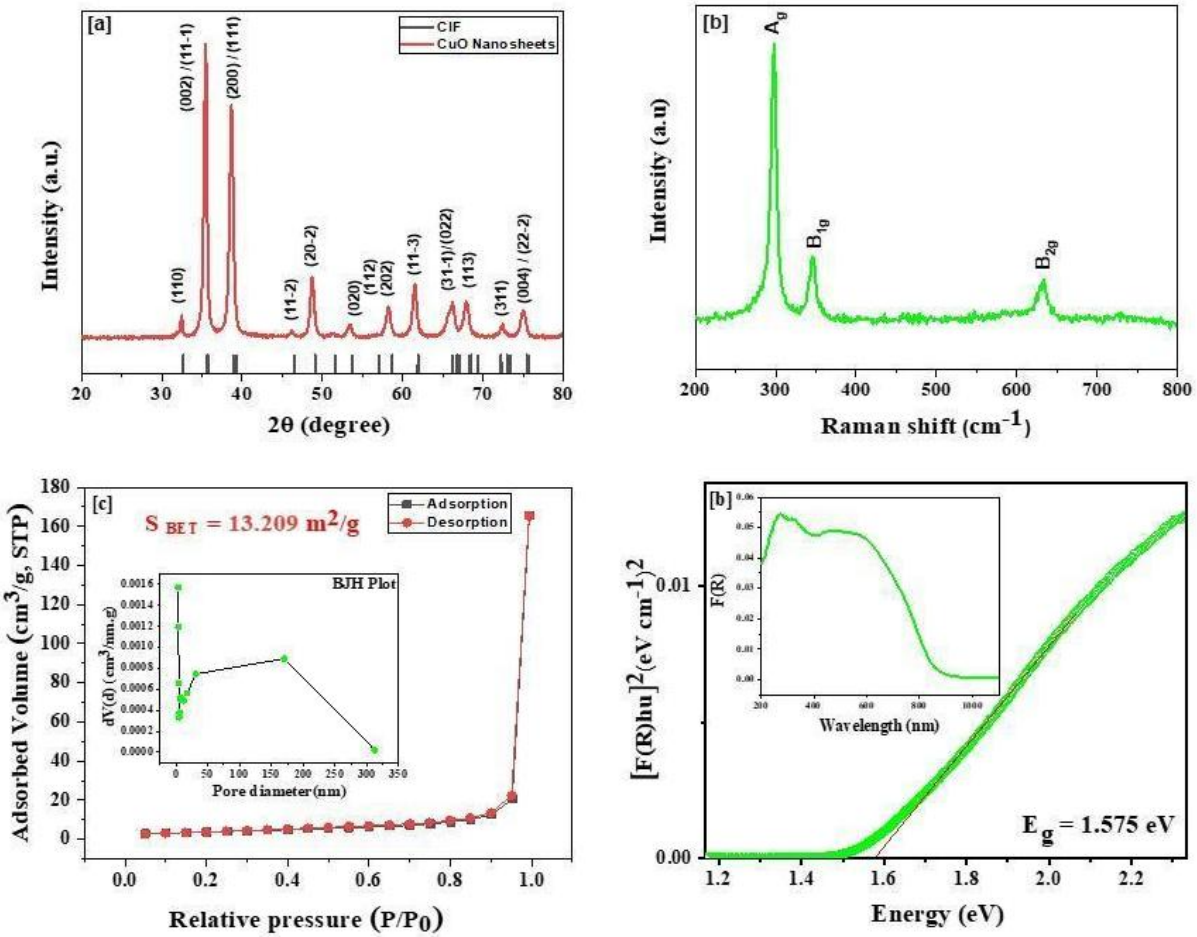


Figure 4.3.1: The monoclinic structure and phonon modes of the CuO nanosheets were investigated from (a) the XRD pattern and (b) the Raman spectra. The pore size of the nanosheets was estimated at ~3.42 nm from the (c) BET adsorption-desorption isotherms, with the inset representing the corresponding BJH pore size distribution. The band gap was estimated at ~ 1.575 eV using the (d) tauc plot of the DRS spectra (inset).

The morphologies of the as-prepared sample were studied by FESEM and High-Resolution Transmission Electron Microscopy (HRTEM) [Figure 4.3.2]. The FESEM image revealed a sheet-like morphology with an average width of ~580 nm and an average length of 1240 nm. Nanosheet morphology has been confirmed from the TEM-bright field image shown in Figure 4.3.2 (b). Figure 4.3.2(c) shows the HRTEM phase contrast image of the nanosheets, which exhibits distinct lattice spacings of 0.273 nm, corresponding to the (110) plane of CuO (ICSD 98-006-9757). The selected area electron diffraction pattern in Figure 4.2.2 (d) shows the polycrystalline nature of CuO nanosheets with evidence of reflections from the (110), (002),

(20-2), (022), (220), (203), and (22-2) planes. The elemental composition extracted from EDX spectroscopy revealed three intense characteristic peaks for Cu at 1, 8.1, and 9 keV and a peak at 0.6 keV for O [Table 4.3.1]. A weak peak, other than those belonging to Cu and O, can be attributed to C at 0.35 keV, most likely from the carbon-coated copper grid used to hold the sample [Figure 4.3.3]. The absence of any other elements further adds to the claim of phase purity of the nanosheets.

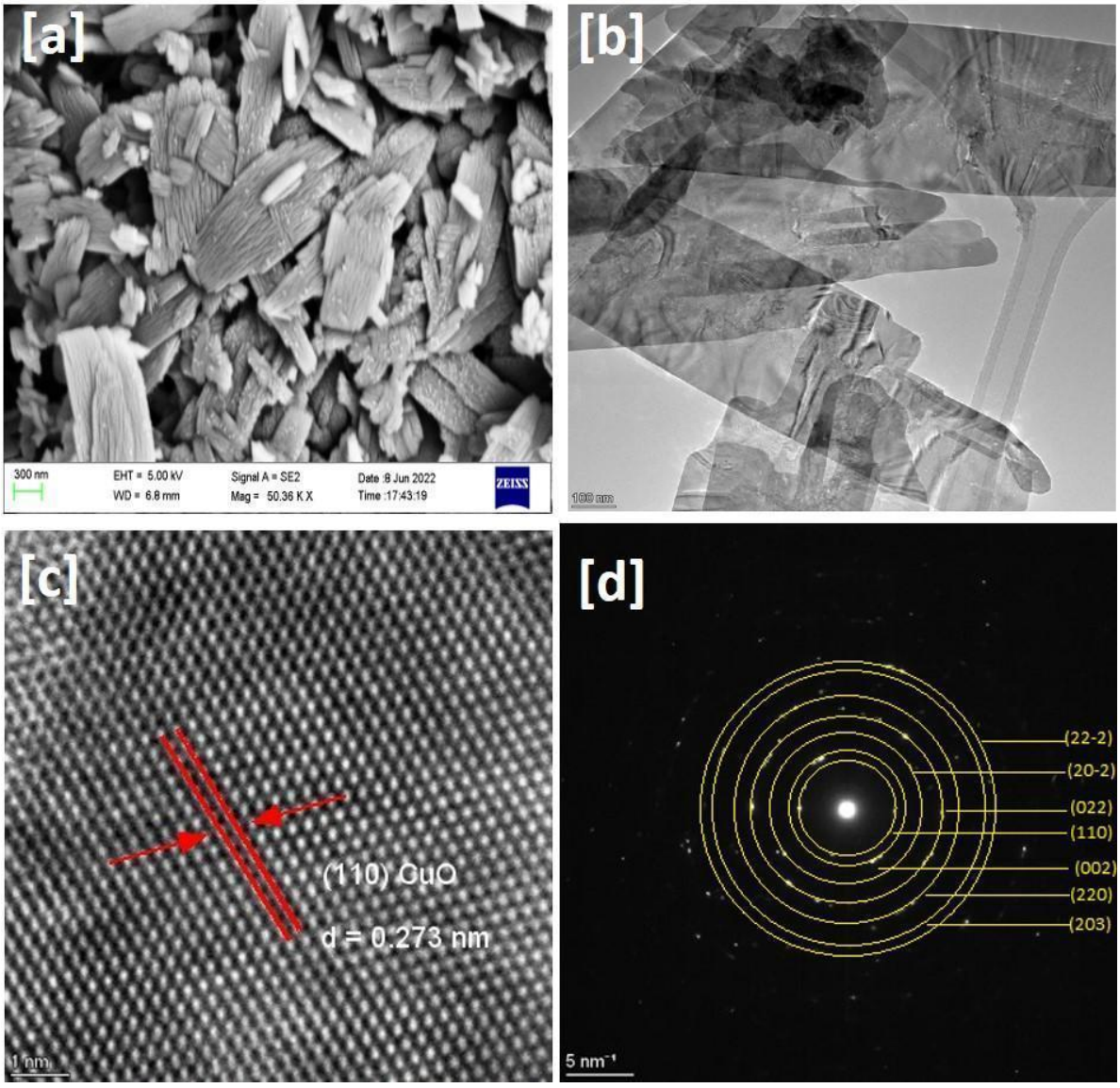


Figure 4.3.2: The nanosheet morphology with a width of ~580 nm and a length of ~1240 nm was estimated using (a) FESEM. The (b, c) TEM bright field micrograph confirms a similar morphology. In contrast (c), the corresponding HRTEM image confirms the crystalline nature of the samples, with a lattice spacing of 0.273 nm corresponding to a CuO 110 plane. (d) The

SAED pattern further confirms the presence of the CuO phase.

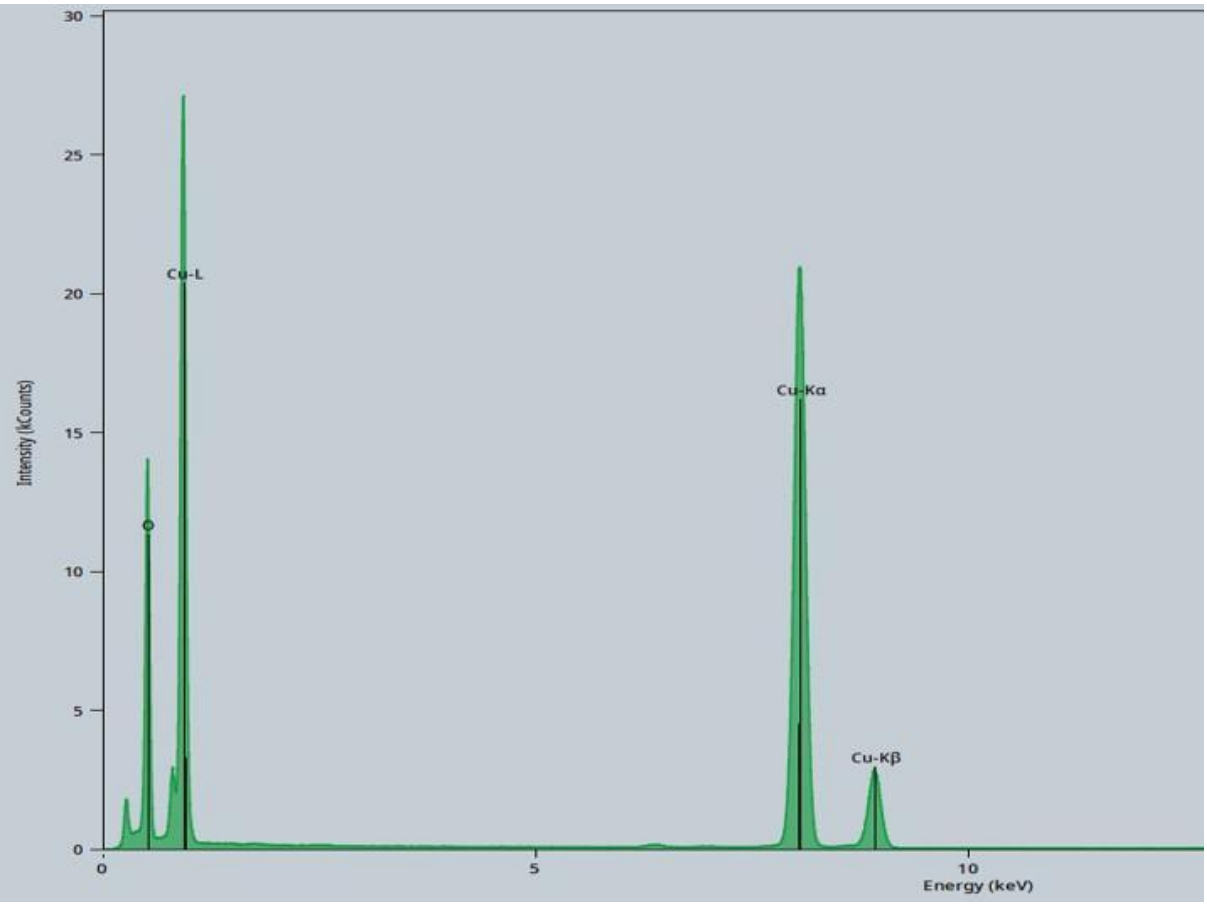


Figure 4.3.3: The EDX Analysis of the CuO nanosheets obtained from TEM.

Table 4.3.1: summarizes the data obtained from the EDX analysis, which indicates the elemental composition of the prepared nanosheets.

Atomic number (Z)	Element	Family	Atomic fraction %	Weight fraction %
8	O	K	40.35	14.55

29	Cu	K	59.65	85.45

From Table 4.3.1, the atomic fraction of Cu is higher compared to that of O, which may suggest slight oxygen deficiency, although EDX quantification of light elements is semi-quantitative; this observation is therefore treated as indicative.

Dynamic Light Scattering [DLS] is a technique that primarily measures three important parameters of the samples: zeta potential (V_ξ) (ξ-potential), hydrodynamic size (D_h) [HDS], and polydispersity index (PDI). D_h is the effective size of the particles inside a specific fluid medium. The V_ξ is an estimate of the surface charge of the colloid, while the PDI is a measure of the size distribution in the given fluid.

The zeta potential (V_ξ) (ξ-potential) is a voltage generated at the slipping plane, where the slipping plane is the plane in between the fluid layer that is electrostatically attached to the colloid and the external free fluid. The value of V_ξ was positive for the as-synthesized nanosheets, which is 30 ± 0.11 mV, which is sufficient to have good colloidal stability inside the solution [130]. V_ξ can also be expressed as the average value of the surface charges, which is the resultant of all surface terminations of the nanoparticles. A positive zeta potential indicates a net positive surface charge under the measurement conditions, consistent with good colloidal stability. D_h is the effective spherical size that has the same translational diffusion coefficient as the particle itself. The value of D_h was found to be 1321 ± 0.66 nm, which is consistent with the result obtained from FESEM (average length = 1240 nm), and the PDI value was found to be 0.538. This confirms the mid-range polydispersity nature of the sample [131].

4.4. Photocatalytic Performance and Kinetics

The general trend for checking a photocatalytic activity is to use a high-power (250~300 W) UV/xenon lamp or direct sunlight. The lamp is expensive and consumes considerable power. In this work, an attempt was made to check the photocatalytic activity of the nanosheets to degrade textile wastewater in the presence of a normal, cheap, commercially available, low-pressure mercury-vapor discharge UV lamp that emits shortwave UV radiation at 253.7 nm (Philips TUV 11W PLS). Also, direct sunlight illumination was used as a separate experiment. MB and RhB dyes are frequently used in industries. The photocatalytic activity of these dyes

was performed with CuO nanosheets as catalysts.

4.4.1. Photocatalysis with commercially available 11 W UV light

Several factors influence photocatalytic activity, including the wavelength and intensity of incident light, reactant concentration, catalyst loading, and pH [168]. It was found that, in addition to these parameters, the reaction temperature is also of prime importance. It is interesting to note that the reaction temperature increases with increasing light irradiation time due to high-power light illumination. Accordingly, several factors influencing photocatalytic activity were systematically investigated, including catalyst loading, the addition of external oxidizing agents, and temperature. Among these parameters, the reaction temperature is of prime importance. Accordingly, the temperature of the reaction medium was optimized first. Subsequently, the effect of CuO nanosheet concentration on photocatalytic degradation was examined.

Effect of Temperature on Dye Degradation

Under high-power irradiation, the solution temperature can increase with irradiation time [169]. At the same time, higher temperatures seem to increase the photocatalytic degradation of organic dyes in water [133]. However, in this study, a simple 11 W light was used, which did not increase the temperature. Hence, it was necessary to separate the effects of light and temperature in the study, which remains overlooked. Hence, external heating was performed while irradiating the light simultaneously to distinguish the effect of light alone from the thermal effect.

Reports are claiming that by elevating the reaction temperature from RT to 80°C, the photocatalytic activity increases. This may be due to the improvement of interfacial charge transfer from solid to liquid [170]. However, a reaction temperature greater than 80°C promotes the recombination of charge carriers and disfavours the adsorption of organic compounds on the catalyst surface [171]. A reaction temperature below 80°C favours adsorption. On the other hand, at lower temperatures, at 0°C, an increase in the apparent activation energy is observed [172]. Therefore, the temperature range of 20 to 80°C has been regarded in the literature as the optimal temperature for effective photo-mineralization of organic content. Also, the thermodynamic rate of reaction increases with temperature due to the increased number of collisions between the reactive species.

To perform temperature-dependent photocatalysis, the temperature of the experimental setup was stabilized at three different temperatures: 25°C, 35°C, and 45°C. Maximum dye degradation was obtained at a temperature of 45°C. These temperatures have been intentionally chosen to consider only naturally obtainable temperatures on the Earth's surface. Above 45°C, the increased temperature may favour the increased charge recombination rate and lead to more thermodynamically affected processes, thereby decreasing the photocatalytic activity. Moreover, these temperatures are not investigated to avoid unrealistic, unnatural conditions. High temperatures of up to 45°C are sometimes carried by the wastewater from the textile industry itself and can therefore be used as a self-treatment process [137].

At each fixed temperature, the photocatalytic activity was observed, and the corresponding photodegradation was measured [Figure 4.4.1]. For all temperatures, the change in relative concentration due to photodegradation followed first-order chemical kinetics, and the corresponding rate constants and degradation percentages were calculated. The photodegradation of MB dye without a photocatalyst in dark and UV light illumination was negligible, i.e., 2.8%, 5.6%, and 6.5% at 25°C, 35°C, and 45°C, respectively, and it increased significantly with the presence of a photocatalyst as well as the addition of the extra oxidizing agent H_2O_2 and UV light, as can be seen from Figure 4.4.1. The adsorptive capacity of the photocatalyst at different temperatures was calculated to be 19% at 25°C, 15% at 35°C, and 7% at 45°C, respectively [Fig 4.4.1], held in dark conditions for the first 60 min. Thus, the adsorption of dye on the surface of the photocatalyst at higher temperatures seems to be less compared to room temperature, which is in good agreement with the other literature reported elsewhere [133], [170].

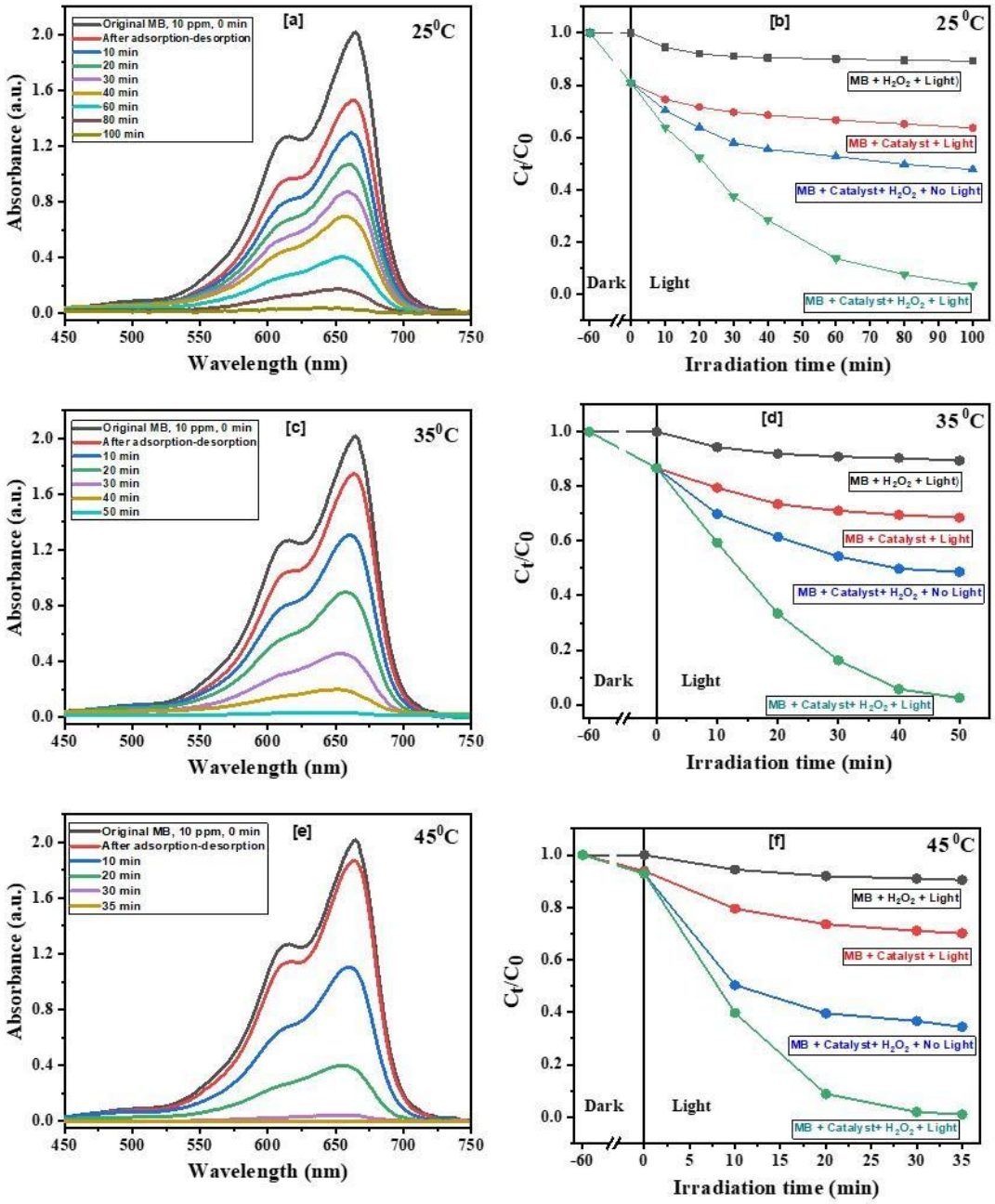


Figure 4.4.1: (Left Panel) Photocatalytic properties of the CuO nanosheets (with catalyst concentration = 1 mg/mL and H_2O_2 concentration = 50 mM) revealed from the reduction of absorbance from the MB dye with time at different temperatures at (a) 25°C, (c) 35°C, and (e) 45°C (Right Panel) Relative concentration change with UV-irradiation time at (b) 25°C, (d) 35°C, and (f) 45°C for four different situations: MB + H_2O_2 + Light (black), MB + Catalyst + Light (red), MB + Catalyst + H_2O_2 + No Light (blue), and MB + Catalyst + H_2O_2 + Light (green), revealing the fastest degradation for the MB + Catalyst + H_2O_2 + Light combination.

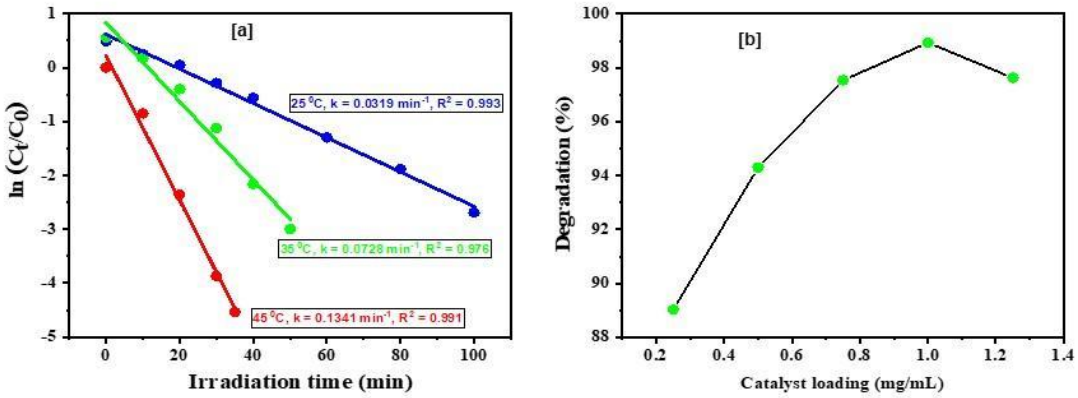


Figure 4.4.2: (a) Rate of change of concentration of MB dye with time for different temperatures, revealing faster kapp with increasing temperature. (b) CuO nanosheet concentration dependence of the degradation process at 45°C and H_2O_2 concentration = 50 mM, revealing the highest degradation at 1 mg/mL.

Effect of Catalyst Loading

After optimizing the temperature of the reaction medium, the concentration of the CuO nanosheets was varied to see the photocatalytic degradation effect. For this, the photocatalytic degradation was checked simultaneously for different concentrations of ~ 0.25 mg/mL, 0.5 mg/mL, 0.75 mg/mL, 0.1 mg/mL, and 1.25 mg/mL at 45°C. The time of loading was approximately 35 minutes of light irradiation [Figure 4.4.2(b)]. As the amount of catalyst loading increases from 0.25 mg/mL to 1 mg/mL, the degradation of MB increases from 89% to 99%, then decreases to 97% for the 1.25 mg/mL catalyst. The increasing dye photodegradation with increasing catalyst amounts is a feature of heterogeneous photocatalysis as the number of collisions between reactants increases [138]. As the number of active sites on the photocatalyst surface increases, the formation of OH radicals also increases, thereby enhancing the degradation of dyes within the solution. Beyond a certain amount of catalyst, the solution becomes turbid, which further blocks the radiation needed for the reaction to proceed. Therefore, the degradation percentage starts decreasing [139]. The optimum concentration has thus been set at 1 mg/mL.

Photocatalytic activity with Rhodamine B

Similarly, considering all the optimized conditions, i.e., catalyst concentration = 1 mg/mL and reaction medium temperature = 45°C, the photocatalytic performance of the as-synthesized nanosheets was also evaluated using Rhodamine B dye. The adsorption percentage was about 3.5%, which is lower compared to MB, i.e., 7% at 45°C. This can be correlated to the surface charge of the RhB, which interacts with the nanosheets. Figure 4.4.3 shows the absorbance and relative concentration change for RhB dye with irradiation time. The total degradation percentage and calculated rate constants at different reaction conditions for MB, as well as RhB, are presented in Table 4.4.1.

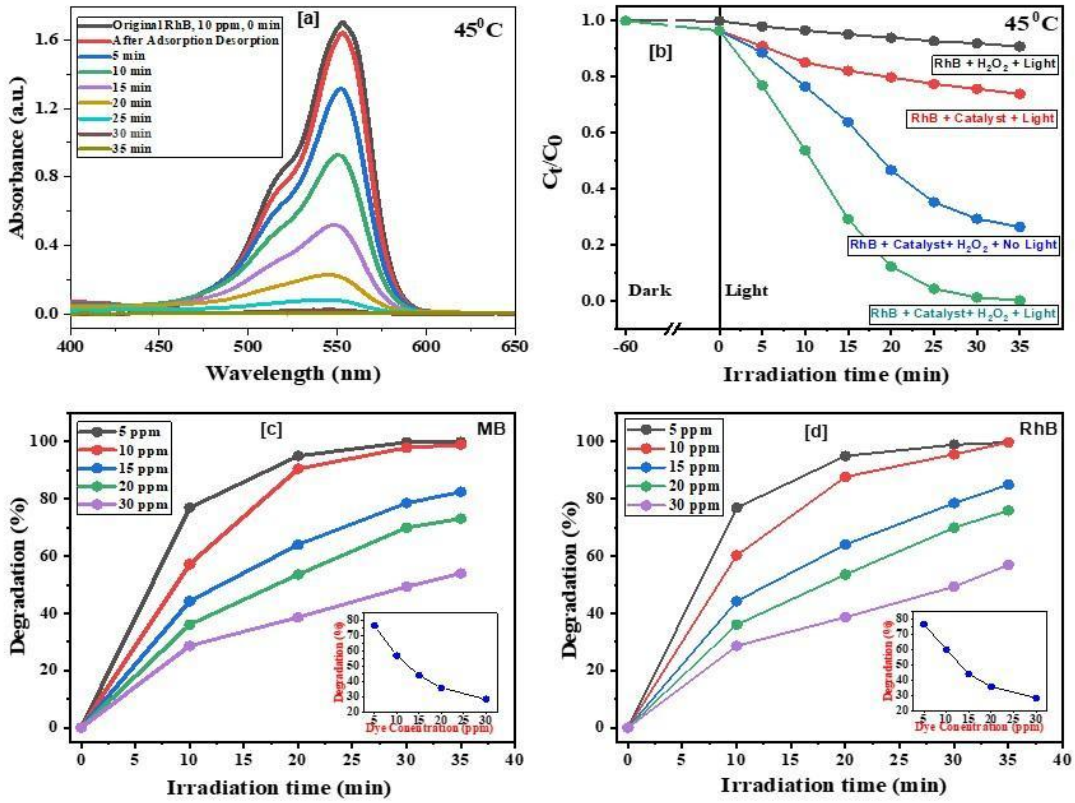


Figure 4.4.3: (a) Photocatalytic properties of the CuO nanosheets (with catalyst concentration = 1 mg/mL and H_2O_2 concentration = 50 mM) revealed from the reduction of absorbance from the RhB dye with time at 45°C. (b) Relative concentration change with UV-irradiation time at 45°C for four different situations: RhB + H_2O_2 + Light (black), RhB + Catalyst + Light (red), RhB + Catalyst + H_2O_2 + No Light (blue), and RhB + Catalyst + H_2O_2 + Light (green), revealing the fastest degradation for the RhB + Catalyst + H_2O_2 + Light combination. (c, d) Effect of pollutant (organic dye) concentration on photocatalytic degradation, where the insets

show the degradation percentage with varying concentrations of dye for 10 min of light illumination for MB and RhB, respectively.

Table 4.4.1: Irradiation time, degradation percentage, calculated rate constants, and linear correlation coefficients at different temperatures for MB and RhB dyes.

Temperature (°C)	*Reaction Condition*	*Time (min)*	*Degradation (%)*	*Rate constants (min^{-1})*	*R^2*
25	MB + Light	100	2.84	0.00037	0.99
	MB + H_2O_2 + Light	100	10.8	0.0028	0.98
	MB + Catalyst + Light	100	36.4	0.0045	0.99
	MB + Catalyst + H_2O_2 + No Light	100	52.3	0.0092	0.99
	MB + Catalyst + H_2O_2 + Light	100	96.6	0.0319	0.99
35	MB + Light	50	5.6	0.0017	0.98
	MB + H_2O_2 + Light	50	10.5	0.0036	0.99
	MB + Catalyst + Light	50	31.4	0.0068	0.99
	MB + Catalyst + H_2O_2 + No Light	50	51.3	0.0189	0.99
	MB + Catalyst + H_2O_2 + Light	50	97.5	0.0728	0.99
45	MB + Light	35	7	0.0026	0.98

	MB + H_2O_2 + Light	35	9.5	0.0045	0.99
	MB + Catalyst + Light	35	29.9	0.0116	0.99
	MB + Catalyst + H_2O_2 + No Light	35	65.6	0.0408	0.99
	MB + Catalyst + H_2O_2 + Light	35	99	0.1341	0.99
	RhB + Light	35	6.8	0.0026	0.99
	RhB + H_2O_2 + Light	35	9.2	0.0028	0.99
	RhB + Catalyst + Light	35	26.1	0.0109	0.99
	RhB + Catalyst + H_2O_2 + No Light	35	73.6	0.0299	0.99
	RhB + Catalyst + H_2O_2 + Light	35	99.8	0.0943	0.99

Effect of Pollutant (Organic Dye) Concentration

The initial dye concentration plays a crucial role in determining the overall degradation efficiency of the photocatalyst. Usually, at higher dye concentrations, lower degradation has been reported [173]. This is due to the formation of several layers of adsorbed dye molecules on the catalyst surface. This inhibits the photoreaction since there was no direct contact between the catalyst and the light. Hence, ROS could not be generated. Moreover, the pH of the dye solution changed due to alterations in the dye concentration. This is crucial for dye removal. Anionic dyes performed better during photodegradation at lower pH values, while higher pH values were required for cationic dyes [174].

The effect of pollutant concentration was studied at different dye concentrations, ranging from 5 ppm to 30 ppm, for both MB and RhB, while keeping all other parameters constant: reaction temperature (45°C), catalyst concentration (1 mg/mL), and total irradiation time (35 min). The variation in photodegradation effectiveness as a function of dye concentration is evident in Figure 4.4.1.3(c, d). The photodegradation efficiency decreased by around 46% for MB dyes and 42% for RhB dyes as the dye concentration increased from 5 to 30 ppm.

4.4.2. Photocatalysis under Direct Sunlight

To make this methodology more practical and usable with respect to the most abundant energy available on the Earth's surface, the photocatalytic activity was carried out under direct sunlight without controlling the reaction temperature. The temperature of the surroundings was between 30°C and 35°C, with bright sunlight conditions (measured illuminance ~6×10^5 lx), representative of strong outdoor illumination. For this experiment, all parameters were kept constant, i.e., the initial dye concentration was set at 10 ppm (10 mg/L), and the catalyst loading was 1 mg/mL. The photocatalytic performance was taken for both dyes. Almost both dyes degraded within 70 minutes under natural sunlight without controlling the outside temperature [Figure 4.4.4]. Table 4.4.2 summarizes all the obtained results from photocatalysis under natural sunlight.

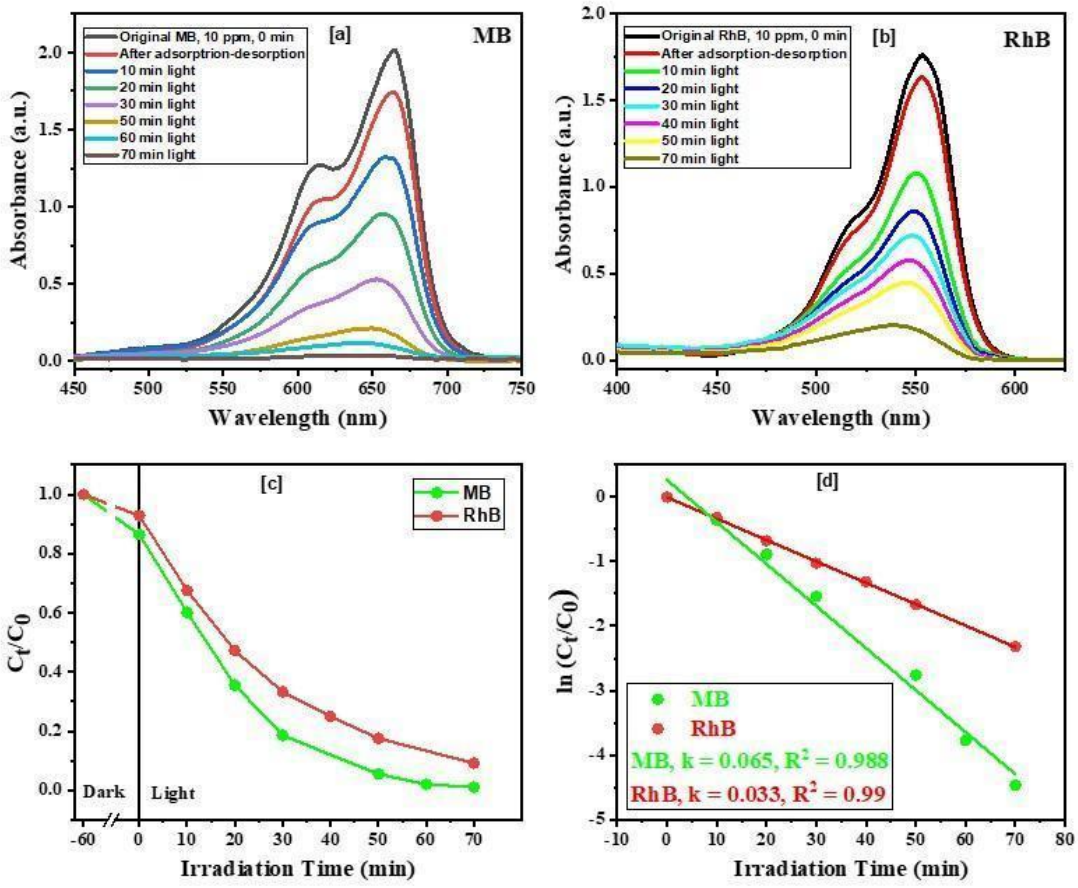


Figure 4.4.4: (Top Panel) Photocatalytic properties of the CuO nanosheets (with catalyst concentration = 1 mg/mL and H_2O_2 concentration = 50 mM) were revealed from the reduction

of absorbance from the (a) MB and (b) RhB dye with time at ambient conditions. (Bottom Panel) Relative concentration changes with natural sunlight-irradiation at ambient conditions for Dye catalyst, H_2O_2, and light, revealing (c) faster degradation for MB (green) than RhB (red) and (d) faster rate constant for MB (green) than RhB (red)

Table 4.4.2: Degradation percentage, rate constants, and corresponding values of R^2 under direct sunlight irradiation of 70 min for both dyes.

Name of the Dyes	*Degradation percentage (%)*	*Rate constants (min^{-1})*	*R^2*
MB	99	0.065	0.988
RhB	90	0.033	0.99

4.5. Photo-Fenton-Like Degradation Mechanism

The detailed mechanism of dye degradation has already been explained in detail in the literature [175], [176]. The mechanism can be schematically explained as follows [Figure 4.5.1].

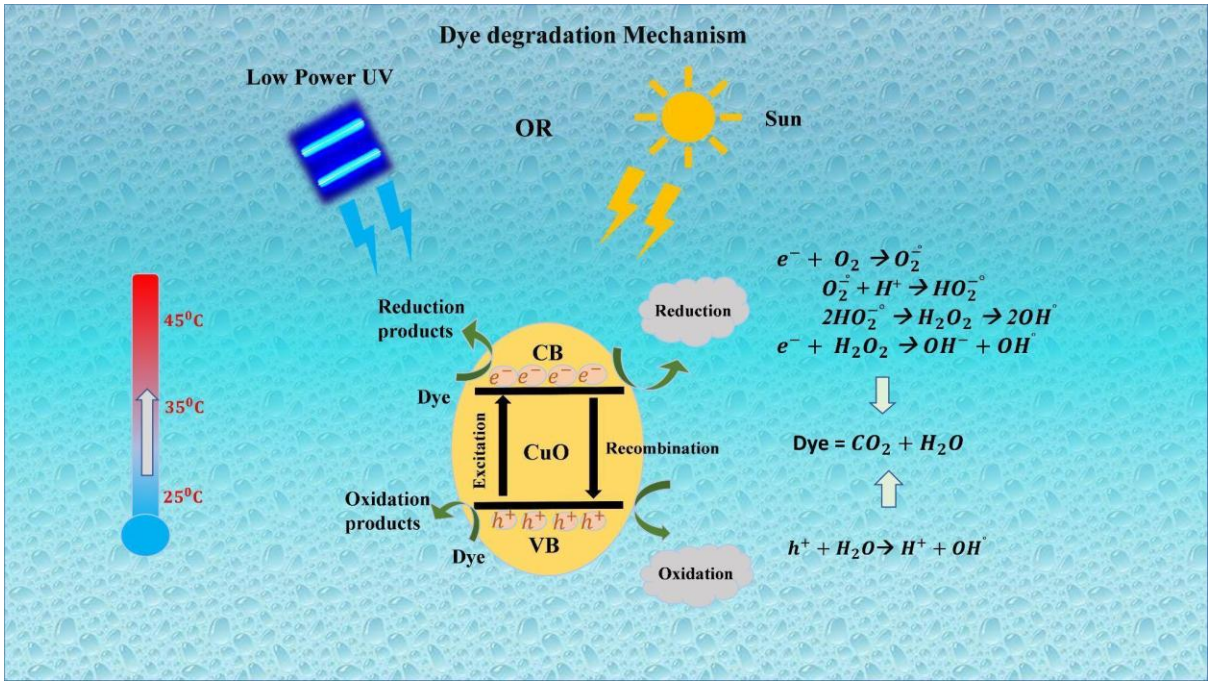


Figure 4.5.1: Mechanism of dye degradation involving photon-irradiated e-h pair generation and subsequent radical formation during oxidation and reduction processes.

The mechanism behind increased photodegradation at increased temperatures is an important aspect to be investigated. Two important factors may contribute to the increase in chemical reaction rate with rising temperature. The apparent rate constant of the reaction, k_{app} follows an Arrhenius equation: $k_{app} = A.\ exp(-E_A/RT)$, where A is the Arrhenius factor, E_A is the activation energy, $R = 8.314$ J/K mol is the ideal gas constant, and T is the temperature (K). Taking natural logarithms on both sides, the equation can be rewritten as a straight-line equation between k_{app} and $1/T$ as $ln\ k_{app} = lnA - E_A/RT$. This is an empirical relationship widely used in literature. On the other hand, the Eyring Equation, a part of the Transition State Theory, is based on collision theory and involves a statistical approach to relate k_{app} and T. The Eyring equation [97] can be expressed as $k_{app} = A_t (k_B T/h).\ exp\ (-\Delta^{\ddagger}G/RT)$, where k_B is the Boltzmann constant, h is Planck's constant, A_t is the transmission coefficient, which is the probability that a chemical reaction takes place, which can be taken to be 1 (for surface reactions), and $\Delta^{\ddagger}G$ is the free energy of activation. The equation can be rewritten as a straight-line equation between $ln\ (k_{app}/T)$ *versus* $1000/T$, as $ln(k_{app}/T) = ln(k_B/h) - \Delta^{\ddagger}G/RT$. The value $\Delta^{\ddagger}G = \Delta^{\ddagger}H^o - T\Delta^{\ddagger}S^0$, where $\Delta^{\ddagger}H^o$ is the change in standard enthalpy of activation, and $\Delta^{\ddagger}S^0$ is the change in standard entropy of activation. Figure 4.5.2 shows the Arrhenius plot and the Eyring plot, and Table 4.5.1

summarizes all the thermodynamic parameters associated with both equations. The increasing value of k_{app} and the positive values of $\Delta^{\ddagger}H^{o}$ with increasing temperature indicate thermally activated kinetics. Such behaviour is consistent with a kinetically controlled interfacial process rather than adsorption-limited degradation [155]. It can also be seen that the positive values of the standard Gibbs free energy change of activation ($\Delta^{\ddagger}G° > 0$) increased with an increase in experimental temperature. The increase in $\Delta^{\ddagger}G°$ with temperature reflects the free-energy barrier associated with the kinetically controlling step under the present operating conditions (fixed photon flux and composition). This parameter should not be interpreted as the thermodynamic spontaneity of the overall degradation. Instead, it indicates that the observed kinetics are governed by a temperature-sensitive interfacial reaction/charge-transfer step, while adsorption becomes weaker at higher temperatures, consistent with the reduced dark adsorption fraction. This opposing trend of reduced dark adsorption but faster light-driven kinetics supports a mechanism where temperature primarily accelerates charge-carrier transport/detrapping and interfacial reaction steps, rather than improving surface coverage. Hence, an increase in temperature helps the photocatalytic reactions compete more efficiently with electron-hole pair recombination. So, the photocatalytic activity of the sample increased with increasing temperature.

The use of hydrogen peroxide (H_2O_2) seemed beneficial. With the support of H_2O_2 and CuO nanosheets, the reaction mechanism of the fast degradation of MB and RhB without using any external source of irradiation with photons proceeds according to the following [165], [177] chemical processes:

Step 1: $[Cu\ (II)] + H_2O_2 \rightleftharpoons [Cu\ (II)] \ldots .H_2O_2 \rightarrow [Cu(I)] + \bullet OOH + H^+$

$[Cu(I)] + H_2O_2 \rightleftharpoons [Cu(I)] \ldots .H_2O_2 \rightarrow [Cu\ (II)] + \bullet OH + HO^-$

Step 2: $\bullet OOH + H_2O_2 \rightarrow H_2O + \bullet OH + O_2$

$\bullet OH + H_2O_2 \rightarrow H_2O + \bullet OOH$

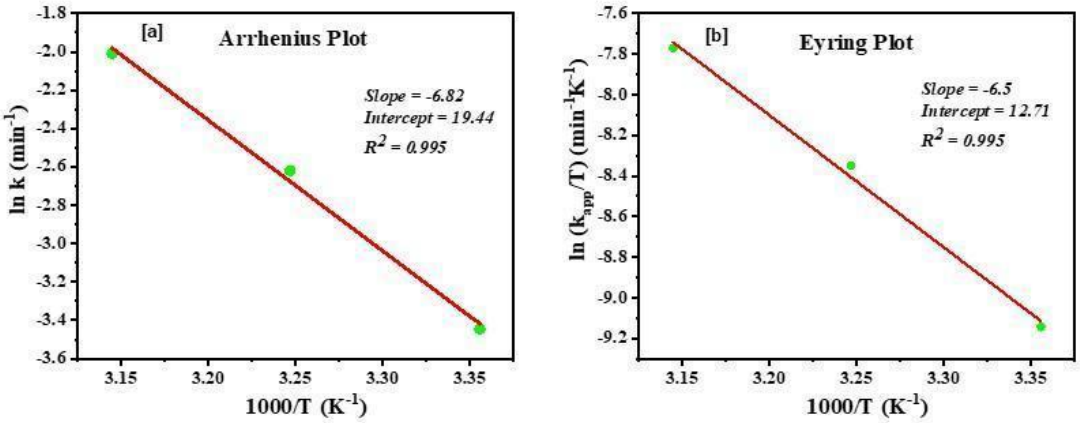


Figure 4.5.2: (a, b) shows Arrhenius plots and Eyring plots for the chemical reactions.

Table 4.5.1: All the thermodynamic parameters associated with Arrhenius's Theory and Transition State Theory of the chemical reaction with copper oxide nanosheets.

				Arrhenius Theory			**Transition State Theory**				
Photocatalyst	**T (K)**	k_{app} **(min^{-1})**	**ln (k_{app}/T) (Min^{-1} K^{-1})**	**A (× 10^7) (min^{-1})**	**E_a (kJ/mol.)**	**R^2**	**$\Delta^{\ddagger}H^{o}$ (kJ/mol.)**	**$\Delta^{\ddagger}S^{o}$ (kJ/mol. K)**	**$\Delta^{\ddagger}G^{o}$ (kJ/mol.)**	**A (× 10^11) (min^{-1})**	**R^2**

CuO Nano sheet	298	0.032	-9.14	27.7	56.7	0.995	54.04	-0.06	71	1.03	0.995
	308	0.073	-8.35						71.6	1.06	
	318	0.134	-7.77						72.2	1.1	

Scavenger test

The scavenger test is typically used to identify the types of radicals that play a crucial role in the photocatalytic degradation of organic dyes. Different chemicals, such as isopropanol (IPA), ammonium oxalate (AO), and p-benzoquinone (BQ), were used to trap hydroxyl radicals, holes, and superoxide radicals, respectively [158]. MB and RhB dyes are degraded by chemical reactions involving electrons and holes, as well as hydroxyl and superoxide radicals [178]. According to the literature, the suggested concentration of the above chemicals has already been optimized. The optimized concentrations of chemicals were taken from the literature and are as follows: IPA (60 µL/mL), AO (0.124 mg/mL), and p-BQ (0.108 mg/mL). The degradation percentages were found to be the least (17% and 18% for RhB and MB, respectively) in the presence of the hydroxyl radical scavenger, IPA. The presence of IPA reduces the concentration of the hydroxyl radical, which could have contributed to the degradation process, thereby confirming the important role of this radical in the degradation process. The degradation was considerably high for the superoxide scavenger, p-BQ, with a degradation of 91% for RhB and 89.6% for MB. The most degradation was observed for the hole scavenger, AO, with degradation of 95% for RhB and 97% for MB [Figure 4.5.3]. A similar logic reveals the least effectiveness of the superoxide radical in the degradation of RhB and MB dyes.

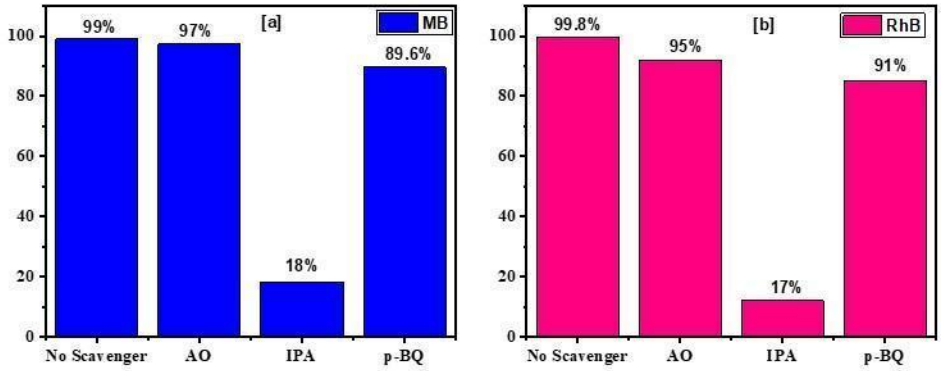


Figure 4.5.3: (a, b) Scavenger test of the nanosheets for MB and RhB dye, confirming the role of different reactive oxygen species that contribute to the photocatalytic process, respectively.

4.6. Stability, Reusability, and Practical Implications

Three cycles of the degradation process were run to ensure the stability and reusability of the nanosheets for MB and RhB dyes. After each cycle of photocatalytic degradation, the samples were collected by centrifuging, washed with a mixture of distilled water and ethanol, and then dried in a hot air microwave oven. The samples were reused for the photocatalytic degradation of the dye again. All experimental conditions, such as temperature and catalyst amount, were kept constant. Figure 4.6.1 (a, b) shows the reusability of the prepared nanosheets for the two dyes. The phase stability can be observed from the XRD pattern [Figure 4.6.2] of the sample after three times of repeated use. The photocatalytic efficiency of the prepared sample was observed to decrease nominally for the next consecutive cycles from 99% to ~98%. The small reduction in the photocatalytic properties is probably due to the loss of nanomaterials during washing and the filtering process.

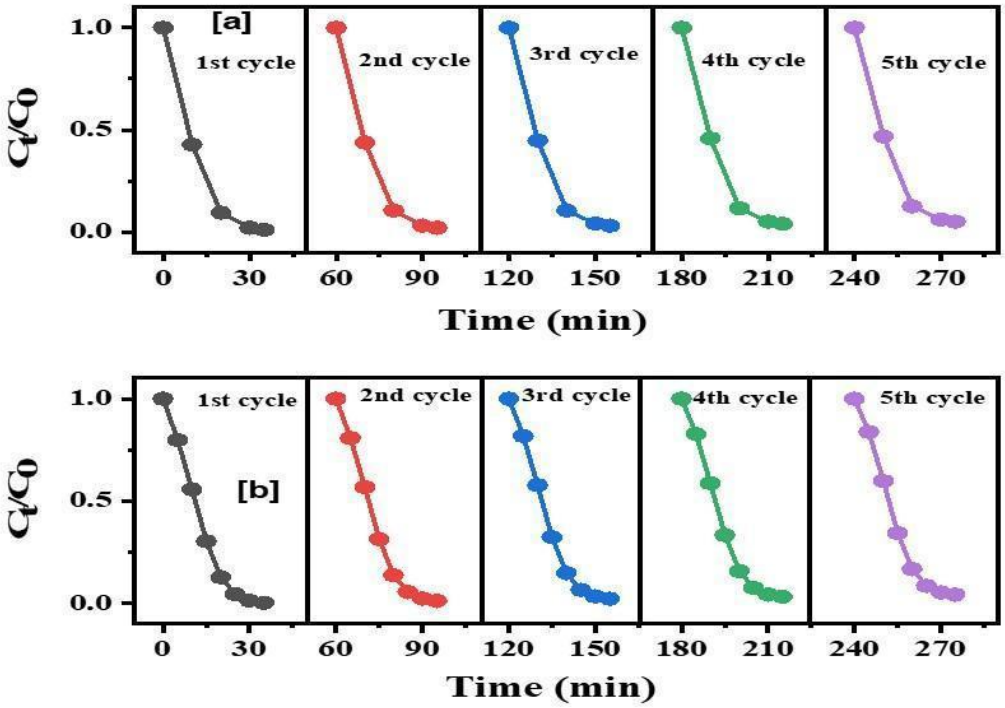


Figure 4.6.1: (a, b) Assurance of reusability of the nanosheets for MB and RhB dye, respectively.

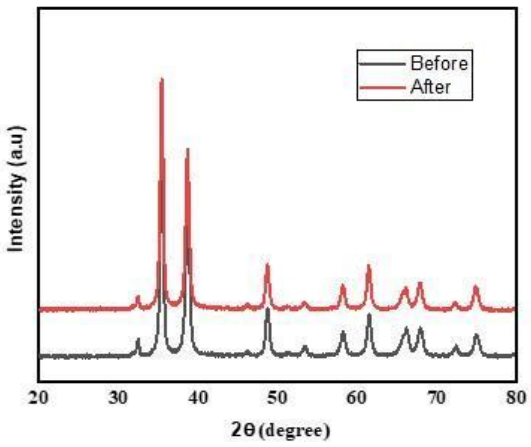


Figure 4.6.2: XRD of the CuO Nanosheets before and after Photocatalytic Degradation.

A vital aspect of this study is the stability and the toxicity of the byproducts of the degradation process. To study these factors, the photodegraded filtrate was subjected to ICP-OES detection for Cu leaching. The leaching amounts of Cu were found to be 0.668 ppm, which is a very low number in terms of toxicity. Hence, almost no difference in secondary pollution was observed, which could be attributed to leaching and related toxicity. The steady reusability and recoverable percentage of the recycled samples, along with the non-toxic nature of the materials, further indicate the stability of the photocatalyst even after repeated use.

The potential of the CuO nanosheets as a promising candidate for sustainable environmental application can be seen by comparing the photodegradation results with the existing literature [Table 4.6.1]

Table 4.6.1: A comparative study of the photocatalytic properties of CuO nanostructures for the degradation of various organic dyes, including the present study.

Surface Morphology	Synthesis Method	Reaction Condition	Temp.	Degradation (%)	Rate Constant(min^{-1})	Ref.
Leaf-like CuO NS	Hydrothermal	UV light, MB, MV, 15 ppm 0.05 mg/mL catalyst	RT RT	89%, 3 h 96%, 3 h	NM	[179]
CuO 3D flower-like NS	Hydrothermal	40 W tungsten lamp, MO, 10 ppm 0.16 mg/mL	RT	96.2%, 50 min	NM	[180]

CuO Spherical NPs	Chemical Precipitation	UV light, MB, 10 ppm 0.5 mg/mL	RT	56%, 1 h	0.00937	[181]
CuO/ZnO NPs composite	incipient wetness impregnation	400 W UV lamp MB, MO (Conc. Not mentioned)	45 °C	99%, 15 min 99%, 75 min	0.288 0.060	[165]
CuO Nanosheets	Hydrothermal	11 W UV light, MB, RhB, 10 ppm 1 mg/mL	45 °C	99% in 35 min 99.8% in 35 min	0.1341 0.0943	This work
CuO nanosheets	Hydrothermal	Direct Sunlight, MB, RhB, 10 ppm 1 mg/mL	Ambient Temp.	99%, 70 min 90%, 70 min	0.065 0.033	This work

*Not mentioned = NM, NS = Nanostructures, MB = Methylene Blue, MV = Methylene violet, MO = Methyl orange, RhB = Rhodamine B

4.7. Chapter Summary

This chapter systematically examined the role of reaction temperature in governing the photocatalytic degradation of organic pollutants using morphology-engineered, undoped CuO nanosheets as a model system. Building on the temperature-dependent trends observed in the Al^{3+}-doped photo-Fenton systems discussed in Chapter 3, the present study was designed to

decouple thermal effects from dopant-induced electronic and redox contributions.

Phase-pure monoclinic CuO nanosheets were synthesized via a facile hydrothermal route and exhibited a two-dimensional morphology, mesoporous/agglomeration-related porosity surface structure, moderate band gap, and good colloidal stability-features that collectively enabled efficient photocatalytic activity under low-power irradiation. Photocatalytic degradation of methylene blue and rhodamine B under 11 W UV light and direct natural sunlight followed pseudo-first-order kinetics, with reaction rates showing a strong and reproducible dependence on temperature within environmentally relevant limits.

Kinetic analysis using Arrhenius and transition-state models revealed thermally activated kinetics, with elevated temperatures facilitating faster interfacial charge transfer/ROS generation and improved utilization of photogenerated carriers. Radical scavenging experiments identified hydroxyl radicals as the dominant reactive species, confirming temperature-assisted reactive oxygen species generation as a key mechanistic factor. The CuO nanosheets demonstrated excellent stability and reusability with negligible copper leaching, underscoring their suitability for sustainable wastewater treatment.

Although heterojunction engineering can improve charge separation in low-bandgap CuO-based photocatalysts, the present chapter intentionally employs single-phase CuO nanosheets to isolate the role of temperature on photocatalytic/photo-Fenton-like degradation kinetics. Introducing a heterojunction would add additional interfacial charge-transfer and band-alignment effects, making it difficult to decouple the intrinsic temperature-assisted kinetic contribution of CuO.

The observed degradation behavior is consistent with a photocatalytic/photo-Fenton-like advanced oxidation pathway; however, direct identification of degradation intermediates and mineralization products was beyond the scope of the present work.

Overall, this chapter provides mechanistic clarity on temperature-assisted photocatalysis in CuO-based systems and establishes a structure–temperature–reactivity framework that rationalizes and supports the enhanced performance observed in doped photo-Fenton catalysts. The insights gained here serve as a mechanistic bridge between morphology-driven photocatalysis and compositionally engineered CuO systems, which are explored in subsequent chapters. Having isolated morphology and temperature-assisted transport effects in an undoped

system, the subsequent chapter introduces a redox-active dopant to evaluate whether catalytic enhancement arises from fundamentally altered redox accessibility rather than kinetic acceleration alone.

Chapter 5 Redox-Active Fe-Substituted CuO: Photo-Fenton-Like Oxidation and Reaction-Pathway Switching

Abstract: *Building upon the temperature-dependent photo-Fenton-like degradation behaviour of pure CuO nanosheets (Chapter 4) and the defect-engineering framework established for Al^{3+}-substituted CuO (Chapter 3), this chapter investigates the role of redox-active Fe^{3+} substitution in modulating the photocatalytic degradation of organic pollutants. Unlike Al^{3+}, which primarily alters lattice strain, defect populations, and surface charge without introducing new redox centers, Fe^{3+} incorporation adds an explicit dopant-mediated redox pathway that operates within the intrinsic Cu–O electronic framework.*

A systematic series of Fe-doped CuO nanostructures was synthesized to isolate the combined effects of lattice distortion, electronic structure modification, and Fe^{3+}/Fe^{2+} redox cycling. Structural and spectroscopic analyses confirm substitutional incorporation of Fe^{3+} into the CuO lattice, accompanied by increased disorder, modified Cu-O bonding, and enhanced defect density. Photocatalytic degradation experiments under visible-light illumination demonstrate that Fe-doped CuO exhibits significantly higher reaction rates than both pristine CuO and Al-doped CuO under comparable conditions.

Kinetic analysis reveals that, unlike the predominantly thermally assisted enhancement observed for pure CuO nanosheets, Fe substitution enables degradation kinetics that are no longer dominated by thermal activation, indicating a mechanistic shift toward dopant-assisted radical generation. Scavenger and fluorescence studies confirm hydroxyl radicals as the dominant reactive species, with Fe^{3+}/Fe^{2+} cycling acting as an efficient redox mediator that promotes sustained radical production. Stability and recyclability tests further establish Fe-doped CuO as a robust heterogeneous photo-Fenton catalyst with minimal metal leaching.

Overall, this chapter demonstrates that Fe^{3+} substitution transforms CuO from a thermally enhanced photocatalyst into a dopant-activated photo-Fenton system, bridging the conceptual gap between defect-engineered photocatalysis and redox-driven catalytic pathways. These insights provide a mechanistic foundation for the electrocatalytic oxygen evolution studies

presented in the subsequent chapter.

5.1. Chapter Introduction and Objectives

Chapters 3 and 4 established two complementary routes to improve CuO-based light-driven oxidation. Chapter 3 showed that aliovalent, non-redox Al^{3+} substitution enhances photo-(Fenton-like) degradation mainly by tuning defects and the Cu–O charge-transfer (ligand-hole) network, thereby improving charge-carrier utilization and redox accessibility under low-power illumination. Chapter 4 then isolated morphology and temperature effects using undoped CuO nanosheets and demonstrated that higher temperature accelerates light-driven kinetics by facilitating detrapping/polaronic hopping and interfacial redox steps, even when dark adsorption does not increase.

A key limitation of these two approaches is that the radical-generation step remains constrained by the intrinsic redox accessibility of CuO and by how efficiently the Cu–O network can deliver redox equivalents to the surface. This motivates the mechanistic question addressed here: can a redox-active dopant introduce an additional catalytic pathway for H_2O_2 activation and thereby shift the dominant bottleneck from transport-limited charge delivery toward dopant-assisted redox mediation?

Fe is a natural candidate because the Fe^{3+}/Fe^{2+} couple can mediate Fenton-type radical production, and substitutional Fe in CuO can also reshape local coordination and oxygen chemistry. In a charge-transfer oxide such as CuO, these effects are most consistently discussed in terms of changes to Cu–O covalency/final-state screening (Cu 2p) and oxygenated/defective surface fractions (O 1s), rather than by assigning large changes in formal Cu valence from small binding-energy shifts.

Accordingly, this chapter positions Fe-substituted CuO as a chemically activated photo-Fenton catalyst that bridges the defect-dominated Al-CuO system (Chapter 3) and the transport/temperature-assisted undoped nanosheets (Chapter 4), providing the missing link between ligand-hole-mediated electronic modulation and explicitly dopant-mediated redox cycling.

While the Al^{3+}-substituted CuO system investigated in Chapter 3 demonstrated that aliovalent, non-redox-active dopants can effectively modify defect chemistry, electronic structure, and

photocatalytic activity, the enhancement was primarily associated with defect-mediated charge separation and ligand-hole-related processes. However, Al^{3+} does not directly participate in catalytic redox cycling. This raises an important question: can the introduction of a redox-active dopant simultaneously modify the CuO lattice and actively participate in the generation of reactive oxygen species? To address this question, Fe^{3+} was selected as the next dopant because of its ability to undergo Fe^{3+}/Fe^{2+} redox cycling and promote photo-Fenton-like pathways. The transition from Al^{3+} to Fe^{3+} substitution, therefore, enables a systematic comparison between defect-mediated and redox-assisted catalytic enhancement mechanisms within the same CuO host lattice.

Objectives and Scope

The primary objective of this chapter is to elucidate the role of redox-active Fe^{3+} substitution in CuO in governing photo-Fenton-like degradation kinetics and mechanisms under low-power visible-light illumination.

The specific objectives are to:

- Synthesize chemically homogeneous Fe-substituted CuO nanostructures with controlled dopant concentrations using a scalable sol–gel route.
- Establish structure–property relationships by correlating Fe incorporation with changes in crystal structure, local bonding, defect density, and electronic structure.
- Evaluate the photocatalytic degradation performance of Fe-doped CuO toward organic dye pollutants under visible-light irradiation and mild operating conditions.
- Systematically compare degradation kinetics and mechanistic trends across pure CuO (Chapter 4), Al^{3+}-doped CuO (Chapter 3), and Fe^{3+}-doped CuO to isolate dopant-specific effects beyond thermal and defect-assisted enhancement.
- Use XPS screening descriptors (Cu 2p mainline/satellite evolution) and O 1s oxygenated components (O_D/O_L) as semi-quantitative proxies to discuss dopant-induced changes in Cu–O covalency/ligand-hole-associated surface fraction and relate them to ROS generation.
- Identify the dominant reactive oxygen species and reaction pathways through scavenger studies, emphasizing the role of Fe^{3+}/Fe^{2+} redox cycling in hydroxyl radical generation.

- Assess catalyst stability, reusability, and metal leaching behavior to determine the practical viability of Fe-doped CuO for sustainable wastewater treatment.

Within the broader scope of this thesis, this chapter demonstrates that redox-active dopant engineering provides a mechanistically distinct and more effective activation route than thermal assistance alone for enhancing photo-Fenton-like processes. The mechanistic insights developed here also establish a conceptual foundation for the electrocatalytic studies of Fe-modified CuO presented in subsequent chapters.

5.2. Synthesis and Experimental Methods

The synthesis of the photocatalysts investigated in this chapter, along with their structural, optical, and surface characterization, is described in detail in Chapter 2. This section, therefore, focuses specifically on the photocatalytic measurement parameters and testing conditions employed to evaluate the degradation performance of the materials discussed in this chapter.

The photocatalytic activity of all the samples was examined under visible light illumination from a household LED, emitting monochromatic light with a maximum intensity at 455 nm, a light intensity of approximately three orders of magnitude lower than AM 1.5G solar irradiance (the spectrum is given in Chapter 2, Figure 2.1.3.1). A 10-ppm strength stock solution of pollutant methylene blue (MB) dye was prepared by mixing 10 mg of the MB dye in 1 L of DIW. Five different concentrations (0.5 mg/mL, 0.75 mg/mL, 1 mg/mL, 1.25 mg/mL, and 1.5 mg/mL) of the catalyst solution were prepared by adding an appropriate amount (10 mg, 15 mg, 20 mg, 25 mg, and 30 mg, respectively) of CuO NPs or Fe-doped CuO NPs to 20 mL of MB dye solution in separate beakers. Initially, 0.115 ml (50 mM) of hydrogen peroxide (H_2O_2) (30% w/v) was added to this solution to enhance the photocatalytic reaction. The obtained mixed solutions were stirred continuously in the dark for 60 minutes to achieve good dispersion and adsorption equilibrium. The concentration of the remaining dye was estimated from the time-dependent absorption spectra (10-minute interval) recorded using a Research India UV-visible spectrophotometer. After each step of the photocatalytic degradation of samples, a 3 mL solution was extracted from the photo-reacted solution. The photo-reacted solutions were centrifuged properly to extract the catalyst nps. The reduction in intensity of the absorption spectra over time was studied for each sample. The photocatalytic degradation efficiency of the organic dyes was calculated using the following formula: $Degradation\ (\%) = [(A_0 -$

$A_t)/A_0] * 100$; where A_0 is the absorbance of the dye solution before the photo-irradiation, and A_t is the absorbance of the solution after photo-irradiation for a specific time t.

5.3. Structural, Optical, and Surface Properties

5.3.1. Structural studies

The XRD pattern of all the samples revealed a single-phase monoclinic tenorite structure with a C2/c space group [Figure 5.3.1.1]. Various diffraction peaks appeared at 2θ = 32.5°, 35.5°, 38.7°, 48.8°, 53.3°, and 58.2°, belonging to the (110), (002)/(11-1), (200)/(111), (20-2), (020), and (202) planes of the tenorite CuO structure [JCPDS card # 48–1548]. Rietveld refinement of the XRD data using GSAS-2 software revealed structural modifications of the tenorite structure with Fe incorporation.

In tenorite (CuO), the Cu atom is in a distorted octahedral local coordination symmetry surrounded by six O atoms. Amongst the six possible Cu-O bonds, two Cu-O bonds are larger (~2.766 Å) than the remaining four (~1.948 Å). Note that there are three sets of diagonally opposite bonds that are linearly connected with the centrally located Cu atom. However, the three sets of such linearly connected oxygen atoms are not perpendicular to each other and are distorted, with angles between the different Cu-O bonds varying from 73.23° to 89.18° and 84.37°. Hence, the octahedron is distorted. Due to the very large Cu-O bonds, in reality, only four O atoms actually bond with a Cu atom, making its effective coordination a four-coordinated Cu atom in the CuO lattice [182].

When Fe^{3+} replaces the Cu^{2+} ion, one can expect a shrinking of the lattice near the dopant Fe^{3+} atom as the Fe^{3+} (high-spin, octahedral coordination ~ 0.645 Å) has a slightly smaller ionic radius than Cu^{2+}(~0.73 Å). However, the charge of Fe^{3+} is greater than that of the Cu^{2+} ion and is supposed to attract a greater number of negatively charged O^{2-} ions to the lattice. It has been reported that p-type conductivity in pure CuO can be traced back to the intrinsic Cu-vacancies in the system [183]. Aliovalent Fe^{3+} substitution may require local charge compensation through copper vacancies or oxygen non-stoichiometry, which can partially offset simple size-driven lattice trends [184]. The smaller size of the Fe^{3+} ion and the associated Cu-loss can be responsible for lattice contraction. Such a trend is observed for CF1 as the lattice volume decreased from 79.986 $Å^3$ (C0) to 79.9719 $Å^3$ (CF1). However, beyond CF1, by further addition of Fe^{3+}, the cell volume increased to 79.981 $Å^3$ in CF2. At the same time, aliovalent

substitution requires charge compensation (e.g., through cation vacancies, oxygen non-stoichiometry, and/or local redistribution of hole density within the Cu–O network), which can partially offset simple size-driven trends. The lattice parameter 'a' decreased from C0 (4.66162 Å) to CF1 (4.66133 Å) and then further increased to 4.66151 Å. The lattice parameter 'b' increased from 3.40606 Å (C0) to 3.440651 Å (CF1) and then decreased to 3.40636 Å (CF2). The lattice parameter 'c' decreased from 5.10544 Å (C0) to 5.10429 Å (CF1) and then increased to 5.10512 Å (CF2). From these values, it seems that the changes are considerable along the 'a' and 'b' axes and comparatively nominal along the 'c' axis. These variations in unit cell parameters and volume indicate changes in the lattice due to the incorporation of the Fe^{3+} ions at the local coordination level, while preserving long-range monoclinic order.

The crystallite size (D) for all the samples was determined from the Scherrer equation ($D = 0.9 \lambda/FWHM*\cos\theta$). FWHM is the full width at half maximum intensity of the XRD peak, and θ is Bragg's diffraction angle. The D value was obtained considering the (110) plane of CuO, which did not vary significantly: 86.73 nm for C0, 86.52 nm for CF1, and 86.86 nm for CF2. The strain was also calculated and found to be nearly invariant: 0.00151 for C0, 0.00155 for CF1, and 0.0015 for CF2. Hence, the incorporation of Fe did not significantly affect the lattice. The minimal change in lattice strain and crystallite size indicates that Fe substitution does not significantly distort the global crystal framework, but instead modifies local coordination environments and defect states. The resulting catalytic behavior is therefore governed by electronic-structure alterations associated with dopant-induced changes in Cu–O hybridization.

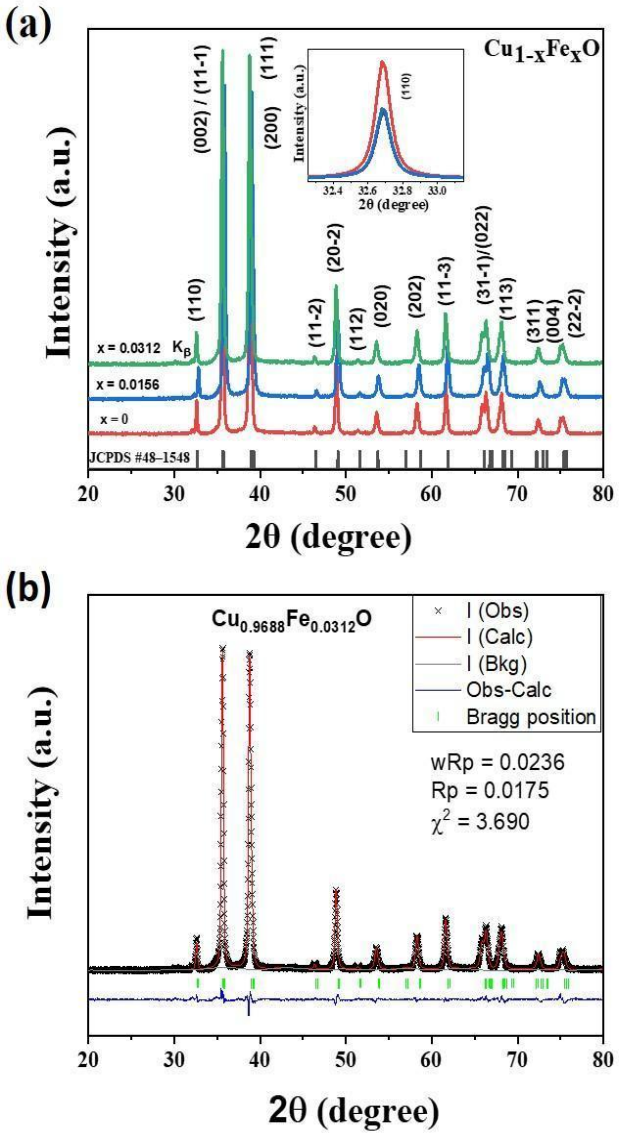


Figure 5.3.1.1: (a) XRD patterns of pure and Fe-doped CuO ($Cu_{1-x}Fe_xO$; x = 0, 0.0156, 0.0312) showing a single-phase monoclinic CuO structure (JCPDS No. 48-1548) without secondary impurities. The inset highlights a shift of the (110) peak toward higher 2θ with increasing Fe content, indicating lattice contraction due to the substitution of smaller Fe^{3+} ions for Cu^{2+}. (b) Rietveld refinement of $Cu_{0.9687}Fe_{0.03125}O$ showing excellent agreement between observed and calculated data (χ^2 = 3.690, wRp = 0.0236, Rp = 0.0175), confirming phase purity and successful Fe incorporation into the CuO lattice

5.3.2. Surface Morphological

Field Emission Scanning Electron Microscopy (FESEM) studies revealed an agglomerated surface morphology for all the samples [Figure 5.3.2.1] with particles of sub-micrometer size. Energy-dispersive X-ray spectroscopy (EDX) studies show the presence of only Cu and O in the undoped C0 sample, and Cu, Fe, and O for the doped samples. The 2D mapping reveals a homogeneous distribution of all the elements throughout the samples, suggesting a non-segregated distribution of the dopant Fe ions.

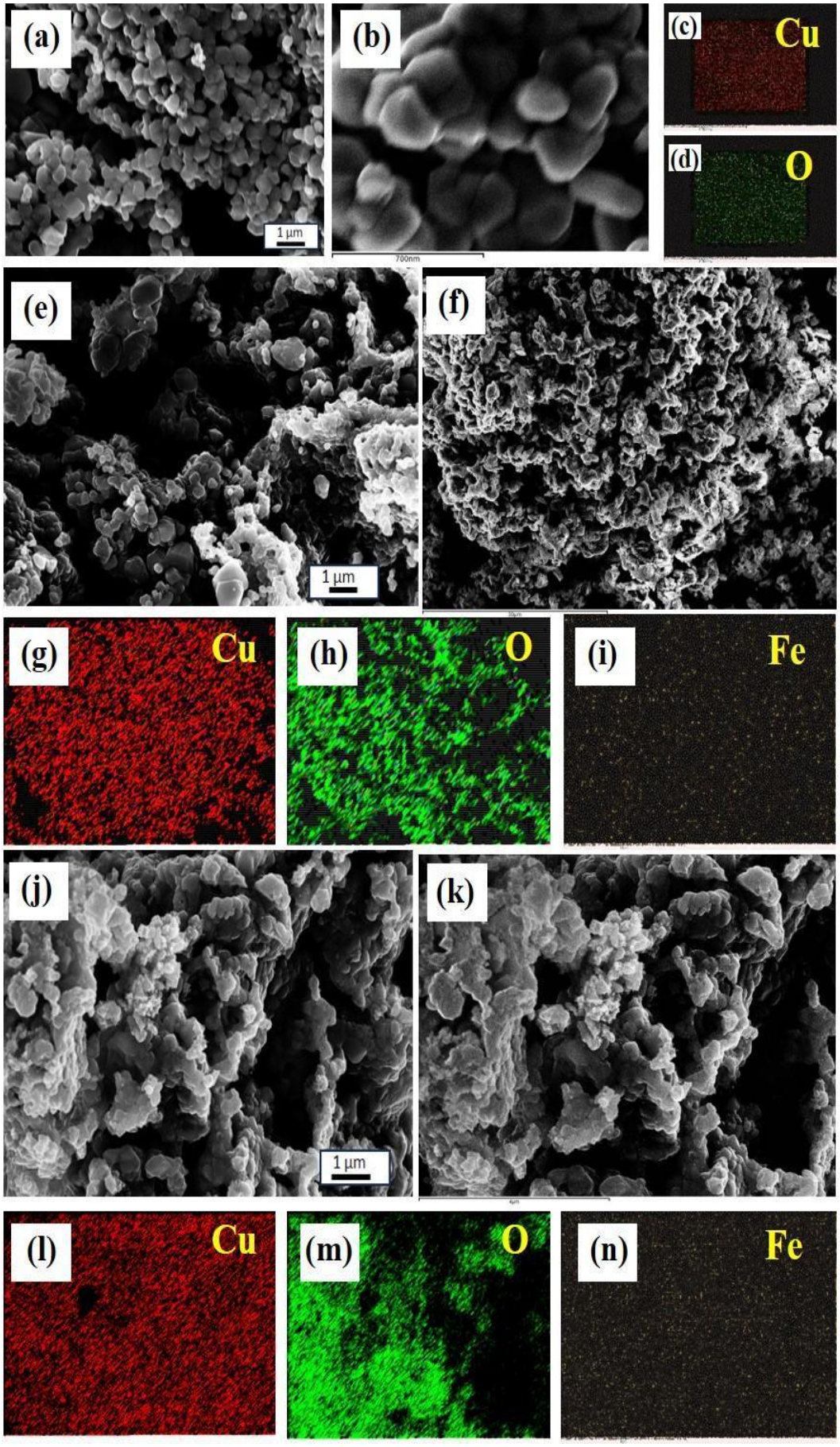

(a)
1 µm
(b)
700nm
(c)
Cu
(d)
O
(e)
1 µm
(f)
(g)
Cu
(h)
O
(i)
Fe
(j)
1 µm
(k)
(l)
Cu
(m)
O
(n)
Fe

Figure 5.3.2.1: FE-SEM images and corresponding EDS elemental mapping of (a–d) pure CuO, (e–i) low Fe-doped CuO, and (j–n) high Fe-doped CuO samples. All samples exhibit agglomerated sub-micrometre grains; Fe incorporation results in increased surface roughness and more irregular aggregates, indicating morphological evolution with partial doping. EDS maps confirm homogeneous spatial distribution of Cu, O, and Fe, with no evidence of Fe-rich secondary phases at the resolution of the technique.

5.3.3. Phonon studies

The group theory analysis, supported by experimental results, confirms the presence of twelve vibrational modes in monoclinic CuO. These include three acoustic modes ($A_u + 2B_u$), six infrared-active modes ($3A_u + 3B_u$), and three Raman-active modes ($A_g + 2B_g$). The active Raman modes are mainly due to vibrations of oxygen atoms because of the symmetry of the crystal structure [4]. The absence of impurity peaks in the recorded Raman spectra confirms the formation of single-phase monoclinic CuO even with the incorporation of Fe in the modified lattice, which is consistent with our XRD findings. The recorded Raman spectra [Figure 5.3.3.1] revealed Raman vibration at 295.8 cm^{-1} (A_g), 344.5 cm^{-1} (B_{1g}), and 630.1 cm^{-1} (B_{2g}). Among the three modes, the most prominent A_g mode is significantly stronger than the other two modes.

A significant blue shift of the A_g mode is observed from 295.8 cm^{-1} in C0 to 296.6 cm^{-1} in the CF1 sample, followed by a negligible red shift to 296.5 cm^{-1} in CF2. Shifts in phonon frequency can be correlated to the bond strength and the effective mass of the vibrating atoms. As the mass of Fe is less than that of Cu, a probable correlation of the mass to the blueshift in Ag for CF1 can be linked to this change in mass. However, an increase in bond strength cannot be ruled out due to the effective valence state of the cations, which increases with the incorporation of Fe^{3+} in place of Cu^{2+}. again, Fe^{3+} (high-spin, octahedral coordination ~ 0.645 Å) has a slightly smaller ionic radius than Cu^{2+}(~0.73 Å). Hence, the effective Fe-O bond length may decrease because of the smaller ionic size as well as the greater electrostatic attraction between the Fe^{3+} and O^{2-} ions than the Cu^{2+} and O^{2-} ions. Hence, the strength of the dopant cationic bonds may be stronger, resulting in a blueshift as well. While the lower atomic mass of Fe relative to Cu may contribute marginally, the primary origin of the Ag mode blue shift is more consistently attributed to strengthened local Fe–O bonding and modified force

constants resulting from aliovalent substitution. In the case of CF2, nominal redshift may be a result of increasing lattice distortion or strain, resulting in weaker bonds. The full width at half maximum (FWHM) of the A_g mode decreased for CF1 but increased for CF2. A decrease in FWHM often suggests increased molecular order or crystallinity in a material [185] while an increase in FWHM often hints at a loss of order or the presence of strain in the lattice. Overall, the Ag-mode FWHM trends suggest that higher Fe content increases local disorder/strain. Consistent with aliovalent substitution, Fe incorporation is expected to perturb oxygen-defect equilibria, which can contribute to local strain without disrupting long-range monoclinic order.

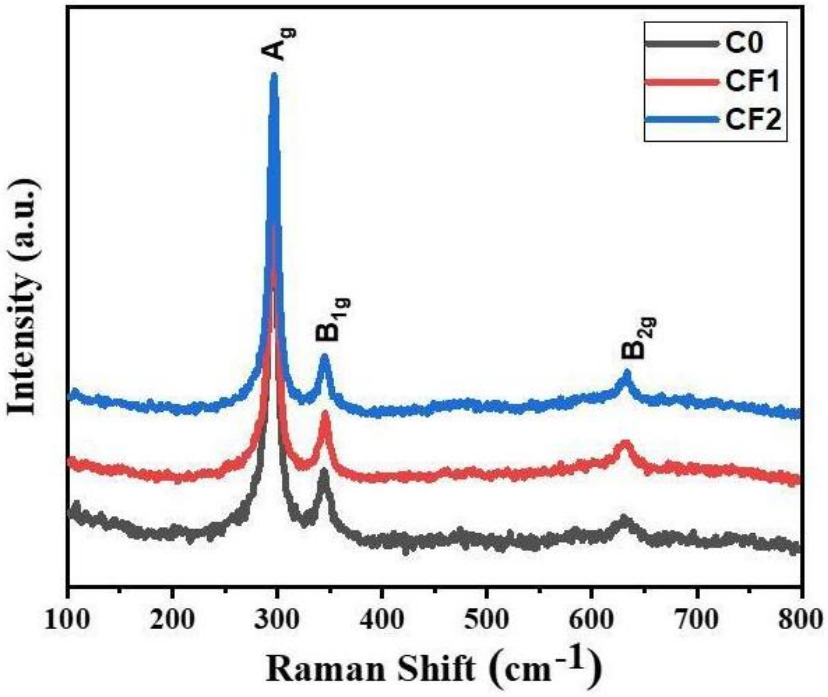


Figure 5.3.3.1:Raman spectra of pure CuO (C0) and Fe-doped CuO samples (CF1 and CF2). All samples exhibit the characteristic monoclinic CuO vibrational modes at ~298 cm^{-1} (A_g), ~345 cm^{-1} (B_{1g}), and ~627 cm^{-1} (B_{2g}). The slight blue shifts and intensity variations with Fe incorporation indicate lattice distortion and changes in local symmetry resulting from the substitutional partial doping of Fe ions within the CuO lattice. A slight blue shift and FWHM modulation of the A_g mode with partial Fe doping reflect changes in local bond strength and lattice disorder induced by substitutional Fe.

FTIR spectra of the synthesized nanostructures were obtained in the wavenumber range of 400–4000 cm^{-1} to analyze the bonds existing on the surface and the vibrational variations of

the atoms [Figure 5.3.3.2]. There is a significant difference in the intensity in the region 900 to 2500 cm^{-1}. The pronounced intensity differences in the 900 to 2500 cm^{-1} region likely reflect variations in morphology, surface adsorbates, and crystallinity between the undoped and Fe-doped samples, rather than simple particle-size effects.

Cu-O stretching modes were reported at 473 cm^{-1} (A_u mode along [1 0 1] direction), 538 cm^{-1}, and 595 cm^{-1} (B_u mode along [-101] direction) [114], [182]. The impact of partial Fe doping on the modes was evident. The A_u mode was observed at 474 cm^{-1} in C0, which blueshifts to 476 cm^{-1} in CF1 and slightly redshifts to 475 cm^{-1} in CF2. Shifts in the FTIR modes indicate changes in the phonon energy. A blue shift, i.e., shifting of the FTIR peaks to higher frequencies, can suggest an increase in bond strength or a change in hybridization states, generally a more vital interaction within the electron clouds, leading to higher conductivity in Fe-modified CuO [184]. Note that this trend is similar to that obtained in Raman spectroscopy.

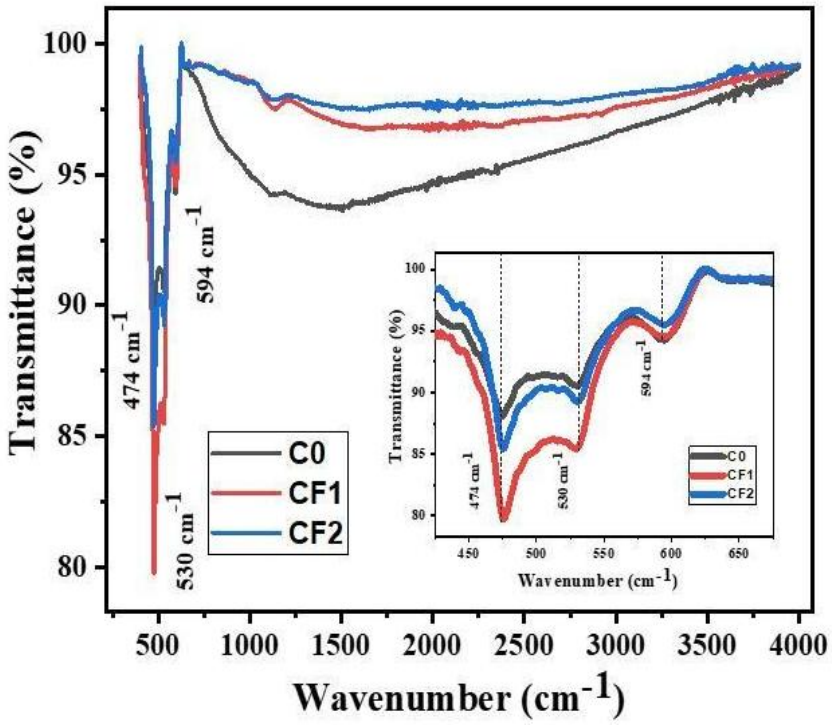


Figure 5.3.3.2: FTIR spectra of pure CuO (C0) and Fe-doped CuO samples (CF1 and CF2). The characteristic Cu-O vibrational bands observed at ~474, 530, and 594 cm^{-1} correspond to metal–oxygen stretching modes of monoclinic CuO. The inset highlights these absorption peaks, where slight shifts and intensity variations upon Fe incorporation indicate modifications

in the Cu-O lattice environment and local bonding symmetry due to Fe substitution.

5.3.4. Optical Studies

The UV-Vis Diffuse Reflectance Spectra for all the samples were acquired over the range of 200~800 nm [Figure 5.3.4.1]. The band gap (E_g) is determined from these spectra using the Kubelka-Munk function: $F(R) = (1-R)^2/2*R$ [186], where R is the diffuse reflectivity of the samples. The absorption coefficient, α, is close to the F(R). The E_g was calculated from energy-dependent optical absorbance data using the Tauc method [119]. The E_g was determined by the Tauc equation: $-(\alpha h\nu)^{1/n} = A(h\nu-E_g)$ [187], where α is the absorption coefficient, ν is the photon's frequency, h is Planck's constant, and A is a proportionality constant. The nature of the transition between the conduction band (CB) and valence band (VB) is determined by the power n; n = 1/2, 3/2, 2, and 3 for direct allowed, direct forbidden, indirect allowed, and indirect forbidden transitions, respectively.

The hybridization between Cu 3d and O 2p states results in the formation of CB and VB in CuO. At the same time, VB is predominantly O 2p in character, while the CB has strong Cu 3d character [121]. The incorporation of Fe^{3+} ions increases the direct E_g from 1.435 eV (C0) to 1.5 eV (CF1) and 1.63 eV (CF2). The observed blue shift of the absorption edge and corresponding increase in optical bandgap are attributed to Fe-induced perturbation of the Cu–O electronic network. Substitution of the smaller Fe^{3+} ion for Cu^{2+} introduces local lattice distortion and modifies the Cu 3d–O 2p hybridized states that govern the optical transition. Consequently, the absorption edge shifts toward higher energies, resulting in an apparent widening of the optical bandgap.

In p-type CuO, cation vacancies (V_{Cu}) act as acceptors with levels located close to the valence band maximum (VBM), thereby contributing to intrinsic hole conduction and the characteristic p-type semiconducting behavior of the material. In contrast, oxygen vacancies are generally donor-like and can introduce mid-gap or shallow levels below the CB minima, contributing to band-tail formation and localized states within the band gap.

When Fe^{3+} substitutes for Cu^{2+}, local charge compensation becomes necessary due to the difference in valence. This compensation may occur through a combination of mechanisms, including the formation of copper vacancies (V_{Cu}), oxygen interstitial (O_i), or partial

modulation of the Cu valence state through local charge redistribution within the Cu–O network. The exact balance of these mechanisms depends on dopant concentration and local coordination environment.

Fe substitution is therefore expected to perturb the intrinsic defect equilibria of CuO rather than simply increasing or decreasing a single defect type. A reduction in donor-like states associated with oxygen vacancies could suppress band-tail states and lead to a widening of the apparent optical band gap, as observed in CF1. Simultaneously, an increase in acceptor-like defects such as V_{Cu} or O_i may enhance p-type character by increasing hole concentration near the valence band.

At higher Fe concentrations (e.g., CF2), additional defect states associated with oxygen interstitials or dopant-induced disorder may contribute to localized electronic states near the valence band edge, further modifying the electronic structure. These combined effects highlight that Fe^{3+} substitution primarily alters the defect landscape and electronic hybridization of CuO, thereby influencing its optical and redox behavior.

However, the progressive widening of the apparent band gap in CF2 cannot be explained solely by defect-state modulation, since increased defect density would typically introduce localized states that reduce the effective optical gap. This suggests that additional electronic-structure effects must be considered. In particular, hybridization between Fe 3d and O 2p orbitals modifies the CuO band structure by perturbing both valence- and conduction-band edges. As Fe concentration increases, the extent of Fe–O–Cu hybridization correspondingly increases, leading to systematic band-edge reconstruction and a continuous evolution of the apparent band gap. Fe incorporation may also influence carrier concentration through dopant-induced charge redistribution within the Cu–O framework. Increased carrier density and band-filling effects near the band edges may contribute to an apparent blue shift, although a classical Burstein–Moss mechanism (typically associated with degenerate n-type semiconductors) cannot be conclusively confirmed without Hall measurements [188], [189], [190]. Partial doping with aliovalent ions inevitably perturbs lattice symmetry and local coordination, increasing structural disorder. This is reflected in the Urbach energy (E_U), which characterizes band-tail states arising from disorder-induced localized states. The absorption coefficient follows the exponential relation $\alpha = \alpha_o.\exp(h\nu/E_U)$, where α_o is a constant. Natural logarithm on both sides results in a linear relation between $\ln(\alpha)$ and E: $\ln[\alpha] = \ln[\alpha_o] + (E/E_U)$, leading to a linear

dependence in ln(α) versus photon energy plots [120]. The extracted E_U values increase from 55 meV (C0) to 82 meV (CF1) and 131 meV (CF2), confirming progressive disorder with increasing Fe content. Although increasing Urbach energy indicates enhanced disorder and defect-related band-tail states, the dominant optical response appears to be governed by Fe–3d/O–2p hybridization and associated band-edge reconstruction, rather than by isolated mid-gap defect levels. Thus, the observed band-gap widening is best interpreted as a combined consequence of dopant-induced electronic hybridization, modified band-edge alignment, and increased carrier density, rather than simple defect suppression or creation alone.

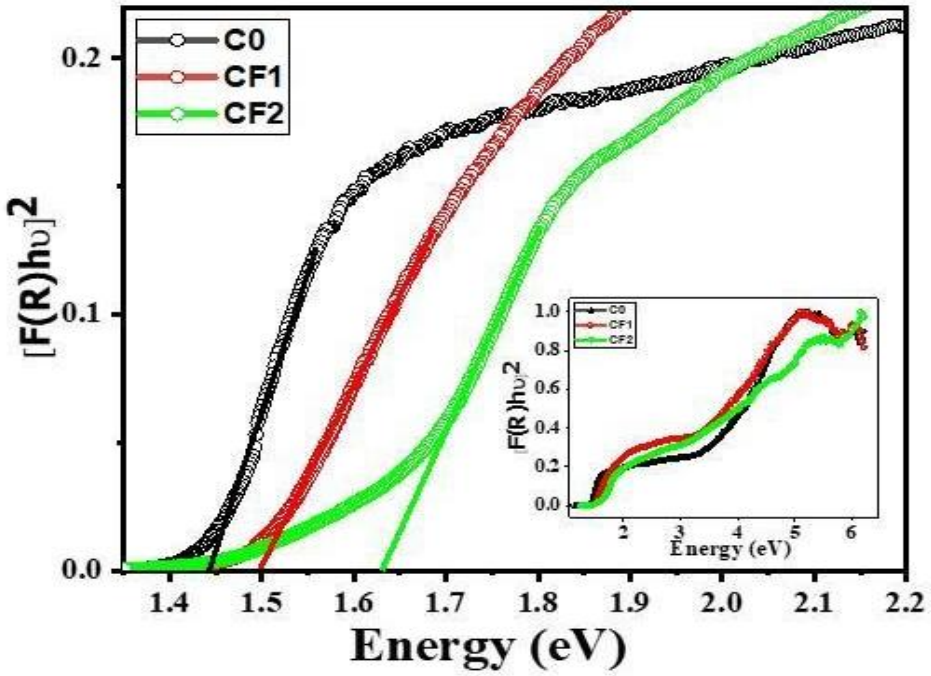


Figure 5.3.4.1: Tauc plots $[F(R)h\nu]^2$ versus photon energy for pure CuO (C0) and Fe-doped CuO samples (CF1 and CF2), showing the band gap variations. The estimated optical band gaps increase from ~1.435 eV (C0) to ~1.5 eV (CF1) and ~1.63 eV (CF2), indicating that Fe incorporation widens the apparent band gap through combined band-structure modification and altered defect chemistry. The inset shows the extended optical absorption edge in the visible region.

5.3.5. Surface Area Analysis

The Brunauer-Emmett-Teller (BET) surface areas for all the samples were analyzed using N_2

adsorption and desorption data [Figure 5.3.5.1]. The specific surface area first increases rapidly from 1.49 m^2/g for C0 to 6.448 m^2/g for CF1 and then decreases to 4.891 m^2/g for CF2 samples. CF1 has the maximum pore volume of 0.031 cm^3/g, while C0 has the minimum of ~ 0.012 cm^3/g. The values of the specific surface area, the average pore diameter, and the total pore volume of all the samples are given in Table 5.3.5.1. The BET results indicate that Fe incorporation modifies the textural characteristics of CuO and increases surface accessibility relative to pristine CuO. However, because the photocatalytic activity does not correlate directly with the measured surface area, the observed catalytic enhancement cannot be attributed solely to the BET surface area. Instead, textural changes act in conjunction with Fe-induced electronic and redox modifications.

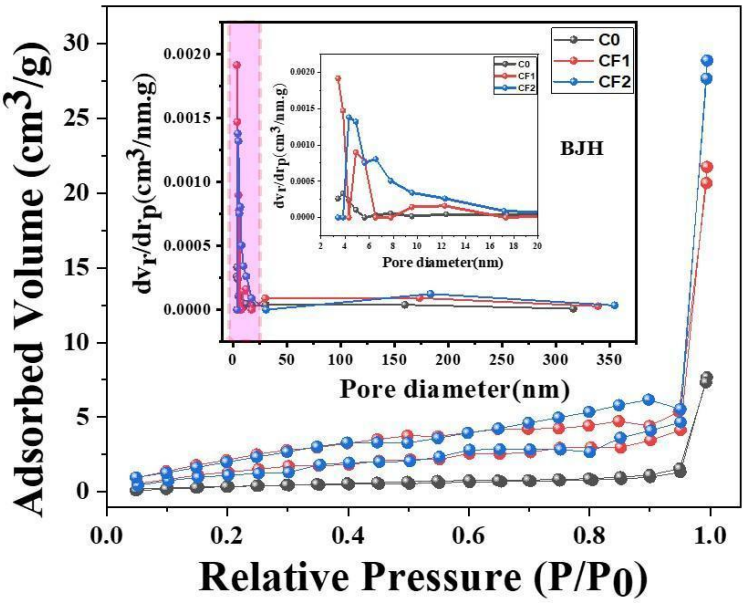


Figure 5.3.5.1: N_2 adsorption-desorption isotherm, and BJH pore-size distributions (insets) for C0, CF1, and CF2. Partial Fe doping markedly increases the specific surface area and pore volume from C0 to CF1, followed by a moderate decrease in CF2, while all samples retain textural/interparticle pore features. These textural changes provide additional accessible active sites but are not the sole factor governing the observed photocatalytic trends.

Table 5.3.5.1: Representation of specific surface area, total pore volume, and average pore

diameter for all the samples.

Catalyst	BET Constant (C)	Specific Surface Area (S_{BET}) (m^2 g^{-1})	Total Pore Volume (V_{pore}) (cm^3 g^{-1})	Average Pore Diameter (D_{pore}) (nm)
C0	18.839	1.49	0.012	3.813
CF1	9.762	6.448	0.031	3.407
CF2	12.417	4.891	0.043	4.302

5.3.6. Chemical Composition Analysis

XPS was used to examine surface composition and electronic-structure descriptors relevant to charge-transfer oxides. Survey spectra confirmed the presence of Cu, O, and Fe (with adventitious carbon at 284.8 eV) and no detectable secondary impurities [Figure 5.3.6.1]. High-resolution Cu 2p spectra show the characteristic Cu $2p_{3/2}$–Cu $2p_{1/2}$ spin–orbit doublet and shake-up satellite structure associated with CuO, reflecting strong electron correlation and charge-transfer screening in the Cu–O network [191].

Rather than interpreting small shifts or multiple components as direct evidence for bulk $Cu^{2+} \rightarrow Cu^{+}/Cu^{0}$ reduction, we treat the evolution of the Cu 2p mainline/satellite envelope as a proxy for changes in final-state screening and Cu–O covalency (i.e., charge-transfer character). Fe substitution modifies the relative weight of well-screened vs poorly screened final states, consistent with a dopant-perturbed Cu–O electronic network that can influence interfacial redox accessibility during H_2O_2 activation.

Any additional higher-binding-energy contribution near ~936 eV is assigned to surface

hydroxide/carbonate environments (e.g., $Cu(OH)_2$/basic carbonate) [192], which are sensitive to surface hydration/aging and do not by themselves define the active lattice state. Accordingly, trends in this component are discussed in terms of surface speciation and accessibility of reactive sites rather than as changes in bulk phase composition.

The O 1s spectra were deconvoluted into a lattice oxygen component (O_L, ~529.5 eV) and higher-binding-energy components associated with oxygenated/defective surface environments (O_D, typically ~530.5–531.2 eV; encompassing oxygen near vacancies/cation vacancies, chemisorbed O^-/O_2^{2-}, and oxyhydroxide-like species) together with a weak adsorbed water contribution (~532–533 eV). Because these assignments can overlap, we use area ratios (e.g., O_D/O_L) only as semi-quantitative descriptors of the oxygenated/defective surface fraction.

For the Fe-substituted series, the O_D/O_L ratio changes with dopant content, indicating that Fe alters the balance between lattice oxygen and oxygenated/defective surface species. Within the bottleneck framework of this thesis, an increased oxygenated/defective surface fraction is interpreted as a higher density of redox-accessible oxygen environments (including ligand-hole-associated states) that can facilitate ROS generation, provided these species do not form a passivating layer.

The Fe 2p signal is weak because of the low substitution level (<3.12%) and partial overlap with Cu Auger features; therefore, Fe is assigned qualitatively as present and predominantly Fe^{3+}-like, while minor Fe^{2+} contributions under reaction conditions cannot be excluded (Figure 5.3.6.3). This limitation reinforces the need to connect Fe chemistry to function through kinetic/mechanistic probes rather than relying solely on ex-situ XPS peak positions.

Overall, XPS indicates that Fe incorporation perturbs (i) Cu 2p final-state screening (Cu–O covalency/charge-transfer character) and (ii) the oxygenated/defective surface fraction (O_D/O_L). These descriptors are consistent with the synopsis logic: Fe not only introduces a potential Fe^{3+}/Fe^{2+} redox mediator for H_2O_2 activation, but also reshapes the Cu–O electronic network that governs redox accessibility in CuO-based catalysts.

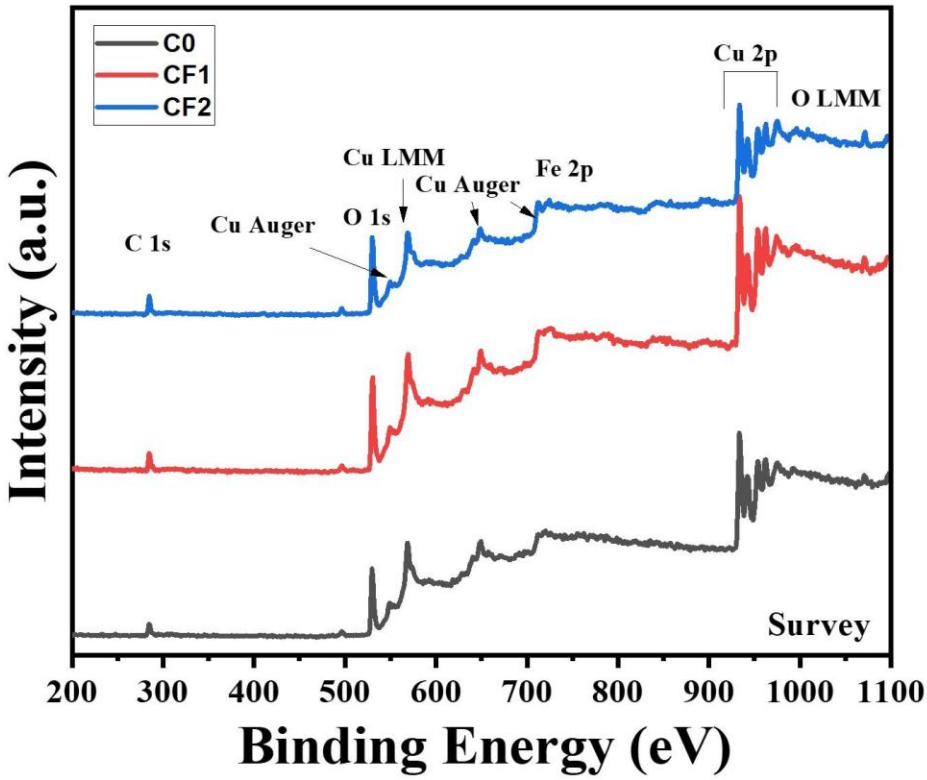


Figure 5.3.6.1: The XPS survey scans of all the samples, representing no impurity except carbon contamination from the atmosphere (Adventitious carbon) located at a binding energy (BE) of 284.8 eV.

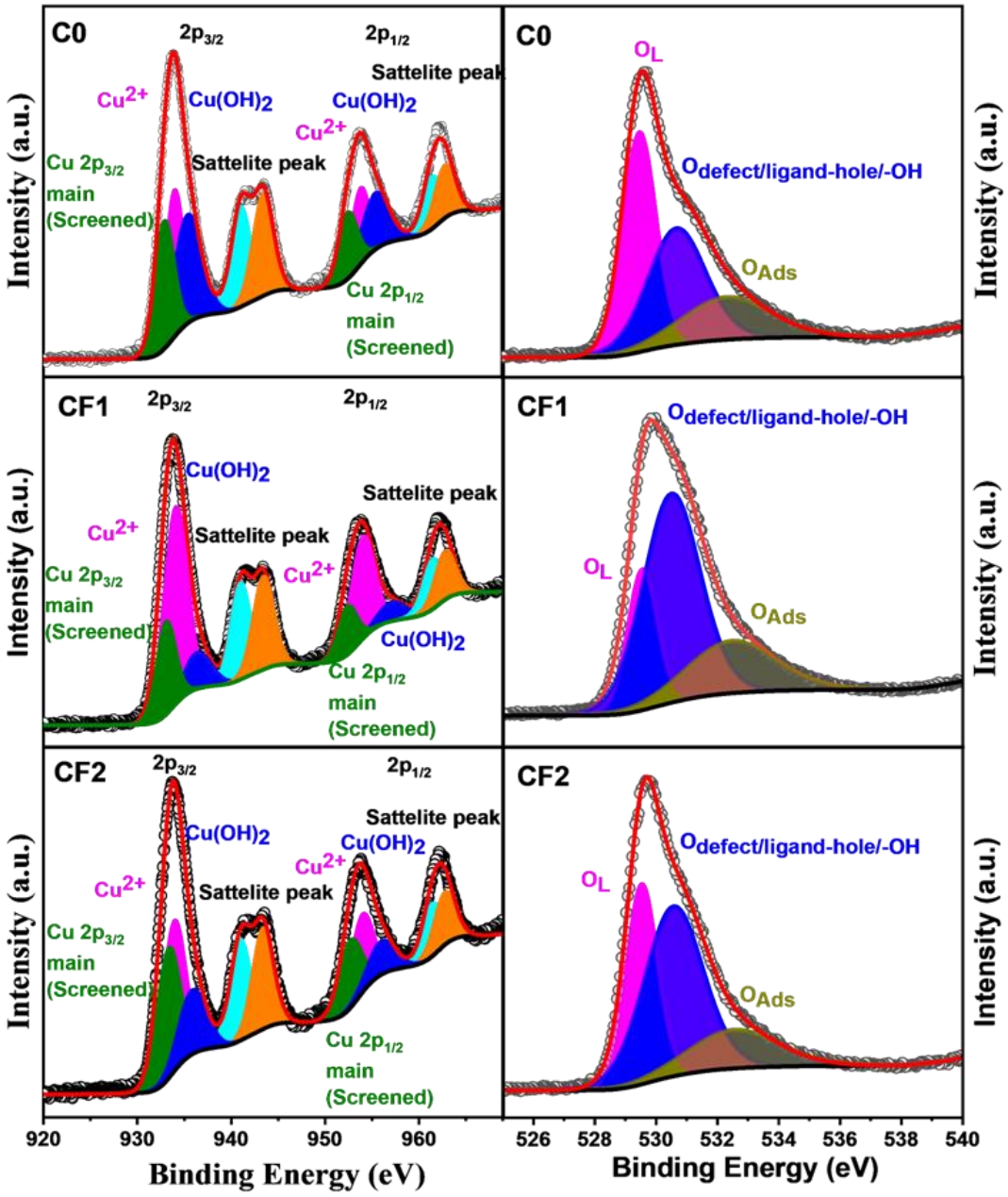


Figure 5.3.6.2: High-resolution XPS spectra of (left) Cu 2p and (right) O 1s regions for pure CuO (C0, top) and Fe-doped CuO (CF1, CF2, bottom). The Cu 2p spectra show Cu^{2+} main peaks with shake-up satellites characteristic of CuO, along with deconvoluted contributions associated with variations in final-state screening and Cu–O covalency (~933 eV), rather than definitive bulk Cu^{+}/Cu^{0} formation. The O 1s spectra are resolved into lattice oxygen (O_L), a defect/chemisorbed/oxyhydroxide-related component near 530.7 eV, and adsorbed water at ~532.8 eV; their relative fractions evolve with Fe content, evidencing Fe-induced changes in

defect oxygen and surface adsorption environments.

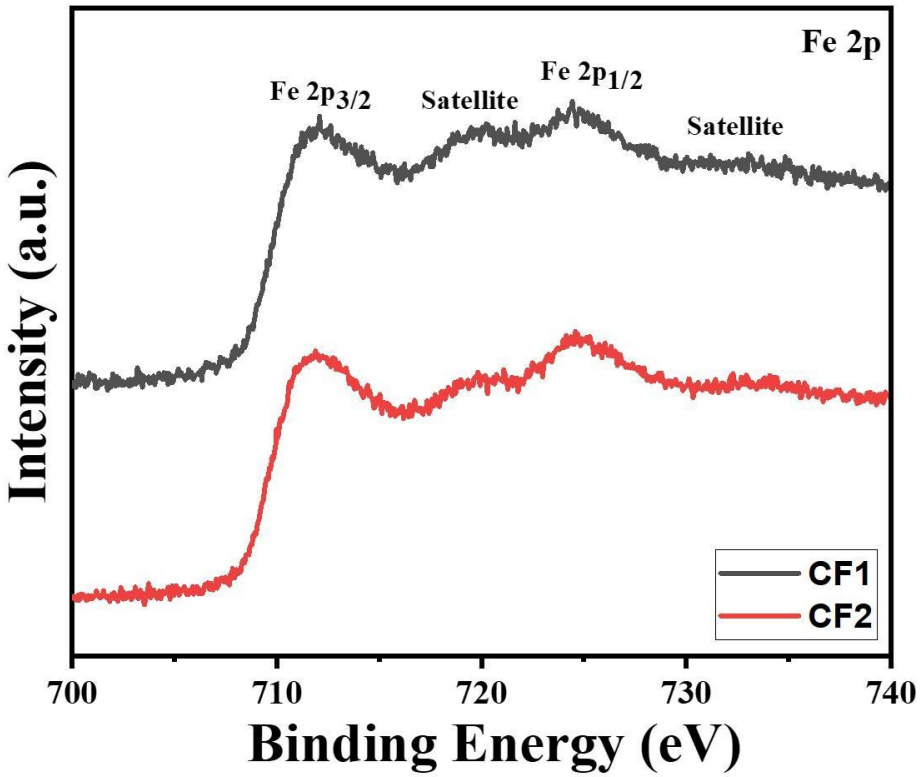


Figure 5.3.6.3: High-resolution XPS spectra of the Fe 2p region for Fe-doped CuO samples CF1 and CF2. The Weak Fe $2p_{3/2}$ and Fe $2p_{1/2}$ features around 711–712 eV and 724–725 eV, partially overlapping with Cu Auger lines, confirm successful incorporation of Fe species into the CuO lattice at low concentrations. The line shape is consistent with predominantly Fe^{3+} in an oxide environment, although the limited signal-to-noise precludes a fully quantitative assessment of Fe valence states.

5.3.7. Surface Charge and Hydrodynamic Analysis

Dynamic light scattering (DLS) is a powerful tool for understanding particle size and dynamics, providing supplementary insight into colloidal behavior relevant to dye adsorption. The behaviors of the samples in a colloidal solution can be characterized by three essential parameters: the Zeta potential (Vξ: ξ-potential), the hydrodynamic size (Rh) [HDS], and the

Polydispersity Index (PDI), which describe the Brownian motion of macromolecules in solution. R_h is the effective spherical size of a molecule of the particles, which provides the same friction in the fluid as the molecule itself. The V_ξ is an estimate of the surface charge of crystals, while the PDI measures the broadness of the size distribution of the particles in a sample. R_h showed a random variation. The R_h of C0 is 454 ± 6 nm, CF1 is 597 ± 4 nm, and CF2 is 528 ± 3 nm. The C0 sample revealed a PDI value of 0.3. The PDI value of CF1 was 0.394, while that of CF2 was 0.419, conferring a mid-range polydispersity nature to all the samples. Similarly, the Zeta potential (V_ξ) for C0 was ~ -14.63 mV, whereas for CF1, it was ~ -8 mV, and for CF2, it was ~ -14.43 mV. The negative V_ξ for all samples indicates that they will exhibit better adsorption kinetics for cationic dyes.

5.4. Photo-Fenton activity of Fe-doped and Kinetics

The most common practice for checking photocatalytic activity is using a conventional high-power illumination setup (250~300 W) UV/Xenon lamp. In this work, these Fe-doped CuO ceramics are evaluated as low-power photo-Fenton catalysts under 455 nm household LED illumination, in order to link their defect-engineered properties to functional performance.

All photocatalytic experiments were conducted at room temperature (30°C) and normal atmospheric pressure [Figure 5.3.7.1a]. Before the light illumination, the obtained mixed solutions were stirred continuously in the dark for 60 minutes to achieve good dispersion and adsorption equilibrium. The dark adsorption in the presence of H_2O_2 (no illumination) resulted in 17.4% (C0), 18% (CF1), and 23 % (CF2) MB removal, indicating limited but non-negligible dark Fenton-like contribution.

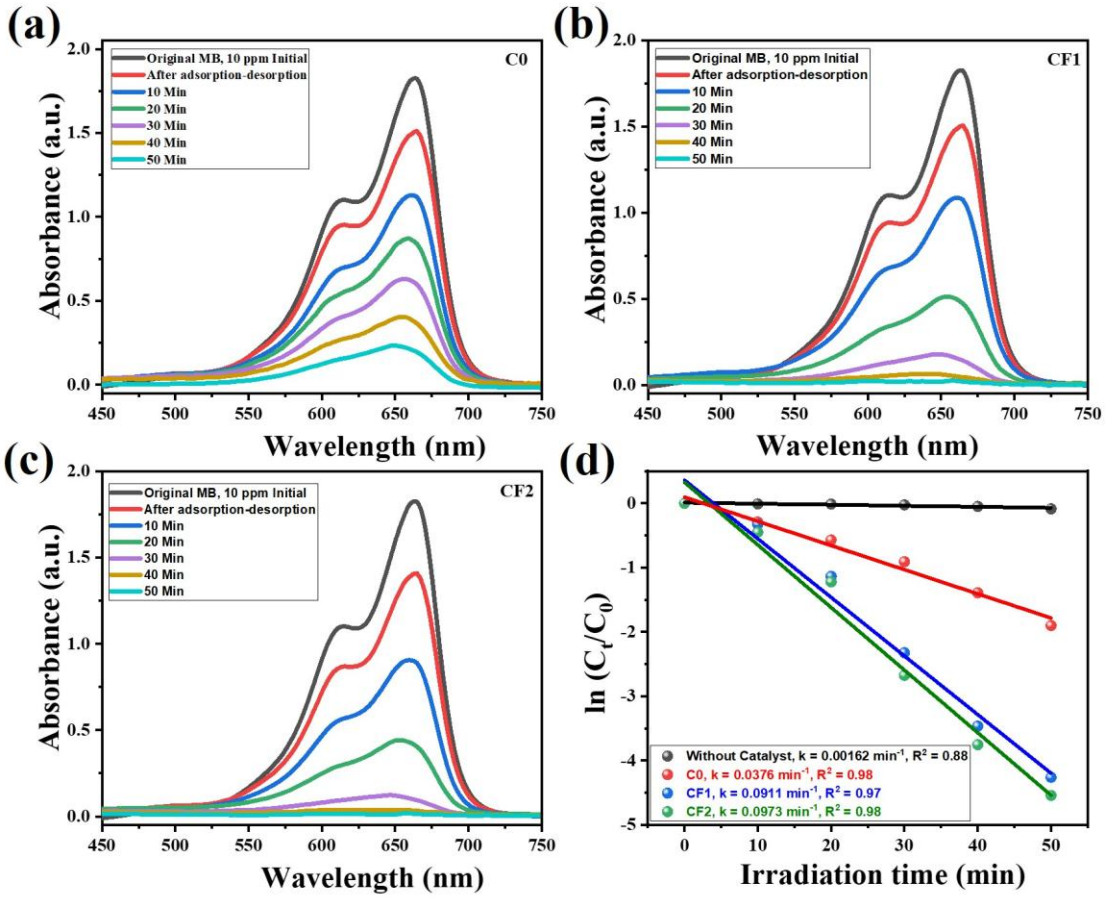


Figure 5.3.7.1a: Represents the reduction of absorbance of the MB dye with time (a, b, c), while the fitted rate constant is obtained from the graph (d).

The absorption spectra exhibit a dominant band near ~664 nm, corresponding to the characteristic π–π* transition of monomeric methylene blue molecules. A secondary shoulder peak observed around ~610–620 nm is attributed to aggregated (dimeric) methylene blue species and associated vibronic transitions. As irradiation proceeds, both the primary and secondary absorption bands decrease progressively, indicating not only a reduction in dye concentration but also the destruction of aggregated dye species and the gradual breakdown of the chromophoric structure. The simultaneous reduction of both peaks therefore provides additional evidence for effective photocatalytic degradation rather than simple adsorption of the dye molecules.

Upon illumination with light, the rate of change of MB concentration followed pseudo-first-

order kinetics. The apparent rate constant was calculated using the equation $ln(\frac{C_0}{C_t}) = k_{app}t$. where C_0 and C_t represent the MB concentrations at 0 min and t min (after dark adsorption correction), respectively, and k_{app} is the apparent rate constant. K_{app} was found to be 0.00162 min^{-1} for the MB solution with H_2O_2 without a catalyst, while 0.0376 min^{-1} for C0, 0.0911 min^{-1} for CF1, and 0.0973 min^{-1} for CF2 [Figure 5.3.7.1a]. Partial Fe doping increases the apparent rate constant from 0.0376 min^{-1} (C0) to 0.0973 min^{-1} (CF2), corresponding to a 2.58-fold enhancement of the photo-Fenton degradation rate.

Again, the photocatalytic degradation by pure CuO was found to be 87.7%. However, with the introduction of Fe in CuO systems, there is an increase in photocatalytic degradation, reaching 98.8% for CF1 and 99.1% for CF2, under the same conditions of catalyst loading and light exposure time/intensity [Figure 5.3.7.2(b)]. Hence, partial Fe-doping seems to enhance the dye degradation properties of CuO. It should be noted that although CF1 exhibits the highest BET surface area (6.448 m^2/g), CF2 delivers slightly higher degradation performance (99.1% vs 98.8%), indicating that surface chemistry and defect structure, especially the balance of redox-accessible Cu sites and oxygen-related surface species, which are more critical than surface area alone in governing Fenton-like photoactivity.

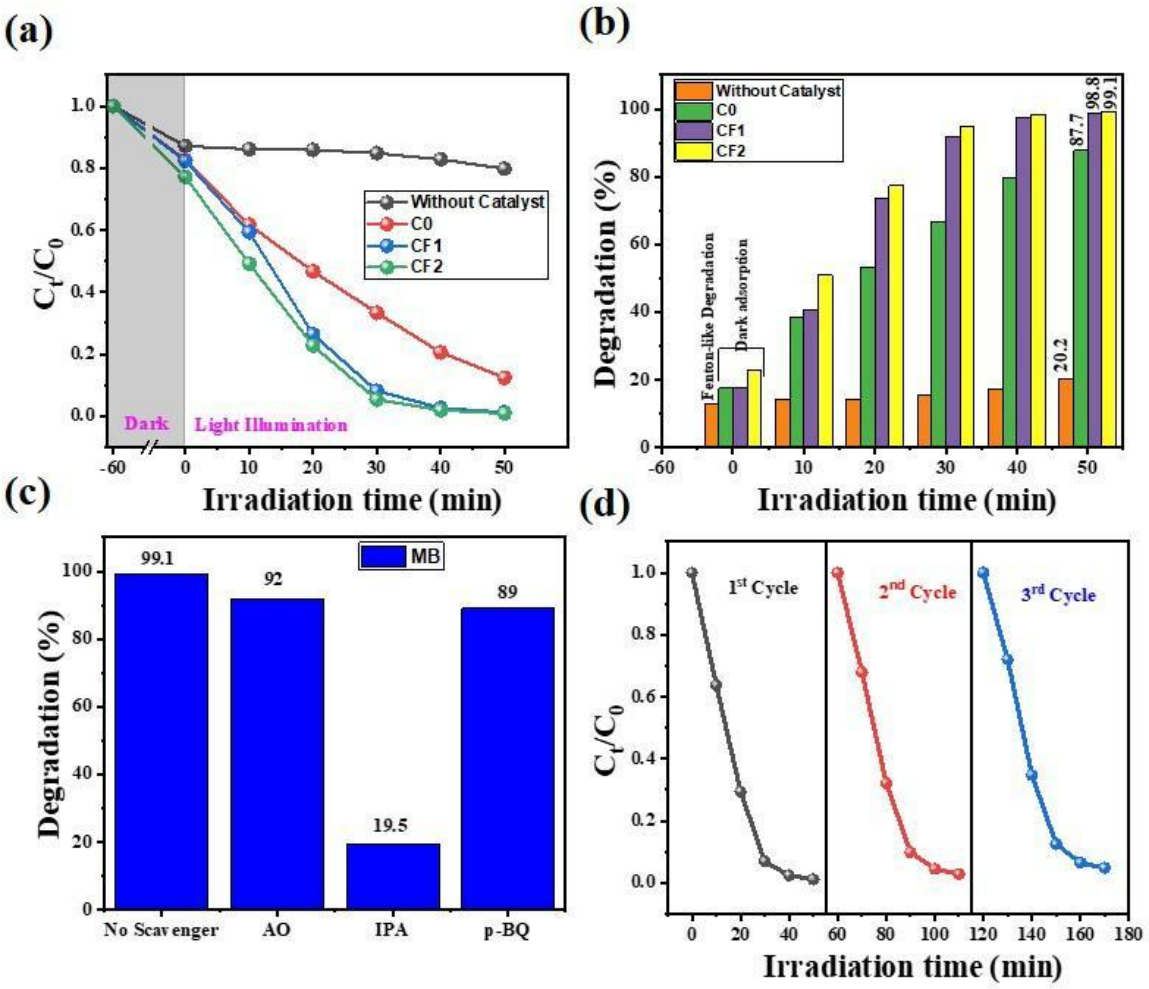


Figure 5.3.7.2: (a) the relative concentration changes of the dye molecules inside the solution over time, showing (b) the degradation percentage of all the samples, in the dark as well as in the presence of light. While (c) shows the scavengers test confirming that the majority of the degradation reactions are contributed from the IPA scavenged OH· radicals, and (d) a recyclability test to show not much degradation in terms of efficiency for three repeated cycles, which were conducted using the CF2 sample.

A concentration-dependent study of the CF2 NPs on the photocatalytic degradation of MB dye was performed at five different concentrations of the NPs. A 1 litre of stock solution was prepared of the MB dye concentration of ~10 ppm. 20mL of the stock solution was taken in five separate beakers, and 10mg, 15mg, 20mg, 25mg, and 30mg of the nps were added to these separate beakers thereby resulting in the following concentration of the nps: 0.5 mg/mL, 0.75 mg/mL, 1 mg/mL, 1.25mg/mL, and 1.5 mg/mL, respectively. These catalyst-containing MB

dye solutions were exposed to light for 50 min [Figure 5.3.2]. As the catalyst loading increases from 0.5 mg/mL to 1 mg/mL, the degradation of MB increases from 97% for 0.5mg/mL to 98.3% for 0.75mg/mL, and reaches the highest degradation of 99.2% in 1mg/mL. Further increasing the catalyst concentration led to a decrease in degradation to ~98.8% for 1.25 mg/mL and finally to 97.4% for 1.5 mg/mL. The increasing photodegradation with increasing catalyst concentration is due to the increasing number of collisions between reactants and the catalyst, increases. As the number of active sites on the photocatalyst surface increases, the formation of OH• radicals increases, which can take part in the breaking of the dye molecule, resulting in the decolouration of the dye solution. However, excessive concentration of the catalyst blocks the light from reaching the active sites and thereby reduces the degradation rate. Hence, the optimum concentration was found to be 1 mg/mL.

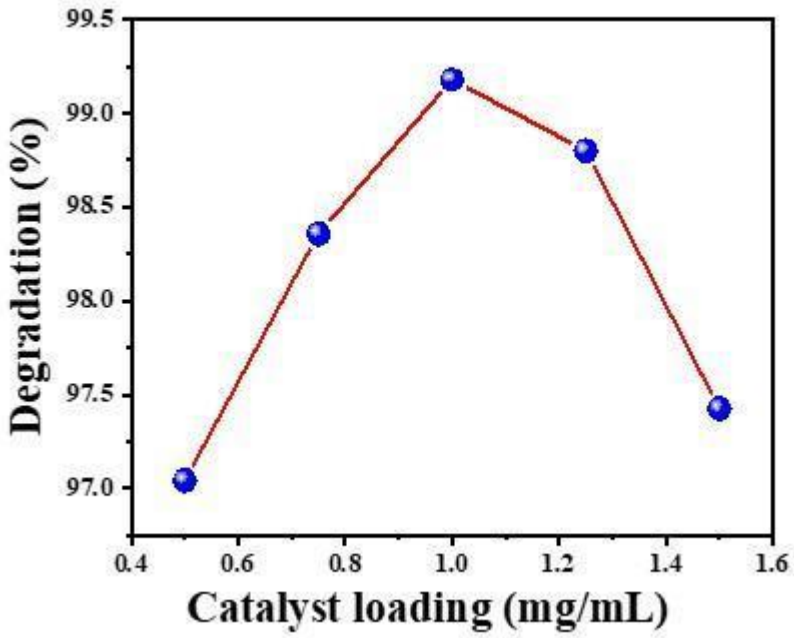


Figure 5.3.7.3: Degradation percentage of MB dye with increasing catalyst loading. As observed from 0.5 mg/mL to 1 mg/mL, the degradation of MB increases from 97% to 99%, then decreases to 97.5% for a catalyst with 1.5 mg/mL.

The scavenger test is a suitable method to estimate the amount of radicals (hydroxyl, superoxide, and holes) that play a major role in the photocatalytic degradation of the organic dye. In this test, three different types of chemicals were employed to trap three different

radicals: p-benzoquinone (BQ) for superoxide radicals, ammonium oxalate (AO) for hole radicals, and isopropanol (IPA) for hydroxyl radicals. The amount of different chemicals taken was, according to the previous work [182]. In this work, it was observed that as IPA drastically reduces the hydroxyl radical concentration, the degradation was found to be the least [Figure 5.3.7.2(c)].

Additionally, three cycles of the degradation process were run to ensure the stability and reusability of the nps for the MB dyes [Figure 5.3.7.2(d)]. The catalyst nps were recovered after each cycle by centrifugation. The recovered nps were washed with ethanol and DIW, and thereafter dried in a microwave oven. The dried nps were reused for photocatalytic dye degradation. The efficiency of the catalysts nominally decreased (<5%) after three complete cycles, which was due to the loss of nanomaterials during the filtering and washing process.

5.5. Photo-Fenton-Like Degradation Mechanism

The detailed mechanism of dye degradation has been extensively explained in the literature [73]. The role of Fe^{3+} in CuO for catalytic degradation can be explained by the oxidation and reduction capability of the material [Figure 5.3.7.1b]. The position of the valence band (E_{VB}) and the conduction band (E_{CB}) plays an important role is the oxidation-reduction process. The potential of valence band edge (E_{VB}) and conduction band edge (E_{CB}) were measured using the formulas: $E_{VB} = X - E^c + 0.5E_g$ and $E_{CB} = E_{VB} - E_g$, where X is the Mulliken electronegativity of the photocatalyst (5.81 eV for CuO), E^c is the free electron energy (4.5 eV v_s NHE), and E_g is the band gap energy. The values of E_{VB} and E_{CB} for the pure and doped samples were calculated and summarised in Table 5.3.7.1 [182]. It can be observed that the incorporation of Fe^{3+} into the copper oxide system increases its band gap. It also altered the E_{VB} and E_{CB}. The conduction-band and valence-band positions illustrated in Figure 5.3.7.1b were estimated using the Mulliken electronegativity approach described above and the experimentally determined optical bandgap values obtained from DRS measurements.

Table 5.3.7.1: represents the standard EVB and ECB values for different samples.

Sample	E_{VB}	E_{CB}

C0	2.025	0.595
CF1	2.06	0.56
CF2	2.125	0.495

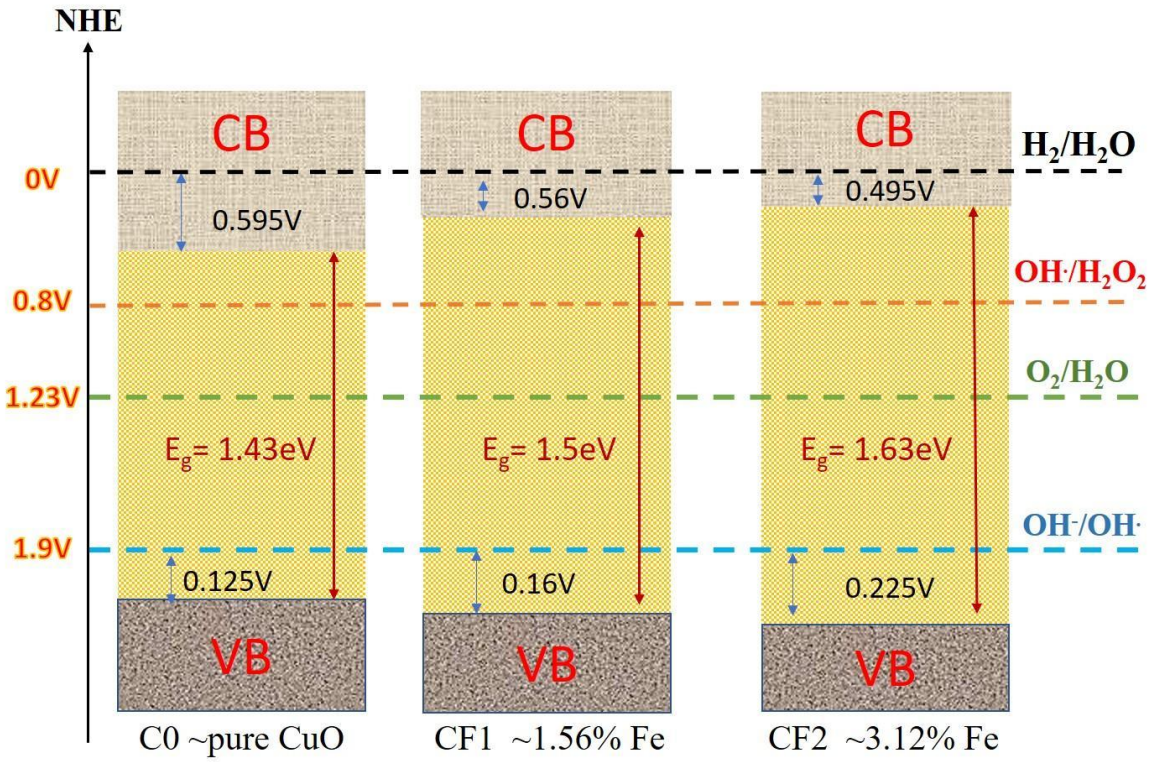


Figure 5.3.7.1b: Schematic illustration of bandedge positions of pure and Fe-doped CuO for Enhancement in the degradation process. Note that the band gap energy (eV) is estimated from the Kubelka-Munk function and the Tauc plot (Figure 5.2.4.1). The NHE scale is referred to as pH 0.

Under visible-light irradiation, Fe-doped CuO absorbs photons and generates electron-hole pairs by exciting the electrons from the VB to the CB. These e-h pairs drive synergistic photo-Fenton-like reactions. Photo-Fenton-like reactions are advanced oxidation processes

(AOPs) that use light with catalysts and H_2O_2 to generate highly reactive hydroxyl radicals for breaking down organic pollutants, enhancing the standard Fenton reaction by using light to regenerate the active catalyst and promote radical formation, often using solid catalysts for easier recovery. The mechanism combines direct photocatalytic ROS generation with classical Fenton-like Cu/Fe-mediated H_2O_2 activation, sustaining a high steady-state concentration of hydroxyl radicals (•OH) responsible for rapid dye degradation.

A. Photoexcitation and Primary Redox Steps

a. Light Absorption and Electron–Hole Pair Generation:

$$Fe - CuO + h\nu \rightarrow Fe - CuO(e_{CB}^{-} + h_{VB}^{+})$$

Here, $h\nu$ is energy of the incident photon and h_{VB}^{+} is the hole in the valence band. Photons with energy ≥ E_g (1.50-1.63 eV for Fe-doped CuO) excite electrons from the valence band to the conduction band, leaving behind hole carriers. Fe incorporation narrows the effective band gap and enhances light absorption in the visible region (455 nm).

b. Valence Band Hole Oxidation:

$$h_{VB}^{+} + H_2O/OH^{-} \rightarrow \bullet OH + H^{+}$$

Photogenerated valence-band holes directly oxidise surface water and hydroxide ions to hydroxyl radicals, which are highly reactive oxidising species.

c. Conduction Band Electron Reduction of Oxygen:

$$e_{CB}^{-} + O_2 \rightarrow \bullet O_2^{-}$$

Conduction-band electrons reduce dissolved oxygen to superoxide radicals, which further undergo protonation and dismutation to generate additional hydroxyl species:

$$\bullet O_2^{-} + H^{+} \rightarrow HO_2^{\bullet}$$

$$2HO_2^{\bullet} \rightarrow H_2O_2 + O_2$$

d. Conduction Band Electron Reduction of H_2O_2:

$$e_{CB}^{-} + H_2O_2 \rightarrow \bullet OH + OH^{-}$$

Electrons also directly reduce H_2O_2 to hydroxyl radicals, providing an additional path for ROS generation.

e. Photogenerated Carrier-Assisted Metal Redox Cycling:

Photogenerated electrons further promote the reduction of lattice Cu^{2+} and Fe^{3+} ions:

$$Cu^{2+} + e_{CB}^{-} \rightarrow Cu^{+}$$

$$Fe^{3+} + e_{CB}^{-} \rightarrow Fe^{2+}$$

This continuous reduction of Cu/Fe centres by photogenerated electrons sustains the Fenton-like catalytic cycle. This photoreduction of Cu^{2+} and Fe^{3+} overcomes the rate-limiting step in traditional dark Fenton reactions, continuously regenerating the highly reactive Cu^{+} and Fe^{2+} species needed for efficient H_2O_2 activation.

B. Cu/Fe-Mediated Fenton-Like Activation of H_2O_2

It was discussed in the XPS section that Fe is present in both Fe^{2+} and Fe^{3+} states, while Cu is predominantly Cu^{2+}. The dominant Cu^{2+}-Fe^{3+} contribution can gain an electron due to the creation of an e-h pair from a neighboring site and get transformed to a Cu^{2+}-Fe^{2+} combination. Also, Cu^{2+} can be transformed to Cu^{+}. Moreover, the H_2O_2 can participate directly in a typical Fenton-like redox reaction, thereby decomposing into highly reactive hydroxyl and hydroperoxyl radicals:

$$Cu^{2+} + H_2O_2 \rightarrow Cu^{+} + \bullet OOH + H^{+}$$

$$Cu^{+} + H_2O_2 \rightarrow Cu^{2+} + \bullet OH + OH^{-}$$

$$Fe^{3+} + H_2O_2 \rightarrow Fe^{2+} + \bullet OOH + H^{+}$$

$$Fe^{2+} + H_2O_2 \rightarrow Fe^{3+} + \bullet OH + OH^{-}$$

These reactions are the core of the Fenton-like mechanism. The key advantages of the photo-Fenton system are that photogenerated electrons continuously regenerate Cu^{+} and Fe^{2+} from their oxidized forms, sustaining a high steady-state concentration of reactive radicals and overcoming the slow Cu^{2+}/Fe^{3+} reduction that limits dark Fenton processes.

C. Propagation and Regeneration of Radicals

The initially formed ·OH and ·OOH radicals can participate in further reactions that amplify ROS production and facilitate radical chain propagation:

$$\bullet OOH + H_2O_2 \rightarrow H_2O + \bullet OH + O_2$$

$$\bullet OH + H_2O_2 \rightarrow H_2O + \bullet OOH$$

Additionally, both Cu and Fe species can participate in scavenging or regenerating radicals:

$$Fe^{2+} + \bullet OH \rightarrow Fe^{3+} + OH^-$$

$$Fe^{3+} + \bullet OOH \rightarrow Fe^{2+} + H^+ + O_2$$

$$Fe^{2+} + \bullet OOH \rightarrow Fe^{3+} + HO_2^-$$

$$Cu^{+} + \bullet OH \rightarrow Cu^{2+} + OH^-$$

$$Cu^{2+} + \bullet OOH \rightarrow Cu^{+} + H^+ + O_2$$

$$Cu^{+} + \bullet OOH \rightarrow Cu^{2+} + HO_2^-$$

These propagation reactions ensure that ROS are continuously generated and recycled, maintaining a high oxidative flux at the catalyst–solution interface.

D. Dye Oxidation and Mineralization

The highly reactive hydroxyl radicals(·OH) are the dominant oxidizing species responsible for MB degradation, as confirmed by scavenger experiments. These radicals attack the aromatic rings and functional groups of MB through electrophilic addition and hydrogen abstraction, leading to stepwise breakdown:

$$\text{MB} + \cdot\text{OH}/\cdot\text{OOH} \rightarrow \text{intermediates} \rightarrow CO_2 + H_2O + \text{inorganic ions}$$

The complete mineralization pathway involves ring opening, demethylation, desulfurization, and eventual conversion of all organic carbon to CO_2 and water, with nitrogen and sulfur released as inorganic ions (NH_4^+, NO_3^-, SO_4^{2-}) [182].

In summary, the exceptional photocatalytic performance of Fe-doped CuO (98.8–99.1% MB degradation in 50 min under low-power blue LED) arises from the following synergistic effects:

- Visible-light photoexcitation generates e^-/h^+ pairs that directly produce ·OH and $\cdot O_2^-$ radicals and simultaneously reduce Cu^{2+}/Fe^{3+} to their highly reactive Cu^+/Fe^{2+} states.
- Continuous photoregeneration of Cu^+ and Fe^{2+} overcomes the rate-limiting step in traditional Fenton reactions, sustaining rapid H_2O_2 decomposition into ·OH and ·OOH.
- The dual Cu^+/Cu^{2+} and Fe^{2+}/Fe^{3+} Fenton couples operate in parallel, increasing the number of active redox sites and enhancing overall ROS generation compared to single-metal systems.
- Fe-induced defect engineering (increased Cu^+/Cu^0-like species, defect-related oxygen, and surface-adsorbed species as shown by XPS) creates additional adsorption and redox-active sites that facilitate H_2O_2 activation and radical stabilization.
- Band-edge tuning maintains favorable alignment with $OH^-/\cdot OH$ and $H_2O_2/\cdot OH$ redox couples, ensuring thermodynamically feasible ROS generation.
- The enhanced surface area (6.4 m^2/g for CF1) and favorable zeta potential (−8 to −15 mV) facilitate efficient MB adsorption and interfacial charge transfer.

This light-mediated photo-Fenton-like mechanism demonstrates that Fe-doped CuO operates as a multifunctional photocatalyst, where visible-light absorption, semiconductor charge separation, and heterogeneous Fenton chemistry are seamlessly integrated. The result is a highly efficient, robust, and practical system for organic pollutant degradation under low-energy illumination (455 nm blue LED), with apparent rate constants (~0.0973 min^{-1}) that are competitive with or exceed those of many reported CuO-based systems operated under UV or high-power visible light. A comparison table from existing literature references with the present work is given in Table 5.3.7.2.

Table 5.3.7.2: Literature comparison table from existing references with the present work

Catalyst/system	**Light source/wavelength range**	**Dye/pollutant**	**Time (min)**	**Degradation (%)**	**k_{app} (min^{-1})**	**Ref**
Mo-doped CuO	Visible (400-700 nm)	MB	150	91	~0.012	[193]
Zn-doped CuO nanosheets	Visible (400-700 nm)	MB	270	66	~0.004	[194]
Fe-doped CuO nanosheets	Visible (400-700 nm)	MB	270	73	~0.005	[194]
Fe-doped CuO thin film (6% Fe)	UV lamp (254-365 nm)	MB	180	≈100	~0.025–0.03	[195]
(Ag,Fe) co-doped CuO NPs	Visible (400-700 nm)	Methyl orange / MB	60–90	>90	~0.02–0.04	[196]

CuO/$Sr_{0.76}Ce_{0.16}WO_4$ (3 wt% CuO)	Visible+H_2O_2 (photo-Fenton) (400-700 nm)	MB	120	~100	0.0127	[197]
Zn-/Fe-doped CuO nanosheets	Visible (400-700 nm)	MB / MG	270	66–73	~0.004–0.005	[198]
CF2	455 nm low-power LED	MB (simulated dye)	50	99.1	0.0973	This Work

The wavelength ranges listed correspond to the dominant emission wavelength or effective spectral range reported for each light source. Inclusion of this information enables a more direct comparison of photocatalytic performance under different excitation conditions, since photon energy and spectral distribution significantly influence photocatalytic reaction kinetics

5.6. Chapter Summary

This chapter investigated the role of redox-active Fe^{3+} substitution in governing the photo-Fenton-like degradation of organic pollutants using CuO-based catalysts under low-power visible-light illumination. Building directly on the defect-engineering approach established for Al^{3+}-doped CuO in Chapter 3 and the temperature-dependent kinetic analysis of pure CuO nanosheets in Chapter 4, this study was designed to isolate how dopant redox chemistry fundamentally modifies photocatalytic reaction pathways.

Fe-substituted CuO nanostructures were synthesized via a scalable sol–gel route, yielding phase-pure materials with controlled dopant incorporation. Structural, optical, and surface analyses confirmed the substitutional incorporation of Fe^{3+} within the CuO lattice, accompanied by enhanced lattice disorder, modified Cu–O coordination, and increased defect

density. These changes led to pronounced modulation of the electronic structure and surface redox states, directly influencing the activation of hydrogen peroxide and the generation of reactive oxygen species.

Photocatalytic degradation studies revealed that Fe-doped CuO exhibits significantly enhanced degradation rates compared to both pristine CuO and Al-doped CuO under comparable operating conditions. Unlike the thermally assisted enhancement observed for pure CuO nanosheets, the performance improvement in Fe-doped systems was achieved without reliance on elevated reaction temperatures, indicating a mechanistic shift toward dopant-assisted redox activation. Radical scavenging experiments identified hydroxyl radicals as the dominant reactive species, highlighting the crucial role of Fe^{3+}/Fe^{2+} redox cycling in sustaining efficient photo-Fenton-like reactions.

Stability, recyclability, and leaching analyses demonstrated that Fe-doped CuO maintains structural integrity and catalytic activity over repeated cycles with minimal metal release, underscoring its suitability for practical wastewater treatment applications. Overall, this chapter establishes redox-active dopant engineering as a more effective strategy than thermal activation alone for enhancing photo-Fenton-like processes in CuO-based systems. The effectiveness of Fe^{3+} substitution in promoting photo-Fenton activity further highlights the importance of dopant valency and d-electron configuration in stabilizing oxidized surface states and facilitating redox cycling within the CuO lattice. This observation suggests that dopants with different valence states relative to the Cu^{2+} ($3d^9$) host are likely to influence oxidation and reduction reactions in fundamentally different ways. A systematic examination of this valence-dependent behaviour under electrochemical bias is therefore undertaken in the subsequent chapters.

Chapter 6 Resolving Oxidation-Side Catalytic Bottlenecks in Alkaline Oxygen Evolution Using Fe-Substituted CuO

Abstract: *The electrochemical oxygen evolution reaction (OER) represents a major kinetic bottleneck in alkaline water electrolysis due to its multistep proton-coupled electron transfer (PCET) mechanism and the requirement to form high-energy oxygenated intermediates. Within the bottleneck-driven framework of this thesis, this chapter investigates how higher-valent Fe^{3+} substitution redistributes oxidation-side kinetic limitations in CuO-based electrocatalysts under electrochemical bias. Building on Chapter 5, where Fe^{3+} was shown to enhance light-driven oxidation via redox accessibility, the present chapter tests whether similar electronic modulation alleviates oxidation bottlenecks during electrocatalytic OER.*

Electrochemical impedance spectroscopy measured at 0.65 V vs Hg/HgO in 1 M KOH, combined with distribution of relaxation time (DRT) analysis, resolves distinct kinetic regimes associated with double-layer charging, interfacial proton–electron transfer, and slower surface-reaction steps. Moderate Fe^{3+} substitution enhances redox accessibility and reduces interfacial charge transfer resistances, thereby alleviating dominant oxidation bottlenecks. However, further increases in Fe content led to over-stabilisation of oxygenated intermediates, resulting in a promoter–inhibitor crossover and diminished catalytic efficiency. These findings establish dopant-valency-controlled redox accessibility as a reaction-specific design parameter for oxidation electrocatalysis.

6.1. Chapter Introduction and Objectives

The electrochemical oxygen evolution reaction (OER) is widely recognized as the principal kinetic bottleneck in alkaline water electrolysis due to its complex multistep proton-coupled electron transfer (PCET) mechanism and the requirement to form and stabilize high-energy oxygenated intermediates [199], [200], [201]. For earth-abundant transition-metal oxides, achieving high OER activity while maintaining structural and kinetic stability remains a central challenge. Conventional optimisation strategies based solely on increasing surface area, conductivity, or nominal oxidation state often fail to address the fundamental kinetic limitations

governing OER under operating conditions.

In earlier chapters of this thesis, distinct catalytic bottlenecks associated with oxidation chemistry were identified under non-electrochemical conditions. Chapter 5 demonstrated that photo-Fenton-like degradation on CuO is governed by the accessibility of redox-active surface states and efficient charge separation rather than thermal activation alone. These findings highlighted the critical role of dopant-induced electronic modulation in facilitating oxidation pathways. Under electrochemical bias, however, additional constraints emerge, including interfacial charge-transfer resistance and surface-reaction kinetics, which cannot be resolved through static structural or spectroscopic characterisation alone.

CuO serves as a particularly instructive model system for probing oxidation-side electrocatalytic bottlenecks. As a p-type semiconductor with a Cu^{2+} ($3d^9$) electronic configuration, CuO exhibits strong lattice distortion and limited intrinsic conductivity, which together impose significant barriers to OER kinetics [202], [203].

Dopant substitution offers a rational strategy to overcome these limitations by modifying local electronic structure, redox accessibility, and metal-oxygen bonding characteristics. Among potential dopants, Fe^{3+} is of particular interest due to its higher valency relative to Cu^{2+} and its ability to participate in reversible redox processes, which are essential for oxidation reactions [204], [205], [206]. The high-spin d^5 configuration of Fe^{3+} further provides an optimal balance between metal-oxygen covalence and redox flexibility, enabling stabilisation of *OH, *O, and *OOH species without excessive localisation of oxidising equivalents[207]. Moreover, Fe incorporation is known to soften metal-oxygen bonding [208], [209] and lower the formation energy of oxygen vacancies, potentially promoting the lattice oxygen mechanism (LOM) or a hybrid of the adsorption-exchange mechanism (AEM) and LOM [210].

Despite extensive reports on Fe-containing oxide catalysts for OER [211], [212], a critical unresolved question remains: *which specific catalytic bottlenecks are alleviated by Fe substitution, and under what conditions does such substitution become inhibitory rather than promotive?* Addressing this question requires moving beyond apparent activity metrics and surface descriptors toward a kinetic framework capable of deconvoluting interfacial and surface-reaction processes under operating conditions.

Although CuO is a p-type oxide and has also been explored for HER-related applications, the

present chapter intentionally focuses on OER because oxygen evolution represents the major oxidation-side kinetic bottleneck in alkaline water electrolysis. Here, CuO is used as a semiconducting model oxide to investigate how Fe-induced electronic modification redistributes interfacial charge-transfer and surface-reaction limitations under anodic bias, rather than as a benchmark industrial OER catalyst.

Accordingly, this chapter adopts an impedance-resolved approach to systematically identify and quantify oxidation-side bottlenecks in Fe-substituted CuO electrocatalysts under alkaline conditions. Electrochemical impedance spectroscopy measured at an OER-relevant applied potential, combined with distribution of relaxation time (DRT) analysis and complementary electronic-structure insights, enables the separation of double-layer charging, interfacial PCET, and slower surface-reaction-limited steps [213], [214], [215]. This approach reveals a promoter–inhibitor crossover as a function of Fe content, demonstrating that enhanced redox accessibility alone is insufficient for sustained OER activity if oxygenated intermediates become over-stabilised [216], [217].

Within the broader narrative of this thesis, this chapter extends the oxidation-focused bottleneck framework established in Chapter 5 to electrochemical conditions and provides mechanistic insight that informs ongoing investigations of reduction-side catalytic limitations.

Position of Chapter 6 in the Thesis Narrative:

Earlier chapters of this thesis systematically identified and addressed distinct catalytic bottlenecks across different reaction regimes. Chapter 3 established how defect engineering via Al^{3+} substitution alleviates charge-separation limitations in photocatalytic degradation. Chapter 4 isolated the role of thermal activation in overcoming kinetic constraints in pristine CuO nanosheets. Chapter 5 demonstrated that photo-Fenton activity in Fe-substituted CuO is governed by redox accessibility rather than thermal effects alone.

The present chapter extends this bottleneck-oriented progression to electrocatalytic oxygen evolution under alkaline bias, where additional constraints arise from interfacial charge transfer and surface reaction kinetics. By resolving these oxidation-side bottlenecks through impedance-resolved analysis, this chapter shows that redox-active dopants can either promote or inhibit OER, depending on which kinetic limitation dominates.

Together, Chapters 5 and 6 establish a unified, oxidation-focused framework that shows that dopant-controlled electronic structure must be matched to reaction-specific kinetic requirements. These insights motivate further investigation of reduction-side bottlenecks being addressed in subsequent ongoing work.

Objectives and Scope

The primary objective of this chapter is to identify and resolve oxidation-side catalytic bottlenecks governing the alkaline oxygen evolution reaction (OER) in CuO-based electrocatalysts. Rather than optimizing OER performance solely through empirical material modification, this study seeks to disentangle the specific kinetic and interfacial processes that limit catalytic efficiency under electrochemical bias.

The specific objectives of this chapter are to:

- Examine how Fe^{3+} substitution in CuO influences oxidation-side kinetics relative to the Cu^{2+} ($3d^9$) host lattice.
- Deconvolute interfacial charge-transfer and surface-reaction limitations using electrochemical impedance spectroscopy measured at a fixed OER-relevant applied potential and DRT analysis.
- Identify the mechanistic origin of the promoter–inhibitor crossover observed with increasing Fe content.
- Establish dopant-valency-controlled redox accessibility as a governing design parameter for oxidation reactions in CuO-based electrocatalysts.

The scope of this chapter is limited to alkaline OER under steady electrochemical bias and focuses on kinetic and interfacial bottlenecks. Long-term device durability, full electrolyzer optimization, and overall water-splitting performance are not treated as primary objectives. Reduction reactions and lower-valent dopant effects fall outside the present scope and are considered separately in ongoing and future investigations.

6.2. Synthesis and Electrochemical Experimental Methods

The synthesis of pristine and Fe-substituted CuO nanostructures, together with electrode fabrication procedures and electrochemical measurement protocols for alkaline OER, is

described in detail in **Chapter 2**. To avoid redundancy, the present chapter does not repeat these methodological details. Instead, the focus here is placed on the analysis and interpretation of OER performance and impedance-resolved kinetic behaviour, with particular emphasis on identifying oxidation-side catalytic bottlenecks.

6.3. Results and Discussion

6.3.1. Structural and Electronic Baseline: Context for Oxidation Kinetics

Before examining oxidation-side electrocatalytic bottlenecks, it is essential to establish the structural and electronic baseline of pristine and Fe-substituted CuO electrocatalysts. This section provides the necessary context for interpreting kinetic behaviour under electrochemical bias, while explicitly distinguishing between static descriptors and dynamic catalytic limitations.

X-ray diffraction and vibrational spectroscopic analyses confirm that Fe substitution does not disrupt the monoclinic CuO crystal framework, indicating that the observed electrocatalytic trends arise from electronic and interfacial modulation rather than phase transformation or secondary phase formation. The crystallite size and lattice strain remain essentially invariant across the series, ruling out significant morphological restructuring as the origin of catalytic differences. Raman and infrared features further suggest subtle local perturbations in the Cu–O lattice upon Fe incorporation, consistent with dopant-induced modification of the metal–oxygen bonding environment without altering the bulk phase integrity.

Nitrogen adsorption–desorption analysis reveals an increase in BET surface area upon Fe substitution, with CF1 exhibiting the highest surface area, followed by CF2 and pristine CuO. Although this increase indicates enhanced geometric surface accessibility, the non-monotonic OER activity trend observed in subsequent sections demonstrates that surface area alone does not govern catalytic performance.

To further evaluate accessible active surface sites under electrochemical conditions, the electrochemically active surface area (ECSA) was estimated from double-layer capacitance measurements. Fe incorporation increases C_{dl} relative to pristine CuO, confirming the presence of enhanced electrochemically accessible surface sites. However, the activity trend does not scale proportionally with either BET surface area or ECSA, indicating that oxidation kinetics

are not controlled solely by surface site density.

Surface-sensitive spectroscopic analysis reveals that Fe substitution modifies the electronic landscape of CuO by altering oxygen coordination environments and charge-screening behaviour within the Cu–O network. Variations in relative oxygen species (e.g., O_D/O_L ratios) and Cu 2p satellite-to-main peak intensity descriptors indicate changes in surface redox accessibility with increasing Fe content. These trends are consistent with the higher valency of Fe^{3+} relative to the Cu^{2+} ($3d^9$) host lattice and suggest enhanced stabilisation of oxidized surface states at moderate substitution levels.

While such structural and electronic descriptors provide insight into potential redox activation, they remain fundamentally static and cannot capture the dynamic interplay between interfacial charge transfer, proton-coupled electron transfer, and surface-reaction kinetics that govern OER under bias. The absence of direct correlation between these baseline descriptors and apparent catalytic activity underscores the need for a kinetic framework capable of resolving competing rate-limiting processes.

Accordingly, the following section first examines apparent OER activity using conventional polarization metrics, then transitions to impedance-resolved kinetic analysis.

6.3.2. Apparent OER Performance

Having established that structural and surface electronic descriptors do not directly predict OER behaviour, the apparent electrochemical performance of the catalysts is first evaluated using conventional metrics.

The alkaline OER performance of pristine CuO (C0) and Fe-substituted samples (CF1: x = 0.0156; CF2: x = 0.0312) was first evaluated using conventional electrochemical metrics to establish apparent activity trends prior to kinetic deconvolution. Linear sweep voltammetry in 1 M KOH reveals a clear enhancement in activity upon moderate Fe substitution, followed by partial deterioration at higher Fe loading.

CF1 exhibits the lowest overpotential, requiring 338 mV to achieve 10 mA cm^{-2}, compared with 415 mV for pristine C0 and 367 mV for CF2 [Figure 6.3.2.1(a)]. This non-monotonic trend immediately indicates that Fe substitution does not lead to a simple linear improvement

in OER performance but rather introduces an optimal compositional window.

Tafel analysis further supports this observation. The Tafel slope decreases substantially from 117 mV dec^{-1} (C0) to 69 mV dec^{-1} (CF1), indicating improved reaction kinetics at moderate Fe content. However, at higher substitution (CF2), the Tafel slope increases again to 103 mV dec^{-1}, suggesting that kinetic facilitation is not sustained with further Fe incorporation [Figure 6.3.2.1 (b)].

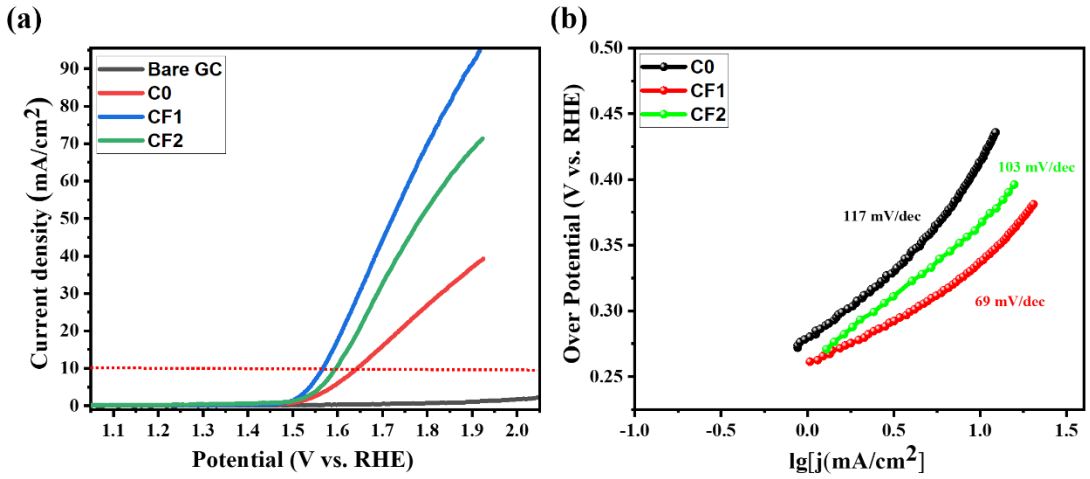


Figure 6.3.2.1: (a) Linear sweep voltammetry curves of C0, CF1, and CF2 in 1 M KOH. (b) Corresponding Tafel plots extracted from the linear kinetic region. Moderate Fe substitution (CF1) exhibits reduced overpotential and lower Tafel slope relative to pristine CuO, while higher Fe loading (CF2) results in partial kinetic deterioration, indicating a promoter–inhibitor crossover.

To determine whether differences in accessible surface area account for this activity trend, the electrochemically active surface area (ECSA) was estimated from double-layer capacitance measurements. Fe incorporation increases C_{dl} relative to pristine CuO, confirming the presence of enhanced electrochemically accessible surface sites. However, although CF2 retains substantially higher ECSA and BET surface area than C0, it does not outperform CF1 in OER activity. This demonstrates that surface area, whether geometric (BET) or electrochemically estimated (ECSA) is not the governing descriptor for catalytic performance.

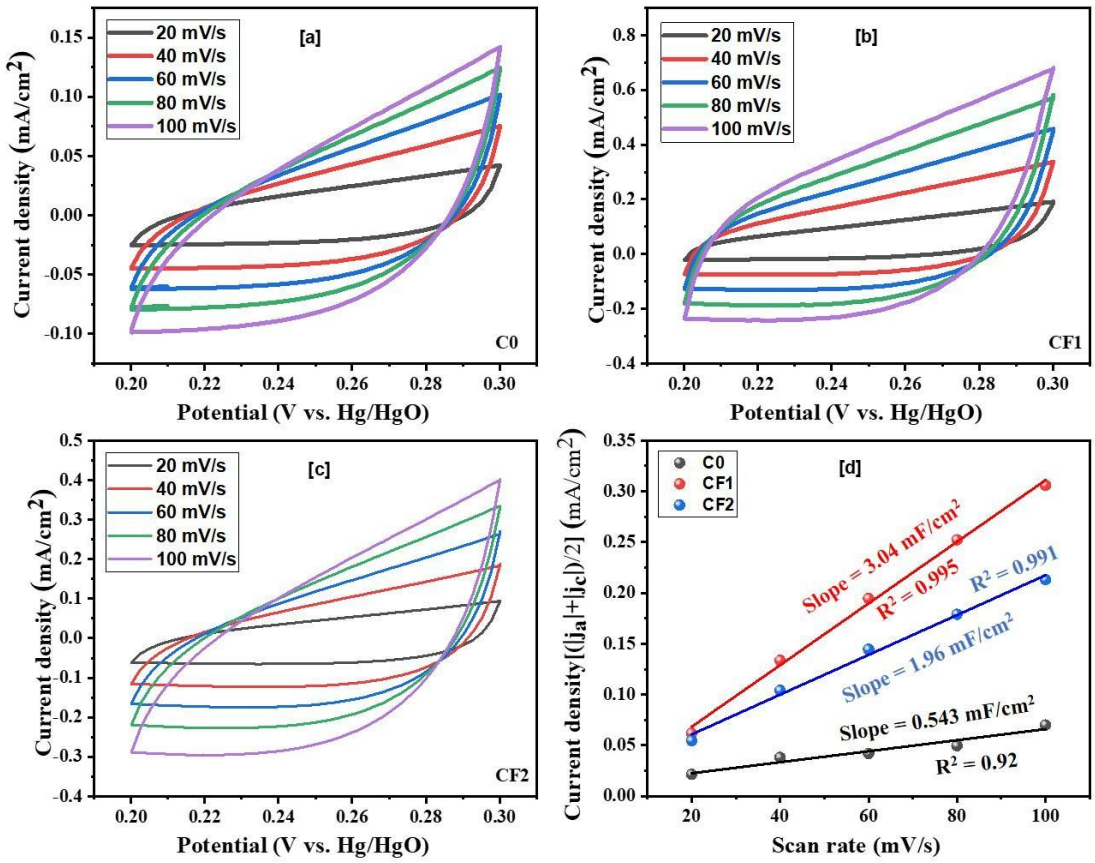


Figure 6.3.2.2: (a–c) Cyclic voltammograms recorded in the non-Faradaic potential region at varying scan rates (20-100 mV s^{-1}) for (a) pristine CuO (C0), (b) CF1 (x = 0.0156), and (c) CF2 (x = 0.0312) in 1 M KOH. (d) Corresponding double-layer capacitance (C_{dl}) plots obtained from the linear relationship between capacitive current density and scan rate, used to estimate the electrochemically active surface area (ECSA).

Similarly, structural parameters such as crystallite size and lattice strain remain essentially invariant across the series, ruling out morphological effects as the dominant factor. Collectively, these observations indicate that the non-monotonic activity behaviour arises from a redistribution of underlying kinetic limitations rather than a simple increase in active site density.

At this stage, overpotential and Tafel slope establish the existence of a promoter–inhibitor crossover but do not reveal its mechanistic origin. These global kinetic descriptors cannot distinguish whether performance is limited by interfacial proton–electron transfer, charge-

transfer resistance at the catalyst–electrolyte interface, or slower surface-reaction steps involving oxygenated intermediates.

Accordingly, impedance-resolved analysis is required to deconvolute these overlapping contributions and identify the dominant oxidation-side bottlenecks under OER-relevant bias.

6.3.3. Impedance-Resolved Kinetic Analysis of Oxidation-Side Bottlenecks

Unlike overpotential or Tafel analysis, impedance spectroscopy enables separation of overlapping processes occurring across different characteristic time scales, thereby providing mechanistic insight into interfacial and surface-reaction dynamics under electrochemical bias.

6.3.3.1. Impedance-Resolved Kinetic Analysis of Oxidation-Side Bottlenecks

To resolve the kinetic origins of the promoter–inhibitor crossover observed in polarization measurements, electrochemical impedance spectroscopy (EIS) was measured at 0.65 V vs Hg/HgO in 1 M KOH. The resulting Nyquist plots (Figure 6.3.3.1) exhibit two distinguishable semicircular features across the catalyst series, indicating the presence of multiple kinetically significant processes.

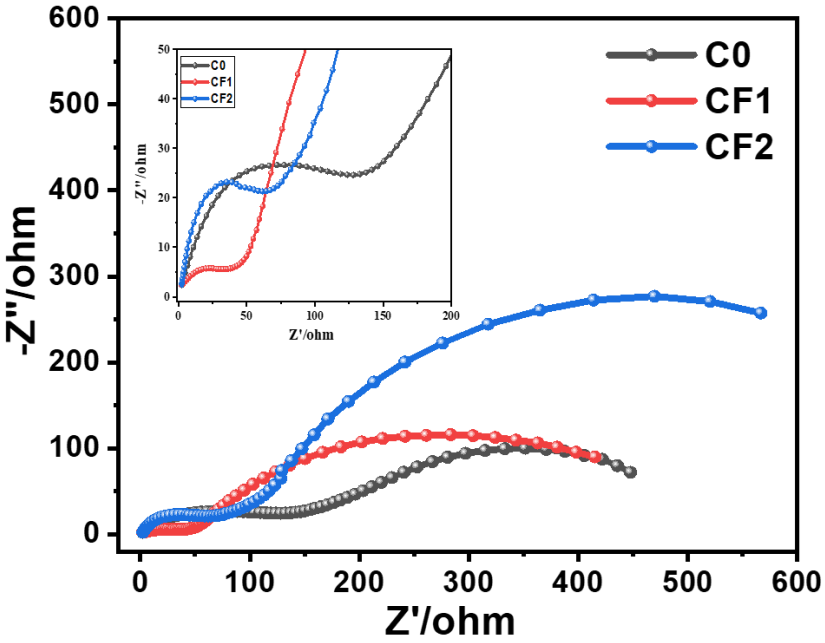


Figure 6.3.3.1: Nyquist plots of pristine CuO (C0) and Fe-substituted samples CF1 (x = 0.0156) and CF2 (x = 0.0312) measured at 0.65 V vs Hg/HgO in 1 M KOH. The impedance response exhibits two distinguishable frequency-dependent features across the catalyst series. Moderate Fe substitution (CF1) shows a reduced overall semicircle relative to pristine CuO, indicating lower kinetic resistance, whereas higher Fe loading (CF2) displays an increased low-frequency contribution, suggesting redistribution of oxidation-side kinetic limitations.

Pristine CuO (C0) displays the largest overall impedance response, consistent with substantial kinetic resistance under oxidation bias. Upon moderate Fe substitution (CF1), the overall semicircle diameter decreases markedly, indicating reduced kinetic resistance. However, at higher Fe loading (CF2), although the impedance response remains smaller than that of pristine CuO, an increased low-frequency contribution becomes evident, suggesting redistribution of the dominant kinetic limitation.

These qualitative differences indicate that Fe substitution alters not only the magnitude of resistance but also the relative contributions of distinct electrochemical processes governing OER.

6.3.3.2. Equivalent Circuit Fitting and Resistance Deconvolution

To quantitatively interpret the impedance response, the spectra were fitted using an equivalent circuit model consisting of a solution resistance (R_1) in series with three parallel R–CPE elements representing high-, mid-, and low-frequency processes, respectively (Figure 6.3.3.2). The fitted curves reproduce the experimental data closely, confirming the validity of the multi-time-constant interpretation.

The high-frequency resistance component (R_2) is primarily associated with interfacial charge-transfer processes involving proton-coupled electron transfer at the catalyst–electrolyte interface. The intermediate-frequency component (R_3) reflects coupled interfacial and surface processes, while the low-frequency component (R_4) corresponds to slower surface-reaction or mass-transport-coupled steps related to the formation and transformation of oxygenated intermediates.

Quantitative comparison of fitted resistance values reveals a non-monotonic dependence on Fe content. Moderate Fe substitution (CF1) significantly reduces the interfacial resistance component relative to pristine CuO, consistent with enhanced redox accessibility and improved electronic communication within the Cu–O lattice. However, at higher Fe loading (CF2), although interfacial resistance remains lower than that of C0, the intermediate-frequency resistance component (R_3) increases substantially, indicating the emergence of a surface-reaction–limited regime despite continued reduction in interfacial resistance.

The Bode response (Figure 6.3.3.3) further confirms the redistribution of characteristic relaxation frequencies, with CF1 exhibiting faster relaxation behaviour compared to both C0 and CF2. This redistribution of resistance components provides the first mechanistic indication of a promoter–inhibitor crossover driven by dopant concentration.

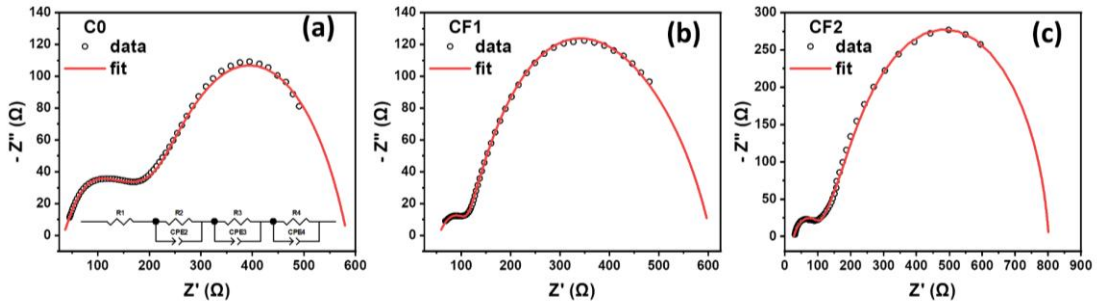


Figure 6.3.3.2: Nyquist plot of the electrochemical impedance spectroscopy (EIS) data fitted using an equivalent circuit consisting of a series resistance (R1) and three parallel resistances (R) - constant phase element (CPE) elements. The symbols represent the experimental impedance data, while the solid red line corresponds to the fitted response. The series resistance (R_1) accounts for the solution and contact resistance. In contrast, the three R-CPE elements describe charge transfer, interfacial processes, and low-frequency contributions to surface-reaction and mass-transport-coupled processes.

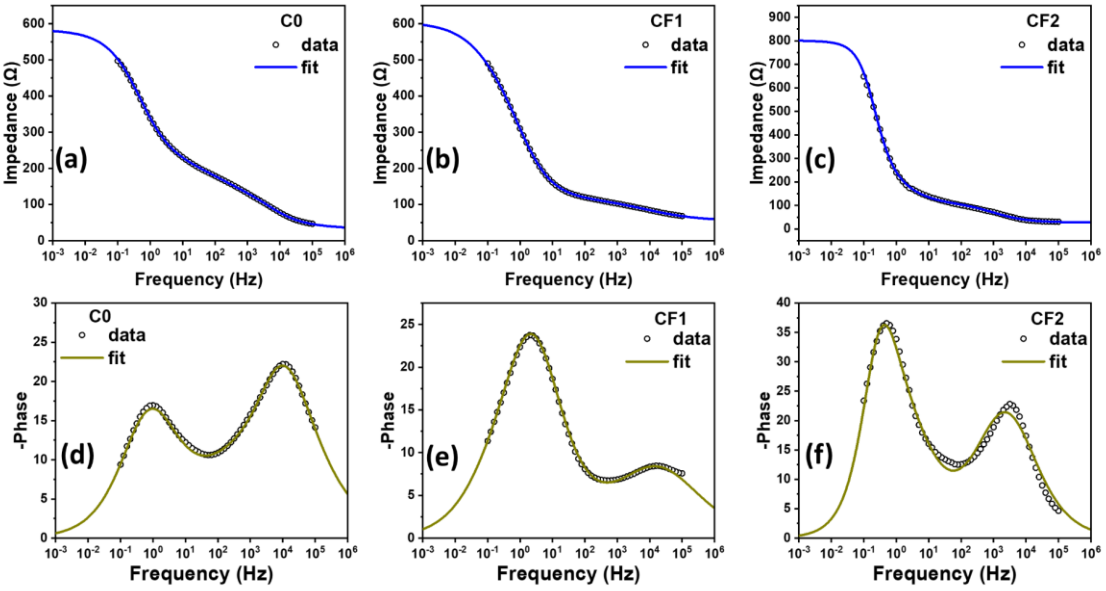


Figure 6.3.3.3: Bode plots (|Z| vs. frequency and phase angle vs. frequency) for three different samples, measured over the same frequency range. The symbols represent the experimental impedance data, while the solid red line corresponds to the fitted response.

Table 6.3.3.1: Fitted electrochemical impedance spectroscopy (EIS) parameters for C0, CF1, and CF2 catalysts measured at 0.65 V vs Hg/HgO in 1 M KOH using an equivalent circuit comprising three parallel R-CPE elements connected in series with the solution resistance, representing high-, mid-, and low-frequency processes, respectively.

Sample	**R_1**	**R_2**	**CPE_2-T (10^{-5})**	**CPE_2-P**	**R_3**	**CPE_3-T (10^{-5})**	**CPE_3-P**	**R_4**	**CPE_4-T (10^{-5})**	**CPE_4-P**
C0	32.67	149	33.083	0.41291	351.2	160.28	0.66525	50.94	1.0017	0.73573
CF1	54.86	61.18	10.918	0.46525	313.1	107.25	0.67266	175.7	701.96	0.59592
CF2	27.7	80.23	5.0051	0.64575	588.4	164.13	0.92783	105.5	197.02	0.62755

6.3.3.3. Distribution of Relaxation Time (DRT) Analysis

While equivalent circuit fitting provides quantitative resistance values, overlapping frequency domains can obscure the precise separation of electrochemical processes. To validate and refine the kinetic interpretation without imposing predefined circuit constraints, distribution of relaxation time (DRT) analysis was performed.

The DRT spectra (Figure 6.3.3.4) reveal three dominant relaxation regimes corresponding to high-, mid, and low-frequency processes. The high-frequency peak is attributed to double-layer and rapid interfacial charge-transfer contributions, the mid-frequency peak corresponds to

proton–electron transfer and surface activation processes, and the low-frequency peak is associated with slower surface-reaction and mass-transport-coupled processes.

Although mass-transport-coupled processes contribute to the low-frequency impedance response, the relatively thin catalyst layer and stirred electrolyte conditions employed in this study minimize external diffusion limitations. Consequently, the dominant bottlenecks identified here arise primarily from interfacial and surface-reaction kinetics rather than bulk mass transport constraints.

Moderate Fe substitution (CF1) suppresses the intensity of the interfacial relaxation peak relative to pristine CuO, confirming reduced interfacial resistance. In contrast, higher Fe loading (CF2) exhibits an enhanced, slower relaxation contribution consistent with the substantial increase in R_3 extracted from circuit fitting. This behaviour indicates that excessive Fe incorporation shifts the dominant bottleneck toward surface-reaction-limited processes rather than interfacial charge transfer.

Importantly, these DRT results corroborate the resistance trends obtained from equivalent circuit fitting and confirm that the non-monotonic OER activity arises from redistribution of kinetic limitations rather than uniform acceleration of all electrochemical steps.

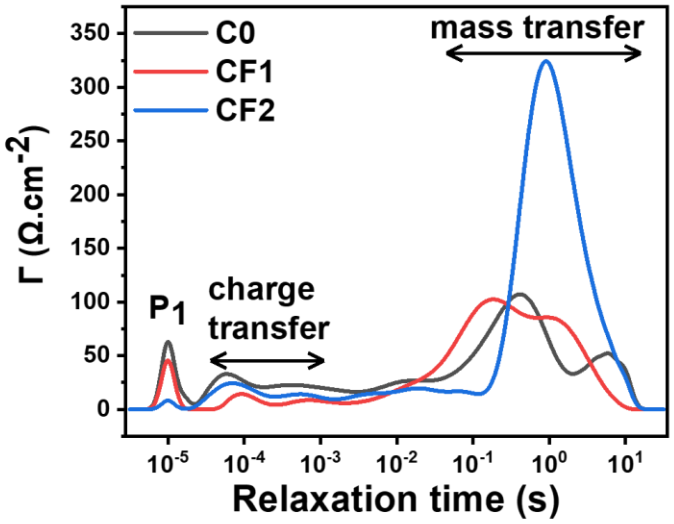


Figure 6.3.3.4: DRT spectra derived from electrochemical impedance measurements of pristine CuO (C0), moderately Fe-substituted CuO (CF1), and higher Fe-loaded CuO (CF2)

recorded at 0.65 V vs Hg/HgO in 1 M KOH. Distinct relaxation regimes are observed across high-, intermediate-, and low-frequency domains. Moderate Fe substitution (CF1) suppresses interfacial relaxation intensity relative to C0, while higher Fe loading (CF2) exhibits a pronounced intermediate-frequency relaxation contribution, consistent with the redistribution of impedance components identified through equivalent circuit analysis.

6.3.4. Promoter–Inhibitor Crossover and Dopant-Valency Effects

The combined polarization and impedance analyses establish the existence of a promoter–inhibitor crossover as a function of Fe substitution in CuO. Moderate Fe incorporation (CF1) enhances OER performance, whereas higher substitution levels (CF2) result in partial kinetic deterioration despite continued electronic modification of the surface.

Equivalent circuit fitting reveals that CF1 exhibits a substantial reduction in the interfacial resistance component (R_2) relative to pristine CuO, indicating improved charge-transfer efficiency across the catalyst–electrolyte interface. This behaviour is consistent with enhanced redox accessibility induced by Fe^{3+} substitution within the Cu–O lattice. The higher valency of Fe^{3+} relative to the Cu^{2+} host promotes electronic redistribution and facilitates proton-coupled electron transfer processes, thereby alleviating the interfacial kinetic bottleneck that dominates in pristine CuO.

However, further increase in Fe content (CF2) does not lead to continued improvement. Instead, impedance analysis reveals a pronounced increase in the intermediate-frequency resistance component (R_3), indicating the emergence of a surface-reaction–limited regime. This increase occurs despite R_2 remaining lower than that of pristine CuO, demonstrating that the dominant kinetic limitation shifts from interfacial charge transfer to surface-reaction processes involving oxygenated intermediates.

Surface-sensitive XPS analysis supports this interpretation. Fe substitution alters the relative abundance of defect-related oxygen species (O_D/O_L ratio) and shifts the Cu 2p satellite features, indicating increased stabilization of oxidized surface states. While moderate stabilization enhances redox accessibility and facilitates early oxidation steps, excessive stabilization at higher Fe loadings likely increases the energetic barrier to the turnover of key oxygenated intermediates.

Density functional theory calculations further corroborate this trend. At moderate Fe substitution, adsorption energies of OER intermediates approach thermoneutral values, lowering the theoretical overpotential. At higher substitution, however, stronger binding of intermediates, particularly at Fe-influenced sites, leads to over-stabilization of the potential-determining step, increasing the thermodynamic barrier for subsequent transformation.

Collectively, these results demonstrate that Fe^{3+} substitution acts as a redox promoter only within an optimal compositional window. Beyond this threshold, excessive electronic perturbation redistributes the dominant kinetic bottleneck toward slower surface-reaction steps, thereby reducing overall catalytic efficiency. The promoter–inhibitor crossover, therefore, arises not from structural degradation or loss of active surface area, but from valency-controlled redistribution of oxidation-side kinetic limitations.

This finding establishes dopant valency as a reaction-specific design parameter: higher-valent substitution can alleviate interfacial charge-transfer resistance but must be balanced against the risk of over-stabilizing oxygenated intermediates that govern surface-reaction kinetics.

Thus, the promoter–inhibitor crossover is governed by a redistribution of rate-determining steps rather than by structural degradation or active-site loss.

6.3.5. Mechanistic Framework: Electronic Structure–Kinetics Coupling in Fe-Substituted CuO

The impedance-resolved analysis established that Fe substitution redistributes the dominant oxidation-side kinetic bottleneck from interfacial charge-transfer control (C0) to surface-reaction-limited behaviour (CF2). To rationalize this redistribution mechanistically, surface electronic descriptors derived from XPS are integrated with density functional theory (DFT) calculations to link dopant-induced electronic modulation with experimentally observed resistance components.

6.3.5.1. Surface Electronic Descriptors and Interfacial Kinetics

X-ray photoelectron spectroscopy confirms that Fe substitution does not introduce secondary phases but modifies the local Cu–O electronic environment. The high-resolution Cu 2p and O 1s spectra for pristine and Fe-substituted CuO samples are shown in Figure 6.3.5.1.

Deconvolution reveals systematic variation in the relative contributions of lattice oxygen (O_L), defect- or ligand-hole-associated oxygen species (O_D), and adsorbed oxygen components (O_{ads}), alongside subtle modulation of Cu 2p satellite intensity and screening behaviour.

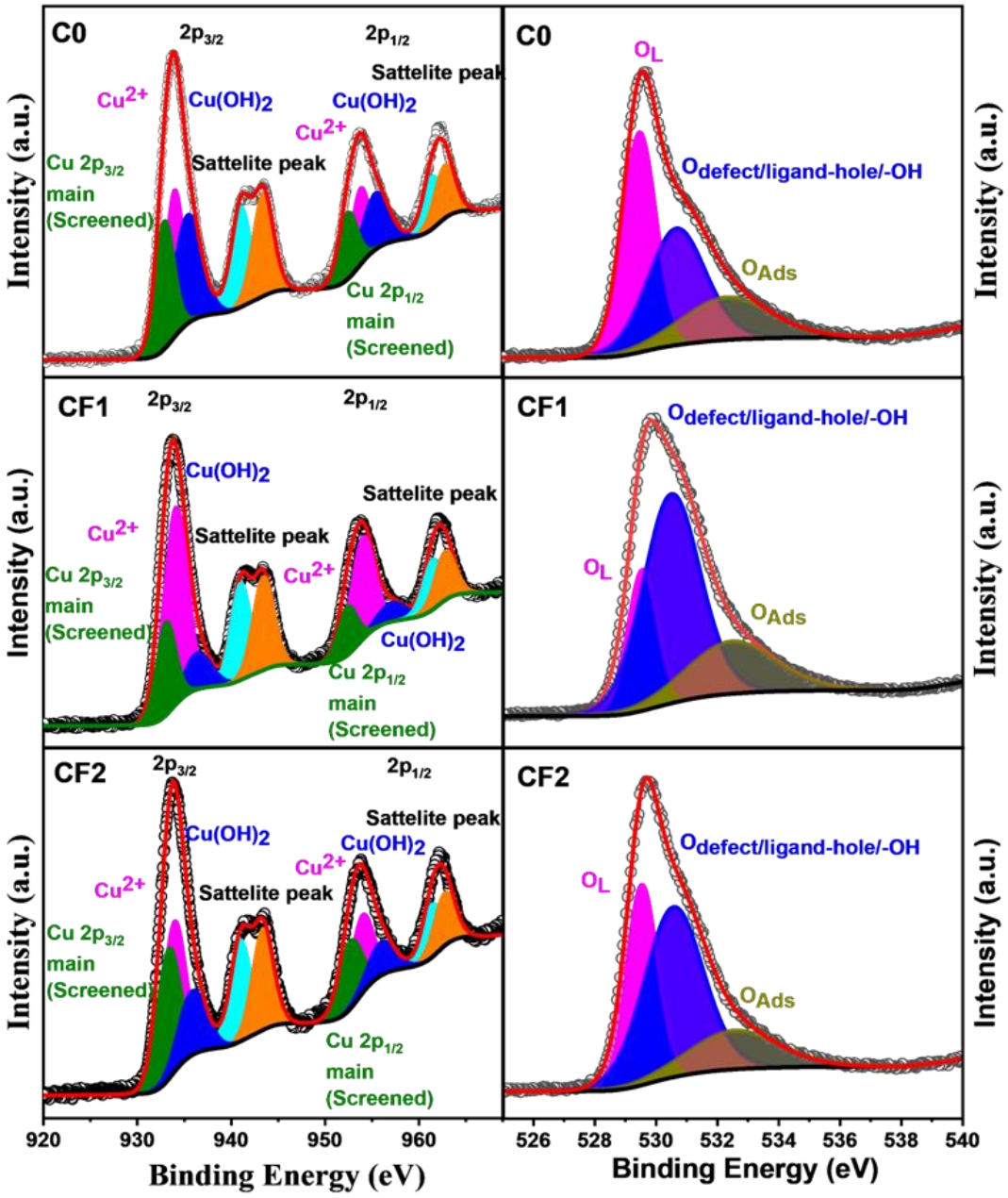


Figure 6.3.5.1: High-resolution XPS spectra of (left) Cu 2p and (right) O 1s regions for pristine CuO (C0), moderately Fe-substituted CuO (CF1), and higher Fe-loaded CuO (CF2). Deconvolution reveals systematic variation in defect- or ligand-hole-associated oxygen species (O_D) and satellite screening features upon Fe substitution. The evolution of O_D/O_L ratios

correlates with impedance-derived redistribution of interfacial (R_2) and surface-reaction (R_3) resistance components.

Analysis of the O 1s spectra reveals systematic variation in the ratio of defect-related oxygen species (O_D) to lattice oxygen (O_L). Moderate Fe substitution (CF1) exhibits the highest O_D/O_L ratio relative to pristine CuO, indicating enhanced stabilization of oxygen-associated surface states. At higher Fe loading (CF2), this ratio decreases relative to CF1, suggesting a non-monotonic evolution of surface oxygen coordination environments. The evolution of defect- or ligand-hole-associated oxygen components in the O 1s spectra suggests that Fe substitution modulates the Cu–O charge-transfer network, thereby altering ligand-hole density and influencing interfacial charge-transfer resistance during alkaline OER.

Complementary analysis of Cu 2p satellite-to-main peak intensity ratios further indicates altered charge-screening behaviour within the Cu–O network upon Fe incorporation. While CF1 retains satellite characteristics comparable to pristine CuO, higher Fe loading results in a reduction in satellite intensity, consistent with increased electronic delocalization and modified ligand–metal interactions.

Direct spectroscopic confirmation of Cu(III) formation was not carried out in the present work. Therefore, any discussion of Cu(III)-like or highly oxidized Cu–O states is based on established CuO OER literature and should be regarded as a plausible mechanistic interpretation rather than direct experimental confirmation.

These electronic trends correlate directly with the interfacial resistance component (R_2) extracted from equivalent circuit fitting. The substantial reduction in R_2 for CF1 reflects improved proton–electron transfer kinetics across the catalyst–electrolyte interface. The enhanced O_D/O_L ratio and the modified charge-screening environment at moderate Fe substitution, therefore, provide a surface-electronic basis for alleviating interfacial kinetic limitations. Importantly, although CF2 maintains lower interfacial resistance than pristine CuO, further electronic perturbation does not translate into continued performance enhancement, indicating the emergence of a different dominant bottleneck.

To directly correlate surface electronic descriptors with impedance-resolved kinetic parameters, the key spectroscopic and electrochemical metrics are summarized in Table

6.3.5.1.

Table 6.3.5.1: Correlation between surface electronic descriptors derived from XPS and impedance-extracted kinetic parameters for pristine CuO (C0) and Fe-substituted samples (CF1 and CF2) measured at 0.65 V vs Hg/HgO in 1 M KOH. The table highlights the non-monotonic relationship between dopant-induced electronic modulation (O_D/O_L ratio and Cu 2p satellite-to-main peak intensity ratio) and redistribution of interfacial (R_2) and surface-reaction (R_3) resistive components, illustrating the promoter–inhibitor crossover in alkaline OER.

Sample	**Overpotential @10 mA cm^{-2} (mV)**	**R_2 (Ω) – Interfacial**	**R_3 (Ω) – Surface/Intermediate**	**O_D/O_L Ratio**	**$R_{sat/Main}$ (Cu 2p)**	**Dominant Kinetic Regime**
C0	415	149	351	1.33	0.81	Interfacial-limited
CF1	338	61	313	2.86	0.80	Optimized (balanced)
CF2	367	80	588	1.60	0.66	Surface-reaction-limited

The correlation reveals that moderate Fe substitution (CF1) simultaneously maximizes the O_D/O_L ratio and minimizes interfacial resistance (R_2), consistent with enhanced redox accessibility and improved proton–electron transfer. In contrast, higher Fe loading (CF2) is characterized by a substantial increase in R_3 despite a reduction in R_2, indicating a redistribution of the dominant bottleneck toward surface-reaction processes. This non-monotonic descriptor–kinetic relationship underpins the promoter–inhibitor crossover

observed in polarization measurements.

6.3.5.2. DFT-Derived Energetics and Surface-Reaction Limitations

To establish the atomistic origin of the promoter–inhibitor crossover identified experimentally, density functional theory (DFT) calculations were performed on pristine and Fe-substituted CuO (111) surfaces [218], [219]. Computational results provide energetic and bonding-level insight into how dopant-induced electronic modulation redistributes oxidation-side kinetic limitations.

Free Energy Analysis of OER Intermediates

The calculated free energy profiles for alkaline OER on pristine and Fe-substituted CuO surfaces are shown in Figure 6.3.5.2.

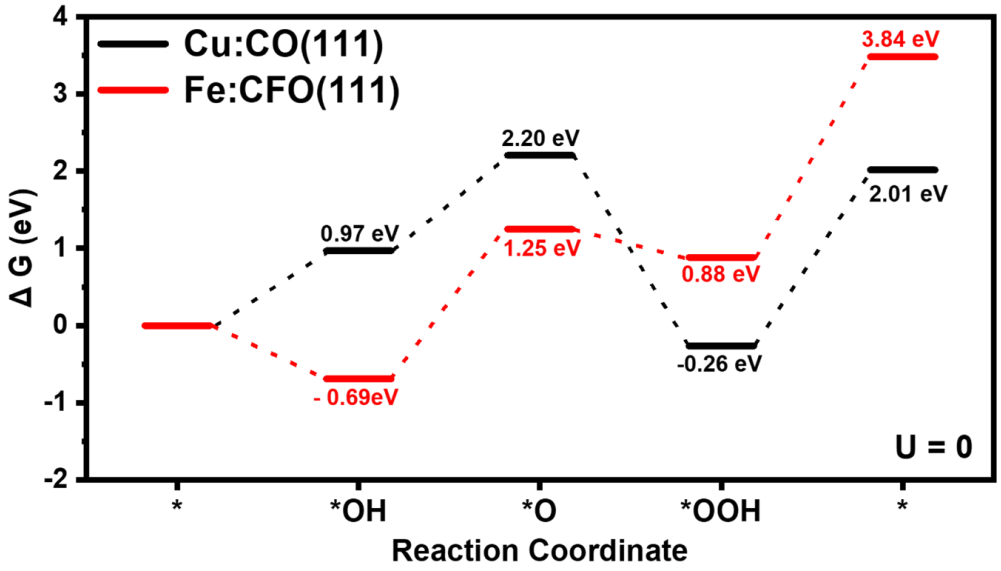


Figure 6.3.5.2: Calculated free energy diagram for alkaline OER on pristine CuO and Fe-substituted CuO (111) surfaces at U = 0 V. Moderate Fe substitution lowers the free energy barrier of the potential-determining step, whereas higher Fe loading strengthens adsorption of oxygenated intermediates and increases the thermodynamic penalty for intermediate turnover.

Moderate Fe substitution lowers the thermodynamic barrier of the potential-determining step

relative to pristine CuO, reducing the theoretical overpotential. This trend is consistent with the experimentally observed decrease in overpotential and substantial reduction in interfacial resistance (R_2) for CF1.

However, the Fe-enriched surface model qualitatively changes the free energy landscape. The adsorption energies of oxygenated intermediates, particularly *O and *OOH species, become increasingly negative, indicating stronger binding at Fe-influenced sites. While moderate strengthening facilitates intermediate formation, excessive stabilization raises the energetic barrier for subsequent transformation and O_2 release. This over-stabilization increases the thermodynamic penalty associated with intermediate turnover, consistent with the experimentally observed increase in the intermediate-frequency resistance component (R_3) for CF2.

Bonding Analysis via Integrated Crystal Orbital Hamilton Population (ICOHP)

To further quantify the strengthening of metal–oxygen interactions upon Fe substitution, integrated crystal orbital Hamilton population (ICOHP) analysis was performed [220]. The spin-resolved −pCOHP curves for Cu–O and Fe–O interactions are shown in Figure 6.3.5.3, and the corresponding integrated ICOHP values are summarized in Table 6.3.5.2.

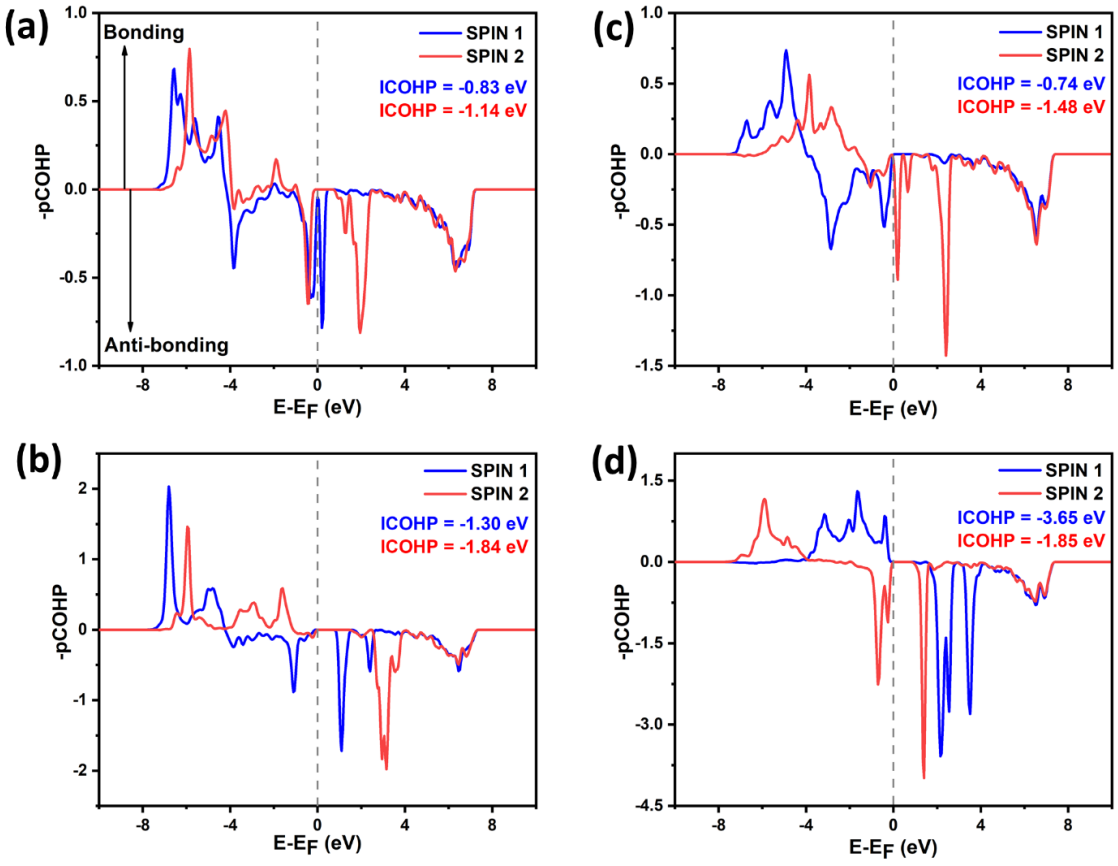


Figure 6.3.5.3: Spin-resolved projected crystal orbital Hamilton population (−pCOHP) analysis for oxygen-intermediate adsorption on Cu and Fe catalytic sites. Integrated crystal orbital Hamilton population (ICOHP) values indicate significantly stronger Fe–O covalent interactions relative to Cu–O bonding. Enhanced Fe–O covalency at higher substitution levels supports the DFT-predicted over-stabilization of oxygenated intermediates and correlates with the experimentally observed increase in surface-reaction resistance (R_3).

Table 6.3.5.2: Integrated ICOHP Values for Metal–Oxygen Interactions.

Catalytic Site	**ICOHP (eV) – Spin 1**	**ICOHP (eV) – Spin 2**	**Dominant Bonding Character**
Cu site	−1.30	−1.84	Moderate covalency

Fe site (moderate)	−0.83	−1.14	Enhanced metal–oxygen covalency
Fe site (high)	−3.65	−1.85	Strong covalency

The ICOHP values demonstrate that Fe–O interactions exhibit more negative integrated ICOHP values than Cu–O interactions, indicating stronger covalent bonding between Fe sites and adsorbed oxygen intermediates. This strengthening becomes particularly pronounced at higher Fe substitution levels. While moderate Fe–O bonding enhances redox accessibility and supports intermediate stabilization, excessive covalency increases the energetic barrier for intermediate turnover and oxygen evolution.

The stronger Fe–O bonding, evidenced by the more negative ICOHP values, therefore provides a bonding-level explanation for the substantial increase in R_3 observed experimentally for CF2. In this regime, surface-reaction kinetics dominate despite improved interfacial charge-transfer characteristics.

Electronic Redistribution and Work Function Considerations

In addition to adsorption energetics, Fe substitution moderately lowers the calculated surface work function relative to pristine CuO (Figure 6.2.5.2.3), indicating improved electronic communication between the catalyst surface and the electrolyte [221]. This reduction provides a theoretical basis for the experimentally observed decrease in R_2 at moderate Fe substitution [222].

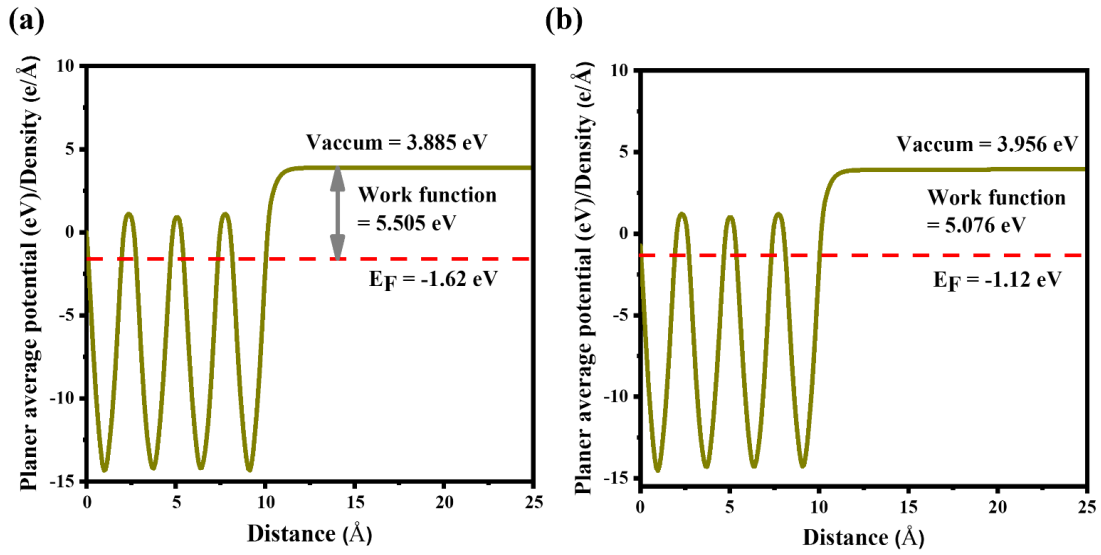


Figure 6.3.5.4: Planar-averaged electrostatic potential and calculated work function for pristine and Fe-substituted CuO surfaces. Moderate Fe incorporation reduces the work function, indicating improved electronic communication across the catalyst–electrolyte interface and supporting the experimentally observed reduction in interfacial resistance (R_2).

Taken together, the DFT-derived work function reduction, optimized intermediate energetics at moderate substitution, and enhanced Fe–O covalency at higher loading collectively explain the impedance-resolved redistribution of oxidation-side bottlenecks [223], [224]. Moderate Fe incorporation promotes OER by balancing interfacial charge transfer and intermediate binding strength. Excessive substitution, however, shifts the dominant kinetic limitation to surface-reaction processes due to over-stabilization of oxygenated intermediates.

6.3.5.3. Unified Oxidation-Side Kinetic Model

The combined XPS, DFT, and impedance analyses support a three-regime oxidation model for Fe-substituted CuO:

i. **Interfacial-Limited Regime (C0):**

   Limited redox accessibility and high work function result in substantial interfacial resistance, with charge-transfer processes dominating overall kinetics.

ii. **Optimized Redox Regime (CF1):**

Moderate Fe^{3+} substitution enhances electronic redistribution, increases surface oxygen activation (O_D/O_L), lowers work function, and reduces interfacial resistance without excessively stabilizing intermediates. Interfacial and surface processes remain balanced, yielding optimal catalytic performance.

iii. **Surface-Reaction-Limited Regime (CF2):**

Excess Fe substitution intensifies Fe–O covalency and strengthens the adsorption of oxygenated intermediates. However, interfacial resistance remains reduced relative to pristine CuO; the dominant bottleneck shifts to slower surface-reaction kinetics, reflected experimentally by the substantial increase in R_3 and corresponding DRT relaxation features.

This model demonstrates that dopant valency governs not only electronic structure but also the balance between interfacial charge-transfer efficiency and intermediate-binding energetics. Catalytic promotion arises when electronic redistribution alleviates the dominant kinetic barrier; inhibition occurs when excessive stabilization of reaction intermediates redistributes the bottleneck to surface turnover.

The promoter–inhibitor crossover observed here highlights that higher-valent substitution cannot be evaluated solely through static descriptors or apparent activity metrics. Instead, effective dopant engineering must account for how electronic modulation redistributes the rate-limiting processes under operating conditions. In Fe-substituted CuO, optimal performance emerges only within a compositional window that balances redox accessibility with controlled intermediate binding strength.

More broadly, this framework establishes that oxidation electrocatalysis in earth-abundant oxides is governed by a dynamic redistribution of kinetic limitations rather than a monotonic enhancement of a single property, such as conductivity or surface area. The integration of impedance-resolved kinetics with electronic-structure descriptors provides a generalizable strategy for rational dopant selection in oxidation-driven reactions.

6.4. Chapter Summary and Forward Link

This chapter resolved the oxidation-side catalytic bottlenecks governing the alkaline oxygen evolution reaction (OER) in Fe-substituted CuO electrocatalysts through a combined

polarization, impedance, spectroscopic, and theoretical framework.

Conventional activity metrics established a non-monotonic dependence of OER performance on Fe content, revealing the presence of an optimal substitution window. However, apparent overpotential and Tafel slope trends alone could not identify the mechanistic origin of this behaviour. By integrating electrochemical impedance spectroscopy measured at a fixed OER-relevant potential with equivalent circuit modelling and distribution of relaxation time analysis, distinct interfacial and surface-reaction contributions were quantitatively separated.

Moderate Fe^{3+} substitution significantly reduced interfacial charge-transfer resistance (R_2), consistent with enhanced redox accessibility within the Cu–O lattice. At higher substitution levels, however, the dominant kinetic limitation shifted toward surface-reaction processes, as reflected by the substantial increase in the intermediate-frequency resistance component (R_3). This redistribution of rate-limiting processes explains the observed promoter–inhibitor crossover and demonstrates that enhanced redox accessibility alone is insufficient for sustained catalytic improvement.

Integration of XPS-derived electronic descriptors with DFT-calculated intermediate energetics further revealed that excessive Fe incorporation leads to over-stabilization of oxygenated intermediates, increasing the barrier for surface turnover despite improved interfacial charge transfer. Thus, dopant valency governs not only electronic structure but also the balance between interfacial and surface-reaction kinetics.

Collectively, this chapter establishes that oxidation electrocatalysis in earth-abundant oxides is controlled by the redistribution of kinetic-dominant bottlenecks rather than monotonic enhancement of a single descriptor. For OER in CuO-based systems, higher-valent substitution promotes performance only within a defined compositional window that optimally balances redox accessibility and intermediate binding strength.

Within the broader thesis framework, this chapter completes the oxidation-side analysis initiated in Chapter 5 by extending redox-controlled activity from photo-driven systems to electrochemical bias. Together, these findings provide general design principles for reaction-specific dopant engineering in oxide electrocatalysts, demonstrating that catalytic promotion and inhibition arise from shifts in dominant kinetic limitations rather than simple compositional scaling.

Importantly, these oxidation-side findings reinforce the ligand-hole-associated electronic modulation framework introduced in Chapter 1, demonstrating that dopant-valency-driven redistribution of Cu–O covalency and redox accessibility governs both photonic and electrochemical oxidation regimes.

Although CuO-based oxides possess inherent limitations, including moderate electronic conductivity and possible susceptibility to reconstruction under prolonged anodic polarization, these characteristics also make CuO a useful model system for investigating how dopant-induced electronic modifications influence catalytic bottlenecks. Consequently, the present work should be viewed as a mechanistic study of electronic-structure engineering in semiconducting oxides rather than a demonstration of a commercially optimized OER catalyst.

Chapter 7 Conclusions and Scope for Future Work

Abstract: *This chapter consolidates the findings of the thesis and presents an integrated interpretation of catalytic bottlenecks in CuO-based oxide systems under photonic, thermal, and electrochemical driving forces. The work demonstrates that catalytic performance in strongly correlated CuO is governed not solely by adsorption energetics or band alignment, but by the selective relief of charge-delivery and interfacial kinetic limitations. Through controlled dopant valency engineering, morphology design, temperature-dependent analysis, and impedance-resolved electrochemical evaluation, distinct mechanisms for bottleneck mitigation were identified. Non-redox Al^{3+} substitution enhanced electronic charge utilization, temperature-assisted transport improved interfacial kinetics, and Fe^{3+} incorporation introduced redox-mediated activation pathways. Under alkaline oxygen evolution conditions, impedance analysis revealed separable kinetic regimes and a dopant-dependent promoter–inhibitor crossover. Collectively, these findings establish a bottleneck-oriented framework for rational catalyst design. Across all reaction regimes, ligand-hole density, redox accessibility, and interfacial charge-transfer resistance emerged as interdependent descriptors governing bottleneck redistribution in CuO-based oxides. The chapter concludes by outlining current limitations, ongoing investigations, and future research directions aimed at extending this framework toward predictive and device-relevant oxide catalysis.*

7.1. Chapter-wise Conclusion

This thesis systematically investigated catalytic bottlenecks in CuO-based oxide systems under photonic, thermal, and electrochemical driving forces. Each chapter addressed a distinct limitation within a unified framework.

7.1.1. Chapter 3 - Al^{3+} Substituted CuO: Non-Redox Electronic Modulation

First, aliovalent Al^{3+} substitution was introduced as a non-redox dopant strategy to isolate purely electronic effects in CuO. The goal was to determine whether photo-Fenton-like activity could be enhanced without introducing additional redox cycles.

The results showed that:

- Phase-pure monoclinic CuO was preserved after Al incorporation.

- Moderate Al^{3+} substitution enhanced visible-light degradation under low-power LED and natural sunlight.
- Radical scavenging experiments identified •OH as the dominant reactive oxygen species.
- The improvement arose from dopant-induced electronic redistribution within the Cu–O network rather than from new redox centers.

Therefore, Chapter 3 demonstrated that non-redox electronic modulation improves charge utilization and interfacial oxidation kinetics in CuO.

7.1.2. Chapter 4 - CuO Nanosheets: Temperature-Dependent Kinetics

Next, morphology-engineered CuO nanosheets were synthesized to isolate temperature-assisted transport and interfacial effects independent of dopant chemistry.

The study revealed that:

- Degradation kinetics followed thermally activated behavior.
- Rate constants increased significantly between 25-45 °C.
- Dark adsorption did not increase proportionally with temperature.
- The rate-limiting step was governed by interfacial charge transfer and ROS generation rather than photon absorption.

These results indicated that temperature enhances carrier detrapping and hopping transport in CuO, accelerating interfacial redox reactions without altering the fundamental mechanism.

Thus, Chapter 4 clarified that temperature functions as a kinetic lever in strongly correlated oxide photocatalysis.

7.1.3. Chapter 5 - Fe^{3+} Substitution: Dopant-Mediated Redox Activation

After isolating electronic and thermal effects, Fe^{3+} substitution was introduced to test whether a redox-active dopant fundamentally alters the photo-Fenton pathway.

- The findings showed that:
- Fe incorporation did not disrupt the CuO phase.

- Visible-light degradation rates increased significantly compared to pristine and Al-doped systems.
- The dominant ROS remained hydroxyl radicals.
- The enhancement was consistent with Fe^{3+}/Fe^{2+} cycling enabling sustained H_2O_2 activation.
- The system became less dependent on thermal acceleration.

Therefore, Chapter 5 demonstrated mechanistic switching: the bottleneck shifted from transport-limited activation toward dopant-mediated redox regeneration.

This established redox-active dopant engineering as a distinct activation pathway in CuO oxidation chemistry.

7.1.4. Chapter 6 - Fe-CuO for Alkaline OER: Impedance-Resolved Bottleneck Separation

Finally, the thesis extended oxidation studies to electrochemical bias through alkaline OER.

The results revealed:

- Moderate Fe substitution reduced OER overpotential and Tafel slope.
- Electrochemical impedance spectroscopy separated interfacial charge transfer and surface-reaction resistances.
- Distribution of relaxation time (DRT) analysis confirmed multiple kinetic regimes.
- A promoter–inhibitor crossover occurred with increasing Fe content.
- Excess Fe stabilized oxygenated intermediates and shifted the bottleneck toward surface-reaction limitation.

Thus, Chapter 6 demonstrated that dopant valency redistributes oxidation-side kinetic limitations under electrochemical conditions.

This provided a mechanistic bridge between photocatalytic oxidation and electrocatalytic OER.

7.2. Advancement Beyond Existing CuO Literature

Before the present thesis work, CuO was already known as a narrow-bandgap p-type transition-

metal oxide with applications in photocatalysis, photo-Fenton-like pollutant degradation, and electrochemical energy conversion. Previous studies had shown that CuO performance could be improved through morphology control, elemental doping, heterostructure formation, and defect engineering. However, much of the existing literature primarily emphasized performance metrics such as degradation efficiency, apparent rate constants, overpotential, and stability, while comparatively less attention was given to identifying the specific catalytic bottlenecks responsible for limiting activity in different reaction environments.

The present thesis advances the understanding of CuO-based oxide systems by shifting the focus from performance improvement alone to bottleneck-resolved catalyst design. Rather than treating photocatalysis, photo-Fenton-like degradation, and electrocatalytic oxygen evolution as isolated reactions, this work establishes a unified framework in which catalytic performance is governed by the selective mitigation or redistribution of charge-transfer, transport, redox-accessibility, and surface-reaction limitations.

The key advancement from this thesis is the demonstration that different modification strategies relieve different bottlenecks in CuO. Non-redox Al^{3+} substitution primarily improves electronic charge utilization and defect-mediated photocatalytic activity without introducing additional redox pathways. Morphology-controlled CuO nanosheets reveal that temperature can act as a kinetic lever by assisting carrier detrapping, polaronic hopping, and interfacial charge transfer. Redox-active Fe^{3+} substitution introduces an additional Fe^{3+}/Fe^{2+}-mediated pathway for photo-Fenton-like degradation, thereby shifting the dominant enhancement mechanism from defect-mediated charge utilization to redox-assisted reactive oxygen species generation.

Under alkaline OER conditions, the thesis further advances CuO research by using Fe-substituted CuO as a semiconducting model oxide to disentangle interfacial charge-transfer resistance from slower surface-reaction-related kinetic limitations. The combined use of EIS/DRT analysis, XPS-derived surface electronic descriptors, and DFT calculations revealed a dopant-concentration-dependent promoter–inhibitor crossover, where moderate Fe substitution improves interfacial charge transfer, while excessive Fe incorporation promotes surface-reaction limitation through stronger stabilization of oxygenated intermediates.

Therefore, the main contribution of the thesis is not merely the preparation of improved CuO-

based catalysts, but the development of a reaction-specific bottleneck framework for understanding how dopant valency, defect chemistry, morphology, temperature, redox accessibility, and interfacial resistance collectively govern catalytic performance in CuO-based oxide systems.

7.3. Integrated Overall Conclusion

As defined in Chapter 1, a catalytic bottleneck corresponds to the dominant rate-limiting physicochemical constraint under specific reaction conditions; the present work demonstrates that this constraint can be selectively shifted through dopant-valency-controlled electronic modulation.

As defined in Chapter 1, a catalytic bottleneck corresponds to the dominant physicochemical constraint under specific operating conditions; the present work demonstrates that such bottlenecks can be selectively redistributed through dopant-valency-controlled electronic modulation.

Rather than treating catalytic performance as solely adsorption- or bandgap-limited, this work demonstrated that:

- Electronic modulation (Al^{3+}) enhances charge utilization.
- Thermal activation accelerates detrapping and interfacial processes.
- Redox-active doping (Fe^{3+}) introduces new catalytic channels.
- Under electrochemical bias, bottlenecks can be deconvoluted into separable kinetic regimes.

Therefore, the central achievement of this thesis is the formulation and experimental validation of a bottleneck-oriented catalyst design framework for CuO-based oxides.

This framework unifies photocatalysis and electrocatalysis within a single mechanistic language.

7.4. Thematic Synthesis

All chapters collectively address the core research question: *How can catalytic bottlenecks in strongly correlated oxides be identified and selectively relieved?*

The thesis shows that:

a) CuO is a strongly correlated charge-transfer oxide exhibiting localized carrier dynamics.
b) Catalytic efficiency depends on effective charge delivery to surface redox sites.
c) Different levers relieve different bottlenecks:
    - Non-redox dopants tune electronic structure
    - Temperature improves transport kinetics.
    - Redox dopants enable chemical activation.
    - Electrochemical bias reveals redistribution of rate-determining steps.

Thus, catalytic optimization must match dopant valency and electronic structure to the dominant kinetic regime.

7.5. Scientific Contributions

Primary Contributions

a) Development of a bottleneck-resolved catalytic framework.
b) Demonstration of non-redox dopant-driven electronic enhancement.
c) Experimental isolation of thermally activated photocatalytic transport.
d) Identification of dopant-mediated reaction pathway switching.
e) Impedance-resolved separation of OER kinetic regimes.
f) Establishment of promoter–inhibitor crossover governed by dopant valency.

Secondary Contributions

- Low-power light photocatalysis under realistic conditions.
- Semi-quantitative XPS descriptors for electronic screening and oxygenated surface fraction.
- Integration of DFT insights with electrochemical impedance interpretation.

7.6. Limitations

Despite significant insights, several limitations exist.

- First, XPS descriptors are ex situ and semi-quantitative. Operando validation of ligand-hole dynamics remains desirable.
- Second, ROS quantification is based on scavenger and fluorescence methods rather than absolute radical flux measurements.
- Third, long-term electrolyzer device integration was not the focus of this work.
- Fourth, reduction-side catalysis (e.g., HER) remains under investigation and is not included as a core chapter in this thesis.

These limitations define clear opportunities for future work.

7.7. Ongoing Work

Ongoing investigations include:

- Dopant-charge-driven modulation of alkaline HER using Li^{+} and Zn^{2+} substitution.
- Advanced impedance analysis for reduction-side bottlenecks.
- Expanded DFT modeling of intermediate energetics.
- Optimization of Fe–CuO compositions for stability under extended OER operation.

These studies extend the bottleneck-oriented framework toward reduction reactions.

7.8. Scope for Future Work

Short-Term Directions

- Operando Raman and XAS to directly probe redox dynamics.
- Quantitative radical detection techniques.
- Systematic variation of dopant valency beyond Fe^{3+}.

Mid-Term Expansion

- Integration into photo-reactor platforms.
- Translation into alkaline or AEM electrolyzer electrodes.
- Stability mapping under industrial current densities.

Long-Term Vision

- Development of predictive ligand-hole and impedance descriptors for correlated oxides.
- Data-driven screening of earth-abundant doped oxides.
- Bridging photocatalytic and electrocatalytic frameworks under unified transport-reaction models.

7.9. Broader Impact and Technological Relevance

This work contributes to:

- Sustainable wastewater remediation under low-energy light sources.
- Earth-abundant alternatives for alkaline OER.
- Mechanistically informed catalyst design.
- Reduced dependence on noble metals.

By focusing on bottleneck identification rather than empirical optimization, this thesis provides a rational pathway toward scalable oxide catalyst development.

7.10. Final Closing Statement

In conclusion, this thesis demonstrates that catalytic performance in CuO-based oxides is governed not merely by adsorption strength or band alignment, but by the selective relief of charge-delivery and interfacial kinetic bottlenecks.

Through systematic dopant valency control, morphology engineering, temperature isolation, and impedance-resolved electrochemical analysis, this work establishes a unified framework for understanding and optimizing oxidation catalysis in strongly correlated oxides.

Although developed using CuO as a model system, the framework presented here provides a transferable strategy for the rational optimization of earth-abundant transition metal oxides across photocatalytic and electrocatalytic applications.

The insights generated in this thesis advance the mechanistic foundation of oxide catalysis and offer a pathway toward predictive, device-relevant catalyst design for sustainable energy conversion and environmental remediation.

Appendix-A: DFT used

Methodology: Density Functional Theory (DFT) calculations in this study were performed using the Vienna Ab Initio Simulation Package (VASP) version [225]. To describe how valence electrons interact with the ion cores, we employed the Projector Augmented Wave (PAW) method, which effectively combines features of both pseudo-potentials and the linear augmented plane wave method. A plane-wave basis set was used, with a kinetic energy cutoff of 520 eV, to ensure accurate results. For the exchange-correlation (XC) interaction, we employed the Perdew-Burke-Ernzerhof (PBE) functional [226] within the generalised gradient approximation (GGA) framework[227]. To study the electronic properties of bulk CuO and the effects of doping, a 2×2×2 supercell of monoclinic CuO (space group C2/c) was built, consisting of 64 atoms. In the doped structure, one Cu atom was replaced with an Fe atom. Antiferromagnetic ordering of the CuO lattice has been imposed to obtain an accurate electronic structure[228]. All these structures were fully relaxed until the Hellmann-Feynman forces [229], [230] on each atom were less than 0.001 eV/Å, and the electronic self-consistency loop was converged with an energy threshold of 10^{-4} eV. For k-point sampling in these bulk calculations, we used a 5×5×3 Monkhorst-Pack grid, corresponding to a k-spacing of 0.03 × 2π/Å [231].

To examine the catalytic activity of the material, a surface model (slab) was also constructed, consisting of 128 atoms, exposing the (111) crystal plane [232]. For these surface calculations, a 3×3×1 Gamma-centred k-point grid was used. To prevent interactions between repeating slabs, a 20 Å vacuum layer was included along the [111] direction. Additionally, a dipole correction was applied in the same direction to eliminate any artificial electric fields induced by polar surface [233]. Van der Waals (vdW) interactions, which are important for surface and adsorption studies, were included using Grimme's DFT-D3 method [234], [235]. During slab calculations, the structures were relaxed until atomic forces were below 0.01 eV/Å, and the

total energy difference between iterations was less than 10^{-3} eV [229], [230]. The LOBSTER code was employed to calculate the integrated crystal orbital Hamilton population (ICOHP) at the catalytically active sites, allowing for a quantitative analysis of the bonding interactions between the catalyst and oxygenated reaction intermediates[236].

Since standard DFT often struggles to describe strong electron-electron interactions in transition-metal oxides accurately, a DFT+U+J approach was employed based on Dudarev's formalism[237]. This method introduces a Hubbard U correction to improve the behaviour of localised d-electrons in Cu and Fe. The values used were U = 9.17 eV and J = 0.98 eV for Cu, and U = 4.0 eV and J = 0 eV for Fe. The valence electron configurations considered were Cu (3d, 4s), Fe (3d, 4s), and O (2s, 2p). Finally, VASPKIT [238] was used for post-processing, and VESTA[239] for visualising charge density differences and structural features.

Working Procedure:

The adsorption energy (E_{ads}) tells how strongly a molecule sticks to the surface. It is defined as the following equation [240], [241]:

$$E_{ads} = E_{Total} - E_{Slab} - E_{Molecule}$$

where E_{Total} is the total energy of the molecule adsorbed on the slab, E_{Slab} is the total energy of the slab, and $E_{Molecule}$ is the total energy of the free molecule in the gas phase. If the adsorption energy is negative, it means the molecule prefers to stay on the surface, and the process releases energy (exothermic).

To understand why partial Fe-doping enhances the oxygen evolution reaction (OER) activity of CuO, we employed density functional theory (DFT) calculations to examine the energy changes for various reaction steps. The OER following adsorbed exchange mechanism (AEM) takes place in four main steps, each involving specific intermediates and products [242], [243].

$$* + OH^-(aq.) \rightarrow * - OH_{adsorbed} + e^-$$

$$* - OH_{adsorbed} + OH^-(aq.) \rightarrow * - O_{adsorbed} + H_2O + e^-$$

$$* - O_{adsorbed} + OH^-(aq.) \rightarrow * - OOH_{adsorbed} + e^-$$

$$* - OOH_{adsorbed} + OH^-(aq.) \rightarrow * + O_2(g) + H_2O + e^-$$

where M represents the surface active site and stands for the intermediates absorbed on the active sites during OER. Reaction energy (ΔE) of each step mentioned above has been calculated purely from the DFT total energy difference, without adding zero-point energy (ZPE) or entropic corrections (TS) [241].

$$\Delta E_1 = E_{*-OH_{adsorbed}} - E_* - E_{H_2O} + E_{\frac{1}{2}H_2(g)}$$

$$\Delta E_2 = E_{*-O_{adsorbed}} - E_{*-OH_{adsorbed}} + E_{\frac{1}{2}H_2(g)}$$

$$\Delta E_3 = E_{*-OOH_{adsorbed}} - E_{*-O_{adsorbed}} - E_{H_2O} + E_{\frac{1}{2}H_2(g)}$$

The Gibbs free-energy changes of these steps at the equilibrium potential of OER are calculated as follows [244]:

$$\Delta G_1 = \Delta E_1 + (\Delta ZPE - T\Delta S)_{OH} - (\Delta ZPE - T\Delta S)_{H_2O} + (\Delta ZPE - T\Delta S)_{H_2}$$

$$\Delta G_2 = \Delta E_2 + (\Delta ZPE - T\Delta S)_{O} - (\Delta ZPE - T\Delta S)_{OH} + (\Delta ZPE - T\Delta S)_{H_2}$$

$$\Delta G_3 = \Delta E_3 + (\Delta ZPE - T\Delta S)_{OOH} - (\Delta ZPE - T\Delta S)_{O} - (\Delta ZPE - T\Delta S)_{H_2O} + (\Delta ZPE - T\Delta S)_{H_2}$$

Due to self-interaction errors and spin-state issues, DFT failed to accurately describe the energy of O_2 (g). In OER thermodynamics, the total Gibbs free energy change (ΔG) for the overall

reaction is 4.92 eV (experimentally known fact). So, instead of calculating energy directly (which introduces errors), the change in Gibbs' free energy associated with the 4th step can be calculated as[241]:

$$\Delta G_4 = \Delta G - (\Delta G_1 + \Delta G_2 + \Delta G_3)$$

Table AA1: *Contributions of Entropy (T and Zero-Point Energy) to the Free Energies of Gaseous and Adsorbed OER Species As Calculated by Valdes et al.* [245]

	ΔZPE (eV)	TΔS (eV)	$(\Delta ZPE - T\Delta S)$ (eV)
$H_2(g)$	0.27	0.41	-0.14
$H_2O(g)$	0.56	0.67	-0.11
$H_2O(l)$	0.56	0.10	0.46
*OH	0.35	0	0.35
*O	0.05	0	0.05
*OOH	0.41	0	0.41

The energy values of the hydrogen molecule in gaseous form, used for the change in Gibbs' free energy calculation, are $E_{H_2(g)} = -6.8\ eV$ [246], and the energy of the water molecule in liquid form is $E_{H_2O(l)} = -14.19\ eV$.

In our calculations, we didn't include the effects of the solvent or the constant applied voltage, even though these factors can be important for electrochemical reactions, especially in the case of 2D materials. This means that the exact numbers we report for free energies might change if those effects were included, but the overall trends and conclusions should still remain valid.

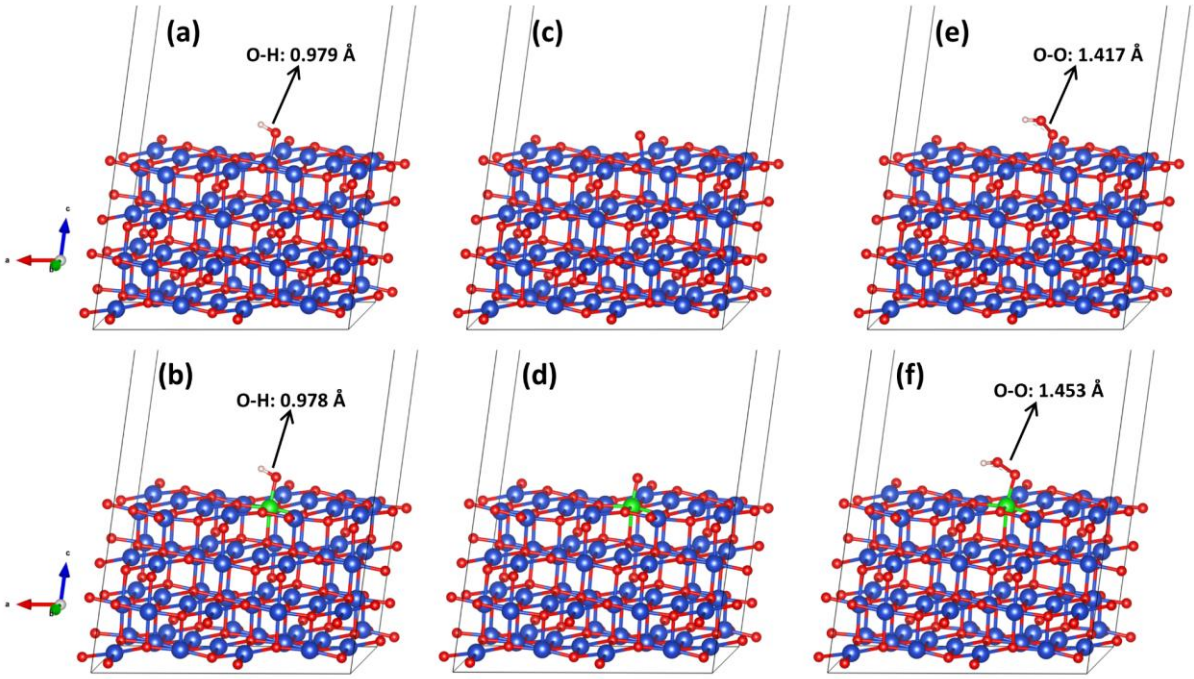


Figure AA1*: Variation in the structural geometry and bond lengths for different intermediate equilibrium states of OER, i.e; *OH ((e) and (f)), *O ((g) and (h)), *OOH ((i) and (j)) (Solid spheres having colour of blue, green, red and white represents Cu, Fe, O and H atom respectively).*

Table AA2: *Total energy of the systems as obtained from DFT calculation.*

System	Energy (eV)

	*	*OH	*O	*OOH
CO	-531.27	-540.79	-534.70	-545.46
CFO	-535.74	-546.92	-541.78	-551.40

Table AA3: *Total energy of the systems as obtained from DFT calculation* [246].

	Energy (eV)
OH (g)	-7.408
H_2O (g)	-14.19
H_2 (g)	6.80

Appendix-B: XPS peak fittings

1. XPS Peak Fitting Methodology and Descriptor Definition

High-resolution X-ray photoelectron spectroscopy (XPS) spectra of Cu 2p and O 1s regions were analysed to extract relative surface electronic and speciation descriptors relevant to interfacial OER kinetics. All peak fitting was performed using a Shirley (Smart) background and mixed Gaussian-Lorentzian (GL) line shapes. Binding energies were calibrated using adventitious carbon (C 1s = 284.8 eV). No asymmetric line shapes were employed. Peak positions were allowed to vary by ±0.2 eV to ensure physically meaningful fits.

Importantly, XPS-derived parameters were not interpreted as absolute measures of oxygen vacancy concentration, hydroxyl coverage, or Cu oxidation state. Instead, relative ratios and fractions were used as comparative descriptors to correlate surface electronic structure with impedance-resolved kinetics (EIS/DRT) and DFT-predicted electronic trends.

1.1. 1s Deconvolution and O_D/O_L Descriptor

The O 1s spectrum was deconvoluted into three components: O_L (lattice oxygen), centred at ~529.5-529.7 eV, which was assigned to lattice O^{2-} in CuO. The second component, O_D (defect/oxyhydroxide oxygen), centred around ~530.5-530.7 eV, was assigned to defect-associated, oxyhydroxide-like, or strongly chemisorbed oxygen species relevant to interfacial PCET. The third component was assigned to O_{ads} (adsorbed species) centred around ~532.4-532.8 eV, corresponding to weakly bound molecular oxygen or surface adsorbates.

The first descriptor, the O_D/O_L ratio, was defined as $O_D/O_L = A(O_D)/A(O_L)$, where A denotes the fitted peak area.

Table AB1*: O 1s Fitted Peak Parameters and Derived Ratios*

Sample	Component	BE (eV)	FWHM (eV)	Area (CPS·eV)	Descriptor (A (O_D)/A (O_L))
C0	O_L	529.54	1.21	42,859	
	O_D	530.71	2.51	57,154	O_D/O_L = 1.33
	O_{ads}	532.79	3.26	17,198	
CF1	O_L	529.57	1.18	36,941	
	O_D	530.52	2.32	105,776	O_D/O_L = 2.86
	O_{ads}	532.49	3.11	40,286	
CF2	O_L	529.55	1.16	43,903	
	O_D	530.58	2.18	70,252	O_D/O_L = 1.60
	O_{ads}	532.55	3.05	23,512	

1.2. Cu $2p_{3/2}$ Deconvolution and Electronic Flexibility Descriptors

The Cu $2p_{3/2}$ region was fitted using A Main Cu^{2+} component centred around ~933–934 eV (lattice-like CuO environments), a Surface Cu-O component around ~935.8–936.1 eV, which was assigned to oxygenated surface Cu species (Cu–OH_x/carbonate-like), and a Shake-up satellites peaks centred around ~941–943 eV, which is Characteristic of Cu^{2+} multiplet

structure.

***Table AB2**: Cu $2p_{3/2}$ Fitted Peak Parameters and assigned components*

Sample	BE (eV)	FWHM (eV)	Area (CPS·eV)	Descriptor group	Assignment
C0	932.88	2.33	76,471	Main (screened)	Lower-BE Cu species (screened Cu^{2+} / Cu^{+}-like contribution)
C0	933.96	2.21	83,366	Main (lattice)	Cu^{2+} (CuO lattice)
C0	935.35	3.36	93,685	Surface (A_{surf})	Oxygenated surface Cu ($Cu–OH_x$/carbonate-like)
C0	941.00	2.46	63,616	Satellite (A_{sat})	Cu^{2+} shake-up satellite
C0	943.43	2.54	66,432	Satellite (A_{sat})	Cu^{2+} shake-up satellite
CF1	933.11	2.41	90,960	Main (screened)	Lower-BE Cu species (screened Cu^{2+} / Cu^{+}-like contribution)
CF1	934.34	2.40	135,705	Main (lattice)	Cu^{2+} (CuO lattice)
CF1	936.10	3.36	63,980	Surface	Oxygenated surface Cu

				(A_{surf})	(Cu–OH_x/carbonate-like)
CF1	941.02	2.44	90,960	Satellite (A_{sat})	Cu^{2+} shake-up satellite
CF1	943.45	2.52	89,618	Satellite (A_{sat})	Cu^{2+} shake-up satellite
CF2	933.34	2.83	80,932	Main (screened)	Lower-BE Cu species (screened Cu^{2+} / Cu^{+}-like contribution)
CF2	933.94	2.79	92,411	Main (lattice)	Cu^{2+} (CuO lattice)
CF2	935.88	3.36	47,377	Surface (A_{surf})	Oxygenated surface Cu (Cu–OH_x/carbonate-like)
CF2	940.97	2.55	56,844	Satellite (A_{sat})	Cu^{2+} shake-up satellite
CF2	943.41	2.63	58,339	Satellite (A_{sat})	Cu^{2+} shake-up satellite

Please note: Descriptor grouping ($A_{Sat,}$ *and* A_{main}) was used to compute $f_{Cu,\ surf,}$ and $R_{sat/main}$; however, individual components are not interpreted as absolute oxidation-state fractions.

Two descriptors were extracted:

A. Shake-up to the main peak ratio: $R_{sat/main} = A_{Sat}/A_{main}$

where A_{main} is the sum of lattice-like Cu^{2+} components, and A_{sat} is the sum of shake-up satellite

areas.

***Table AB3**: Cu $2p_{3/2}$ Fitted Parameters and Derived Descriptors*

Sample	A_{main}	A_{surf}	A_{sat}	$R_{sat/main}$
C0	*159837*	*93685*	*130048*	***0.81***
CF1	*226,666*	*63,981*	*180,579*	***0.80***
CF2	*173,342*	*47,377*	*115,183*	***0.66***

Interpretation Scope of XPS Descriptors

The descriptors O_D/O_L, $R_{sat/main}$ are used exclusively as relative, comparative indicators of surface oxygen activation and Cu^{2+} electronic flexibility. They are not intended to quantify oxygen vacancies, Cu^{+}/Cu^{3+} fractions, or intrinsic catalytic turnover frequencies. Instead, these parameters provide a spectroscopic consistency check that complements impedance-resolved kinetics:

A. O_D/O_L correlates with the mid-frequency (interfacial charge-transfer) domain in EIS/DRT.
B. $R_{sat/main}$ reflects the Cu–O network's ability to accommodate charge without excessive localisation.
C. The non-monotonic evolution of these descriptors mirrors the transition from interfacial charge-transfer-controlled kinetics (CF1) to surface-reaction-limited behaviour at higher Fe content (CF2).

Appendix-C: Preliminary Investigation of Li^+ and Zn^{2+} Substitution in CuO for Alkaline HER

This appendix presents preliminary results on Li^+ and Zn^{2+} substitution in CuO for alkaline hydrogen evolution reaction (HER). These investigations extend the bottleneck-oriented framework toward reduction-side catalysis and are part of ongoing work. The results are included to illustrate early trends in dopant-charge-driven electronic modulation and ligand-hole activation under cathodic polarization.

The structural integrity of Li- and Zn-modified CuO samples was first examined to ensure that aliovalent substitution does not induce secondary phases. XRD patterns confirm retention of the monoclinic tenorite structure across all compositions. A systematic shift of selected diffraction peaks toward higher 2θ values is observed for Li incorporation, consistent with lattice contraction arising from substitution of smaller Li^+ ions for Cu^{2+}. Raman spectroscopy further confirms phase purity through the preservation of A_g and B_g vibrational modes, with slight peak broadening indicative of defect-induced lattice distortion.

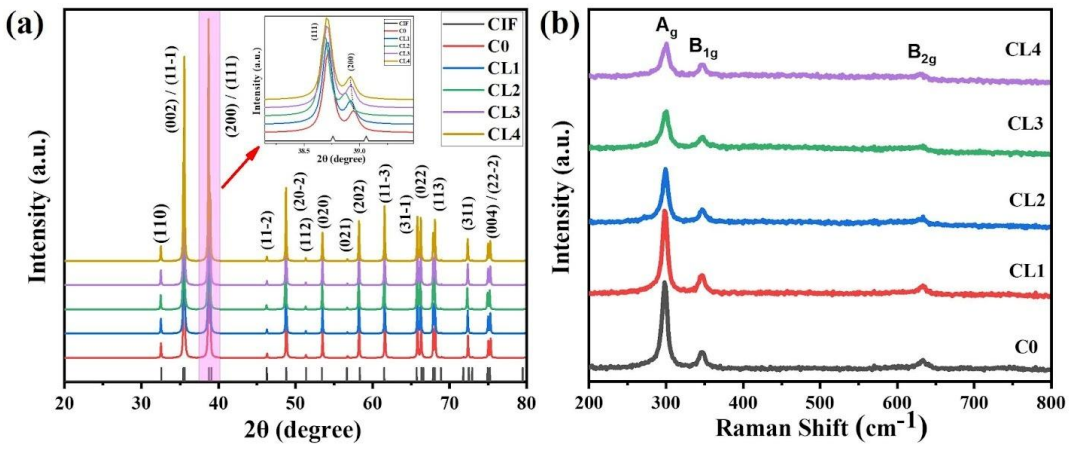


Figure AC1: *(a) X-ray diffraction (XRD) patterns of pure and Li-doped CuO (C0–CL4) samples showing retention of the monoclinic tenorite phase. The inset highlights peak shifts toward higher 2θ with increasing Li content, indicating lattice contraction. (b) Raman spectra displaying A_g and B_g modes of CuO, with peak broadening reflecting defect-induced lattice distortion and strain effects.*

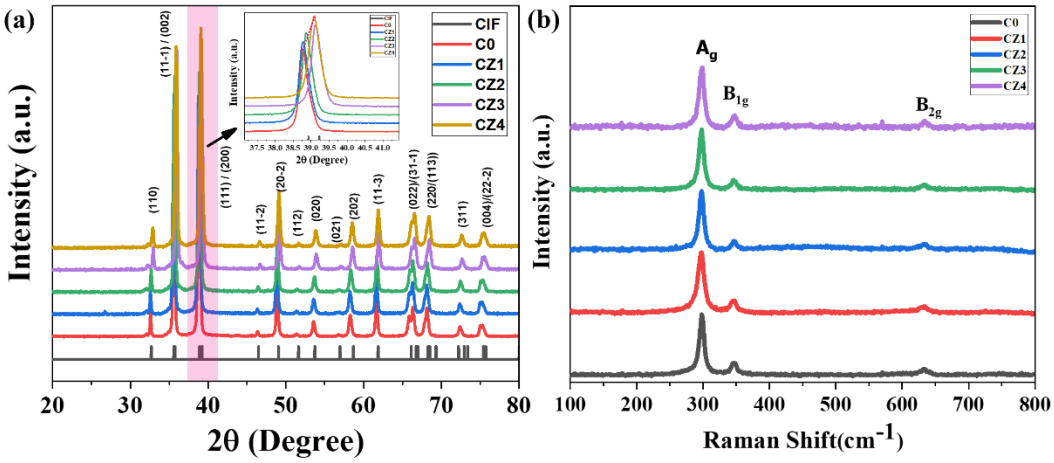


Figure AC2: *(a) X-ray diffraction (XRD) patterns of pure and Li-doped CuO (C0–CZ4) samples showing retention of the monoclinic tenorite phase. The inset highlights peak shifts toward higher 2θ with increasing Li content, indicating lattice contraction. (b) Raman spectra displaying A_g and B_g modes of CuO, with peak broadening reflecting defect-induced lattice distortion and strain effects.*

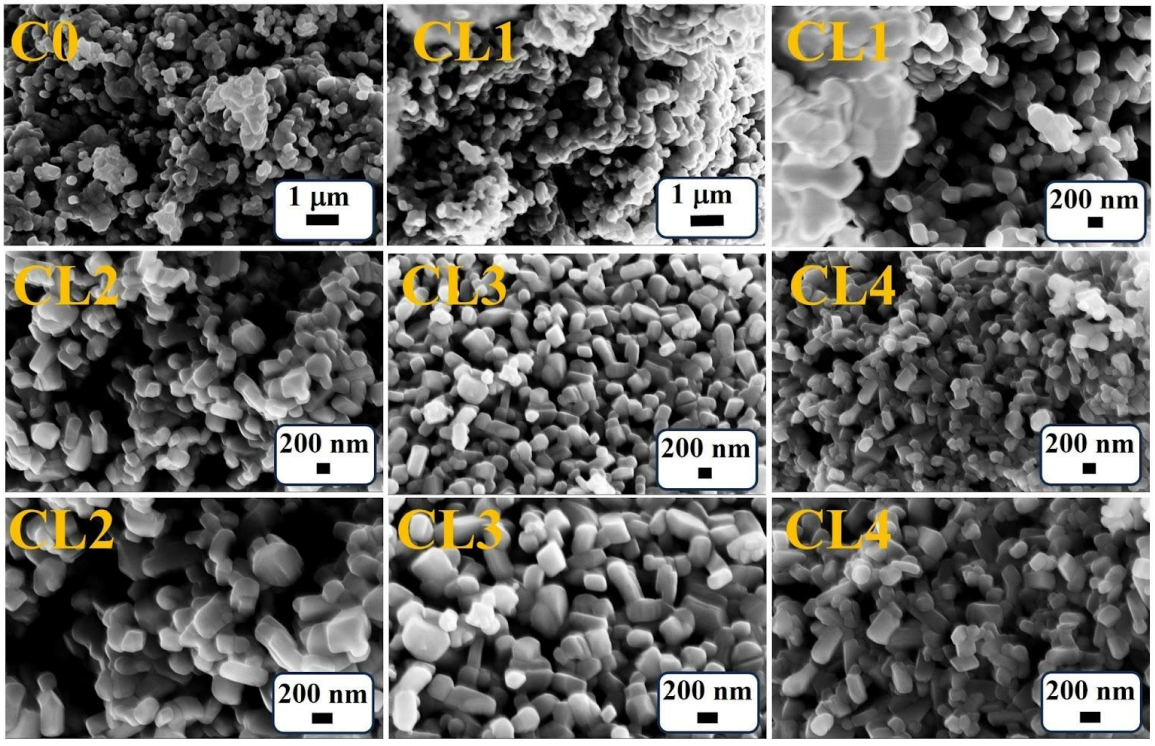


Figure AC3*: FESEM images of pristine (C0) and Li-doped CuO samples (CL1–CL4) recorded at different magnifications. Pristine CuO shows irregularly aggregated particles, whereas Li*

incorporation leads to gradual evolution toward more uniformly distributed nanograins. No distinct secondary phases or morphological collapse are observed, indicating structural integrity across the doping series.

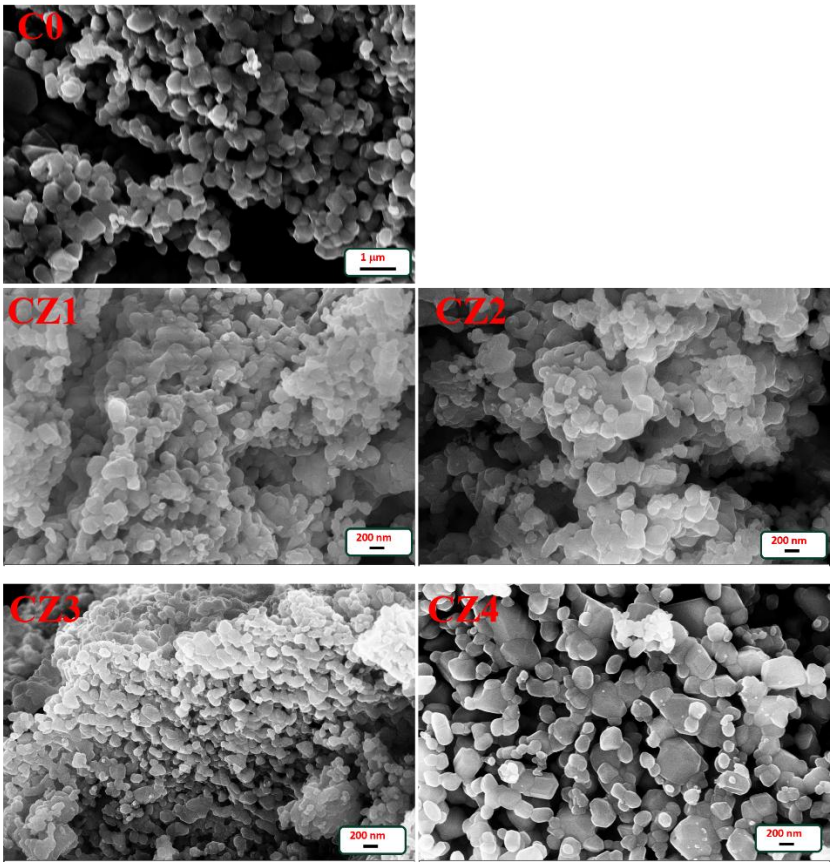


Figure AC4*: FESEM images of pristine (C0) and Zn-modified CuO samples (CZ1–CZ4). All samples preserve the characteristic aggregated granular morphology of monoclinic CuO. Zn substitution results in subtle variations in particle size distribution and surface roughness without evidence of secondary phase formation or structural collapse.*

To evaluate charge-delivery characteristics, current–voltage (I–V) measurements were performed. All samples exhibit linear I–V behavior, confirming ohmic contact. A monotonic increase in current response with Li substitution is observed, demonstrating enhanced bulk electronic conductivity. This improvement is consistent with aliovalent substitution-induced electronic modulation and supports mitigation of charge-transfer limitations under cathodic polarization.

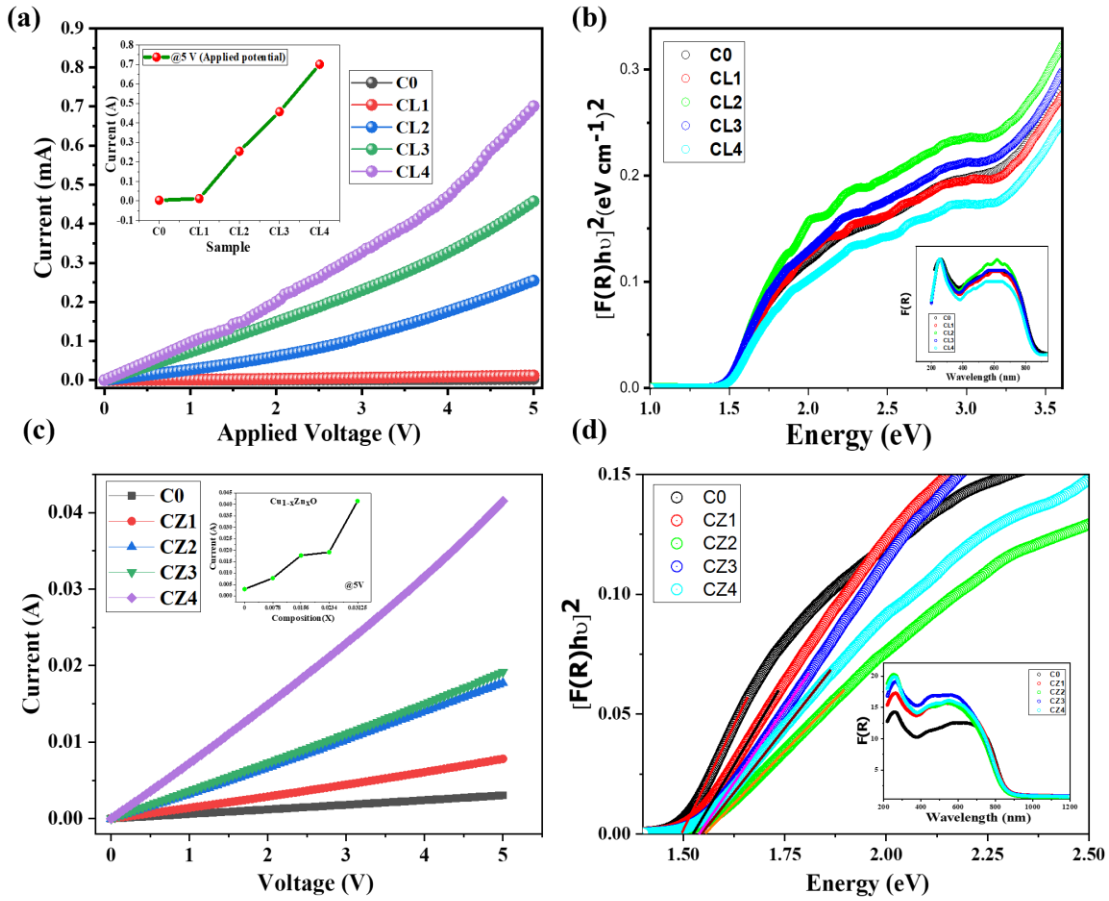
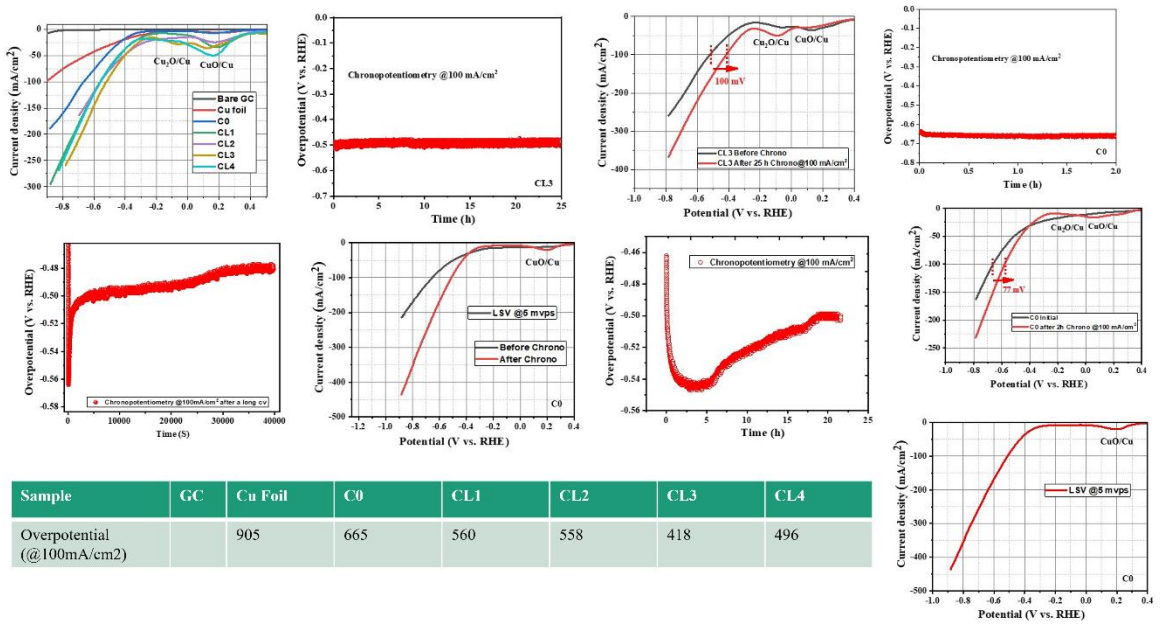


Figure AC4: *Electrical and optical properties of pristine and doped CuO samples. (a) Current–voltage (I–V) characteristics of pristine CuO (C0) and Li-doped CuO (CL1–CL4), showing linear ohmic behavior and progressive enhancement in current response with increasing Li content (inset current measured at 5 V). (b) UV–Vis diffuse reflectance spectra of C0 and CL-series samples, indicating dopant-induced modulation of optical absorption and band-edge characteristics. (c) I–V characteristics of pristine CuO (C0) and Zn-doped CuO (CZ1–CZ4), demonstrating comparatively moderate changes in electrical conductivity. (d) UV–Vis diffuse reflectance spectra of C0 and CZ-series samples, showing subtle variations in absorption profiles consistent with isovalent substitution. The contrasting electrical trends between aliovalent Li^{+} and isovalent Zn^{2+} substitution highlight the role of dopant charge imbalance in modifying electronic transport properties without inducing phase transformation.*



Sample	GC	Cu Foil	C0	CL1	CL2	CL3	CL4
Overpotential (@100mA/cm2)		905	665	560	558	418	496

Figure AC5: *Preliminary alkaline hydrogen evolution reaction (HER) performance of pristine and Li-modified CuO electrodes. (a) Linear sweep voltammetry (LSV) curves of Cu foil, pristine CuO (C0), and Li-doped CuO samples (CL1–CL4) recorded in alkaline electrolyte. (b,d,f) Chronopotentiometry stability profiles at 100 mA cm^{-2} for selected compositions, demonstrating steady-state overpotential behavior. (c,g) Comparison of LSV curves before and after chronopotentiometry testing, indicating minimal performance degradation. (h) Summary of overpotential values at 100 mA cm^{-2} for all samples, highlighting reduced overpotential for CL3 relative to pristine CuO. Li substitution results in a notable decrease in overpotential compared to pristine CuO, whereas Cu foil and glassy carbon serve as reference electrodes. These results are presented as preliminary evidence that aliovalent substitution enhances cathodic performance in CuO-based systems.*

References

[1] ‘Global landscape of energy transition finance 2025’, 2025.

[2] F. Perera, ‘Pollution from Fossil-Fuel Combustion is the Leading Environmental Threat to Global Pediatric Health and Equity: Solutions Exist’, *Int. J. Environ. Res. Public. Health*, vol. 15, no. 1, p. 16, Jan. 2018, doi: 10.3390/ijerph15010016.

[3] Q. Zeng, C. Li, and C. Magazzino, ‘Impact of green energy production for sustainable economic growth and green economic recovery’, *Heliyon*, vol. 10, no. 17, p. e36643, Sep. 2024, doi: 10.1016/j.heliyon.2024.e36643.

[4] ‘Geopolitics of the energy transition: Energy security’.

[5] O. Alšauskas, ‘World Energy Outlook 2024’.

[6] U. A. Bhatti *et al.*, ‘Global production patterns: Understanding the relationship between greenhouse gas emissions, agriculture greening and climate variability’, *Environ. Res.*, vol. 245, p. 118049, Mar. 2024, doi: 10.1016/j.envres.2023.118049.

[7] M. E. Munawer, ‘Human health and environmental impacts of coal combustion and post-combustion wastes’, *J. Sustain. Min.*, vol. 17, no. 2, pp. 87–96, Jan. 2018, doi: 10.1016/j.jsm.2017.12.007.

[8] ‘PDF’. Accessed: Nov. 18, 2025. [Online]. Available: https://www.irena.org/-/media/Files/IRENA/Agency/Publication/2024/Apr/IRENA_Geopolitics_transition_energy_security_2024.pdf

[9] Ipcc, *Global Warming of 1.5°C: IPCC Special Report on Impacts of Global Warming of 1.5°C above Pre-industrial Levels in Context of Strengthening Response to Climate Change, Sustainable Development, and Efforts to Eradicate Poverty*, 1st edn. Cambridge University Press, 2022. doi: 10.1017/9781009157940.

[10] S. A. Khalil and U. A. Rahoma, ‘Verification of Solar Energy Measurements by (ERA-5) and Its Impact on Electricity Costs in North Africa’, *Int. J. Astron. Astrophys.*, vol. 12, no. 4, pp. 301–327, Nov. 2022, doi: 10.4236/ijaa.2022.124018.

[11] K. Chen, W. Dong, Y. Huang, F. Wang, J. L. Zhou, and W. Li, ‘Photocatalysis for sustainable energy and environmental protection in construction: A review on surface engineering and emerging synthesis’, *J. Environ. Chem. Eng.*, vol. 13, no. 5, p. 117529, Oct. 2025, doi: 10.1016/j.jece.2025.117529.

[12] A. M. Sadeq *et al.*, ‘Hydrogen energy systems: Technologies, trends, and future prospects’, *Sci. Total Environ.*, vol. 939, p. 173622, Aug. 2024, doi: 10.1016/j.scitotenv.2024.173622.

[13] B. Reda, A. A. Elzamar, S. AlFazzani, and S. M. Ezzat, ‘Green hydrogen as a source of renewable energy: a step towards sustainability, an overview’, *Environ. Dev. Sustain.*, May 2024, doi: 10.1007/s10668-024-04892-z.

[14] ‘Green hydrogen for sustainable industrial development: A policy toolkit for developing countries’.

[15] M. M. Hossain Bhuiyan and Z. Siddique, ‘Hydrogen as an alternative fuel: A comprehensive review of challenges and opportunities in production, storage, and transportation’, *Int. J. Hydrog. Energy*, vol. 102, pp. 1026–1044, Feb. 2025, doi: 10.1016/j.ijhydene.2025.01.033.

[16] S. Imran and M. Hussain, ‘Emerging trends in water splitting innovations for solar hydrogen production: Analysis, comparison, and economical insights’, *Int. J. Hydrog. Energy*, vol. 77, pp. 975–996, Aug. 2024, doi: 10.1016/j.ijhydene.2024.06.254.

[17] S. Aslam *et al.*, ‘Electrochemical hydrogen production: sustainable hydrogen economy’, *Green Chem.*, vol. 25, no. 23, pp. 9543–9573, 2023, doi: 10.1039/D3GC02849F.

[18] R. Al-Tohamy *et al.*, ‘A critical review on the treatment of dye-containing wastewater: Ecotoxicological and health concerns of textile dyes and possible remediation approaches for environmental safety’, *Ecotoxicol. Environ. Saf.*, vol. 231, p. 113160, Feb. 2022, doi: 10.1016/j.ecoenv.2021.113160.

[19] ‘Environmental Impact: Concept, Consequences, Measurement’, Jan. 2017, doi: 10.1016/B978-0-12-809633-8.02380-3.

[20] A. Malik, E. Grohmann, and R. Akhtar, Eds, *Environmental Deterioration and Human Health: Natural and anthropogenic determinants*. Dordrecht: Springer Netherlands, 2014. doi: 10.1007/978-94-007-7890-0.

[21] S. Mani and R. Bharagava, ‘Textile Industry Wastewater: Environmental and Health Hazards and Treatment Approaches’, 2018.

[22] M. Clark, ‘Handbook of Textile and Industrial Dyeing: Principles, Processes and Types of Dyes’, vol. 1, pp. 1–652, Jan. 2011.

[23] R. Sangamnere, T. Misra, H. Bherwani, A. Kapley, and R. Kumar, ‘A critical review of conventional and emerging wastewater treatment technologies’, *Sustain. Water Resour. Manag.*, vol. 9, no. 2, p. 58, Mar. 2023, doi: 10.1007/s40899-023-00829-y.

[24] S. Sheikhi, R. Dehghanzadeh, and H. Aslani, ‘Advanced oxidation processes for chlorpyrifos removal from aqueous solution: a systematic review’, *J. Environ. Health Sci. Eng.*, vol. 19, no. 1, pp. 1249–1262, Jun. 2021, doi: 10.1007/s40201-021-00674-1.

[25] A. Fujishima and K. Honda, ‘Electrochemical Photolysis of Water at a Semiconductor Electrode’, *Nature*, vol. 238, no. 5358, pp. 37–38, Jul. 1972, doi: 10.1038/238037a0.

[26] M. A. Hassaan, M. A. El-Nemr, M. R. Elkatory, S. Ragab, V.-C. Niculescu, and A. El Nemr, ‘Principles of Photocatalysts and Their Different Applications: A Review’, *Top. Curr. Chem.*, vol. 381, no. 6, p. 31, Oct. 2023, doi: 10.1007/s41061-023-00444-7.

[27] S. Chen, T. Takata, and K. Domen, ‘Particulate photocatalysts for overall water splitting’, *Nat. Rev. Mater.*, vol. 2, no. 10, p. 17050, Aug. 2017, doi: 10.1038/natrevmats.2017.50.

[28] D. Frederichi, M. H. N. O. Scaliante, and R. Bergamasco, ‘Structured photocatalytic systems: photocatalytic coatings on low-cost structures for treatment of water contaminated with micropollutants—a short review’, *Environ. Sci. Pollut. Res.*, vol. 28, no. 19, pp. 23610–23633, May 2021, doi: 10.1007/s11356-020-10022-9.

[29] L. F. T. Novaes, J. Liu, Y. Shen, L. Lu, J. M. Meinhardt, and S. Lin, ‘Electrocatalysis as an enabling technology for organic synthesis’, *Chem. Soc. Rev.*, vol. 50, no. 14, pp. 7941–8002, Jul. 2021, doi: 10.1039/D1CS00223F.

[30] H. Chen, Y. Zhou, W. Guo, and B. Y. Xia, ‘Emerging two-dimensional nanocatalysts for electrocatalytic hydrogen production’, *Chin. Chem. Lett.*, vol. 33, no. 4, pp. 1831–1840, Apr. 2022, doi: 10.1016/j.cclet.2021.09.034.

[31] L. Fei, H. Sun, Y. Li, Y. Gu, W. Zhou, and Z. Shao, ‘Recent advances in innovative systems for electrocatalytic hydrogen production’, *Energy Environ. Sci.*, vol. 18, no. 13, pp. 6456–6529, Jul. 2025, doi: 10.1039/D4EE03084B.

[32] M. S. Shah Danish, ‘Exploring metal oxides for the hydrogen evolution reaction (HER) in the field of nanotechnology’, *RSC Sustain.*, vol. 1, no. 9, pp. 2180–2196, 2023, doi: 10.1039/D3SU00179B.

[33] Y. Zhu, L. Li, H. Cheng, and J. Ma, ‘Alkaline Hydrogen Evolution Reaction Electrocatalysts for Anion Exchange Membrane Water Electrolyzers: Progress and Perspective’, *JACS Au*, vol. 4, no. 12, pp. 4639–4654, Dec. 2024, doi: 10.1021/jacsau.4c00898.

[34] O. van der Heijden, S. Park, R. E. Vos, J. J. J. Eggebeen, and M. T. M. Koper, ‘Tafel Slope Plot as a Tool to Analyze Electrocatalytic Reactions’, *ACS Energy Lett.*, vol. 9, no. 4, pp. 1871–1879, Apr. 2024, doi: 10.1021/acsenergylett.4c00266.

[35] R. Tyburski, T. Liu, S. D. Glover, and L. Hammarström, ‘Proton-Coupled Electron Transfer Guidelines, Fair and Square’, *J. Am. Chem. Soc.*, vol. 143, no. 2, pp. 560–576, Jan. 2021, doi: 10.1021/jacs.0c09106.

[36] D. Tyndall *et al.*, ‘Understanding the effect of MXene in a TMO/MXene hybrid catalyst for the oxygen evolution reaction’, *Npj 2D Mater. Appl.*, vol. 7, no. 1, p. 15, Mar. 2023, doi: 10.1038/s41699-023-00377-1.

[37] S. Lyu *et al.*, ‘Exceptional catalytic activity of oxygen evolution reaction via two-dimensional graphene multilayer confined metal-organic frameworks’, *Nat. Commun.*, vol. 13, no. 1, p. 6171, Oct. 2022, doi: 10.1038/s41467-022-33847-z.

[38] H. B. Tao *et al.*, ‘Identification of Surface Reactivity Descriptor for Transition Metal Oxides in Oxygen Evolution Reaction’, *J. Am. Chem. Soc.*, vol. 138, no. 31, pp. 9978–9985, Aug. 2016, doi: 10.1021/jacs.6b05398.

[39] A. Raveendran, M. Chandran, and R. Dhanusuraman, ‘A comprehensive review on the electrochemical parameters and recent material development of electrochemical water splitting electrocatalysts’, *RSC Adv.*, vol. 13, no. 6, pp. 3843–3876, 2023, doi: 10.1039/D2RA07642J.

[40] U. K. Saint *et al.*, 'Effect of pH on photocatalytic degradation of methylene blue in water by facile hydrothermally grown TiO2 nanoparticles under natural sunlight', *JCIS Open*, vol. 19, p. 100150, Oct. 2025, doi: 10.1016/j.jciso.2025.100150.

[41] R. Saha *et al.*, 'Effect of V5+/V4+ substitution on structural and magnetic orderings of SrFeO3-δ', *Ceram. Int.*, vol. 51, no. 23, Part B, pp. 39855–39865, Sep. 2025, doi: 10.1016/j.ceramint.2025.06.220.

[42] P. Maneesha, K. S. Samantaray, S. C. Baral, R. Mittal, M. K. Gupta, and S. Sen, 'Defect/disorder correlated modification of transport properties from hopping to tunneling processes in BaTiO3–LaFeO3 solid solution', *J. Appl. Phys.*, vol. 135, no. 19, p. 194102, May 2024, doi: 10.1063/5.0195109.

[43] K. S. Samantaray *et al.*, 'Contribution of piezoelectric effect on piezo-phototronic coupling in ferroelectrics: A theory assisted experimental approach on NBT', *J. Chem. Phys.*, vol. 161, no. 18, 2024, Accessed: Nov. 12, 2025. [Online]. Available: https://pubs.aip.org/aip/jcp/article/161/18/184711/3319910

[44] S. C. Baral, P. Maneesha, S. Sen, S. Sen, and S. Sen, 'An Introduction to Metal Oxides', in *Optical Properties of Metal Oxide Nanostructures*, V. Kumar, I. Ayoub, V. Sharma, and H. C. Swart, Eds, Singapore: Springer Nature, 2023, pp. 1–34. doi: 10.1007/978-981-99-5640-1_1.

[45] P. Maneesha, S. Chandra Baral, E. G. Rini, and S. Sen, 'An overview of the recent developments in the structural correlation of magnetic and electrical properties of Pr2NiMnO6 Double perovskite', *Prog. Solid State Chem.*, p. 100402, Mar. 2023, doi: 10.1016/j.progsolidstchem.2023.100402.

[46] P. Maneesha *et al.*, 'Effect of oxygen vacancies and cationic valence state on multiferroicity and magnetodielectric coupling in (1-x)BaTiO3.(x)LaFeO3 solid solution', *J. Alloys Compd.*, p. 172587, Oct. 2023, doi: 10.1016/j.jallcom.2023.172587.

[47] R. K. G. Nguyen Sanjay R. Mishra, Tuan Anh, Ed., *Emerging Applications of Low Dimensional Magnets*. Boca Raton: CRC Press, 2022. doi: 10.1201/9781003196952.

[48] R. K. G. Nguyen Sanjay R. Mishra, Tuan Anh, Ed., *Fundamentals of Low Dimensional Magnets*. Boca Raton: CRC Press, 2022. doi: 10.1201/9781003197492.

[49] P. M. Sen Suresh Chandra Baral, E. G. Rini, Somaditya, 'Nanomagnetic Materials: Structural and Magnetic Properties', in *Fundamentals of Low Dimensional Magnets*, CRC Press, 2022.

[50] S. C. B. Rini P. Maneesha, T. J. Ananya, Srishti Sen, Sagnika Sen, Somaditya Sen, E. G., 'Rare Earth Manganites and Related Multiferroicity', in *Emerging Applications of Low Dimensional Magnets*, CRC Press, 2022.

[51] S. C. Baral, P. Maneesha, E. G. Rini, and S. Sen, 'Recent advances in La2NiMnO6 double perovskites for various applications; challenges and opportunities', *Prog. Solid State Chem.*, p. 100429, Oct. 2023, doi: 10.1016/j.progsolidstchem.2023.100429.

[52] M. B. Gawande *et al.*, ‘Cu and Cu-Based Nanoparticles: Synthesis and Applications in Catalysis’, *Chem. Rev.*, vol. 116, no. 6, pp. 3722–3811, Mar. 2016, doi: 10.1021/acs.chemrev.5b00482.

[53] M. A. Ahmed, S. A. Mahmoud, and A. A. Mohamed, ‘Interfacially engineered metal oxide nanocomposites for enhanced photocatalytic degradation of pollutants and energy applications’, *RSC Adv.*, vol. 15, no. 20, pp. 15561–15603, 2025, doi: 10.1039/D4RA08780A.

[54] S. V. Krivovichev, O. Mentré, O. I. Siidra, M. Colmont, and S. K. Filatov, ‘Anion-Centered Tetrahedra in Inorganic Compounds’, *Chem. Rev.*, vol. 113, no. 8, pp. 6459–6535, Aug. 2013, doi: 10.1021/cr3004696.

[55] C. E. Ekuma, V. I. Anisimov, J. Moreno, and M. Jarrell, ‘Electronic structure and spectra of CuO’, *Eur. Phys. J. B*, vol. 87, no. 1, p. 23, Jan. 2014, doi: 10.1140/epjb/e2013-40949-5.

[56] A. Živković and N. H. de Leeuw, ‘Exploring the formation of intrinsic p-type and n-type defects in CuO’, *Phys. Rev. Mater.*, vol. 4, no. 7, p. 074606, Jul. 2020, doi: 10.1103/PhysRevMaterials.4.074606.

[57] T. J. Smart, A. C. Cardiel, F. Wu, K.-S. Choi, and Y. Ping, ‘Mechanistic insights of enhanced spin polaron conduction in CuO through atomic doping’, *Npj Comput. Mater.*, vol. 4, no. 1, p. 61, Nov. 2018, doi: 10.1038/s41524-018-0118-3.

[58] Y. Wang *et al.*, ‘Electronic structures of $\mathrm{C}{\mathrm{u}}_{2}\mathrm{O},\mathrm{C}{\mathrm{u}}_{4}{\mathrm{O}}_{3}$, and CuO: A joint experimental and theoretical study’, *Phys. Rev. B*, vol. 94, no. 24, p. 245418, Dec. 2016, doi: 10.1103/PhysRevB.94.245418.

[59] Z. Liang *et al.*, ‘Covalent organic frameworks: Fundamentals, mechanisms, modification, and applications in photocatalysis’, *Chem Catal.*, vol. 2, no. 9, pp. 2157–2228, Sep. 2022, doi: 10.1016/j.checat.2022.06.006.

[60] D. Rutkowska-Zbik, V. Kaipanchery, and R. Tokarz-Sobieraj, ‘Single atom and sub-nanometer copper clusters deposited on titania for hydrogen evolution reaction: A density functional study’, *Catal. Today*, vol. 446, p. 115142, Feb. 2025, doi: 10.1016/j.cattod.2024.115142.

[61] J. Kari *et al.*, ‘Sabatier Principle for Interfacial (Heterogeneous) Enzyme Catalysis’, *ACS Catal.*, vol. 8, no. 12, pp. 11966–11972, Dec. 2018, doi: 10.1021/acscatal.8b03547.

[62] S. Xu *et al.*, ‘Role and advances in nonmetal doping of electrocatalysts for the hydrogen evolution reaction: a review’, *Inorg. Chem. Front.*, vol. 12, no. 18, pp. 5258–5288, 2025, doi: 10.1039/D5QI00376H.

[63] S. Keerthana, R. Venkatesh, K. Mahalakshmi, K. Saravanakumar, and C. R. Dhas, ‘Effect of doping level on the photoconduction and chemiresistive ethanol gas sensing of lanthanum-doped CuO films’, *Thin Solid Films*, vol. 804, p. 140500, Sep. 2024, doi: 10.1016/j.tsf.2024.140500.

[64] A. M. Ibrahim, G. H. Munshi, and L. M. Al-Harbi, ‘Copper(II) oxide nanocatalyst preparation and characterization: green chemistry route’, *Bull. Natl. Res. Cent.*, vol. 42, no. 1, p. 6, Sep. 2018, doi: 10.1186/s42269-018-0006-5.

[65] J. C. de Almeida *et al.*, ‘Copper-based Materials for Photo and Electrocatalytic Process: Advancing Renewable Energy and Environmental Applications’, *Adv. Funct. Mater.*, vol. n/a, no. n/a, p. 2502901, doi: 10.1002/adfm.202502901.

[66] M. Benaissa, H. S. Abdelkader, A. I. Abdulkareem, A. Q. Al-Dujaili, A. J. Humaidi, and Y. Menni, ‘Comparative analysis of the substitutional and interstitial Li-, Na-doped, and Li\Na-Codoped Cu2O via density functional calculations’, *Mod. Phys. Lett. B*, vol. 37, no. 25, p. 2350084, Sep. 2023, doi: 10.1142/S0217984923500847.

[67] Z. Wang *et al.*, ‘Identifying Copper Vacancies and Their Role in the CuO Based Photocathode for Water Splitting’, *Angew. Chem.*, vol. 131, no. 49, pp. 17768–17773, Dec. 2019, doi: 10.1002/ange.201909182.

[68] B. Troudi, O. Halimi, M. Sebais, B. Boudine, and A. Djebli, ‘SYNTHESIS, STRUCTURAL AND OPTICAL PROPERTIES OF CuO NANOCRYSTALS EMBEDDED IN POLYVINYL CHLORIDE (PVC) THIN FILMS’, *Thin Films*, vol. 5, no. 2.

[69] H. Shooshtari Gugtapeh, A. H. Aghaii, and A. Simchi, ‘A critical review on the role of structural defects in electrochemical nitrate reduction catalysts: From mechanisms to formation strategies’, *J. Environ. Chem. Eng.*, vol. 13, no. 6, p. 120221, Dec. 2025, doi: 10.1016/j.jece.2025.120221.

[70] S. Sahani, T. Kim, S. P. Asrafali, and S. S. Han, ‘Visible-light assisted hydrogen evolution via water splitting over micro-fluidized Cu-doped polymeric carbon nitride sheets’, *Mol. Catal.*, vol. 575, p. 114895, Mar. 2025, doi: 10.1016/j.mcat.2025.114895.

[71] C.-Y. Chiang, Y. Shin, and S. Ehrman, ‘Dopant effects on conductivity in copper oxide photoelectrochemical cells’, *Appl. Energy*, vol. 164, pp. 1039–1042, Feb. 2016, doi: 10.1016/j.apenergy.2015.01.116.

[72] P. K. Mishra, R. Dobhal, E. G. Rini, M. Kumar, and S. Sen, ‘Rapid organic dye degradation and wavelength dependent sensing study in Cu1-xFexO’, *Ceram. Int.*, vol. 48, no. 5, pp. 5995–6006, Mar. 2022, doi: 10.1016/j.ceramint.2021.11.135.

[73] S. C. Baral *et al.*, ‘Enhanced photocatalytic degradation of organic pollutants in water using copper oxide (CuO) nanosheets for environmental application’, *JCIS Open*, vol. 13, p. 100102, Apr. 2024, doi: 10.1016/j.jciso.2024.100102.

[74] R. Snellings, L. Machiels, G. Mertens, and J. Elsen, ‘Rietveld Refinement strategy for Quantitative Phase analysis of Partially AMorphous zeolitized tuffaceous rocks’, p. 14.

[75] L. B. McCusker, R. B. Von Dreele, D. E. Cox, D. Louër, and P. Scardi, ‘Rietveld refinement guidelines’, *J. Appl. Crystallogr.*, vol. 32, no. 1, pp. 36–50, Feb. 1999, doi: 10.1107/S0021889898009856.

[76] Z. Yang, Y. Lu, X. Liu, F. Li, and J. Chen, 'Application of high energy X-ray diffraction and Rietveld refinement in layered lithium transition metal oxide cathode materials', *Nano Res.*, vol. 16, no. 7, pp. 9954–9967, Jul. 2023, doi: 10.1007/s12274-023-5630-1.

[77] C. V. Raman and K. S. Krishnan, 'A New Type of Secondary Radiation', *Nature*, vol. 121, no. 3048, pp. 501–502, Mar. 1928, doi: 10.1038/121501c0.

[78] 'Instrument Presentation'. Accessed: Jan. 12, 2026. [Online]. Available: https://www.horiba.com/ind/scientific/technologies/raman-imaging-and-spectroscopy/raman-spectrometer-presentation/

[79] Z. Movasaghi, S. Rehman, and Dr. I. ur Rehman, 'Fourier Transform Infrared (FTIR) Spectroscopy of Biological Tissues', *Appl. Spectrosc. Rev.*, vol. 43, no. 2, pp. 134–179, Feb. 2008, doi: 10.1080/05704920701829043.

[80] 'Fourier Transform Infrared (FTIR) Spectroscopy', in *Membrane Characterization*, Elsevier, 2017, pp. 3–29. doi: 10.1016/B978-0-444-63776-5.00001-2.

[81] Z. Bacsik, J. Mink, and G. Keresztury, 'FTIR Spectroscopy of the Atmosphere. I. Principles and Methods', *Appl. Spectrosc. Rev.*, vol. 39, no. 3, pp. 295–363, Dec. 2004, doi: 10.1081/ASR-200030192.

[82] B. J. Inkson, 'Scanning electron microscopy (SEM) and transmission electron microscopy (TEM) for materials characterization', in *Materials Characterization Using Nondestructive Evaluation (NDE) Methods*, Elsevier, 2016, pp. 17–43. doi: 10.1016/B978-0-08-100040-3.00002-X.

[83] 'Phy (H) Vi Nano Material 11 Ajaypratap | PDF | Transmission Electron Microscopy | Microscope', Scribd. Accessed: Jan. 12, 2026. [Online]. Available: https://www.scribd.com/document/533445773/1585214437-Phy-h-Vi-Nano-Material-11-Ajaypratap

[84] 'Minerals, Critical Minerals, and the U.S. Economy - Google Books'. Accessed: Jan. 12, 2026. [Online]. Available: https://www.google.co.uk/books/edition/Minerals_Critical_Minerals_and_the_U_S_E/UaVVAgAAQBAJ?hl=en&gbpv=1&dq=Use/importance+of+HRTEM+for+structural+analysis+in+oxides&pg=PA1&printsec=frontcover

[85] Y. Miyah, A. Lahrichi, M. Idrissi, S. Boujraf, H. Taouda, and F. Zerrouq, 'Assessment of adsorption kinetics for removal potential of Crystal Violet dye from aqueous solutions using Moroccan pyrophyllite', *J. Assoc. Arab Univ. Basic Appl. Sci.*, vol. 23, pp. 20–28, Jun. 2017, doi: 10.1016/j.jaubas.2016.06.001.

[86] W. Wan, J. Su, X. D. Zou, and T. Willhammar, 'Transmission electron microscopy as an important tool for characterization of zeolite structures', *Inorg. Chem. Front.*, vol. 5, no. 11, pp. 2836–2855, 2018, doi: 10.1039/C8QI00806J.

[87] 'Transmission Electron Microscopy (TEM)', in *Membrane Characterization*, Elsevier, 2017, pp. 145–159. doi: 10.1016/B978-0-444-63776-5.00008-5.

[88] J. Torrent and V. Barrón, 'Diffuse Reflectance Spectroscopy', in *SSSA Book Series*, A. L. Ulery and L. Richard Drees, Eds, Madison, WI, USA: American Society of Agronomy and Soil Science Society of America, 2015, pp. 367–385. doi: 10.2136/sssabookser5.5.c13.

[89] G. Kortüm, W. Braun, and G. Herzog, 'Principles and Techniques of Diffuse-Reflectance Spectroscopy', *Angew. Chem. Int. Ed. Engl.*, vol. 2, no. 7, pp. 333–341, Jul. 1963, doi: 10.1002/anie.196303331.

[90] L. Yang and B. Kruse, 'Revised Kubelka–Munk theory I Theory and application', *J. Opt. Soc. Am. A*, vol. 21, no. 10, p. 1933, Oct. 2004, doi: 10.1364/JOSAA.21.001933.

[91] J. H. Nobbs, 'Kubelka-Munk Theory and the Prediction of Reflectance', *Rev. Prog. Color. Relat. Top.*, vol. 15, no. 1, pp. 66–75, Oct. 2008, doi: 10.1111/j.1478-4408.1985.tb03737.x.

[92] J. Tauc, R. Grigorovici, and A. Vancu, 'Optical Properties and Electronic Structure of Amorphous Germanium', *Phys. Status Solidi B*, vol. 15, no. 2, pp. 627–637, 1966, doi: 10.1002/pssb.19660150224.

[93] O. V. Rambadey, A. Kumar, and P. R. Sagdeo, 'Investigating the correlation between the Urbach energy and asymmetry parameter of the Raman mode in semiconductors', *Phys. Rev. B*, vol. 104, no. 24, p. 245205, Dec. 2021, doi: 10.1103/PhysRevB.104.245205.

[94] D. M. Ammann and P. S. Institut, 'X-ray Photoelectron Spectroscopy (XPS)', p. 31.

[95] D. R. Baer *et al.*, 'Practical guides for x-ray photoelectron spectroscopy: First steps in planning, conducting, and reporting XPS measurements', *J. Vac. Sci. Technol. A*, vol. 37, no. 3, p. 031401, May 2019, doi: 10.1116/1.5065501.

[96] M. C. Biesinger, B. P. Payne, A. P. Grosvenor, L. W. M. Lau, A. R. Gerson, and R. St. C. Smart, 'Resolving surface chemical states in XPS analysis of first row transition metals, oxides and hydroxides: Cr, Mn, Fe, Co and Ni', *Appl. Surf. Sci.*, vol. 257, no. 7, pp. 2717–2730, Jan. 2011, doi: 10.1016/j.apsusc.2010.10.051.

[97] N. Hwang and A. R. Barron, 'BET Surface Area Analysis of Nanoparticles'.

[98] P. Sinha, A. Datar, C. Jeong, X. Deng, Y. G. Chung, and L.-C. Lin, 'Surface Area Determination of Porous Materials Using the Brunauer–Emmett–Teller (BET) Method: Limitations and Improvements', *J. Phys. Chem. C*, vol. 123, no. 33, pp. 20195–20209, Aug. 2019, doi: 10.1021/acs.jpcc.9b02116.

[99] D. Dollimore, P. Spooner, and A. Turner, 'The bet method of analysis of gas adsorption data and its relevance to the calculation of surface areas', *Surf. Technol.*, vol. 4, no. 2, pp. 121–160, Mar. 1976, doi: 10.1016/0376-4583(76)90024-8.

[100] J. D. Clogston and A. K. Patri, 'Zeta potential measurement', *Methods Mol. Biol. Clifton NJ*, vol. 697, pp. 63–70, 2011, doi: 10.1007/978-1-60327-198-1_6.

[101] S. Bhattacharjee, 'DLS and zeta potential – What they are and what they are not?', *J.*

Controlled Release, vol. 235, pp. 337–351, Aug. 2016, doi: 10.1016/j.jconrel.2016.06.017.

[102] A. Ch. Lazanas and M. I. Prodromidis, 'Electrochemical Impedance Spectroscopy—A Tutorial', *ACS Meas. Sci. Au*, vol. 3, no. 3, pp. 162–193, Jun. 2023, doi: 10.1021/acsmeasuresciau.2c00070.

[103] P. Vadhva *et al.*, 'Electrochemical Impedance Spectroscopy for All-Solid-State Batteries: Theory, Methods and Future Outlook', *ChemElectroChem*, vol. 8, no. 11, pp. 1930–1947, Jun. 2021, doi: 10.1002/celc.202100108.

[104] T. H. Tran and V. T. Nguyen, 'Copper Oxide Nanomaterials Prepared by Solution Methods, Some Properties, and Potential Applications: A Brief Review', *Int. Sch. Res. Not.*, vol. 2014, p. e856592, Dec. 2014, doi: 10.1155/2014/856592.

[105] M. R. Islam, J. E. Obaid, Md. Saiduzzaman, S. S. Nishat, T. Debnath, and A. Kabir, 'Effect of Al doping on the structural and optical properties of CuO nanoparticles prepared by solution combustion method: Experiment and DFT investigation', *J. Phys. Chem. Solids*, vol. 147, p. 109646, Dec. 2020, doi: 10.1016/j.jpcs.2020.109646.

[106] M. Arfan *et al.*, 'Tailoring of nanostructures: Al doped CuO synthesized by composite-hydroxide-mediated approach', *Results Phys.*, vol. 13, p. 102187, Jun. 2019, doi: 10.1016/j.rinp.2019.102187.

[107] Z. Hajizadeh, R. Taheri-Ledari, and F. R. Asl, '3 - Identification and analytical methods', in *Heterogeneous Micro and Nanoscale Composites for the Catalysis of Organic Reactions*, A. Maleki, Ed., in Micro and Nano Technologies. , Elsevier, 2022, pp. 33–51. doi: 10.1016/B978-0-12-824527-9.00001-0.

[108] V. S. Vinila and J. Isac, 'Chapter 14 - Synthesis and structural studies of superconducting perovskite GdBa2Ca3Cu4O10.5+δ nanosystems', in *Design, Fabrication, and Characterization of Multifunctional Nanomaterials*, S. Thomas, N. Kalarikkal, and A. R. Abraham, Eds, in Micro and Nano Technologies. , Elsevier, 2022, pp. 319–341. doi: 10.1016/B978-0-12-820558-7.00022-4.

[109] U. Holzwarth and N. Gibson, 'The Scherrer equation versus the "Debye-Scherrer equation"', *Nat. Nanotechnol.*, vol. 6, no. 9, Art. no. 9, Sep. 2011, doi: 10.1038/nnano.2011.145.

[110] M. Bin Mobarak, Md. S. Hossain, F. Chowdhury, and S. Ahmed, 'Synthesis and characterization of CuO nanoparticles utilizing waste fish scale and exploitation of XRD peak profile analysis for approximating the structural parameters', *Arab. J. Chem.*, vol. 15, no. 10, p. 104117, Oct. 2022, doi: 10.1016/j.arabjc.2022.104117.

[111] A. Önsten, M. Göthelid, and U. O. Karlsson, 'Atomic structure of Cu2O(111)', *Surf. Sci.*, vol. 603, no. 2, pp. 257–264, Jan. 2009, doi: 10.1016/j.susc.2008.10.048.

[112] S. S. Gaikwad *et al.*, 'Oxygen induced strained ZnO nanoparticles: an investigation of Raman scattering and visible photoluminescence', *J. Mater. Chem. C*, vol. 2, no. 35, pp. 7264–7274, Aug. 2014, doi: 10.1039/C4TC00566J.

[113] X. Chen and H. Zhu, '3.01 - Catalysis by Supported Gold Nanoparticles', in *Comprehensive Nanoscience and Technology*, D. L. Andrews, G. D. Scholes, and G. P. Wiederrecht, Eds, Amsterdam: Academic Press, 2011, pp. 1–11. doi: 10.1016/B978-0-12-374396-1.00095-7.

[114] H. Siddiqui, M. R. Parra, M. S. Qureshi, M. M. Malik, and F. Z. Haque, 'Studies of structural, optical, and electrical properties associated with defects in sodium-doped copper oxide (CuO/Na) nanostructures', *J. Mater. Sci.*, vol. 53, no. 12, pp. 8826–8843, Jun. 2018, doi: 10.1007/s10853-018-2179-6.

[115] T. Jan *et al.*, 'Structural, Raman, optical and novel antibacterial characteristics of Al doped CuO nanostructures', *Mater. Res. Express*, vol. 6, no. 10, p. 1050a3, Sep. 2019, doi: 10.1088/2053-1591/ab3f8c.

[116] L.-J. Chen, G.-S. Li, and L.-P. Li, 'CuO nanocrystals in thermal decomposition of ammonium perchlorate', *J. Therm. Anal. Calorim.*, vol. 91, no. 2, pp. 581–587, Feb. 2008, doi: 10.1007/s10973-007-8496-7.

[117] R. N. Mariammal, K. Ramachandran, G. Kalaiselvan, S. Arumugam, B. Renganathan, and D. Sastikumar, 'Effect of magnetism on the ethanol sensitivity of undoped and Mn-doped CuO nanoflakes', *Appl. Surf. Sci.*, vol. 270, pp. 545–552, Apr. 2013, doi: 10.1016/j.apsusc.2013.01.084.

[118] A. Iqbal *et al.*, 'Photoluminescence study of as-grown vertically standing wurtzite InP nanowire ensembles', *Nanotechnology*, vol. 24, no. 11, p. 115706, Mar. 2013, doi: 10.1088/0957-4484/24/11/115706.

[119] B. D. Viezbicke, S. Patel, B. E. Davis, and D. P. Birnie III, 'Evaluation of the Tauc method for optical absorption edge determination: ZnO thin films as a model system', *Phys. Status Solidi B*, vol. 252, no. 8, pp. 1700–1710, 2015, doi: 10.1002/pssb.201552007.

[120] O. V. Rambadey, A. Kumar, A. Sati, and P. R. Sagdeo, 'Exploring the Interrelation between Urbach Energy and Dielectric Constant in Hf-Substituted BaTiO3', *ACS Omega*, vol. 6, no. 47, pp. 32231–32238, Nov. 2021, doi: 10.1021/acsomega.1c05057.

[121] A. Önsten *et al.*, 'Probing the valence band structure of Cu_ {2} O using high-energy angle-resolved photoelectron spectroscopy', *Phys Rev B*, vol. 76, Sep. 2007, doi: 10.1103/PhysRevB.76.115127.

[122] Q. Zhu, J. Lu, Y. Wang, F. Qin, Z. Shi, and C. Xu, 'Burstein-Moss Effect Behind Au Surface Plasmon Enhanced Intrinsic Emission of ZnO Microdisks', *Sci. Rep.*, vol. 6, no. 1, Art. no. 1, Nov. 2016, doi: 10.1038/srep36194.

[123] S. Gahlawat, J. Singh, A. K. Yadav, and P. P. Ingole, 'Exploring Burstein–Moss type effects in nickel doped hematite dendrite nanostructures for enhanced photo-electrochemical water splitting', *Phys. Chem. Chem. Phys.*, vol. 21, no. 36, pp. 20463–20477, Sep. 2019, doi: 10.1039/C9CP04132J.

[124] J. A. Brame and C. S. Griggs, 'Surface area analysis using the Brunauer-Emmett-Teller (BET) method : scientific operation procedure series : SOP-C', 2016, Accessed: Apr. 24,

2023. [Online]. Available: https://erdc-library.erdc.dren.mil/jspui/handle/11681/20339

[125] S. J. Eichhorn and W. W. Sampson, 'Relationships between specific surface area and pore size in electrospun polymer fibre networks', *J. R. Soc. Interface*, vol. 7, no. 45, pp. 641–649, Apr. 2010, doi: 10.1098/rsif.2009.0374.

[126] M. Zhou, Z. Wei, H. Qiao, L. Zhu, H. Yang, and T. Xia, 'Particle Size and Pore Structure Characterization of Silver Nanoparticles Prepared by Confined Arc Plasma', *J. Nanomater.*, vol. 2009, p. e968058, Feb. 2009, doi: 10.1155/2009/968058.

[127] F. Rizzi *et al.*, 'High Surface Area Mesoporous Silica Nanoparticles with Tunable Size in the Sub-Micrometer Regime: Insights on the Size and Porosity Control Mechanisms', *Molecules*, vol. 26, no. 14, Art. no. 14, Jan. 2021, doi: 10.3390/molecules26144247.

[128] J. D. Clogston and A. K. Patri, 'Zeta potential measurement', *Methods Mol. Biol. Clifton NJ*, vol. 697, pp. 63–70, 2011, doi: 10.1007/978-1-60327-198-1_6.

[129] E. Joseph and G. Singhvi, 'Chapter 4 - Multifunctional nanocrystals for cancer therapy: a potential nanocarrier', in *Nanomaterials for Drug Delivery and Therapy*, A. M. Grumezescu, Ed., William Andrew Publishing, 2019, pp. 91–116. doi: 10.1016/B978-0-12-816505-8.00007-2.

[130] T. Mudalige, H. Qu, D. Van Haute, S. M. Ansar, A. Paredes, and T. Ingle, 'Chapter 11 - Characterization of Nanomaterials: Tools and Challenges', in *Nanomaterials for Food Applications*, A. López Rubio, M. J. Fabra Rovira, M. martínez Sanz, and L. G. Gómez-Mascaraque, Eds, in Micro and Nano Technologies. , Elsevier, 2019, pp. 313–353. doi: 10.1016/B978-0-12-814130-4.00011-7.

[131] M. Danaei *et al.*, 'Impact of Particle Size and Polydispersity Index on the Clinical Applications of Lipidic Nanocarrier Systems', *Pharmaceutics*, vol. 10, no. 2, p. 57, May 2018, doi: 10.3390/pharmaceutics10020057.

[132] M. S. Nawaz and M. Ahsan, 'Comparison of physico-chemical, advanced oxidation and biological techniques for the textile wastewater treatment', *Alex. Eng. J.*, vol. 53, no. 3, pp. 717–722, Sep. 2014, doi: 10.1016/j.aej.2014.06.007.

[133] F. Meng *et al.*, 'Temperature dependent photocatalysis of g-C3N4, TiO2 and ZnO: Differences in photoactive mechanism', *J. Colloid Interface Sci.*, vol. 532, pp. 321–330, Dec. 2018, doi: 10.1016/j.jcis.2018.07.131.

[134] Y.-W. Chen and Y.-H. Hsu, 'Effects of Reaction Temperature on the Photocatalytic Activity of TiO2 with Pd and Cu Cocatalysts', *Catalysts*, vol. 11, no. 8, Art. no. 8, Aug. 2021, doi: 10.3390/catal11080966.

[135] 'A review on the factors affecting the photocatalytic degradation of hazardous materials', *Mater. Sci. Eng. Int. J.*, vol. Volume 1, no. Issue 3, Nov. 2017, doi: 10.15406/mseij.2017.01.00018.

[136] M. Umar, H. A. Aziz, M. Umar, and H. A. Aziz, *Photocatalytic Degradation of Organic Pollutants in Water*. IntechOpen, 2013. doi: 10.5772/53699.

[137] D. A. Yaseen and M. Scholz, ‘Textile dye wastewater characteristics and constituents of synthetic effluents: a critical review’, *Int. J. Environ. Sci. Technol.*, vol. 16, no. 2, pp. 1193–1226, Feb. 2019, doi: 10.1007/s13762-018-2130-z.

[138] D. Curcó, J. Giménez, A. Addardak, S. Cervera-March, and S. Esplugas, ‘Effects of radiation absorption and catalyst concentration on the photocatalytic degradation of pollutants’, *Catal. Today*, vol. 76, no. 2, pp. 177–188, Nov. 2002, doi: 10.1016/S0920-5861(02)00217-1.

[139] H. M. Coleman, V. Vimonses, G. Leslie, and R. Amal, ‘Degradation of 1,4-dioxane in water using TiO2 based photocatalytic and H2O2/UV processes’, *J. Hazard. Mater.*, vol. 146, no. 3, pp. 496–501, Jul. 2007, doi: 10.1016/j.jhazmat.2007.04.049.

[140] H. Zeghioud, A. A. Assadi, N. Khellaf, H. Djelal, A. Amrane, and S. Rtimi, ‘Photocatalytic Performance of CuxO/TiO2 Deposited by HiPIMS on Polyester under Visible Light LEDs: Oxidants, Ions Effect, and Reactive Oxygen Species Investigation’, *Materials*, vol. 12, no. 3, p. 412, Jan. 2019, doi: 10.3390/ma12030412.

[141] A. Houas, H. Lachheb, M. Ksibi, E. Elaloui, C. Guillard, and J.-M. Herrmann, ‘Photocatalytic degradation pathway of methylene blue in water’, *Appl. Catal. B Environ.*, vol. 31, no. 2, pp. 145–157, May 2001, doi: 10.1016/S0926-3373(00)00276-9.

[142] Y. Xu and M. A. A. Schoonen, ‘The absolute energy positions of conduction and valence bands of selected semiconducting minerals’, *Am. Mineral.*, vol. 85, no. 3–4, pp. 543–556, Mar. 2000, doi: 10.2138/am-2000-0416.

[143] K. Balu *et al.*, ‘BiOX (X = I or Cl?) modified Na-K2Ti6O13 nanostructured materials for efficient degradation of Tetracycline, Acid Black 1 dye and microbial disinfection in wastewater under Blue LED’, *Sep. Purif. Technol.*, vol. 309, p. 122998, Mar. 2023, doi: 10.1016/j.seppur.2022.122998.

[144] K. Balu *et al.*, ‘Fabrication of Bi2O3/Bismuth Titanates Modified with Metal–Organic Framework-In2S3/CdIn2S4 Materials for Electrocatalytic H2 Production and Its Photoactivity’, *Langmuir*, vol. 39, no. 42, pp. 15055–15066, Oct. 2023, doi: 10.1021/acs.langmuir.3c02031.

[145] B. Krishnakumar, T. Imae, J. Miras, and J. Esquena, ‘Synthesis and azo dye photodegradation activity of ZrS2–ZnO nano-composites’, *Sep. Purif. Technol.*, vol. 132, pp. 281–288, Aug. 2014, doi: 10.1016/j.seppur.2014.05.018.

[146] D. A. Armstrong *et al.*, ‘Standard electrode potentials involving radicals in aqueous solution: inorganic radicals (IUPAC Technical Report)’, *Pure Appl. Chem.*, vol. 87, no. 11–12, pp. 1139–1150, Dec. 2015, doi: 10.1515/pac-2014-0502.

[147] F. Wu *et al.*, ‘ZIF-67/BiOCl Z-Scheme Heterojunction Photocatalyst for Photodegradation of Organic Dyes and Antibiotics’, *ACS Appl. Nano Mater.*, vol. 6, no. 19, pp. 17814–17825, Oct. 2023, doi: 10.1021/acsanm.3c03094.

[148] G. Li *et al.*, ‘Peroxymonosulfate activation with Co3O4 by microstructure engineering for efficient degradation of tetracycline: Efficiency, mechanism and stability’, *Colloids*

Surf. Physicochem. Eng. Asp., vol. 677, p. 132353, Nov. 2023, doi: 10.1016/j.colsurfa.2023.132353.

[149] J. Wang *et al.*, 'Facile fabrication of Fe3O4-Biochar hybrid nanomaterials as catalysts for Photo-Fenton degradation of tetracycline', *Opt. Mater.*, vol. 143, p. 114156, Sep. 2023, doi: 10.1016/j.optmat.2023.114156.

[150] G. Tai *et al.*, 'Enhanced performance and recyclability for peroxymonosulfate activation via controlling the different morphologies of g-C3N4', *Colloids Surf. Physicochem. Eng. Asp.*, vol. 674, p. 131925, Oct. 2023, doi: 10.1016/j.colsurfa.2023.131925.

[151] T. P. Vijayakumar *et al.*, 'Hydrothermal synthesis of CuO/g-C3N4 nanosheets for visible-light driven photodegradation of methylene blue', *Diam. Relat. Mater.*, vol. 121, p. 108735, Jan. 2022, doi: 10.1016/j.diamond.2021.108735.

[152] H. Zhao *et al.*, 'Self-Driven Salt-Thermal Reduction Approach for the Synthesis of Cu2O and AgCl–Cu2O Hybrids with Superior Photocatalytic Activity', *ACS Sustain. Chem. Eng.*, vol. 9, no. 16, pp. 5651–5660, Apr. 2021, doi: 10.1021/acssuschemeng.1c00529.

[153] S. A. Ashter, '6 - Mechanics of Materials', in *Thermoforming of Single and Multilayer Laminates*, S. A. Ashter, Ed., Oxford: William Andrew Publishing, 2014, pp. 123–145. doi: 10.1016/B978-1-4557-3172-5.00006-2.

[154] K. J. Laidler and M. C. King, 'Development of transition-state theory', *J. Phys. Chem.*, vol. 87, no. 15, pp. 2657–2664, Jul. 1983, doi: 10.1021/j100238a002.

[155] Z. Ghasemi, H. Younesi, and A. A. Zinatizadeh, 'Kinetics and thermodynamics of photocatalytic degradation of organic pollutants in petroleum refinery wastewater over nano-TiO2 supported on Fe-ZSM-5', *J. Taiwan Inst. Chem. Eng.*, vol. 65, pp. 357–366, Aug. 2016, doi: 10.1016/j.jtice.2016.05.039.

[156] Y. He *et al.*, 'Hydrophobic CuO Nanosheets Functionalized with Organic Adsorbates', *J. Am. Chem. Soc.*, vol. 140, no. 5, pp. 1824–1833, Feb. 2018, doi: 10.1021/jacs.7b11654.

[157] F. Meng *et al.*, 'Temperature dependent photocatalysis of g-C3N4, TiO2 and ZnO: Differences in photoactive mechanism', *J. Colloid Interface Sci.*, vol. 532, pp. 321–330, Dec. 2018, doi: 10.1016/j.jcis.2018.07.131.

[158] A. Jenifer and S. Sriram, 'Enhanced photocatalytic organic dye degradation activities of pristine and Zn-doped V2O5 nanoparticles', *Appl. Surf. Sci.*, vol. 611, p. 155629, Feb. 2023, doi: 10.1016/j.apsusc.2022.155629.

[159] X. Zheng *et al.*, 'A carnation-like rGO/Bi2O2CO3/BiOCl composite: efficient photocatalyst for the degradation of ciprofloxacin', *J. Mater. Sci. Mater. Electron.*, vol. 30, no. 6, pp. 5986–5994, Mar. 2019, doi: 10.1007/s10854-019-00898-w.

[160] J. C. Barreto, G. S. Smith, N. H. P. Strobel, P. A. McQuillin, and T. A. Miller, 'Terephthalic acid: A dosimeter for the detection of hydroxyl radicals in vitro', *Life Sci.*,

vol. 56, no. 4, pp. PL89–PL96, Dec. 1994, doi: 10.1016/0024-3205(94)00925-2.

[161] G. Žerjav, A. Albreht, I. Vovk, and A. Pintar, 'Revisiting terephthalic acid and coumarin as probes for photoluminescent determination of hydroxyl radical formation rate in heterogeneous photocatalysis', *Appl. Catal. Gen.*, vol. 598, p. 117566, May 2020, doi: 10.1016/j.apcata.2020.117566.

[162] R. Katwal, H. Kaur, G. Sharma, Mu. Naushad, and D. Pathania, 'Electrochemical synthesized copper oxide nanoparticles for enhanced photocatalytic and antimicrobial activity', *J. Ind. Eng. Chem.*, vol. 31, pp. 173–184, Nov. 2015, doi: 10.1016/j.jiec.2015.06.021.

[163] M. Aadil *et al.*, 'Facile synthesis of binary metal substituted copper oxide as a solar light driven photocatalyst and antibacterial substitute', *Adv. Powder Technol.*, vol. 32, no. 3, pp. 940–950, Mar. 2021, doi: 10.1016/j.apt.2021.01.040.

[164] A. George *et al.*, 'Photocatalytic effect of CuO nanoparticles flower-like 3D nanostructures under visible light irradiation with the degradation of methylene blue (MB) dye for environmental application', *Environ. Res.*, vol. 203, p. 111880, Jan. 2022, doi: 10.1016/j.envres.2021.111880.

[165] A. G. Acedo-Mendoza, A. Infantes-Molina, D. Vargas-Hernández, C. A. Chávez-Sánchez, E. Rodríguez-Castellón, and J. C. Tánori-Córdova, 'Photodegradation of methylene blue and methyl orange with CuO supported on ZnO photocatalysts: The effect of copper loading and reaction temperature', *Mater. Sci. Semicond. Process.*, vol. 119, p. 105257, Nov. 2020, doi: 10.1016/j.mssp.2020.105257.

[166] J. I. Pankove, *Optical Processes in Semiconductors*. Courier Corporation, 1975.

[167] P. Makuła, M. Pacia, and W. Macyk, 'How To Correctly Determine the Band Gap Energy of Modified Semiconductor Photocatalysts Based on UV–Vis Spectra', *J. Phys. Chem. Lett.*, vol. 9, no. 23, pp. 6814–6817, Dec. 2018, doi: 10.1021/acs.jpclett.8b02892.

[168] M. Ramesh, 'CuO as efficient photo catalyst for photocatalytic decoloration of wastewater containing Azo dyes', *Water Pract. Technol.*, vol. 16, no. 4, pp. 1078–1090, Jul. 2021, doi: 10.2166/wpt.2021.067.

[169] A. Ajmal, I. Majeed, R. N. Malik, H. Idriss, and M. A. Nadeem, 'Principles and mechanisms of photocatalytic dye degradation on TiO2 based photocatalysts: a comparative overview', *RSC Adv.*, vol. 4, no. 70, pp. 37003–37026, Aug. 2014, doi: 10.1039/C4RA06658H.

[170] Y.-W. Chen and Y.-H. Hsu, 'Effects of Reaction Temperature on the Photocatalytic Activity of TiO2 with Pd and Cu Cocatalysts', *Catalysts*, vol. 11, no. 8, Art. no. 8, Aug. 2021, doi: 10.3390/catal11080966.

[171] K. M. Reza, A. Kurny, and F. Gulshan, 'Parameters affecting the photocatalytic degradation of dyes using TiO2: a review', *Appl. Water Sci.*, vol. 7, no. 4, pp. 1569–1578, Jul. 2017, doi: 10.1007/s13201-015-0367-y.

[172] M. Umar, H. A. Aziz, M. Umar, and H. A. Aziz, *Photocatalytic Degradation of Organic Pollutants in Water*. IntechOpen, 2013. doi: 10.5772/53699.

[173] M. F. Hanafi and N. Sapawe, 'Effect of initial concentration on the photocatalytic degradation of remazol brilliant blue dye using nickel catalyst', *Mater. Today Proc.*, vol. 31, pp. 318–320, Jan. 2020, doi: 10.1016/j.matpr.2020.06.066.

[174] M. Umer, M. Tahir, M. Usman Azam, S. Tasleem, T. Abbas, and A. Muhammad, 'Synergistic effects of single/multi-walls carbon nanotubes in TiO2 and process optimization using response surface methodology for photo-catalytic H2 evolution', *J. Environ. Chem. Eng.*, vol. 7, no. 5, p. 103361, Oct. 2019, doi: 10.1016/j.jece.2019.103361.

[175] K. Hashimoto, H. Irie, and A. Fujishima, 'TiO2 Photocatalysis: A Historical Overview and Future Prospects', *Jpn. J. Appl. Phys.*, vol. 44, no. 12R, p. 8269, Dec. 2005, doi: 10.1143/JJAP.44.8269.

[176] A. Fujishima, T. N. Rao, and D. A. Tryk, 'Titanium dioxide photocatalysis', *J. Photochem. Photobiol. C Photochem. Rev.*, vol. 1, no. 1, pp. 1–21, Jun. 2000, doi: 10.1016/S1389-5567(00)00002-2.

[177] G. Lakhotiya, S. Bajaj, A. K. Nayak, D. Pradhan, P. Tekade, and A. Rana, 'Enhanced catalytic activity without the use of an external light source using microwave-synthesized CuO nanopetals', *Beilstein J. Nanotechnol.*, vol. 8, pp. 1167–1173, 2017, doi: 10.3762/bjnano.8.118.

[178] M. Melchionna and P. Fornasiero, 'Updates on the Roadmap for Photocatalysis', *ACS Catal.*, vol. 10, no. 10, pp. 5493–5501, May 2020, doi: 10.1021/acscatal.0c01204.

[179] S. Sonia, S. Poongodi, P. S. Kumar, D. Mangalaraj, N. Ponpandian, and C. Viswanathan, 'Hydrothermal synthesis of highly stable CuO nanostructures for efficient photocatalytic degradation of organic dyes', *Mater. Sci. Semicond. Process.*, vol. 30, pp. 585–591, Feb. 2015, doi: 10.1016/j.mssp.2014.10.012.

[180] Q. Fan, Q. Lan, M. Zhang, X. Fan, Z. Zhou, and C. Zhang, 'Preparation and photocatalytic activities of 3D flower-like CuO nanostructures*', *J. Semicond.*, vol. 37, no. 8, p. 083002, Aug. 2016, doi: 10.1088/1674-4926/37/8/083002.

[181] B. Nahar, S. B. Chaity, M. A. Gafur, and M. Z. Hossain, 'Synthesis of Spherical Copper Oxide Nanoparticles by Chemical Precipitation Method and Investigation of Their Photocatalytic and Antibacterial Activities', *J. Nanomater.*, vol. 2023, p. e2892081, Feb. 2023, doi: 10.1155/2023/2892081.

[182] S. C. Baral, M. P, P. K. Mishra, P. Dhanapal, and S. Sen, 'Rapid photocatalytic degradation of organic pollutants by Al3+ doped CuO powders under low power visible light and natural sunlight', *Opt. Mater.*, vol. 147, p. 114653, Jan. 2024, doi: 10.1016/j.optmat.2023.114653.

[183] D. S. Murali, S. Kumar, R. J. Choudhary, A. D. Wadikar, M. K. Jain, and A. Subrahmanyam, 'Synthesis of Cu2O from CuO thin films: Optical and electrical

properties', *AIP Adv.*, vol. 5, no. 4, p. 047143, Apr. 2015, doi: 10.1063/1.4919323.

[184] P. Mishra, R. Dobhal, R. E.G, M. Kumar, and S. Sen, 'Rapid organic dye degradation and wavelength dependent sensing study in CuFeO', *Ceram. Int.*, vol. 48, Nov. 2021, doi: 10.1016/j.ceramint.2021.11.135.

[185] M. ul haq, M. Iqbal, M. A. Z. G. Sial, S. Shabbir, M. Siddiq, and A. Iqbal, 'Effect of Fe doping on the crystallinity of CuO nanotubes and the efficiency of the hybrid solar cells', *J. Photochem. Photobiol. Chem.*, vol. 335, pp. 112–118, Feb. 2017, doi: 10.1016/j.jphotochem.2016.11.020.

[186] S. Landi, I. R. Segundo, E. Freitas, M. Vasilevskiy, J. Carneiro, and C. J. Tavares, 'Use and misuse of the Kubelka-Munk function to obtain the band gap energy from diffuse reflectance measurements', *Solid State Commun.*, vol. 341, p. 114573, Jan. 2022, doi: 10.1016/j.ssc.2021.114573.

[187] J. Tauc, R. Grigorovici, and A. Vancu, 'Optical Properties and Electronic Structure of Amorphous Germanium', *Phys. Status Solidi B*, vol. 15, no. 2, pp. 627–637, 1966, doi: 10.1002/pssb.19660150224.

[188] M. Shafayatul Islam, K. Roy Chowdhury, S. Manjura Hoque, and A. Sharif, 'Cationic and oxygen defect modulation for tailoring the bandgap and room temperature ferromagnetism of CuO via multiple d-block cations', *Mater. Adv.*, vol. 5, no. 7, pp. 2946–2967, 2024, doi: 10.1039/D3MA00987D.

[189] M. M. Abrar, A. Kabir, and S. S. Nishat, 'A DFT+U study on the structural, electronic, magnetic, and optical properties of Fe and Co co-doped CuO', *Mater. Today Commun.*, vol. 32, p. 103923, Aug. 2022, doi: 10.1016/j.mtcomm.2022.103923.

[190] G. Zhang, Y. Li, X. Zhao, J. Xu, and Y. Zhang, 'The variation of microstructures, spectral characteristics and catalysis effects of Fe3+ and Zn2+ co-doped CeO2 solid solutions', *J. Rare Earths*, vol. 38, no. 3, pp. 241–249, Mar. 2020, doi: 10.1016/j.jre.2019.04.016.

[191] H. Siddiqui, M. R. Parra, P. Pandey, M. S. Qureshi, and F. Z. Haque, 'Performance evaluation of optimized leaf-shaped two-dimension (2D) potassium doped CuO nanostructures with enhanced structural, optical and electronic properties', *Ceram. Int.*, vol. 46, no. 12, pp. 20404–20414, Aug. 2020, doi: 10.1016/j.ceramint.2020.05.131.

[192] E. Cano, C. L. Torres, and J. M. Bastidas, 'An XPS study of copper corrosion originated by formic acid vapour at 40% and 80% relative humidity', *Mater. Corros.*, vol. 52, no. 9, pp. 667–676, 2001, doi: 10.1002/1521-4176(200109)52:9%3C667::AID-MACO667%3E3.0.CO;2-H.

[193] A. Mehmood *et al.*, 'Innovative approach to synthesize Mo-Doped CuO Nanostructures: Uncovering structural and photocatalytic insights', *J. Mol. Liq.*, vol. 395, p. 123768, Feb. 2024, doi: 10.1016/j.molliq.2023.123768.

[194] T. R. Seling *et al.*, 'Transition metal-doped CuO nanosheets for enhanced visible-light photocatalysis', *J. Photochem. Photobiol. Chem.*, vol. 448, p. 115356, Feb. 2024, doi:

10.1016/j.jphotochem.2023.115356.

[195] A. M. El Sayed and M. Shaban, ‘Structural, optical and photocatalytic properties of Fe and (Co, Fe) co-doped copper oxide spin coated films’, *Spectrochim. Acta. A. Mol. Biomol. Spectrosc.*, vol. 149, pp. 638–646, Oct. 2015, doi: 10.1016/j.saa.2015.05.010.

[196] N. Thakur *et al.*, ‘Antibacterial and photocatalytic activity of undoped and (Ag, Fe) co-doped CuO nanoparticles via microwave-assisted method.’, *Nanofabrication*, vol. 7, 2022, doi: https://doi.org/10.37819/nanofab.007.186.

[197] M. Fu *et al.*, ‘Photo-Fenton Process over an Fe-Free 3%-CuO/Sr0.76Ce0.16WO4 Photocatalyst under Simulated Sunlight’, *ACS Omega*, vol. 6, no. 41, pp. 27297–27304, Oct. 2021, doi: 10.1021/acsomega.1c04107.

[198] T. R. Seling *et al.*, ‘Transition metal-doped CuO nanosheets for enhanced visible-light photocatalysis’, *J. Photochem. Photobiol. Chem.*, vol. 448, p. 115356, Feb. 2024, doi: 10.1016/j.jphotochem.2023.115356.

[199] L. C. Seitz *et al.*, ‘A highly active and stable IrOx/SrIrO3 catalyst for the oxygen evolution reaction’, *Science*, vol. 353, no. 6303, pp. 1011–1014, Sep. 2016, doi: 10.1126/science.aaf5050.

[200] J. Rossmeisl, Z.-W. Qu, H. Zhu, G.-J. Kroes, and J. K. Nørskov, ‘Electrolysis of water on oxide surfaces’, *J. Electroanal. Chem.*, vol. 607, no. 1, pp. 83–89, Sep. 2007, doi: 10.1016/j.jelechem.2006.11.008.

[201] T. Bligaard, J. K. Nørskov, S. Dahl, J. Matthiesen, C. H. Christensen, and J. Sehested, ‘The Brønsted–Evans–Polanyi relation and the volcano curve in heterogeneous catalysis’, *J. Catal.*, vol. 224, no. 1, pp. 206–217, May 2004, doi: 10.1016/j.jcat.2004.02.034.

[202] A. D. Handoko *et al.*, ‘Enhanced activity of H2O2-treated copper(II) oxide nanostructures for the electrochemical evolution of oxygen’, doi: 10.1039/C5CY00861A.

[203] Y. Deng, A. D. Handoko, Y. Du, S. Xi, and B. S. Yeo, ‘In Situ Raman Spectroscopy of Copper and Copper Oxide Surfaces during Electrochemical Oxygen Evolution Reaction: Identification of CuIII Oxides as Catalytically Active Species’, *ACS Catal.*, vol. 6, no. 4, pp. 2473–2481, Apr. 2016, doi: 10.1021/acscatal.6b00205.

[204] L. Reith *et al.*, ‘In Situ Detection of Iron in Oxidation States ≥ IV in Cobalt-Iron Oxyhydroxide Reconstructed during Oxygen Evolution Reaction’, *Adv. Energy Mater.*, vol. 13, no. 12, p. 2203886, 2023, doi: 10.1002/aenm.202203886.

[205] R. Mehmood *et al.*, ‘Confirming High-Valent Iron as Highly Active Species of Water Oxidation on the Fe, V-Coupled Bimetallic Electrocatalyst: In Situ Analysis of X-ray Absorption and Mössbauer Spectroscopy’, *J. Am. Chem. Soc.*, vol. 145, no. 22, pp. 12206–12213, Jun. 2023, doi: 10.1021/jacs.3c02288.

[206] J. Y. C. Chen *et al.*, ‘Operando Analysis of NiFe and Fe Oxyhydroxide Electrocatalysts for Water Oxidation: Detection of Fe4+ by Mössbauer Spectroscopy’, *J. Am. Chem. Soc.*, vol. 137, no. 48, pp. 15090–15093, Dec. 2015, doi: 10.1021/jacs.5b10699.

[207] D. Friebel *et al.*, 'Identification of Highly Active Fe Sites in (Ni,Fe)OOH for Electrocatalytic Water Splitting', *J. Am. Chem. Soc.*, vol. 137, no. 3, pp. 1305–1313, Jan. 2015, doi: 10.1021/ja511559d.

[208] C. Fan *et al.*, 'Fe-Doped α-MnO_2 nanorods for the catalytic removal of NO_x and chlorobenzene: the relationship between lattice distortion and catalytic redox properties', *Phys. Chem. Chem. Phys.*, vol. 21, no. 46, pp. 25880–25888, 2019, doi: 10.1039/C9CP04930D.

[209] F. Shao-jie and Y. Jian-xin, 'TPD/TPR investigation of the stabilization of Fe doping for SrCoO_(3-δ)', *J. Anhui Inst. Archit. Ind.*, 2006, Accessed: Jan. 13, 2026. [Online]. Available: https://www.semanticscholar.org/paper/TPD-TPR-investigation-of-the-stabilization-of-Fe-Shao-jie-Jian-xin/59cfedbf0a76709c4964ed6e1c4d92839e7212a6

[210] B. Yao *et al.*, 'Iron-Induced Localized Oxide Path Mechanism Enables Efficient and Stable Water Oxidation', *Angew. Chem. Int. Ed.*, vol. 64, no. 4, p. e202416141, 2025, doi: 10.1002/anie.202416141.

[211] D. A. Corrigan, 'The Catalysis of the Oxygen Evolution Reaction by Iron Impurities in Thin Film Nickel Oxide Electrodes', *J. Electrochem. Soc.*, vol. 134, no. 2, p. 377, Feb. 1987, doi: 10.1149/1.2100463.

[212] L. Trotochaud, S. L. Young, J. K. Ranney, and S. W. Boettcher, 'Nickel–Iron Oxyhydroxide Oxygen-Evolution Electrocatalysts: The Role of Intentional and Incidental Iron Incorporation', *J. Am. Chem. Soc.*, vol. 136, no. 18, pp. 6744–6753, May 2014, doi: 10.1021/ja502379c.

[213] B. A. Boukamp, 'Electrochemical impedance spectroscopy in solid state ionics: recent advances', *Solid State Ion.*, vol. 169, no. 1, pp. 65–73, Apr. 2004, doi: 10.1016/j.ssi.2003.07.002.

[214] F. Ciucci and C. Chen, 'Analysis of Electrochemical Impedance Spectroscopy Data Using the Distribution of Relaxation Times: A Bayesian and Hierarchical Bayesian Approach', *Electrochimica Acta*, vol. 167, pp. 439–454, Jun. 2015, doi: 10.1016/j.electacta.2015.03.123.

[215] T. H. Wan, M. Saccoccio, C. Chen, and F. Ciucci, 'Influence of the Discretization Methods on the Distribution of Relaxation Times Deconvolution: Implementing Radial Basis Functions with DRTtools', *Electrochimica Acta*, vol. 184, pp. 483–499, Dec. 2015, doi: 10.1016/j.electacta.2015.09.097.

[216] I. C. Man *et al.*, 'Universality in Oxygen Evolution Electrocatalysis on Oxide Surfaces', *ChemCatChem*, vol. 3, no. 7, pp. 1159–1165, 2011, doi: 10.1002/cctc.201000397.

[217] F. Calle-Vallejo *et al.*, 'Finding optimal surface sites on heterogeneous catalysts by counting nearest neighbors', *Science*, vol. 350, no. 6257, pp. 185–189, Oct. 2015, doi: 10.1126/science.aab3501.

[218] A. K. Mishra, A. Roldan, and N. H. de Leeuw, 'CuO Surfaces and CO2 Activation: A Dispersion-Corrected DFT+U Study', *J. Phys. Chem. C*, vol. 120, no. 4, pp. 2198–2214,

Feb. 2016, doi: 10.1021/acs.jpcc.5b10431.

[219] Y. Wu, R. Fang, L. Shen, and H. Bai, 'Dual mechanisms in hydrogen reduction of copper oxide: surface reaction and subsurface oxygen atom transfer', doi: 10.1039/D4RA01240B.

[220] R. Nelson, C. Ertural, J. George, V. L. Deringer, G. Hautier, and R. Dronskowski, 'LOBSTER: Local orbital projections, atomic charges, and chemical-bonding analysis from projector-augmented-wave-based density-functional theory', *J. Comput. Chem.*, vol. 41, no. 21, pp. 1931–1940, 2020, doi: 10.1002/jcc.26353.

[221] H. Radinger, V. Trouillet, F. Bauer, and F. Scheiba, 'Work Function Describes the Electrocatalytic Activity of Graphite for Vanadium Oxidation', *ACS Catal.*, vol. 12, no. 10, pp. 6007–6015, May 2022, doi: 10.1021/acscatal.2c00334.

[222] N. Kitchamsetti *et al.*, 'Theory abide experimental investigations on morphology driven enhancement of electrochemical energy storage performance for manganese titanate perovskites electrodes', *J. Power Sources*, vol. 538, p. 231525, Aug. 2022, doi: 10.1016/j.jpowsour.2022.231525.

[223] S. Trasatti, 'Work function, electronegativity, and electrochemical behaviour of metals: III. Electrolytic hydrogen evolution in acid solutions', *J. Electroanal. Chem. Interfacial Electrochem.*, vol. 39, no. 1, pp. 163–184, Sep. 1972, doi: 10.1016/S0022-0728(72)80485-6.

[224] Z. Chen, T. Ma, W. Wei, W.-Y. Wong, C. Zhao, and B.-J. Ni, 'Work Function-Guided Electrocatalyst Design', *Adv. Mater.*, vol. 36, no. 29, p. e2401568, Jul. 2024, doi: 10.1002/adma.202401568.

[225] G. Kresse and J. Furthmüller, 'Efficient iterative schemes for ab initio total-energy calculations using a plane-wave basis set', *Phys. Rev. B*, vol. 54, no. 16, pp. 11169–11186, Oct. 1996, doi: 10.1103/PhysRevB.54.11169.

[226] J. P. Perdew, K. Burke, and M. Ernzerhof, 'Generalized Gradient Approximation Made Simple', *Phys. Rev. Lett.*, vol. 77, no. 18, pp. 3865–3868, Oct. 1996, doi: 10.1103/PhysRevLett.77.3865.

[227] Y.-M. Juan, E. Kaxiras, and R. G. Gordon, 'Use of the generalized gradient approximation in pseudopotential calculations of solids', *Phys. Rev. B*, vol. 51, no. 15, pp. 9521–9525, Apr. 1995, doi: 10.1103/PhysRevB.51.9521.

[228] B. X. Yang, J. M. Tranquada, and G. Shirane, 'Neutron scattering studies of the magnetic structure of cupric oxide', *Phys. Rev. B*, vol. 38, no. 1, pp. 174–178, Jul. 1988, doi: 10.1103/PhysRevB.38.174.

[229] R. P. Feynman, 'Forces in Molecules', *Phys. Rev.*, vol. 56, no. 4, pp. 340–343, Aug. 1939, doi: 10.1103/PhysRev.56.340.

[230] S. Pathak *et al.*, 'Accurate Hellmann–Feynman forces from density functional calculations with augmented Gaussian basis sets', *J. Chem. Phys.*, vol. 158, no. 1, p.

014104, Jan. 2023, doi: 10.1063/5.0130668.

[231] H. J. Monkhorst and J. D. Pack, ‘Special points for Brillouin-zone integrations’, *Phys. Rev. B*, vol. 13, no. 12, pp. 5188–5192, Jun. 1976, doi: 10.1103/PhysRevB.13.5188.

[232] D. Yu *et al.*, ‘Electronic structure modulation of iron sites with fluorine coordination enables ultra-effective H2O2 activation’, *Nat. Commun.*, vol. 15, no. 1, p. 2241, Mar. 2024, doi: 10.1038/s41467-024-46653-6.

[233] J. Neugebauer and M. Scheffler, ‘Adsorbate-substrate and adsorbate-adsorbate interactions of Na and K adlayers on Al(111)’, *Phys. Rev. B*, vol. 46, no. 24, pp. 16067–16080, Dec. 1992, doi: 10.1103/PhysRevB.46.16067.

[234] S. Grimme, J. Antony, S. Ehrlich, and H. Krieg, ‘A consistent and accurate ab initio parametrization of density functional dispersion correction (DFT-D) for the 94 elements H-Pu’, *J. Chem. Phys.*, vol. 132, no. 15, p. 154104, Apr. 2010, doi: 10.1063/1.3382344.

[235] S. Grimme, S. Ehrlich, and L. Goerigk, ‘Effect of the damping function in dispersion corrected density functional theory’, *J. Comput. Chem.*, vol. 32, no. 7, pp. 1456–1465, 2011, doi: 10.1002/jcc.21759.

[236] R. Nelson, C. Ertural, J. George, V. L. Deringer, G. Hautier, and R. Dronskowski, ‘LOBSTER: Local orbital projections, atomic charges, and chemical-bonding analysis from projector-augmented-wave-based density-functional theory’, *J. Comput. Chem.*, vol. 41, no. 21, pp. 1931–1940, 2020, doi: 10.1002/jcc.26353.

[237] S. L. Dudarev, G. A. Botton, S. Y. Savrasov, C. J. Humphreys, and A. P. Sutton, ‘Electron-energy-loss spectra and the structural stability of nickel oxide: An LSDA+U study’, *Phys. Rev. B*, vol. 57, no. 3, pp. 1505–1509, Jan. 1998, doi: 10.1103/PhysRevB.57.1505.

[238] V. Wang, N. Xu, J.-C. Liu, G. Tang, and W.-T. Geng, ‘VASPKIT: A user-friendly interface facilitating high-throughput computing and analysis using VASP code’, *Comput. Phys. Commun.*, vol. 267, p. 108033, Oct. 2021, doi: 10.1016/j.cpc.2021.108033.

[239] K. Momma and F. Izumi, ‘VESTA 3 for three-dimensional visualization of crystal, volumetric and morphology data’, *J. Appl. Crystallogr.*, vol. 44, no. 6, pp. 1272–1276, Dec. 2011, doi: 10.1107/S0021889811038970.

[240] S. Kattel and G. Wang, ‘Reaction Pathway for Oxygen Reduction on FeN4 Embedded Graphene’, *J. Phys. Chem. Lett.*, vol. 5, no. 3, pp. 452–456, Feb. 2014, doi: 10.1021/jz402717r.

[241] Z. Chen *et al.*, ‘Cu Anchored Ti2NO2 as High Performance Electrocatalyst for Oxygen Evolution Reaction: A Density Functional Theory Study’, *ChemCatChem*, vol. 12, no. 16, pp. 4059–4066, 2020, doi: 10.1002/cctc.202000591.

[242] J. O. Bockris and T. Otagawa, ‘Mechanism of oxygen evolution on perovskites’, *J. Phys. Chem.*, vol. 87, no. 15, pp. 2960–2971, Jul. 1983, doi: 10.1021/j100238a048.

[243] J. O. Bockris and T. Otagawa, ‘The Electrocatalysis of Oxygen Evolution on Perovskites’, *J. Electrochem. Soc.*, vol. 131, no. 2, p. 290, Feb. 1984, doi: 10.1149/1.2115565.

[244] Q. Liang, G. Brocks, and A. Bieberle-Hütter, ‘Oxygen evolution reaction (OER) mechanism under alkaline and acidic conditions’, *J. Phys. Energy*, vol. 3, no. 2, p. 026001, Mar. 2021, doi: 10.1088/2515-7655/abdc85.

[245] Á. Valdés, Z.-W. Qu, G.-J. Kroes, J. Rossmeisl, and J. K. Nørskov, ‘Oxidation and Photo-Oxidation of Water on TiO2 Surface’, *J. Phys. Chem. C*, vol. 112, no. 26, pp. 9872–9879, Jul. 2008, doi: 10.1021/jp711929d.

[246] G. Kresse, ‘Dissociation and sticking of ${\mathrm{H}}_{2}$ on the Ni(111), (100), and (110) substrate’, *Phys. Rev. B*, vol. 62, no. 12, pp. 8295–8305, Sep. 2000, doi: 10.1103/PhysRevB.62.8295.